

ROTARY KILN TRANSPORT PHENOMENA: STUDY OF THE
BED MOTION AND HEAT TRANSFER

By

AKWASI A. BOATENG

M.Sc (ME), People's Friendship University, Moscow, 1982

M.Sc.E (ME), University of New Brunswick, Canada, 1985

A THESIS SUBMITTED IN PARTIAL FULFILLMENT OF
THE REQUIREMENTS FOR THE DEGREE OF
DOCTOR OF PHILOSOPHY

in

THE FACULTY OF GRADUATE STUDIES

(Department of Metals and Materials Engineering)

We accept this as conforming to the
required standard

THE UNIVERSITY OF BRITISH COLUMBIA

July, 1993

© Akwasi A. Boateng

In presenting this thesis in partial fulfilment of the requirements for an advanced degree at the University of British Columbia, I agree that the Library shall make it freely available for reference and study. I further agree that permission for extensive copying of this thesis for scholarly purposes may be granted by the head of my department or by his or her representatives. It is understood that copying or publication of this thesis for financial gain shall not be allowed without my written permission.

(Signature)

Department of Metals & Materials Engineering

The University of British Columbia
Vancouver, Canada

Date July 8, 1993

ABSTRACT

Thermal processing of materials in rotary kilns involves heat transfer from the freeboard to the boundary surfaces of bed material and the distribution of this thermal energy within the granular bed. Although the former has been reasonably well characterized, the latter has not, mainly because of difficulty in predicting flow within the bed. Bed motion in the cross-section is fundamental in determining advective heat transport as well as axial progress of the bed material, but to date studies have been mainly empirical and aimed at determining the overall bed motion but not the detailed information required to evaluate transport phenomena. The current study is therefore aimed at the development of a flow model for the bed transverse plane and the subsequent application of this model in order to determine both segregation and temperature distribution in two-dimensions.

The development of the flow model was based on granular flow theories used for chutes, avalanches etc., since these also involve granular materials and it involves aspects of fluid mechanics, soil mechanics, and rheology. The constitutive equations for such flows draw on the assumption of a continuum similar in some regard to viscous fluids except that the equilibrium states of the theories are not states of hydrostatic pressure but are rather states that are specified by a yield criterion. By considering the active layer (the shearing region near the bed surface) to be thin, relative to the chord length, the applied granular flow equations reduce to the boundary layer equations of Prandtl, which are solved to obtain the active layer thickness and the velocity field in the cross-section.

An experimental campaign was organized in order to study the characteristics of transport mechanisms and to provide the relevant boundary conditions for the flow model. In addition, it provided data for the validation of the mathematical model. Granular flow behavior studies were carried out in an 0.96 m I.D. rotary drum. Granular materials studied included polyethylene pellets, long grain rice, and limestone. Particle velocity measurements were made using optical fibre probes from which the active layer depth was established.

The mathematical model, supported by the experimental studies, found the solids concentration to be the most sensitive parameter of the flow behavior. Hence, as the dilation of the bed increases, the quantity of the material entering into the sheared region (i.e., active layer) also increases. Increasing the coefficient of restitution of the particles by a fraction results in a decrease in the granular temperature, and for that matter, diffusion by tenfold. However, the coefficient of restitution has almost no effect on the shear rate; i.e., on active layer depth or velocity in the active layer. The effect of the angle of repose of the material on the flow behavior is similar to that of the coefficient of restitution of the material. Good agreement is found between model predictions and experimental results. The model was used to establish kinetic diffusion; the velocity field required for the calculation of the advective transport of sensible heat in the bed, and also particle segregation in the bed.

Segregation of particles, due to size and density differences, is known to occur in rotary kilns and promotes temperature nonuniformities but has not been quantified due to inadequate flow models. Most previous studies characterize segregation by statistical methods which, although often helpful, tend to conceal the details of the phenomenon and yield little information. A model was developed to predict the preferential movement of particles in the shearing active layer. This model determines the extent of fine particle segregation and is based on the principle of percolation in the active layer, whereby fines sieve through the matrix of the bed to form a segregated core. Incorporating the flow results, it was possible to establish the dimensions of the segregated core as well as fines (jetsam) concentration in the rest of the bed cross-section. This result is used to assess the effect of segregation on bed temperature nonuniformities.

A mathematical model was developed to predict heat transfer from the freeboard gas to the bed and the redistribution of this energy within the bed. The thermal model incorporates a two dimensional representation of the bed transverse plane into a conventional one-dimensional, plug flow type model for the rotary kiln. The result a quasi-three-dimensional

rotary kiln model, significantly improves the ability to simulate conditions within the bed without the necessity of rigorously accounting for the complex flow and combustion phenomena of the freeboard. The combined axial and bed model, which is capable of predicting the temperature distribution within the bed and the refractory wall at any axial position of the kiln, is used to examine the role of the various mechanisms for heat transfer over a cross-section of a kiln, for example the regenerative action of the wall and the effect of the active layer of bed material on redistribution of energy within the bed. The results from the mathematical model are in agreement with experimental data obtained from a well instrumented 0.41 m I.D by 5.5 m long pilot kiln.

For a stationary kiln (no rotation), measured thermal gradients in the radial direction of the bed are in agreement with model predictions, thus validating the continuum assumption employed by the model. For a rotating kiln the temperature distribution within the bed shows a strong dependence on bed behavior; i.e. the flow pattern in the transverse plane. Because the bed material is turned over about three times per kiln revolution, the Peclet numbers for material flow in the cross-section are sufficiently large to ensure the predominance of advective heat transfer over conduction effects. The model is used to demonstrate that, for a segregated bed of small and large particles, or for zero mixing, as would prevail in some cases of slumping and/or slipping bed behavior, radial temperature gradients (about 100°C) are possible within the bed. Conversely, it is shown that, for uniform size particles, and in the rolling bed mode, self diffusion enhances effective bed thermal conductivity, the temperature gradients will vanish, and the bed material in the transverse plane must be essentially isothermal. The global model consisting of the granular flow model, the segregation model, and the heat transfer model, can be a useful tool to predict temperature nonuniformities in rotary kiln processes and to achieve product quality.



Table of Contents

Abstract	ii
List of Tables	vii
List of Figures	viii
Nomenclature	xvii
Acknowledgements	xxi
CHAPTER 1. INTRODUCTION	1
CHAPTER 2. LITERATURE REVIEW	10
Bed Motion Along the Kiln Axis	10
Bed Motion in the Transverse Plane of the Kiln	12
Modelling the Flow of Granular Materials (Granular Flows)	15
2.3.1 The Equations of Motion for Granular Flows	19
Mixing and Segregation in the Transverse Plane of the Kiln	22
Rotary Kiln Thermal Models	25
2.5.1 One-dimensional Models	26
2.5.2 Heat Transfer Between the Covered Wall and the Bed	27
2.5.3 Heat Transfer in the Kiln Freeboard	28
2.5.4 Effective Thermal Conductivity of Packed Beds	30
Review Summary	32
2.6.1 Bed Motion	32
2.6.2 Heat Transfer	33
CHAPTER 3. OBJECTIVES AND SCOPE OF WORK	42
CHAPTER 4. EXPERIMENTAL STUDY OF GRANULAR SHEAR FLOW IN THE TRANSVERSE PLANE	43
Introduction	43
Experimental Apparatus	44
Materials Employed and Their Characterization	47
Parameters Derived from the Data	48
Experimental Results and Discussion	50
4.5.1 An Overview of the Experimental Results	51
4.5.2 A Detailed Discussion of the Experimental Results	55
Summary and Conclusions	61
Tables and Figures	64
CHAPTER 5. MODELLING THE GRANULAR FLOW IN TRANSVERSE PLANE	91
Introduction	91
Model Description	91
5.2.1 Simplifying Assumptions	92
5.2.2 Governing Equations for Momentum Conservation	93
5.2.2.1 The Integral Equation for Momentum Conservation	98
5.2.3 Solution of the Momentum Equation in the Active Layer of the Bed	102
5.2.3.1 Velocity Profile in the Active Layer	103

5.2.3.2 Density and Granular Temperature Profiles	106
5.2.3.3 The Analytical Expression Developed for the Thickness of the Active Layer	108
5.2.3.4 Numerical Solution for the Momentum Equation	110
Model Validation from the Experimental Results	111
Application of the Flow Model	113
Model Prediction for Flow in the Transverse Plane	117
Summary and Conclusions	118
Tables and Figures	120
CHAPTER 6. MODELLING OF PARTICLE MIXING AND SEGREGATION IN THE TRANSVERSE PLANE	145
Introduction	145
The Model Developed for Segregation within the Bed	146
6.2.1 The Governing Equations for Segregation	149
6.2.2 Boundary Conditions	153
6.2.3 Solution of the Segregation Equation	154
6.2.4 Numerical Solution of the Governing Equations	157
Validation of the Segregation Model	159
6.3.1 Application of Segregation Model	161
6.3.2 Discussion of Mixing Through Density Compensation	163
Summary and Conclusions	164
Figures	166
CHAPTER 7. HEAT TRANSFER PROCESSES IN ROTARY KILNS	180
Introduction	180
Description of the Thermal Model	180
7.2.1 The One-dimensional Thermal Model Applied to the Bed and Freeboard ..	181
7.2.2 The Two-dimensional Model Developed for the Bed	184
7.2.3 The Combined Axial and Cross-sectional: The Quasi- Three- Dimensional Model for the Bed	186
7.2.4 Solution Procedure	188
Experimental	192
Validation of the Thermal Model	193
7.4.1 Validation of the One-dimensional Model	193
7.4.2 Validation of the Cross-Sectional Model	194
7.4.3 Heat Transfer Rates within Kiln Cross-section	199
7.4.4 Effect of Segregation on Bed Temperature Distribution	200
Summary and Conclusions	201
CHAPTER 8. CONCLUSIONS AND RECOMMENDATIONS	230
LITERATURE CITED	234
APPENDICES	240

List of Tables

<u>Table</u>		<u>Page</u>
2.1	Solid-Fluid Heat Transfer Models for Packed Beds with Constant Radial Temperature	34
4.1	Estimated Relevant Properties of Material Used in Flow Experiment	65
4.2	Data on Flow Characteristics for Polyethylene Pellets	66
4.3	Data on Flow Characteristics for Rice Grains	67
4.4	Data on Flow Characteristics for Limestone	68
5.1	Parameter Estimation for Surface Velocity, $C_o = A \omega^a p^b$	120
5.2	Coefficients Resulting from Velocity Profile	120
5.3	Coefficients Resulting from Integro-Momentum Equation	120
5.4	Model Validation for Active Layer Depth	121
7.1	Relevant Physical Properties	204
7.2	Run Conditions for Pilot Kiln Trials Used in Model Validation	204

List of Figures

<u>Figure</u>	<u>Page</u>
1.1 An Axial Section of a Rotary Kiln Depicting it as a Counter-Current Heat Exchanger	5
1.2 Heat Transfer at the Interfacial Surfaces of the Bed Material over a Transverse Section of the Rotary Kiln	6
1.3 Heat Transfer Paths in Packed Beds: 1. Within Particle Conduction; 2. Conduction across Particle-Particle Contact; 3. Particle-to-Particle Radiation; 4. Interstitial Gas Convection	7
1.4 Rolling Bed Motion Depicting Two Distinct Regions <i>Top Section: Active Layer; Bottom Section: Plug Flow Region</i>	8
1.5 Radial Segregation of Particles with Different Sizes in a Rotary Kiln Showing the Segregated Core Dubbed 'The Tongue.'	9
2.1 Transverse Bed Motion Showing Various Modes of Operation	35
2.2 Bed Behavior Diagram for Limestone Depicting Regimes of Operation as Function of Operating Parameters of the Kiln (Henein, 1980)	36
2.3 Schematic Showing Movement of the Centroid of Bed Material Used by Pershin (1988) in the Development of an Equilibrium Model that may Predict Active Layer Depth	37
2.4 Comparison of Granular Flow Behavior with Other Type Flows from Davies (1986)	38
2.5 Random Continuous Network of Segregating Particles from (Savage, 1989)	39
2.6 Schematic of Expected Radial Temperature Profiles in Refractory Wall from Barr (1986)	40
2.7 Packed Bed Models Formulation	41
4.1 The Experimental Apparatus Showing Rotary Drum and Instrumentation for Velocity Measurements	69
4.2 Optic Probe Tip, Fibre Orientation, and Theoretical Response Curves	70
4.3 Typical Cross Correlation Curve for the Two Optical Fibre Probes Placed 5 mm Apart	70

4.4	Velocity Calibration for Optical Fibre Probes Using Empty Drum; Calculated is the Tangential Velocity (ωR_o) for a Local Point on Flange	71
4.5	The Operational Modes for Present Experiment as per Bed Behavior Diagram of Henein <i>et al</i> (1983)	71
4.6	Bulk Velocity at the Exposed Bed Surface for Polyethylene Showing Effect of Glass End-piece (15% Fill and 5 rpm)	72
4.7	Bulk Velocity at the Exposed Bed Surface for Polyethylene Showing Skewness to Base of Transverse Plane: Drum run at 3.3% Fill and 5 rpm ...	72
4.8	Bulk Velocity at the Exposed Bed Surface for Rice Grains Showing Two Parabolic Profile Resulting from Changes in Dynamic Angle of Repose: Drum run at 10% Fill and 5 rpm	73
4.9	Shape of Active Layer for Polyethylene Pellets Showing Symmetry at Mid-chord	73
4.10	Bulk Velocity as Function of Depth and Rotational Speed Taken at Mid-chord Position; Shown here for Polyethylene Pellets at 29% Fill: a) 1 rpm, b) 3 rpm, and c) 5 rpm	74
4.11	Particle Count as Function of Depth and Rotational Speed Taken at Mid-chord Position; Shown here for Polyethylene Pellets at 29% Fill: a) 1 rpm, b) 3 rpm, and c) 5 rpm	75
4.12	Bulk Velocity as Function of Depth at Different Surface Locations Showing Similarities in Profile Irrespective of Surface Location: a) Polyethylene Pellets at 8.5% Fill and 2 rpm, b) Polyethylene Pellets at 15% Fill and 3 rpm	76
4.13	Granular Temperature as a Function of Depth; Shown here for Polyethylene Pellets at 29% Fill: a) 1 rpm, b) 3 rpm	77
4.14	Linear Concentration as Function of Depth; Shown here for Polyethylene Pellets: a) 15% Fill and 3 rpm, b) 29% Fill and 5 rpm	78
4.15	Bulk Velocity as Function of Depth for Different Material at Same Run Conditions; Shown here for 3.3% Fill: a) Polyethylene Pellets, b) Rice Grains, and c) Limestone	79
4.16	Particle Count as Function of Depth for Different Material at Same Run Conditions; Shown here for 3.3% Fill: a) Polyethylene Pellets, b) Rice Grains, and c) Limestone	80

4.17	Bulk Velocity as Function of Depth Depicting Structure Formation at Free surface; Shown here for Rice Grains at 10% Fill: a) 3 rpm, b) 4 rpm, and c) 5 rpm	81
4.18	Flow Characteristics at the Exposed Bed Surface Shown for Rice Grains at 10% Fill and 5 rpm; a) Granular Temperature, b) Linear Concentration	82
4.19	Flow Characteristics at the Exposed Bed Surface Shown for Limestone at 3.3% Fill and 2 rpm; a) Granular Temperature, b) Linear Concentration	83
4.20	Surface Velocity as Function of Chord Length Showing the Formation of Periodic Profiles as a Result of Low Energy Dissipation or Low Coefficient of Restitution; a) Rice Grains at 8.5% Fill and 3 rpm, and b) Limestone at 3.3% Fill and 2 rpm	84
4.21	Surface Velocity as Function of Depth for Polyethylene Pellets Depicting Fully Developed Flow at Mid-chord; a) 8.5% Fill at 5 rpm, and b) 29% Fill at 3 rpm	85
4.22	The Active Layer Depth as a Function of Cylinder Rotation shown for Polyethylene Pellets at 3.3, 8.5, 15, and 29% Fill	86
4.23	The Active Layer Depth as a Function of the Degree of Fill shown for Polyethylene Pellets at 2, 3, 4, and 5 rpm	86
4.24	The Active Layer Depth as a Function of Cylinder Rotation shown for Rice Grains at 3.3, 8.5, and 10% Fill	87
4.25	The Active Layer Depth as a Function of the Degree of Fill shown for Rice Grains at 3, 4, and 5 rpm	87
4.26	The Active Layer Depth as a Function of Cylinder Rotation shown for Polyethylene Pellets, Rice Grains, and Limestone all at 3.3% Fill	88
4.27	The Active Layer Depth as a Function of Cylinder Rotation shown for Polyethylene Pellets, Rice Grains, and Limestone all at 8.5% Fill	88
4.28	Relationship Between the Chord Length and the Degree of Fill	89
4.29	Shear Rate, du/dy , at the Active Layer for Polyethylene run at 3.3, 8.5, 15, and 29% Fill	89
4.30	Shear Rate, du/dy , at the Active Layer for Rice run at 3.3, 8.5, and 10% Fill	90
4.31	Shear Rate, du/dy , at the Active Layer for Limestone run at 3.3 and 8.5% Fill	90

5.1	Schematic of Kiln Cross-section Showing the Domain of the Flow Problem	122
5.2	Schematic Showing Scaling Variables Employed in Normalizing Governing Equations	123
5.3	Schematic of the Control Volume Used in Deriving Integro-Momentum Equations	124
5.4	Schematic Showing Normal and Shear Stresses Acting on a Control Volume of Granular Material	125
5.5	Schematic of Kiln Cross-section Showing the Calculation of Material Balance Between Active Layer and Plug Flow Region	126
5.6	Experimental Normalized Surface Velocity ($C_o = u_s/\omega R$) Shown as Function of Kiln Speed. (a) Polyethylene Pellets and (b) Rice Grains	127
5.7	Comparison of Experimental and Model Fit for Normalized Surface Velocity	128
5.8	The Ratio of the Depth of the Zero Velocity Line to the Depth of the Yield Line (Experimental Observations Through Glass End-piece)	128
5.9	Arbitrary Velocity Profiles Showing the Effect of the Boundary Conditions Imposed on Flow Model. Family of Profiles for (a) $\kappa = 5$; (b) $\kappa = 10$	129
5.10	Schematic of Kiln Cross-section Showing the Mesh Used in Computing Resultant Boundary Layer Equation	130
5.11	The Flow Chart for the Prediction of the Active Layer Depth and Velocity	131
5.12	Predicted and Measured Velocity as Function of Depth at Mid-Chord with Polyethylene in the 1 m I.D Rotary Drum Filled at 29%. (a) 1 rpm; (b) 3 rpm; (c) 5 rpm	132
5.13	Predicted and Measured Velocity as Function of Depth at Mid-Chord with Polyethylene in the 1 m I.D Rotary Drum Filled at 15%. (a) 2 rpm; (b) 3 rpm; (c) 4 rpm; (d) 5 rpm	133
5.14	Predicted and Measured Velocity as Function of Depth at Mid-Chord with Rice Grains in the 1 m I.D Rotary Drum Filled at 3 rpm. (a) 8.5% Fill; (b) 10% Fill	134

5.15	Predicted and Measured Velocity as Function of Depth at Mid-Chord with Limestone in the 1 m I.D Rotary Drum Filled at 3 rpm. (a) 3.3% Fill; (b) 8.5% Fill	135
5.16	Qualitative Comparison of Various Active Layer Depth Estimations	136
5.17	Model Prediction for Velocity in the Active Layer as a Function of Distance from Apex with Operational Conditions of 2 rpm and 12% Fill: (a) 0.41 m I.D Pilot Kiln; (b) 1 m I.D Drum; (c) 2.5 m I.D kiln	137
5.18	Model Prediction for Velocity in the Active Layer as a Function of Distance from Apex with Operational Conditions of 5 rpm and 12% Fill: (a) 0.41 m I.D Pilot Kiln; (b) 1 m I.D Drum; (c) 2.5 m I.D kiln	138
5.19	Predicted Velocity Profiles at Mid-Chord as a Function of Kiln Rotation Rate: (a) 0.41 m I.D Pilot Kiln; (b) 1 m I.D Rotary Drum; (c) 2.5 m I.D Industrial Kiln	139
5.20	Predicted Active Layer Depth as a Function of Kiln Rotation Rate: (a) 0.41 m I.D Pilot Kiln; (b) 1 m I.D Rotary Drum; (c) 2.5 m I.D Industrial Kiln; (d) Active Layer Thickness as Function of Rotational Rate	140
5.21	Predicted Granular Temperature as a Function of Kiln Rotation Rate: (a) 0.41 m I.D Pilot Kiln at 12% Fill; (b) 2.5 m I.D Industrial Kiln at 12% Fill	141
5.22	Predicted Kinetic Diffusion Coefficient as a Function of Kiln Rotation Rate: (a) 0.41 m I.D Pilot Kiln at 12% Fill; (b) 2.5 m I.D Industrial Kiln at 12% Fill	141
5.23	Effect of Solids Concentration on Flow Characteristics for Pilot Kiln at 12% Fill run at 2 rpm: (a) Effect on Velocity; (b) Effect on Active Layer Depth; (c) Effect on Diffusion	142
5.24	Effect of Particle Coefficient of Restitution on Flow Characteristics for Pilot Kiln at 12% Fill run at 2 rpm: (a) Effect on Diffusion; (b) Effect on Granular Temperature	143
5.25	Effect of Static Angle of Repose on the Diffusion Coefficient for 0.41 m I.D Pilot Kiln Filled at 12% and Operated at 2 rpm	143
5.26	Velocity Predictions for a Cross-section of the 0.41 m I.D Pilot Kiln at 12% Fill and 2 rpm	144
6.1	The mechanism of Percolation and the Calculation Domain for the Segregation Problem	166
6.2	Control Volume for the Material Conservation in the Active Layer	167

6.3	Mathematical Description for Material Balance in Control Volume; the Convective Flux, $w = Au(y)$, the Diffusion Flux, $r = D_y A$, and the Segregation Flux, $k = v_p A$	167
6.4	Predicted and Measured Profiles for Jetsam Concentration for a 40 cm Drum: Limestone, 3.11 rpm, 16% Fill. $d_{pF}/d_{pJ} = 8$, ($d_{pF} = 4.2mm$)	168
6.5	Predicted and Measured Profiles for Jetsam Concentration for a 40 cm Drum: Limestone at 3.11 rpm, 16% Fill. $d_{pF}/d_{pJ} = 8$, ($d_{pF} = 4.2mm$)	168
6.6	Predicted and Measured Profiles for Jetsam Concentration for a 40 cm Drum: Limestone at 3.11 rpm, 16% Fill. $d_{pF}/d_{pJ} = 8$, ($d_{pF} = 4.2mm$)	169
6.7	Predicted and Measured Profiles for Jetsam Concentration for a 40 cm Drum: Limestone at 3.19 rpm, 14% Fill. $d_{pF}/d_{pJ} = 8$, ($d_{pF} = 4.2mm$)	169
6.8	Predicted Jetsam Concentration in the Active Layer at the Mid-chord Position for the Three Cases Described in the Text: 0.41 m drum, 2 rpm, 12% Fill; Polyethylene Pellets, $CJ_0 = 0.2$, $d_{pF}/d_{pJ} = 2$	170
6.9	Predicted Jetsam Concentration in the Active Layer at the Mid-chord Position for the Three Cases Described in the Text: 0.41 m drum, 2 rpm, 12% Fill; Polyethylene Pellets, $CJ_0 = 0.3$, $d_{pF}/d_{pJ} = 2$	170
6.10	Predicted Jetsam Concentration in the Active Layer at the Mid-chord Position for the Three Cases Described in the Text: 0.41 m drum, 2 rpm, 12% Fill; Polyethylene Pellets, $CJ_0 = 0.5$, $d_{pF}/d_{pJ} = 2$	171
6.11	Predicted Jetsam Concentration in both Active Layer and Plug Flow Region Shown at the Mid-chord Position for Various Jetsam Loadings	172
6.12	Predicted Jetsam Concentration in both Active Layer and Plug Flow Region Shown at the Mid-chord Position for Various Jetsam Loadings	172
6.13	Predicted Jetsam Concentration in both Active Layer and Plug Flow Region as a Function of rpm at Mid-chord Position for Case I	173
6.14	Predicted Jetsam Concentration in both Active Layer and Plug Flow Region as a Function of rpm at Mid-chord Position for Case III	173
6.15	Predicted Jetsam Concentration Profile as a Function of Chord Length (Case I): 0.41 m Drum	174

6.16	Predicted Jetsam Concentration Profile as a Function of Chord Length (Case III): 0.41 m Drum	174
6.17	Contour Plots of Jetsam Concentration for Case I Predictions Using Operational Conditions of Henein (1980); Jetsam Loading at 9%; Limestone	175
6.18	Contour Plots of Jetsam Concentration for Case III Predictions Using Operational Conditions of Henein (1980); Jetsam Loading at 9%, Limestone	175
6.19	Contour Plots of Jetsam Concentration for Case I: 0.41 m Drum; 2 rpm, 12% Fill; Jetsam Loading at 20%; Polyethylene	176
6.20	Contour Plots of Jetsam Concentration for Case III: 0.41 m Drum; 2 rpm, 12% Fill; Jetsam Loading at 20%; Polyethylene	176
6.21	Comparison of Predictions for Jetsam Concentration in a 0.41 m Drum and a 2.5 m Drum at 12% Fill and Jetsam Loadings of 10%: (a) 2 rpm; (b) 5 rpm	177
6.22	Contour Plots of Jetsam Concentration in a 2.5 m Drum at 12% Fill and Jetsam Loading of 10%: (a) 2 rpm; (b) 5 rpm	178
6.23	Density Compensation of Particle Size Segregation Showing Density Ratio Required for Flotsam to Behave as Jetsam in a Mixture with Specified Size Ratio: (a) Larger size Ratios; (b) Detailed at Smaller Size Ratio	179
7.1	Global Model Layout	205
7.2	Axial and Transverse Slice of Rotary Kiln	206
7.3	Heat Transport Paths and their Thermal Resistance Network	207
7.4	Control Volume for Heat Transfer Calculation	208
7.5	Mesh for cross-sectional Model	209
7.6	Stationary Thermocouple Probe	210
7.7	Predicted and Measured Axial Temperature Profiles for Freeboard Gas, Refractory Wall, and Bed Using One-dimensional Model; (a) <i>Trial 1</i> , (b) <i>Trial 2</i>	211
7.8	Predicted Radiative Heat Transfer Coefficients as Function of Axial Position; (a) <i>Trial 1</i> , (b) <i>Trial 2</i>	212

7.9	Predicted and Measured Axial Average Temperature for Refractory Wall, and Bed Using Two-dimensional Model; (a) <i>Trial 1</i> , (b) <i>Trial 2</i>	213
7.10	Predicted and Measured Temperature for Refractory Wall as Function of Radial Position for Several Freeboard Gas Temperatures; (a) <i>Trial 1</i> , (b) <i>Trial 2</i>	214
7.11	Predicted and Measured Steady-State Wall Heat Lost as Function of Axial Position	215
7.12	Predicted and Measured Temperatures in a Stationary Bed and Wall as Function of Radial Position at Mid-chord	215
7.13	Contour Plots of Temperature Distribution Predicted by Two-dimensional 'Mixed Bed' Model Using Gas Temperature of 631°C for <i>Trial 1</i> : (a) 1.5 rpm; (b) 3 rpm; (c) 5 rpm	216
7.14	Contour Plots of Temperature Distribution Predicted by Two-dimensional 'Mixed Bed' Model Using Gas Temperature of 804°C for <i>Trial 1</i> : (a) 1.5 rpm; (b) 3 rpm; (c) 5 rpm	217
7.15	Contour Plots of Temperature Distribution Predicted by Two-dimensional 'Mixed Bed' Model for <i>Trial 2</i> at 701°C; (a) 1.5 rpm; (b) 3 rpm; (c) 5 rpm	218
7.16	Contour Plots of Temperature Distribution Predicted by Two-dimensional 'Mixed Bed' Model Using Gas Temperature of 953°C for <i>Trial 2</i> : (a) at 1.5 rpm; (b) 5 rpm	219
7.17	Predicted Thermal Conductivity (enhanced) as Function of Axial Position; Superimposed are Freeboard Gas Temperature Profiles	220
7.18	Contour Plots of Temperature Distribution Resulting from Running Two-dimensional Model without y-wise Velocity Vector but with Enhanced Bed Thermal Conductivity; <i>Trial 1</i> with $T_g = 804^\circ\text{C}$: (a) at 1.5 rpm; (b) 5 rpm	221
7.19	Contour Plots of Temperature Distribution Within the Bed Resulting from Running Two-dimensional Model with Percolation Velocity as y-wise Velocity and no Bed Enhanced Thermal Conductivity; <i>Trial 1</i> with $T_g = 804^\circ\text{C}$: (a) at 1.5 rpm; (b) 3 rpm; (c) 5 rpm	222
7.20	Contour Plots of Temperature Distribution Resulting from Running Two-dimensional Model without y-wise Velocity and no Bed Enhanced Thermal Conductivity; <i>Trial 1</i> with $T_g = 804^\circ\text{C}$: (a) at 1.5 rpm; (b) 3 rpm; (c) 5 rpm	223

7.21	Predicted Heat Transfer Rates as Function of Axial Position with Superimposed Freeboard Gas Temperatures: (a) <i>Trial 1</i> , (b) <i>Trial 2</i>	224
7.22	Predicted Exposed Wall Heat Transfer Coefficients as Function of Circumferential Position; (a) <i>Trial 1</i> , (b) <i>Trial 2</i>	225
7.23	Regenerative Action of Refractory Wall: (a) Cycling Wall Surface Temperature as Function of Circumferential Position; (b) Covered Wall Temperature Gradients	226
7.24	Contour Plots of Temperature Distribution in a 'Mixed Bed' at Local Gas Temperature of 1000°C: (a) 1.5 rpm; (b) 5 rpm	227
7.25	Contour Plots of Temperature Distribution in a 'Segregated Bed' at Local Gas Temperature of 1000°C	228
7.26	Contour Plots of Temperature Distribution in a 'Segregated Bed' at Local Gas Temperature of 1050°C	228
7.27	Contour Plots of Temperature Distribution in a 'Segregated Bed' at Local Gas Temperature of 1100°C	229
7.28	Contour Plots of Temperature Distribution in a 'Segregated Bed' at Local Gas Temperature of 1200°C	229
Plate 1	Contour Plots of Fines Concentration at Jetsam Loading of 10%: <i>Top</i> - 0.41 m I.D Drum; <i>Bottom</i> - 2.5 m I.D Drum	229a
Plate 2	Contour Plots of Temperature Distribution in a Cross-section at Local Gas Temperature of 1000°C	229b
Plate 3	Contour Plots of Temperature Distribution in a 'Mixed Bed' at Local Gas Temperature of 631°C	229c
Plate 4	Contour Plots of Temperature Distribution in a 'Mixed Bed' at Local Gas Temperature of 1000°C	229d
Plate 5	Contour Plots of Temperature Distribution in a 'Segregated Bed' at Local Gas Temperature of 1100°C and 1200°C	229e

Nomenclature

Symbol	
a_1', a_2'	Coefficients in momentum-integral equations
A	Interfacial area (m^2)
A_p, A_E, A_W, A_N, A_S	Coefficients in finite difference formulations
\mathbf{b}	Body force
b'	Coefficients resulting from velocity profile
\mathbf{c}	Particle local velocity vector
\mathbf{C}	Velocity fluctuation vector
C_F	Flotsam concentration (-)
c_i	Bagnold's constant for grain inertia
C_J	Jetsam concentration (-)
C_o	Normalized bed surface velocity (-)
C_p	Specific heat capacity at constant pressure, (kJ/kg)
C_{sp}	Characteristic particle spacing (1/m)
C_v	Specific heat of water vapor (kJ/kg)
C'	Apparent viscosity defined by Eq. 5.22
d_p	particle diameter (m)
D	Diffusion coefficient (m^2/s)
e	emissivity
e_o	void fraction
e_p	Coefficient of restitution of particles (-)
\bar{E}	Mean void diameter ratio
E_h	Thermal energy (sensible heat)
E_k	Kinetic energy associated with local average velocity
E_m	Void diameter ratio that results in spontaneous percolation
E_{PT}	Pseudo-thermal energy associated with velocity fluctuations

Fr	Rotational Froude number, ω^2/g , (-)
g	Acceleration due to gravity (m/s^2)
g_o	Pair distribution function in collisional theory
$g_1(v), g_2(v), \dots$	Terms defined in granular flow constitutive equations
G	Mass flow rate of gas (kg/s)
h	Heat transfer coefficient (W/m^2)
H	Bed depth (m)
H_i, H_j	Species enthalpy (KJ/kg)
k	Thermal conductivity (W/mK)
\bar{k}	Segregation flux (m^2s^2)
k_{av}	Ratio of mean voids projected area and mean projected total area
L	Distance from apex of bed cross-section to mid-chord
\dot{m}	mass flow rate (kg/s)
M/N	Ratio of number of voids to number of particles in a layer
n	Number of revolutions (1/s)
\mathbf{P}	Total stress tensor
p	Percent fill as defined in Eq. 5.30
Pe	Peclet number (-)
q	Energy flux
q_h	Flux of sensible energy
q_{PT}	Flux of pseudo-thermal energy
Q	Solids mass flow rate (kg/s)
Q_{net}	Net heat transfer (W)
\bar{r}	Diffusion flux (1/s)
R	Cylinder radius (m)
\mathbf{S}	Deviatoric stress
T	Temperature ($^{\circ}C$)
u	Velocity parallel to bed surface (m/s)
\bar{U}	Tangential velocity of rotary drum (m/s)

V_s	Solids velocity in axial direction (m/s)
v_p	Percolation velocity (m/s)
W	Mass of water in material (free moisture) (kg)
y	Arbitrary distance in active layer (m)
z	Axial distance (m)
Greek	
α	Thermal diffusivity (m^2/s)
β	Kiln slope (m/m)
γ	Energy dissipation due to inelastic collisions
δ, δ_x	Active layer depth at distance, x , from apex (m)
Δ	Active layer depth at mid-chord (m)
η	Expression for coefficient of restitution of particle (-)
$\bar{\eta}$	particle number ratio
θ	Angle subtended by bed material at cylinder center (rad)
κ	Ratio of surface velocity to plug flow velocity near yield line (-)
$\bar{\lambda}$	Dilation factor defined in Eq. 2.4
λ	Conductivity (granular or thermal)
λ	Latent heat of water vapor
μ	Viscosity (kg/m.s)
v	Solids volume concentration (solids fraction) (-)
ξ	Dynamic angle of repose
ρ	Bulk density (kg/m^3)
ρ_p	Particle density (kg/m^3)
σ_{xx}, σ_{yy}	Normal stress components
$\bar{\sigma}$	Particle size ratio (-)
τ	Shear stress
\tilde{T}	Granular temperature (grain temperature) (m^2/s^2)
ϕ	Static angle of repose of material

ω	Angular velocity (1/s)
	Subscript
<i>ax</i>	Axial
<i>AL</i>	Active layer
<i>b</i>	Bed
<i>c</i>	Collisional
<i>cb</i>	Covered bed
<i>cw</i>	Covered wall
<i>eb</i>	Exposed bed
<i>ew</i>	Exposed wall
<i>eff</i>	Effective
<i>f</i>	Frictional
<i>g</i>	Freeboard gas
<i>k</i>	Kinetic
<i>L</i>	Large
<i>PF</i>	Plug flow
<i>s</i>	Small
<i>w</i>	Wall
<i>shell</i>	Outer wall (shell)

Acknowledgements

I would like to extend sincere thanks to my supervisor, Dr. P.V. Barr, for his guidance in the thesis organization. I would also like to thank my supervisory committee, in particular, Dr. Paul Watkinson who always made me feel welcome.

I am indebted to Dr. J.R. Ferron of University of Rochester, for valuable discussions on mathematical problems of rotary reactors. Many technicians contributed to the realization of the experimental aspect of the thesis work.

Finally, I would like to thank my family for their tremendous patience and support without which this work would not have been possible.

Financial support for this research was provided, in part, by Alcan and the Natural Science and Engineering Research Council of Canada.

CHAPTER 1. INTRODUCTION

Rotary kilns are employed by industry to carry out a wide variety of material processing operations; for example calcining of limestone, reduction of oxide ore, clinkering of cementitious materials, reclamation of hydrated lime, calcining of petroleum coke, etc. This widespread usage can be attributed to such factors as the ability to handle varied feedstocks; for example slurries or granular materials having large variations in particle size, or the ability to maintain distinct environments; for example, reducing conditions within the bed coexisting with an oxidizing freeboard (a unique feature of the rotary kiln that is not easily achieved in other reactors). Operators of rotary kilns are not, however, without problems: dust generation, low thermal efficiency and nonuniform product quality being some of the difficulties which plague rotary kiln operations. Although the generally long residence time of the material within the kiln (typically greater than one hour) aids in achieving an acceptably uniform product, there is considerable scope for improving this aspect of kiln performance. In order to achieve this improvement a more quantitative understanding of transport phenomena within the bed material is required; specifically of momentum transport, which determines particle motion and energy transport, which, in turn, determines heating rate for individual particles. The objective of the present work is to provide this quantitative understanding.

Rotary kilns are basically heat exchangers in which energy from a hot gas phase is extracted by the bed material. During its passage along the kiln, the bed material will undergo various heat exchange processes, a typical sequence being drying, heating, and chemical reaction which cover a broad range of temperatures. Although non-contact (i.e., externally heated) rotary kilns are employed for specialized work, most kilns allow direct contact between the freeboard gas and bed material as shown in Figure 1.1. The most common configuration is for counter current flow whereby the bed and gas flows are in opposite directions although, co-current flow may be utilized in some instances.

In most rotary kiln operations the objective is to drive specific bed reactions which, for either kinetic or thermodynamic reasons, often require bed temperatures that, for example in cement kilns, may approach as high as 1800°C. The energy necessary to raise the bed temperature to the level required for reaction, and in some instances, for example the endothermic calcination of limestone, to drive the reactions themselves, originates with the combustion of hydrocarbon fuels in the freeboard near the burner and is subsequently transferred by heat exchange between the freeboard and the bed. Heat transfer between the freeboard and the bed is rather complex and occurs by all the paths and processes shown in Figure 1.2. Because the analytical tools for handling freeboard transport phenomena have been the subject of considerable research, for example the zone method (Guruz and Bac, 1981) for determining radiative heat transfer, or commercial software for calculating fluid flow (and occasionally combustion processes as well), our ability to simulate the freeboard conditions exceeds our ability to accurately determine conditions within the bed. Although numerous rotary kiln models have been proposed (see, e.g., Wes *et al.*, 1976; Tscheng and Watkinson, 1979; Brimacombe and Watkinson, 1979; Gorog *et al.*, 1981; etc.), virtually all of these assume that, at each axial position the bed is well mixed in the transverse plane; i.e. the bed material is isothermal over any transverse section of the kiln. However many kiln operations suffer considerable difficulty in achieving a uniform product, one example being lime kilns which experience chronic problems in preventing dead-burning of larger particles while fully calcining the finer particles. Evidence such as this, as well as operator experience, suggests that a substantial transverse temperature nonuniformity is generated within the bed. Thus the well-mixed assumption, although expedient to the modelling of the rotary kiln, is clearly deficient because it ignores the motion of the bed in the transverse plane or, more precisely, because it ignores the effect of this motion on the redistribution within the bed material of energy absorbed at the bed-freeboard interfacial surfaces.

During the processing of granular material in rotary kilns heat transfer within the bed material occurs by the same mechanisms as in any packed bed; i.e particle-to-particle conduction and

radiation, as well as interstitial gas-to-particle convection; these are shown in Figure 1.3. However, in the rotary kiln the movement of the granular material superimposes an advective component for energy transport which has the potential to dominate heat transfer. In general, the transverse bed motion established in rotary kilns will depend on the rotation rate, degree of fill and rheology of the particles. The most desirable bed motion is usually the rolling mode shown in Figure 1.4 since this promotes good mixing of particles along with rapid surface renewal at the exposed bed surface. For this mode the bed material is characterized by two distinct regions; the relatively thin active layer which is formed as the granular material flows down the sloping upper bed surface and the much thicker 'plug flow' region where the material is carried upward by the rotating wall of the kiln. Thus in this mode the energy imparted by the kiln's rotation is continuously fed into the plug flow region as potential energy which is subsequently released and dissipated in the active layer. The active layer itself is characterized by vigorous mixing of particles and hence a high rate of surface renewal which promotes heat transfer from the freeboard. However, this vigorous particle motion also promotes de-mixing, termed segregation, in which smaller particles tend to sieve downward through the matrix of larger particles. Thus the bed motion tends to concentrate finer material within the core (see, Figure 1.5), and material within the core, because it has very little chance of reaching the exposed bed surface for direct heat transfer from the freeboard, tends to a lower temperature than the surrounding material. Therefore segregation tends to promote temperature gradients within the bed and thus counteract the homogenizing effect of advective energy transport. The net effect of segregation is not necessarily negative, for example in limestone calcination smaller particles react faster than larger ones (at the same temperature) and therefore the segregation of fines to the cooler core may be essential in obtaining uniform calcination of all particles. This suggests that particle size distribution in the feed material might be optimized, which again points to the need for developing our predictive capabilities for the bed material.

The focus of the present work is the quantitative description of the transverse bed motion and segregation of granular materials and the resultant effect of these phenomena on the bed heat transfer.

Although other bed phenomena, such as axial segregation (sequential banding of small and large particles along the kiln length), dusting (evolution of fines from the bed and subsequent carry over from the kiln), and accretion (deposition or growth of material onto the refractory wall forming unwanted dams) are also not well understood, these were not included in the present work. These phenomena can, however, be better explained after careful elucidation of the transverse bed motion, segregation, and heat transfer. The work has been carried out in two parts: (i) An experimental campaign involving the measurement of particle flow in the transverse plane of a 0.964 m I.D (1 m O.D) and 1.0 m long batch rotary drum at room temperature, and the measurement of heat transfer within the bed of a 0.41 m I.D by 5.5 m pilot rotary kiln. (ii) The development of a mathematical model for the bed transport phenomena, utilizing the experimental data for validation purposes. The mathematical model consists of three major components: a granular flow model which predicts the flow patterns of cohesionless granular material in the cross section of the bed; a segregation model which predicts mixing and segregation of binary mixtures of different sizes but the same density; and a model for bed burden heat transfer.

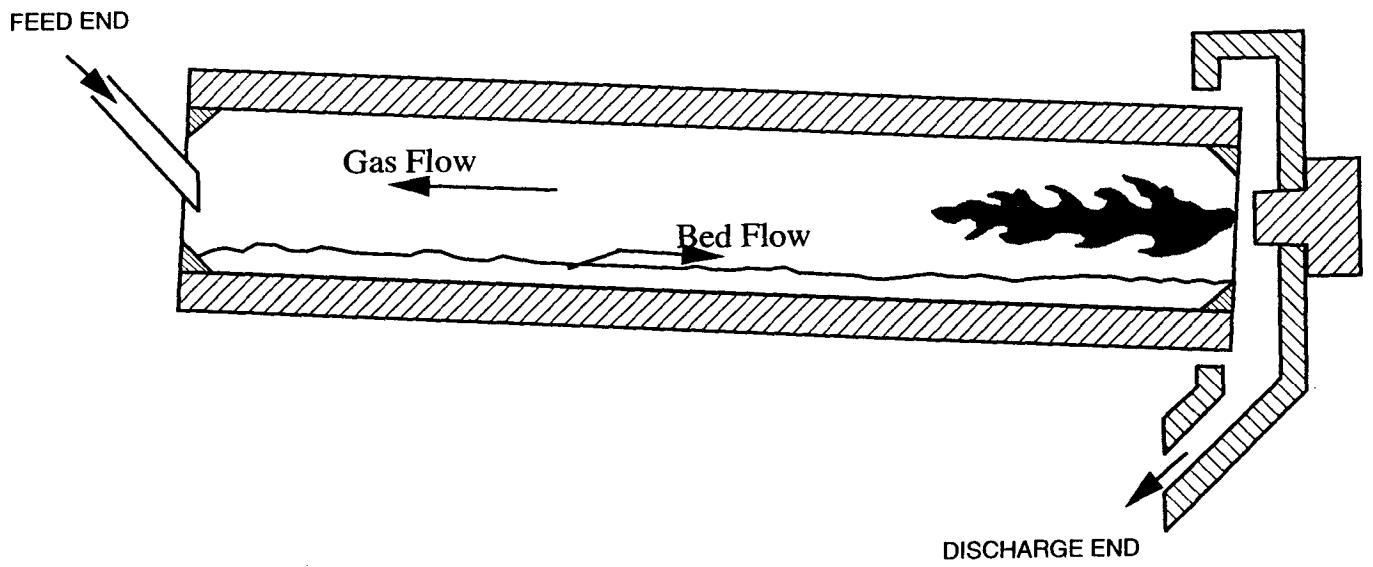


Figure 1.1 An Axial Section of a Rotary Kiln Depicting it as a Counter-Current Heat Exchanger.

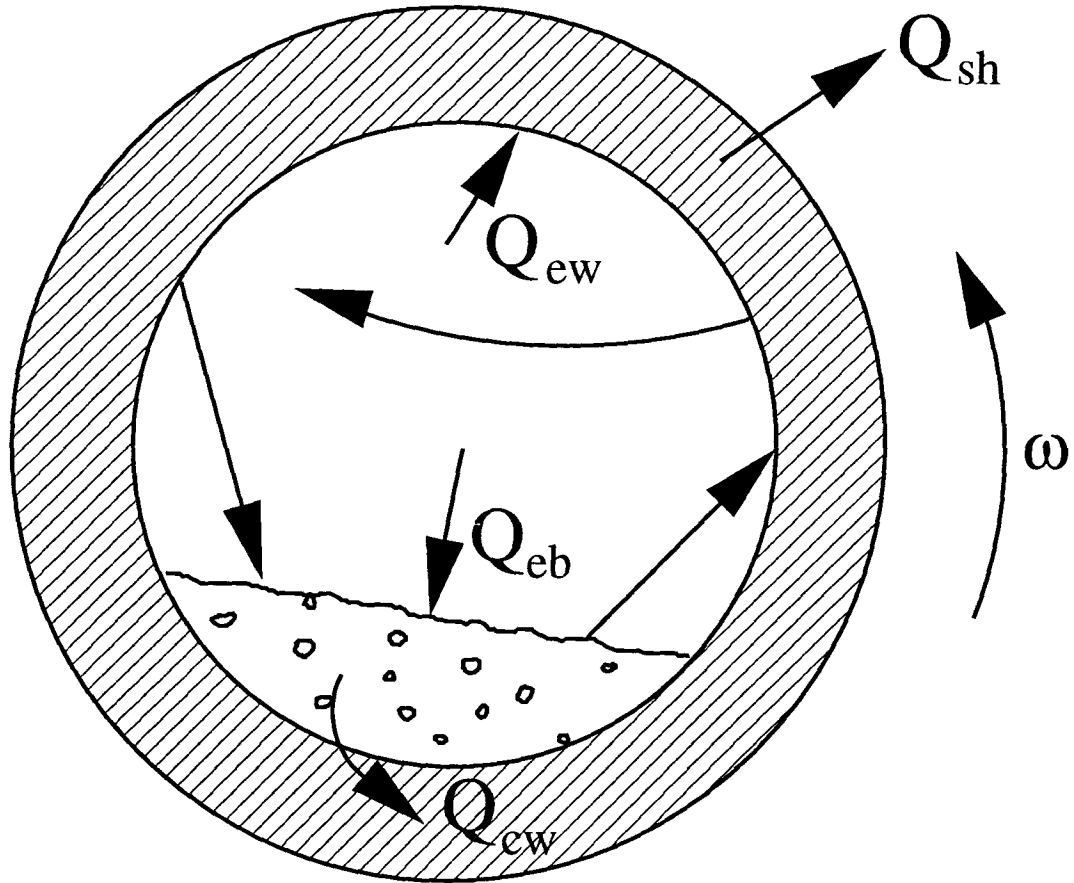


Figure 1.2 Heat Transfer at the Interfacial Surfaces of the Bed Material over a Transverse Section of the Rotary Kiln.

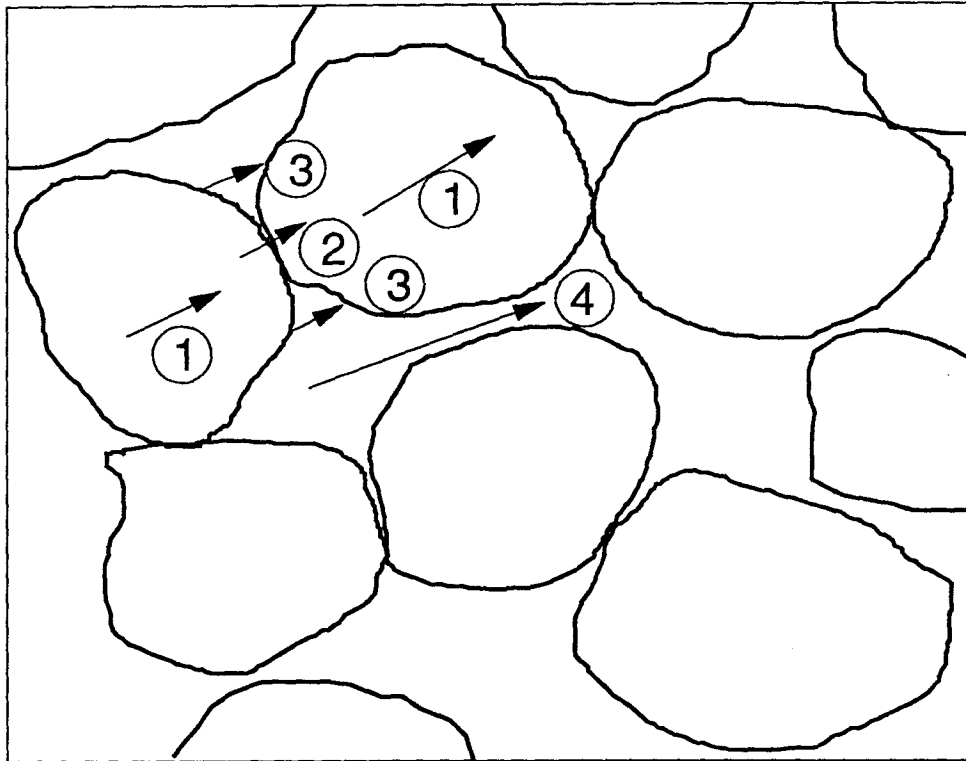


Figure 1.3 Heat Transfer Paths in Packed Beds: 1. Within Particle Conduction; 2. Conduction across Particle-Particle Contact; 3. Particle-to-Particle Radiation; 4. Interstitial Gas Convection.

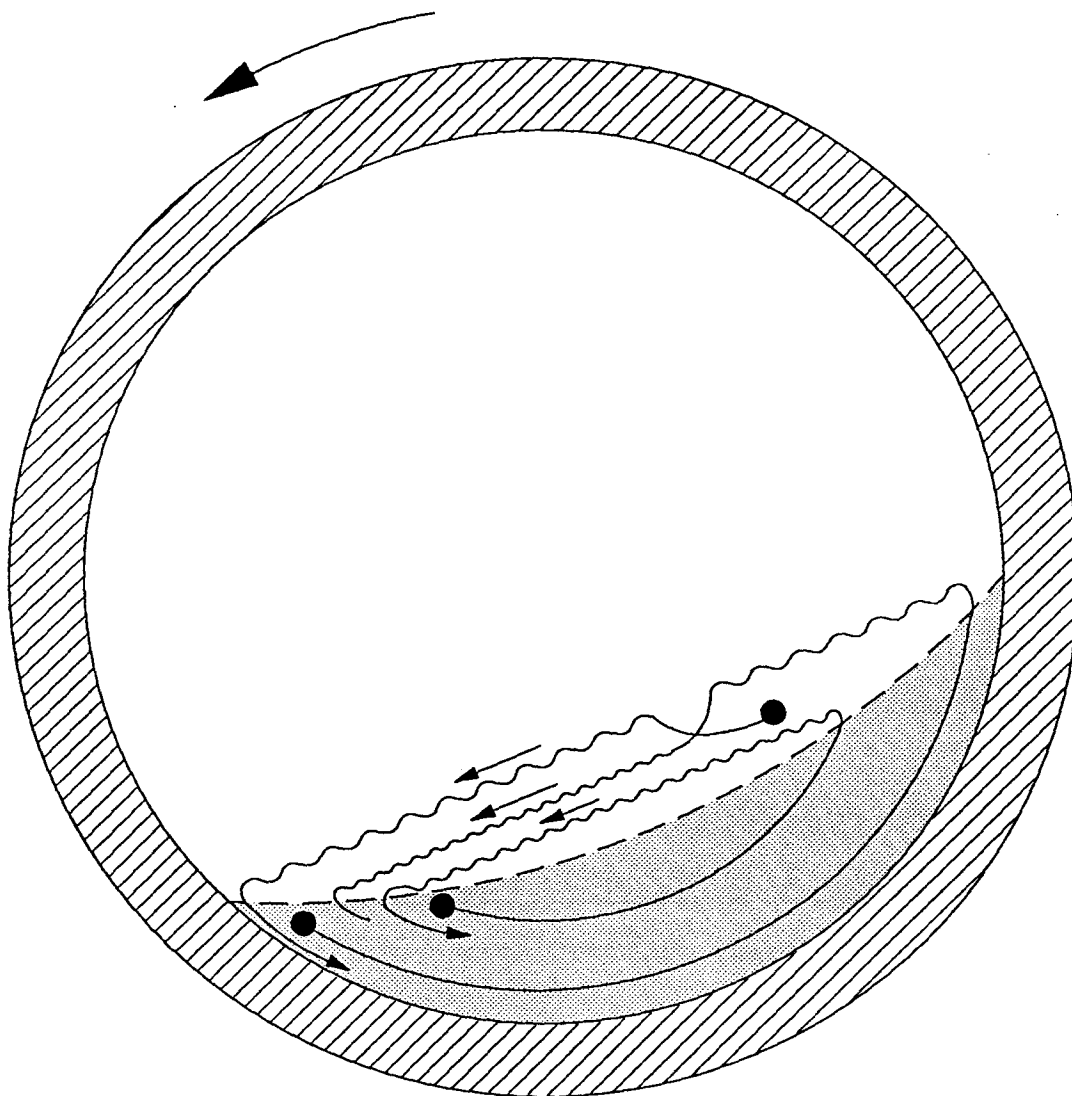


Figure 1.4 Rolling Bed Motion Depicting Two Distinct Regions *Top Section:* Active Layer; *Bottom Section:* Plug Flow Region.

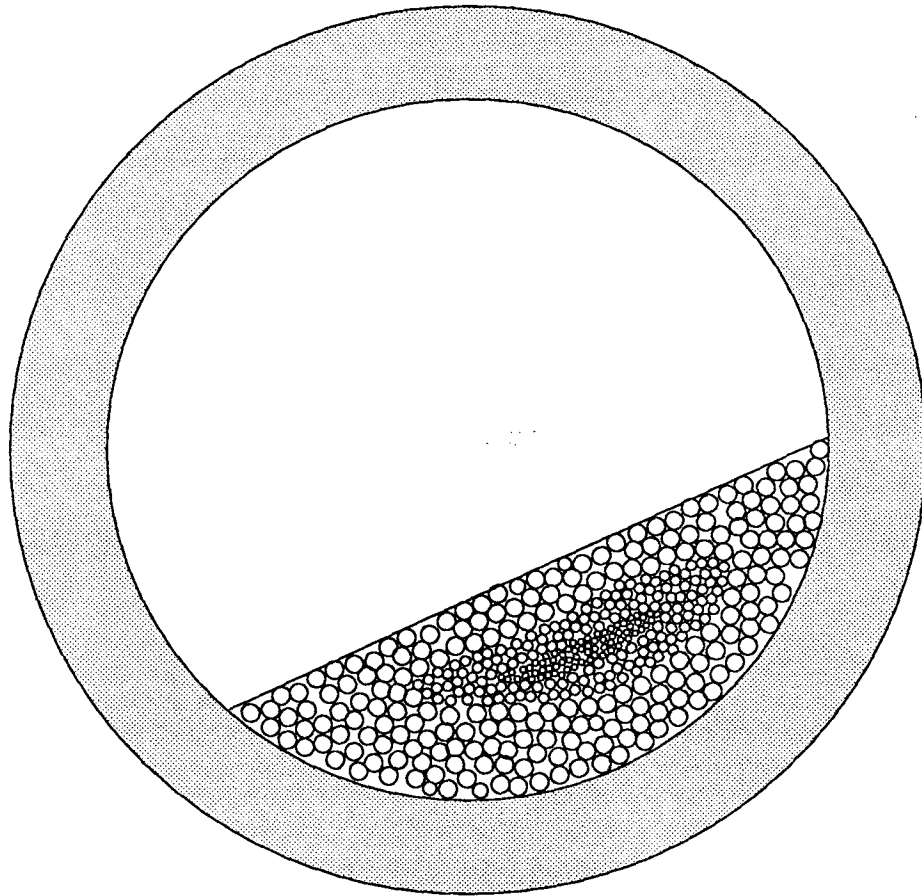


Figure 1.5 Radial Segregation of Particles with Different Sizes in a Rotary Kiln
Showing the Segregated Core Dubbed 'The Tongue.'

CHAPTER 2. LITERATURE REVIEW

It was pointed out in the opening discussion that despite the diversity in materials processed and intended function all rotary kilns share certain common features, the most prominent being the distinct division of the freeboard and the bed. Although the majority of previous work has concentrated on the freeboard processes, the overall performance of any kiln depends on the interaction of the freeboard and bed processes but the latter have received little attention. Because the present work focuses on the bed phenomena, in particular bed motion and heat transfer, it is appropriate to first review the literature relating to the bed, before moving on to a brief examination of the fairly extensive studies pertaining to the freeboard.

2.1 Bed Motion Along the Kiln Axis

The movement of the charge in a rotary kiln can be resolved into two components; i.e., movement in the axial direction along the kiln, which determines residence time, and movement in the transverse plane of the kiln which influences most of the primary bed processes, such as, particle mixing, heat transfer, and reaction rate as well as the axial progress of the material. In fact early works, such as that of Sullivan (1927) and Seaman (1951), determined that axial motion is mainly caused by transverse movement since for every material turn over in the cross section there is an axial material advance (Pickering *et al.*, 1951 and Zablotny, 1965). Although this linkage between particle motion in the transverse plane and particle velocity in the axial direction was established several decades ago, the literature generally deals with these two types of bed motion as independent phenomena. Only recently has an attempt been made to quantitatively link the axial velocity to the transverse motion (Perron and Bui, 1990). Early attempts to predict the mean axial velocity and residence time of the material focused on a few easily measured parameters such as the angle of repose for the bed material or the kiln slope and the rotational speed. The various correlations relating mean axial velocity to the kiln slope, rotational speed, loading (defined as the

fraction of the cross section occupied by the bed) and dynamic or static angle of repose have been summarized by Perron and Bui (1990). Perhaps due to the ease with which it may be applied, the most commonly employed correlation is still that of Seaman

$$V_s = 0.955R\omega\beta/\sin\xi \quad (2.1)$$

where β is the kiln slope, R is the inside radius, ξ is the dynamic angle of repose and ω is the rotation rate. Using a combination of dimensional analysis and a 'plausible' velocity profile for the bed cross section, Perron and Bui (1990) have proposed a new formula to predict axial velocity,

$$V_s = R\beta\omega \left[\frac{L^{\psi/\pi} R^{-1-\psi/\pi}}{R} (H^2 \cos\xi + 2H\sqrt{2HR - H^2 \sin\xi}) \left(\frac{1 - \cos\theta/2}{1 + (2 \tan\theta/2)/\theta} \right) \right] \quad (2.2)$$

In this equation, H is the actual bed depth, θ is the bed depth in angular measure, and ψ and π are exponents determined in the dimensional analysis. This expression is unique in that rather than yielding only a mean axial velocity it allows quantitative predictions for local axial velocity through its inclusion of various local parameters, for example the local transverse velocity profile. However validity of the expression has not, as yet, been clearly established at even the laboratory or pilot scales and the problems of scale-up to the industrial scale remain formidable. Although the work represents an important attempt to quantitatively link the axial velocity to the transverse motion it does not address the basic tasks of determining the latter. In addition to the transverse motion, factors which may influence axial bed motion are internal flights and restrictions that cause sliding, falling and rebounding forward of charge as well as the freeboard gas flow (Rutgers, 1965). For example, in some calcination processes, depending on the particle size distribution and the specific density of the charge the co-current or counter-current gas flow can cause forward or backward axial motion. Such a mechanism lends itself to stochastic analyses (see, e.g., Hogg *et al.*, 1974, Fan and Too, 1981)

2.2 Bed Motion in the Transverse Plane of the Kiln

The particulate material which forms the kiln bed is set in motion by the rotation of the kiln. In the transverse plane this motion has been characterized as centrifuging, cataracting, cascading, rolling, slumping and slipping, all of which are shown in Figure 2.1. Centrifuging, which occurs at very high speeds of revolution, is an extreme condition in which all the bed material rotates with the kiln wall. Cascading, which also occurs at relatively high rates of rotation, is a condition in which the height of the leading edge (called the shear wedge) rises above the bed surface and particles cascade or 'shower' down on the free surface as depicted in the figure. Neither of these conditions is generally considered to be desirable in commercial rotary kiln operation and will not be considered here. Starting at the other extreme, i.e., very low rates of rotation, and moving to progressively higher rates, the bed will typically move from slipping, in which the bulk of the bed material, en-mass, slips against the wall, to slumping, whereby a piece of the bulk material at the shear wedge becomes unstable, yields and empties down the incline, to rolling which involves a steady discharge onto the bed surface. In the slumping mode the dynamic angle of repose varies in a cyclical manner while in the rolling mode the angle of repose remains constant. In the rolling mode two distinct regions, as was shown in Figure 1.4, can be discerned (i) the shearing region (active layer) formed by particles near the top surface and (ii) the non-shearing (plug flow) region which is formed by the remainder of the bed particles and move with the kiln wall. Rolling and slumping are the most important modes in most rotary kiln operations, and for this reason will later be examined in more detail. Rutgers (1965) has indicated that dynamic similarity of rotary kiln behavior, and hence the type of transverse bed motion which occurs, is established by the rotational Froude number, which is defined by

$$Fr = \frac{\omega^2 R}{g} \quad (2.3)$$

where ω is the rotation rate, R is the inside radius of the kiln and g is the acceleration due to gravity. The critical speed of revolution for the onset of centrifuging, N_c , corresponds to a Froude number of unity.

The particular regime chosen for a kiln operation will depend on the purpose of the operation. A survey of various rotary drum type operations (Rutgers, 1965) found most kilns operating in the range of only 0.04 to $0.2N_c$ which is well below the centrifuging mode, and most probably, the cascading mode as well. Unfortunately, defining the relevant parameters and formulating an appropriate non-dimensional relationship among them (such as Eq. 2.3) does not enable prediction of which type of bed motion will actually be present for any particular set of kiln operating conditions. This inadequacy led to the work of Henein *et al.* (1983a) and (1983b), which resulted in the delineation of areas of predominance for the various regimes. The work of Henein *et al.* explained the mode-to-mode transitions and identified the boundaries between slipping/slumping, slumping/rolling and slipping/rolling by combining theory and experimental measurements. Although the results have not been tested beyond the laboratory scale, the work did, for the first time, allow semi-empirical correlations of the transverse motion with a single parameter, i.e., the Froude number. The bed behavior diagram proposed for limestone is shown in Figure 2.2. It should be pointed out that such a diagram incorporates the rheological properties of bed material into a single parameter, the static angle of repose.

Since the rolling mode is characterized by both good particle mixing and a relatively low level of violent agitation (important from the point of view of particle attrition and dust generation) it is generally considered the best mode for kiln operation and therefore warrants additional examination. Referring back to Figure 1.4, the transverse motion in a rolling bed can be characterized by two distinct layers, the non-shearing plug flow region and the shearing active layer of particles cascading down the top surface. In the plug flow region the particles rotate as a rigid body with a velocity (in the transverse plane) which varies linearly with distance from the kiln center-line. At the region near the free surface particles cascade down due to various

deformations and gravity (Henein *et al.*, 1983a). Because of rapid shearing and gravitational influence most of the mixing (and segregation) occur in this region. The demarcation between these two regions is a stagnation plane where particles are momentarily stationary before reversing direction. Thus in the rolling mode there is an active layer close to the free surface where almost all the mixing (and segregation) takes place. Using a plexiglass viewing port on a short section of a rotating drum, Henein *et al.* (1983b), measured the depth of this active layer and found that the maximum thickness increased with particle size, bed depth and rotational speed. For deeper beds, (active layer depth to particle diameter ratios greater than 40) it was suggested that the maximum thickness of the layer would be about 10% of the total bed depth.

Rather few quantitative predictions for the depth of the active layer appear in the literature, probably because there is no deterministic description of the granular flow behavior unless it is approximated by the laws governing conventional non-Newtonian fluid flow. Such an approach does not adequately represent the flow behavior, as the flow properties such as consistency and the power law exponent associated with non-Newtonian flows are not easily measurable in rotary kilns. Pershin (1988), using results from a series of experimental trials on a small rotary drum, was able to mathematically model the shape of a cascading bed and, as a result, was able to predict the boundary between the active layer and the plug flow region to a reasonable degree of accuracy. Pershin's model was based on the fundamental principle of equilibrium theory as is shown in Figure 2.3. The model is based on the theory that if motion is steady in a gravity field then the system will assume the position of minimum potential energy and, as a result, the system's mass will be reduced by moving some of the material beyond the boundary of the system. The model is unique because it gives explicit mathematical expressions which can be used to calculate the centroid of the plug flow region, the plug flow area and consequently the mass of material in the active layer. Although the model falls short of predicting the flow in the active region (where the material is in kinetic motion), an application of mass balance in the transverse plane can offer knowledge on the average mass velocity in the active layer. Unfortunately Pershin's experiments

were conducted at very high speeds of rotation (greater than $0.2N_c$) and the accuracy of the mathematical predictions for slower but rather more industrially important modes such as rolling or slumping is questionable. In addition, the problem of quantifying the flow in the active layer for purposes of determining heat transfer is not really addressed by this methodology.

2.3 Modelling the Flow of Granular Materials (Granular Flows)

The rapid deformation of bulk solids, e.g. sand, ore, coal, grains, ceramic and metal powders, etc., is termed granular flow. The description of the dynamic behavior of these materials involves aspects of traditional fluid mechanics, plasticity theory, soil mechanics and rheology (Savage, 1989). The mechanisms of granular flow have been the subject of intense study in recent years, e.g., gravity flow in hoppers, rockfalls, snow avalanches, mudflows, etc. Knowledge acquired from these studies has not, however, been applied to the specific task of calculating transverse bed motion in a rotary kiln. It was first recognized by Singh (1978) that particle diffusion in rotary kilns proceeds by inter particle collision and later experiments demonstrated that the magnitudes of axial diffusion coefficients lie between that of liquids and gases (Ferron and Singh, 1991). They employed the dilute gas kinetic theory analogy to describe rotary kiln transport phenomena such as mass and heat transfer. Although this granular flow theory was being explored in solving problems associated with chute flows, debris flow and avalanches (see, e.g., Savage, 1989), this approach did not catch on for rotary kiln simulation.

The primary challenge in granular flow modelling is not in setting up the conservation equations, i.e., for mass, momentum, and energy, but in establishing the stress/strain relationship for the particulate mass as this relationship depends on the flow regime and vice versa. Davies (1986) has compared the observed behavior of granular materials, subjected to shear stress, to other common types of flow behavior, shown in Figure 2.4. The figure depicts the shear stress as a function of a dilation factor $\bar{\lambda}$, defined as,

$$\bar{\lambda} = [(v^*/v)^{1/3} - 1]^{-1} \quad (2.4)$$

where v is the volume concentration of solids (or solids fraction) and v^* is its value corresponding to the minimum possible void fraction that the material can maintain. For granular materials in a static condition, the particles fit together into a rigid grid which means that some degree of stress can be sustained without inducing flow. However, as the stress approaches some critical level, the particles begin to ride up on one another and the grid commences dilation. At the critical stress the dilation, $\bar{\lambda}$, reaches a maximum and the material begins to flow. Once this occurs the shear stress shows an incipient steep decline with increasing strain rate and it is this initial behavior which distinguishes granular flow from that of either Bingham or dilatant plastic behavior. Beyond a certain rate of strain the stress begins to increase again and the granular flow behaves as a dilatant plastic; i.e. a nonlinear relationship between the shear stress and the rate of strain.

These fundamental aspects of the flow of granular material or bulk solids similar to flow in rotary kilns have been reviewed by Savage (1979). Many theories have been considered in the effort to establish appropriate constitutive relations for such flows. As mentioned earlier, these theories extend from traditional soil mechanics to all types of viscous flows. The most important conclusions that can be drawn from these works may be stated as:

- (i) Granular flow behavior extends beyond the critical state as defined by traditional soil mechanics literature. As a result of rapid deformation associated with the flow, inertia as well as shear-rate effects must be considered.
- (ii) The dominant effect on the flow arises from particle to particle interactions whereas the interstitial fluid plays a minor role.
- (iii) Transport processes are assumed to be governed by a field quantity called *granular temperature*, \tilde{T} , which can be defined as the kinetic energy per unit mass contained in a random motion of particles.

It is therefore common to assume that the state variables that describe the rapid deformation response of granular materials border on the parameters that describe the behavior of fluids and Coulomb type dissipation of energy. In view of the above it is common to find that the theories governing granular flow are formulated around the assumption of a continuum similar in some regard to viscous fluids; however, the equilibrium states of the theories are not states of hydrostatic pressure as would be in the case of fluids but are rather states that are specified by the Mohr-Coulomb criterion (Cowin, 1974). The advantage of continuum formulations over alternative particulate (stochastic) formulations is that the former are better capable of generating quantitative results. Although in practice at any point in the flow a state variable, such as the solid fraction, v , is either zero or unity depending upon whether or not a granule is present, it is common to represent v by a continuous function of position, its quantitative value thereby representing the average in the neighborhood of that position.

The mechanisms of momentum transfer (and hence stress generation) for granular flows include the following:

- (i) Static stresses resulting from the rubbing between particles (dry Coulomb type rubbing), which is independent of strain rate.
- (ii) Translational stresses resulting from the movement of particles to regions having different velocity.
- (iii) Collisional stresses resulting from inter-particle collision, which result in transfer of both momentum and kinetic energy.

The relative importance of these three mechanisms will depend on both the volume concentration of solids within the bed, i.e., the dilatancy factor, $\bar{\lambda}$, and the rate of strain. The static contribution dominates at high particle concentration and low strain rates; in this situation the particles are in close contact and the shear stresses are of the quasi-static, rate independent Coulomb-type as described in soil mechanics literature (see, e.g., de Jong, 1964; Spencer, 1964;

Mandl and Luque, 1970; and Roscoe, 1970). Conversely, at low particle concentrations and high strain rates, the mean free path of the particles is large compared with particle diameters and the interchange of particles between adjacent layers moving at different mean transport velocities may dominate stress generation. This situation is analogous to 'turbulent' viscosity in fluid flow. At moderate particle concentration and high strain rate, collision between particles instead of translation of particles to layers will dominate stress generation because in this situation there are rarely any void spaces of sufficient size for the interchange of particles over significant distances. The case pertaining to low and moderate particle concentration has been termed as the grain inertia regime (Bagnold, 1954) and under these conditions the dynamics of the actual particle collision becomes important. The kinetic theories include 'hard' sphere models, which assume that the inter-particle collisions are instantaneous and therefore the collision trajectory is determined by the rules governing rigid body collisions (i.e., elastic, inelastic, etc.), and 'soft' sphere models, which assume that particles collisions are of finite duration. Both models have been used to describe the collisional interactions which give rise to the transport of momentum and kinetic energy. In this grain inertia regime, the stress tensor has been considered to be strain rate-dependent (Campbell and Gong, 1986), according to the expression,

$$\tau_{ij} \propto \left(d_p \frac{du}{dy} \right)^2 \quad (2.5)$$

which includes translational and collisional effects but not static. However, according to Savage (1989), most engineering applications (e.g., chute flows) and other natural flow situations (mudflows, snow avalanches, debris flow, etc.) appear to fit into a regime for which the total stress must be represented by a linear combination of a rate-independent static component plus the rate-dependent 'viscous' part just described. The flow patterns observed for material flow in rotary kilns appear to be no different from that described above except, perhaps, for the boundary conditions.

2.3.1 The Equations of Motion for Granular Flows

As was mentioned earlier, the equations of motion for granular flows have been derived by adopting the kinetic theory of dense gases. This approach involves a statistical-mechanical treatment of transport phenomena rather than the kinematical treatment more commonly employed to derive these relationships for fluids. The motivation for going to the formal approach (i.e., dense gas theory) is that the stress field consists of static, translational and collisional components and the net effect of these can be better handled by statistical mechanics because of its capability for keeping track of collisional trajectories. However, when the static and collisional contributions are removed, the equations of motion derived from dense gas theory should (and do) reduce to the same form as the continuity and momentum equations derived using the traditional continuum fluid dynamics approach. In fact the difference between the derivation of the granular flow equations by the kinetic approach described above and the conventional approach via the Navier Stokes equations is that, in the latter, the material properties, e.g. viscosity, are determined by experiment while in the former the fluid properties are mathematically deduced by statistical mechanics of inter particle collision.

Based on the hard sphere kinetic theory of dense gases Lun *et al.* (1984, 1985) have developed equations of motion and the relevant constitutive equations for granular materials. In this derivation a fixed control volume was considered to have a discrete number of smooth but inelastic particles which are undergoing deformation. The resulting system of equations was given as,

(i) conservation of mass:

$$\frac{\partial \rho}{\partial t} = -\nabla \cdot (\rho \mathbf{u}) \quad (2.6)$$

where \mathbf{u} is the velocity of the bulk material, $\rho [= v\rho_p]$ is the bulk density, and v is the bulk solid fraction;

(ii) conservation of momentum:

$$\rho \frac{D\mathbf{u}}{Dt} = \rho \mathbf{b} - \nabla \cdot \mathbf{P} \quad (2.7)$$

where \mathbf{b} is the body force, and \mathbf{P} is the total stress tensor which, unlike continuous fluid flow, comprises the three components mentioned earlier: (i) the static (frictional) stress, P_f ; (ii) the 'kinetic' stress, P_k , that arises from the translation (or streaming) of particles and (iii) the stresses due to particle collisions P_c . It is perhaps worth pointing out that the translational stress, P_k , is analogous to the Reynold's stresses for turbulent flow of fluids.

In addition to mass conservation, Eq. 2.6, and momentum conservation, Eq. 2.7, a third relationship that is required to describe the flow is some form of energy conservation equation. The total energy per unit mass of the granular material, E , may be broken (Johnson and Jackson, 1987) into three components:

(i) The kinetic energy, E_K , associated with the local average velocity, \mathbf{u} , i.e.,

$$E_K = 1/2 |\mathbf{u}|^2 \quad (2.8)$$

(ii) The 'pseudo-thermal' energy, E_{PT} , associated with deviations of the motion of individual particles from the local average; E_{PT} can be represented by the kinetic energy definition of temperature i.e.,

$$E_{PT} = 1/2 \mathbf{C}^2 = 3/2 \tilde{T} \quad (2.9)$$

where \mathbf{c} is the local velocity; $\mathbf{C} = \mathbf{c} - \mathbf{u}$ is called the 'peculiar' velocity and \mathbf{C}^2 is the mean square of the velocity fluctuations about the mean. \tilde{T} in Eq. 2.9 is the kinetic theory definition of temperature called *granular temperature* (Johnson and Jackson, 1987) or *grain temperature* (Lun *et al.*, 1984) which was defined earlier as the kinetic energy per unit mass contained in a random motion of particles (Zhang and Campbell, 1992).

(iii) The sensible heat or the true thermal internal energy of the solid material, E_h .

The total energy flux, q , will therefore, comprise the sensible heat flux q_h , and the flux of the pseudo-thermal energy, q_{PT} . The former is related to the thermodynamic temperature gradient and the effective thermal conductivity of the assembly of solid particles; the latter is related to the gradient in the kinetic theory definition of temperature i.e. the *granular temperature* or *grain temperature*.

The conservation equation for the true thermal energy (sensible heat) is (Johnson and Jackson, 1987)

$$\rho \frac{DE_h}{Dt} = -\nabla \cdot q_h - P_f : \nabla \mathbf{u} + \gamma \quad (2.10)$$

where D/Dt is the material derivative, $P_f : \nabla \mathbf{u}$ represents the rate of working of the frictional component of the stress tensor, while γ is the rate of dissipation due to the inelasticity of collisions between particles. In Eq. 2.10, it is implied that work done by the frictional component of the stress tensor is translated directly into sensible heat and does not contribute to the pseudo-thermal energy (granular temperature) of the particles. It is worth mentioning that Eq 2.10 is the energy equation for the sensible heat or the true thermal energy transport and, since it does not influence the granular flow, is usually treated separately. In addition, the magnitude of the last two terms in Eq. 2.10 (dissipation of frictional energy) is small compared with the thermal (thermodynamic) energy input into energy intensive process devices such as rotary kiln and may therefore be neglected during heat transfer calculations. Hence the conservation of kinetic energy in the absence of the terms that do not influence the flow field has been given (Johnson and Jackson, 1987; Ahn *et al.* 1991; etc.) as:

$$\frac{3}{2} \rho \frac{D\tilde{T}}{Dt} = -\nabla \cdot q_{PT} - (P_k + P_c) : \nabla \mathbf{u} - \gamma \quad (2.11)$$

These conservation equations just described must be closed by constitutive relations for the stress terms P_k , P_c , P_f , the kinetic energy flux, q , and rate of dissipation by inelastic collision, γ , along with suitable boundary conditions. Applying these equations to describe the flow of material in the transverse plane of the rotary kiln will quantify the actual flow properties, for example velocity, in the various modes of operation described by Henein *et al.* (1983a, 1983b).

2.4 Mixing and Segregation in the Transverse Plane of the Kiln

As pointed out in the introduction, the rheological properties of the bed material can be expected to change during the passage of charge through a rotary kiln and changes in properties, such as, particle size, shape and surface character, may result in distinct changes in bed behavior. One such behavioral phenomenon is segregation which, since it acts as mechanism of de-mixing, may influence heat transfer within the bed. Segregation may also influence the rate at which particles are elutriated from the exposed bed surface when, for example, large amounts of gas are being released from the bed. As mentioned earlier, the effect of segregation on heat transfer is of considerable practical importance since it may significantly influence the degree of product homogeneity.

The main causes of segregation are differences in particle size, density, shape, roughness and resilience (Williams and Khan, 1973). Although any of these may produce segregation under certain circumstances, most rotary kiln segregation arises from differences in particle size (Pollard and Henein, 1989) and the current work is focused on this phenomenon. The mechanisms (Williams and Khan, 1973; Bridgwater *et al.*, 1985) by which size segregation occurs are:

- (i) Trajectory segregation: This is due to the fact that, for certain modes of kiln operation, particles being discharged from the plug flow region into the active layer may be projected horizontally from the apex onto the exposed bed surface. This situation may apply in the slumping, rolling and cataracting modes whereby different sized particles are emptied onto the surface during

material turn-around. It has been suggested that the distance that these particles travel is proportional to the square of the particle diameter (Bridgwater, 1976) which means that finer particles will tend to be concentrated at mid-chord section.

(ii) Percolation: When a bed of particles is disturbed so that rearrangement takes place (rapid shearing), the probability that a particle will find a void into which to fall depends on the size of the particles (Savage, 1983). Thus smaller particles will tend to filter downwards through a bed of flowing granular material while large particles will simultaneously tend to be displaced upwards.

Trajectory segregation has been identified (Bridgwater *et al.*, 1985) as the main cause of axial segregation or 'banding' whereby particles of different sizes are selectively collected into bands occurring over the kiln length. This axial segregation is not considered in the present work and therefore not critically reviewed; rather, attention is focused on segregation in the transverse plane, specifically, percolation. Although percolation theory, also known as inverse sieving in granular flow models (Savage, 1989), is reasonably well developed, it has seldom been employed in order to model segregation patterns encountered in rotary kilns. Instead, most of the rotary kiln literature characterizes the rate of segregation by a first or second order type kinetic expression such as (Nityanand *et al.*, 1986 and Pollard and Henein, 1989)

$$S_n = A Fr^b \quad (2.12)$$

where S_n is defined as the normalized rate of segregation, Fr is the rotational Froude number, A and b are the kinetic parameters determined by experiment.

Size segregation in failure zones, e.g. the active (shearing) region of a rolling bed in a rotary kiln or gravity flow on an incline (also known as free surface segregation), has been described by the mechanism of percolation (Bridgwater *et al.*, 1985, Savage, 1989). Size segregation in such

systems is considered as a random continuous network whereby voids are randomly formed and distributed as shown in Figure 2.5. For gravity flow on an incline Savage and Lun (1988) approached the problem by considering three events:

(i) The probability of voids forming which are of sufficient size for the smaller particles to percolate into. The probability of such voids forming has been given as

$$p(E) = \frac{1}{\bar{E} - E_m} \exp\left\{-\frac{E - E_m}{\bar{E} - E_m}\right\} \quad (2.13)$$

where E is the void diameter ratio which is defined as the ratio of the void diameter to the average voids diameter, i.e., $E = D_v/\bar{D}$. E_m is the minimum possible void diameter ratio and \bar{E} is the mean void diameter ratio. $E_m = 0.154$ is the value for which voids in a packing will result in spontaneous percolation (Bridgwater *et al.*, 1971).

(ii) The capture of particles by voids in the underlying layer. For this event the number of particles 'captured' by a void per unit time is dependent on the velocity differences between two neighboring shear layers.

(iii) The establishment of a mass flux of small particles. When this occurs the average percolation velocities in the plane normal to the bed surface can be determined by material balance.

This proposed sequence of events is useful in that it explores the possibility of employing the physically derived continuum equations to solve for the concentration gradients with a minimum probabilistic input. The latter approach, i.e. stochastic methods, tend to conceal the detailed behavior and the mechanisms that are the source of industrial problems (Bridgwater, 1976). This may also be said about the characterization of segregation by degree of mixedness or by kinetic expressions like the one given in Eq 2.12. Such expressions will conceal all the inter-particle mechanisms in a single parameter which serves little or no industrial purpose.

Although classification as applied to solids is synonymous with different sizes of the same material it should be pointed out that other classifications, such as particle density or mass and even particle shape can also cause mixing or segregation. It has recently been established (Alonso *et al.*, 1992) that size and density differences can, indeed, be combined to reduce segregation through mutual compensation.

2.5 Rotary Kiln Thermal Models

In most rotary kiln operations the primary objective is to transfer the maximum amount of energy to (or in some instances from) the bed in order to drive the various processes such as drying, chemical reaction or simple heating (or cooling). Virtually all of this energy input occurs as heat transfer, since the power required to rotate the kiln (and hence drive the bed motion) is insignificant compared with that supplied by fuel combustion. Although the prediction of the net heat transfer to the bed is paramount in the development of any kiln heat transfer model, the task is not an easy one owing to the complex interaction of the various paths and processes for heat transfer as shown in Figure 1.2. The source of energy for heat transfer is the combustion process and this energy is transferred directly to the walls and bed surface by radiation (either from the emitting products of combustion, i.e., H₂O and CO₂, or by particulate emission in the flame region) and freeboard convection. However, the wall interacts radiatively with the bed surface (and vice versa) as well as with other sections of the wall. In addition, only a portion of the energy absorbed by the inside wall surface during exposure to the freeboard is lost through the shell, with the remainder being transferred to the bottom surface of the bed. This regenerative action may enhance heat transfer to the bed or, under some circumstances, may operate in reverse drawing energy from the bed (Barr, 1986). To complicate the situation still further the 'receptiveness' of the bed surfaces to heat transfer will depend on the ease with which energy received at the surface is dispersed within the bed. As may be inferred from the previous section, a bed which is characterized by poor mixing (particularly in the transverse plane) will also be a poor receptor for heat transfer since the temperature gradients associated with a large conductive component within the bed will mean

high bed surface temperatures and hence reduced driving force for heat transfer from the freeboard. Although virtually all past models for kiln heat transfer have been concerned primarily with directing energy to the bed surface (both the top surface which is exposed to the freeboard and the bottom surface which contacts the wall), a truly complete model must also include the subsequent distribution of energy within the bed. Having now set out the heat transfer problem, it is instructive to review the work aimed at solving the problem.

2.5.1 One-dimensional Models

By assuming that the bed and the freeboard gas are well mixed and move in plug flow the axial gradients of bed temperature and gas temperature can be related to the local rates of heat transfer by the ordinary differential equations (Sass, 1967).

$$\frac{dT_s}{dz} = \frac{1}{C_{ps}G_s}[\alpha_2(T_g - T_s) + \alpha_3(T_w - T_s)] \quad (2.17)$$

$$\frac{dT_g}{dz} = \frac{1}{C_{pg}G_g}[\alpha_2(T_g - T_s) + \alpha_1(T_g - T_w)] \quad (2.18)$$

where, $\alpha_i = h_i A_i$, is the product of the heat transfer coefficient, h , of the interface with area A , C_{pg} and C_{ps} are the specific heats of gas and solid respectively; T is the local thermodynamic temperature and G is the mass flow rate.

These equations form the basis for the various one-dimensional kiln models which have appeared in the literature (see, e.g., Wes *et al.*, 1976; Brimacombe and Watkinson, 1978; etc.). In these models an energy balance on the wall must be included, as well as the kinetic expressions for any reactions. The latter lead to a set of mass conservation expressions which must be solved along with the energy equation. For example, if the evaporation of free moisture is controlled by heat transfer, rather than mass transfer, an additional thermal balance on the moisture can be included as

$$\frac{dW}{dz} = \frac{1}{G_1 \lambda} [\alpha_2(T_g - T_s) + \alpha_3(T_w - T_s)] \quad (2.19)$$

$$\lambda = \lambda_0 + C_v(T_g - T_s) \quad (2.20)$$

where W is the mass of water, λ_0 is the latent heat of liquid water and C_v is the specific heat of water vapor.

The variations occurring among one-dimensional models are attributable mainly to the efforts made by various investigators to improve the heat transfer coefficients employed at the interface between the bed and the surrounding boundaries. Since the present work is primarily concerned with modeling the kiln bed, the most pertinent literature is that directed toward evaluating either the boundary conditions for the bed surfaces, i.e., at the covered wall-bed interface and at the exposed bed surface, or heat transfer within the bed.

2.5.2 Heat Transfer Between the Covered Wall and the Bed

Various 'estimated' heat transfer coefficients have been employed to calculate the covered wall-bed exchange. Evaluation of this coefficient has generally been either by pure guess work or by adopting some type of surface renewal or penetration model. Typical 'guess-estimated' values for wall-solid heat transfer coefficient lie within the range of 50-100 W/m²K (Gorog *et al.*, 1982). One of the earlier surface renewal-penetration models was that of Wes *et al.* (1976). In such case, heat conduction between a wall and granular material is calculated using the familiar equation for one-dimensional unsteady state conduction (see, e.g., Sullivan and Sabersky, 1975)

$$\frac{\partial T}{\partial t} = \alpha \frac{\partial^2 T}{\partial y^2} \quad (2.21)$$

Implicitly, the granular material is treated as a continuum having averaged or 'effective' thermophysical properties and the heat transfer coefficient at the wall is calculated as;

$$h(x) = \sqrt{\frac{2nR}{x}(k\rho C_p)_{eff}} \quad (2.22)$$

where, $x = 2\pi nRt$, is the distance travelled by a particle from the lower edge along the circumference of the kiln, R is the kiln radius and n is the kiln revolution. Such early models were not very successful and led to many versions of more complex ones, e.g., by considering an 'effective gap' as a result of packing defects, interstice, etc (Lehmberg, 1977; Gorog, 1982; etc). Except for Barr (1986), earlier models for the covered wall interface considered only half of the problem, i.e., the bed, and not the wall, but in refractory lined rotary kilns the thermal diffusivities in the bed and that in the wall are of the same order of magnitude and thus the problems at the wall and contacting bed cannot be solved independently of each other. In addition, the covered wall/bed interaction depends partly on the radial temperature distribution in the wall and cannot be solved independently of the freeboard problem. The resultant effect of all these interactions can partly be seen in Figure 2.6 which shows the radial temperature profiles to be expected within the refractory wall.

Although Barr's work considers most of the interfacial couplings mentioned above, it does not extend the model to the entire bed burden. The extension of this approach should be the focus if heat transfer within the bed is to be addressed.

2.5.3 Heat Transfer in the Kiln Freeboard

The two modes of heat transfer operating in the freeboard are radiation and convection. The sources of thermal radiation in the freeboard are primarily the emitting gases (H_2O and CO_2) resulting from combustion, and suspended particulate material. These particulates include dust as well as intermediate carbon particles formed during combustion. The evaluation of the heat exchange is complex because the participating surfaces are gray and reflect energy. The basic tasks of a freeboard model are (i) to simulate the emissivity of the gas mixture (Hottel and Sarofim, 1967) and (ii) to evaluate the radiative exchanges using some form of view factors or

exchange areas. The most common approach to the latter is either by ray tracing (radiation paths) and/or the Monte Carlo techniques or the zone method of Hottel and Cohen (1958). With either of these techniques, one has the option of simulating the entire kiln freeboard in all three dimensions (see, e.g., Jenkins and Moles, 1981) or the cross section (two-dimensional) which can be coupled with the one-dimensional kiln model mentioned in the earlier section. The latter was employed by Gorog *et al.* (1981). An adequate model for calculating the rate of heat transfer to an exposed bed surface having a specified temperature distribution has been developed by Barr (1989).

The various forms of the convective heat transfer coefficients for the freeboard found in the literature are expressions which have been derived from the boundary layer flow. These include the classic cases such as (i) flow over a flat plate in the case of heat transfer from the freeboard gas to the exposed bed surface, and (ii) pipe flow, in the case of gas-to-wall heat transfer. Mathematical models as well as experimental works have been carried out by Manitus (1974), Watkinson and Brimacombe (1978) and Tscheng and Watkinson (1979). The findings of pilot kiln heat transfer studies conclude that (i) convection heat transfer plays a minor role compared with radiation at elevated temperatures, and (ii) the gas-to-solids heat transfer by convection can be attributed to the bed behavior regimes (Henein *et al.*, 1983) with the lowest heat transfer rate being encountered during slumping and the highest during rolling as was mentioned earlier. Generally, it can be said that convection models based on flat plate or pipe flow correlations do not work particularly well for kilns. Thus, while Tscheng and Watkinson (1979) have reported that measured values of the gas-to-bed heat transfer coefficients are approximately ten times that for the gas-to-wall, Barr (1986) found only about a three-to-one relationship by subtracting the radiation component from the total heat transfer in the kiln freeboard.

2.5.4 Effective Thermal Conductivity of Packed Beds

Heat transfer in the bed of a rotary kiln is similar to heat transfer in particle assemblages (packed beds) as shown in Figure 1.3 except that in the former an additional component of energy transfer occurs as a result of advection of the bed material itself. It is therefore necessary to review some of the packed bed models used in determining particulate heat transfer.

The mathematical models that describe heat transmission in packed beds of granular material (granular bed) can be grouped as (i) the traditional approach, and (ii) the volume averaging technique. In the traditional approach, a uniform axial velocity of the charge is assumed. In such cases partial differential equations for heat transfer in the particulate medium must be coupled with the local heat flux that expresses the energy conservation over a solid particle and the interstitial fluid separately. The solutions to the energy balance may be categorized into two groups (see, e.g., Votruba and Hlavacek, 1977) viz: discrete and continuous models. The discrete models include, among others, mixing cell models (as shown in Figure 2.7b and 2.7c) and can be extended to account for radiative exchange between adjacent cells. The major disadvantage of the cell model is the difficulty in evaluating the view factors and emissivities (Huber and Jones, 1988). Continuous models, with control volume shown in Figure 2.7a, comprise two subgroups i.e., the *dispersion concentric* (DC) models and the *continuous solid* phase (CS) models. In the DC models the local solid phase is assumed spherical with centrally symmetric temperature profiles; particle to particle conduction is not considered (see, e.g., Wakao, 1976 and Wakao *et al.*, 1977). Unlike the DC models the solid phase in the CS models is treated as a continuum and thermal conduction is permitted; the solid phase temperature is not locally distributed (Littman *et al.*, 1968). For the continuous models the partial differential equations (PDE) for the fluid phase contain the source term for the interface heat transport. In both cases the choice of the effective thermal conductivity to use in the calculations is not an easy task.

A more rigorous mathematical treatment of packed bed models than the traditional approach is the volume averaging technique (see Figure 2.7d). In this approach exact equations are derived for the volume-averaged solid and fluid temperatures based on the mathematics of spatial averages (Whitaker, 1980 and Levac and Carbonell, 1980). Although the approach validates the use of a homogeneous or one-equation for both solid and fluid as a packet, numerous new parameters (of which we have no previous knowledge) are introduced as a result of the mathematical derivation. Also, because the theory is new and it is only recently formulated, equations are not derived in terms of particle surface temperatures essential to the evaluation of the radiative and interface transfer. Table 2.1 from Kaguei *et al.* (1977) presents some fundamental equations for the DC and CS models described above. In these equations the radial temperature gradients in e.g., a cylindrical packed bed, are neglected in comparison with the axial gradients.

Although heat diffusion through the bed of a rotary kiln has been ignored, the packed bed approach indicates the possibility of such an evaluation. In formalizing models for heat transmission in a rotary kiln bed burden the dispersion concentric model may seem appropriate since the local particle dynamics can describe better the heterogeneous reaction kinetics in the reactor. Nonetheless, unlike packed beds, the temperature effects of the interstitial fluid flow in the rotary kiln bed may be negligible due to very low Reynolds numbers. It is therefore convenient to resort to the continuous solid phase models with effective properties and this is the way the present work is directed.

Based on the evaluation of heat transfer following the paths shown in Figure 1.3 numerous models have been proposed to determine effective thermal conductivity, k_{eff} , of a packed bed. The simplest correlation for the effective thermal conductivity is that of Diessler and Eian (1952) which neglects radiation effects. However, in order to account for radiation a term involving the radiation parameter may be included (Schotte, 1960) as

$$k_{eff}^r = \frac{1 - e_o}{1/k_s + 1/4\sigma\epsilon d_p T^3} + e_o 4\sigma\epsilon d_p T^3 \quad (2.28)$$

Although more complicated correlations exist in the literature (see, e.g., Yagi and Kunii, 1957 and Kunii and Smith, 1960), for most applications Eq. 2.28 may be adequate since the advantages of more complex models have not been adequately verified.

2.6 Review Summary

In completing the discussion of the previous work it is necessary to reiterate some of the important points which set out the objectives and scope of the work undertaken in this thesis.

2.6.1 Bed Motion

- (i) The conditions within the bed are primarily dependent on the transverse bed motion. The transverse motion also determines the residence time of the material within the kiln.
- (ii) Despite the work of Henein *et al.* (1983a and 1983b) and Pershin (1988) the detailed prediction of the transverse motion is still not possible.
- (iii) Although an attempt has been made to model the axial velocity of the bed (Perron and Bui, 1990) by making certain assumptions about the transverse motion no comprehensive model for flow within the bed in the transverse plane of the kiln has yet appeared.
- (iv) As in chute flow and avalanche problems the constitutive relations based on the principle of kinetic energy should be an appropriate approach to model the bed motion. Although this approach has been recognized by Ferron and Singh (1991) for rotary kilns, the prediction of the active layer depth and velocity gradients which will quantify heat transfer is still unexplored.
- (v) Size segregation should be analyzed on a continuum basis by employing the result of an adequate flow model. Stochastic process models, although credible, tend to conceal the aspects of segregation which constitute the segregation problem.

2.6.2 Heat Transfer

- (i) Unidirectional heat transfer models exist where the axial movement of the solid charge is assumed uniform (plug flow). These models assume a well-mixed bed where cross-sectional bed temperature is uniform.
- (ii) No models exist that describe the redistribution of the boundary energies in the bed itself because of the well-mixed assumption. However, this assumption may not be adequate as the transverse flow patterns have been ignored.
- (iii) Beside convection (advection), conduction heat transfer through the bed is necessary as in any other packed (fixed) beds and it is therefore important to describe a complete bed heat transfer model. This model should describe both the advection (due to granular flow) and conduction in the bed transverse plane and should be coupled with interfacial transfer mechanisms.

Table 2.1 Solid-Fluid Heat Transfer Models for Packed Beds with Constant Radial Temperature

Fundamental Equations		
Model	Fluid	Solid
	Dispersed Plug Flow	Center Symmetric Temperature
Dispersion-Concentric (DC)	$\frac{\partial T_f}{\partial t} = \alpha_{ax} \frac{\partial^2 T_f}{\partial x^2} - U \frac{\partial T_f}{\partial x} - \frac{h_p a_v}{e_b C_f \rho_f} (T_f - T_s)_R$	$\frac{\partial T_s}{\partial t} = \alpha_s \left(\frac{\partial^2 T_s}{\partial r^2} + \frac{2}{r} \frac{\partial T_s}{\partial r} \right)$ $k_s \left(\frac{\partial T_s}{\partial r} \right) = h_p (T_f - T_s), \quad @ \quad r = R$
	Dispersed Plug Flow	Axially Continuous Solid Phase
Continuous Solid Phase (CS)	$\frac{\partial T_f}{\partial t} = \frac{k_{ef}}{e_b C_f \rho_f} \frac{\partial^2 T_f}{\partial x^2} - U \frac{\partial T_f}{\partial x} - \frac{h_p a_v}{e_b C_f \rho_f} (T_f - T_s)$	$(1 - e_b) \frac{\partial T_s}{\partial t} = \frac{k_{es}}{C_s \rho_s} \frac{\partial^2 T_s}{\partial x^2} + \frac{h_p a_v}{C_s \rho_s} (T_f - T_s)$

Axial Bed Effective Thermal Diffusivity, $\alpha_{ax} = k_{eff,ax} / (e_b C_f \rho_f)$

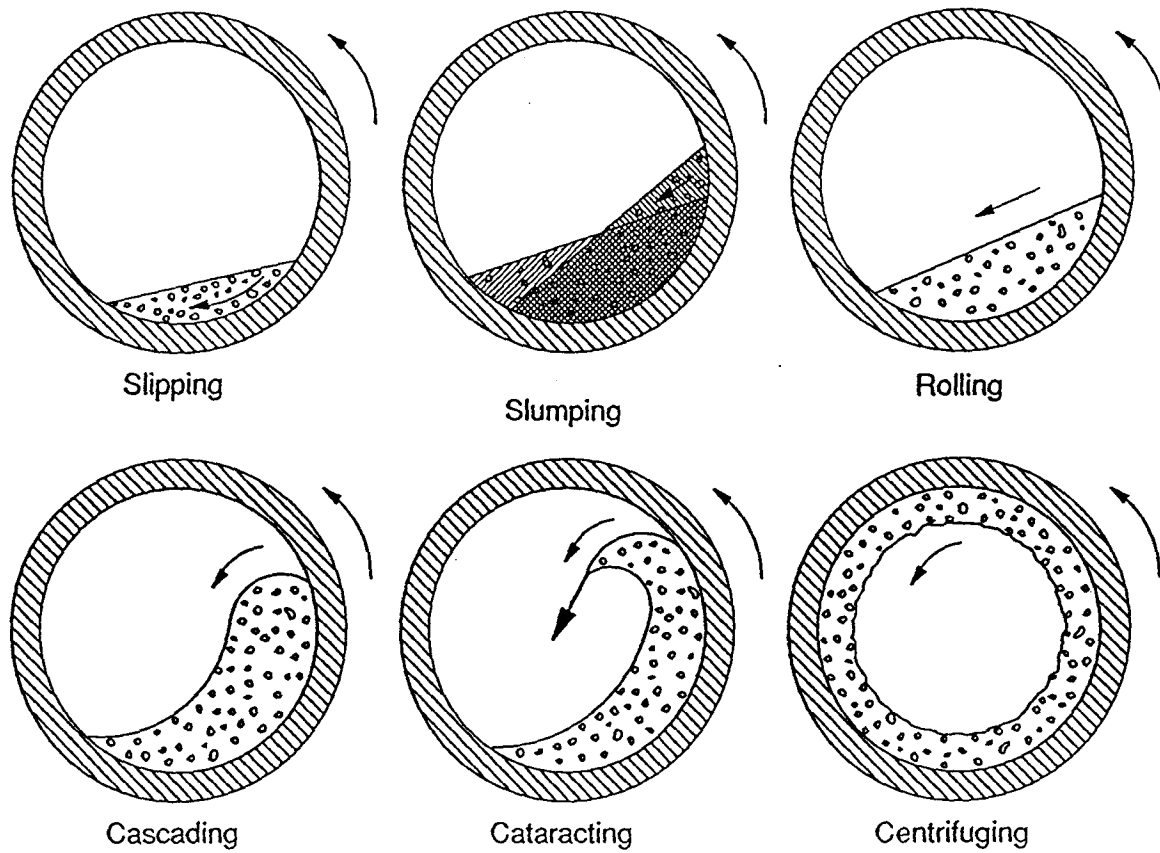


Figure 2.1 Transverse Bed Motion Showing Various Modes of Operation.

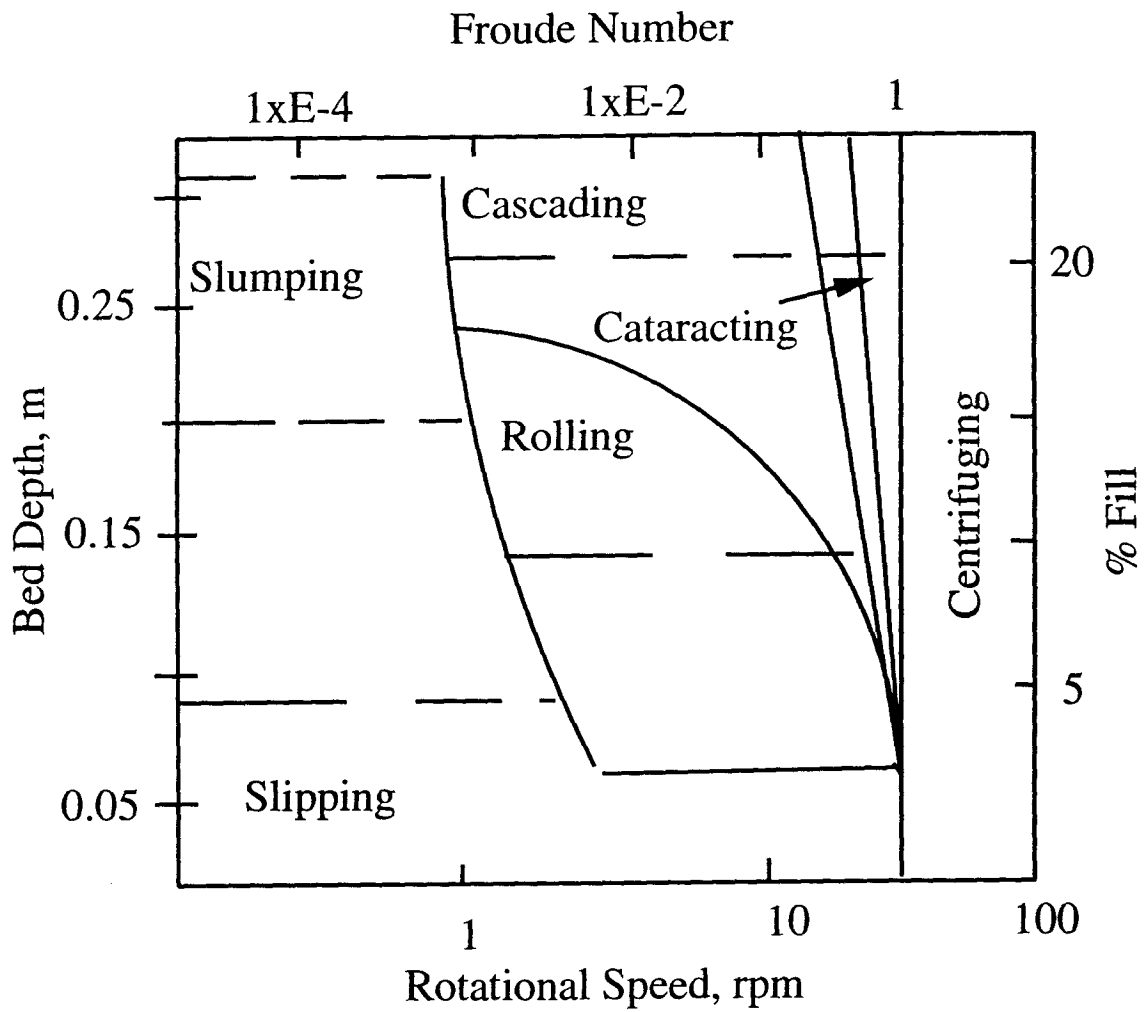


Figure 2.2 Bed Behavior Diagram for Limestone Depicting Regimes of Operation as Function of Operating Parameters of the Kiln (Henein, 1980).

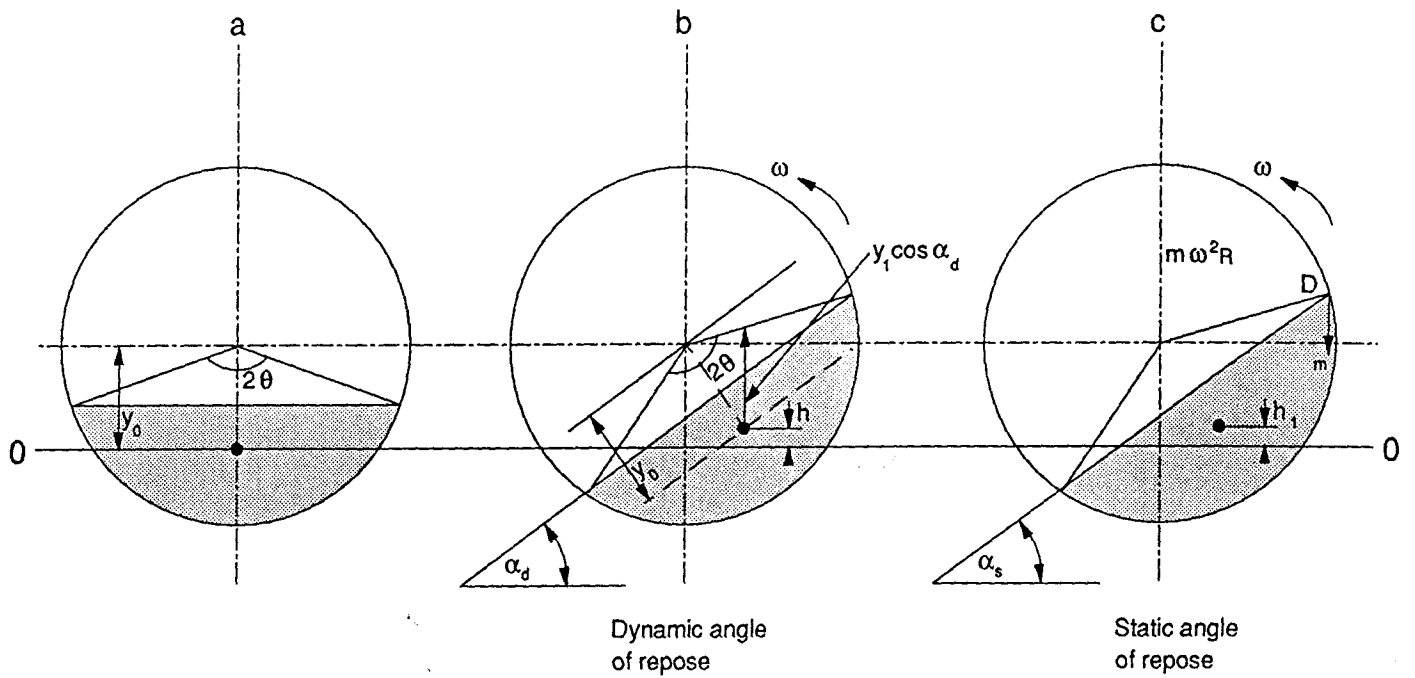


Figure 2.3 Schematic Showing Movement of the Centroid of Bed Material Used by Pershin (1988) in the Development of an Equilibrium Model that may Predict Active Layer Depth.

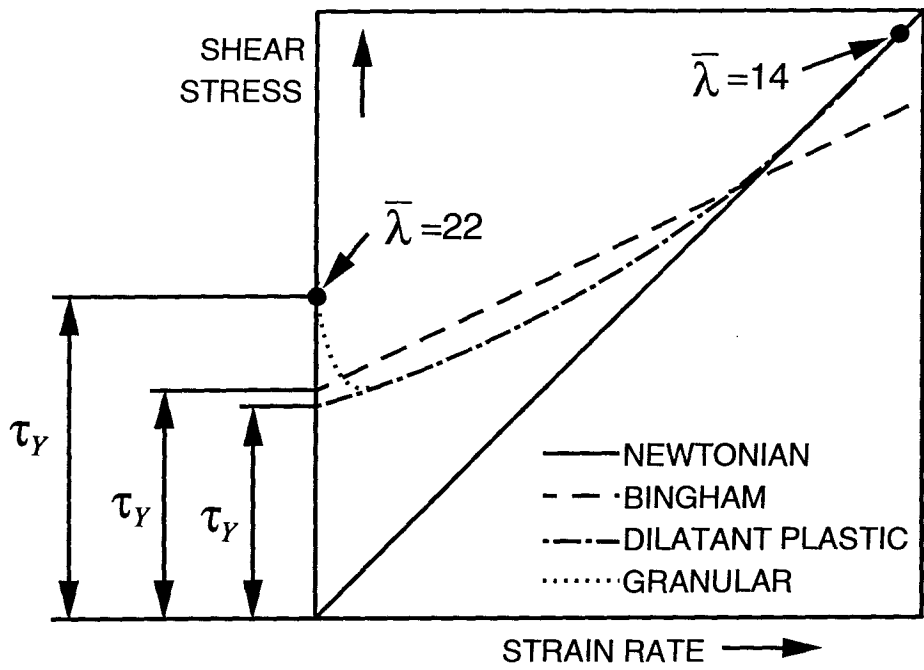


Figure 2.4 Comparison of Granular Flow Behavior with Other Type Flows from Davies (1986).

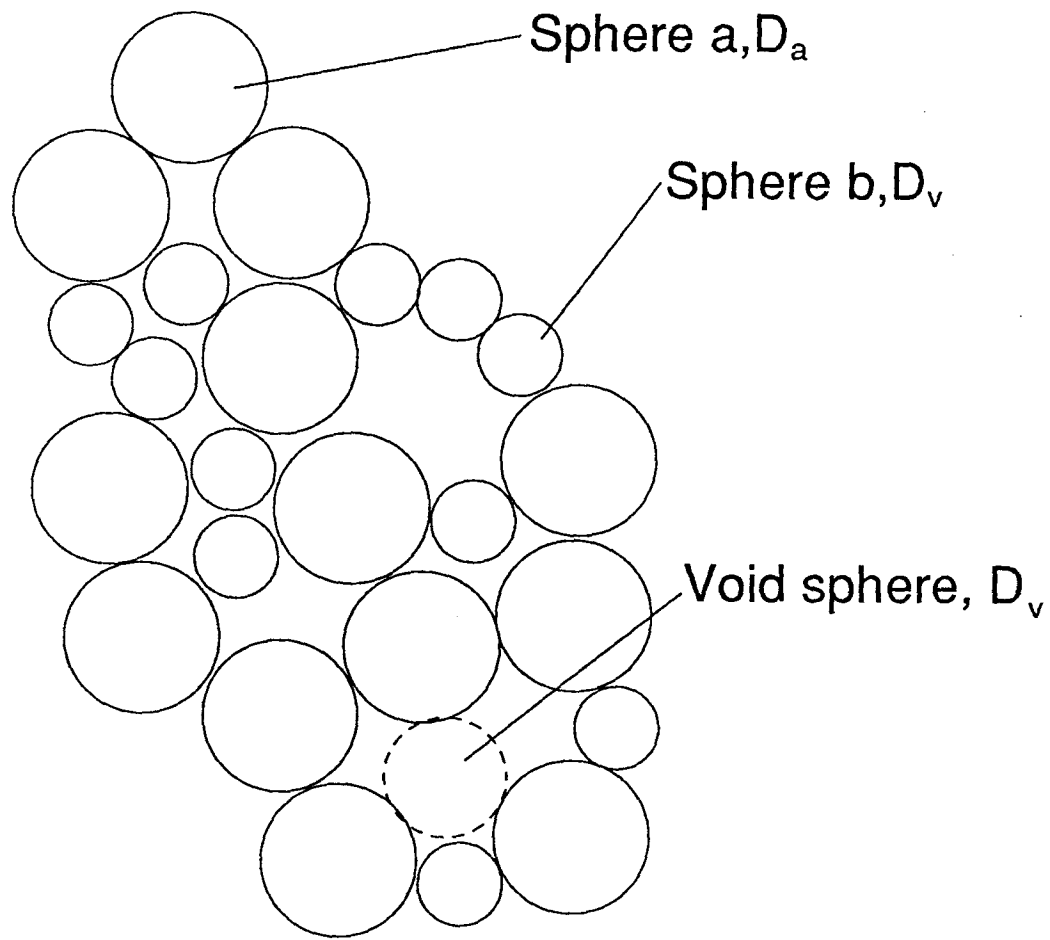
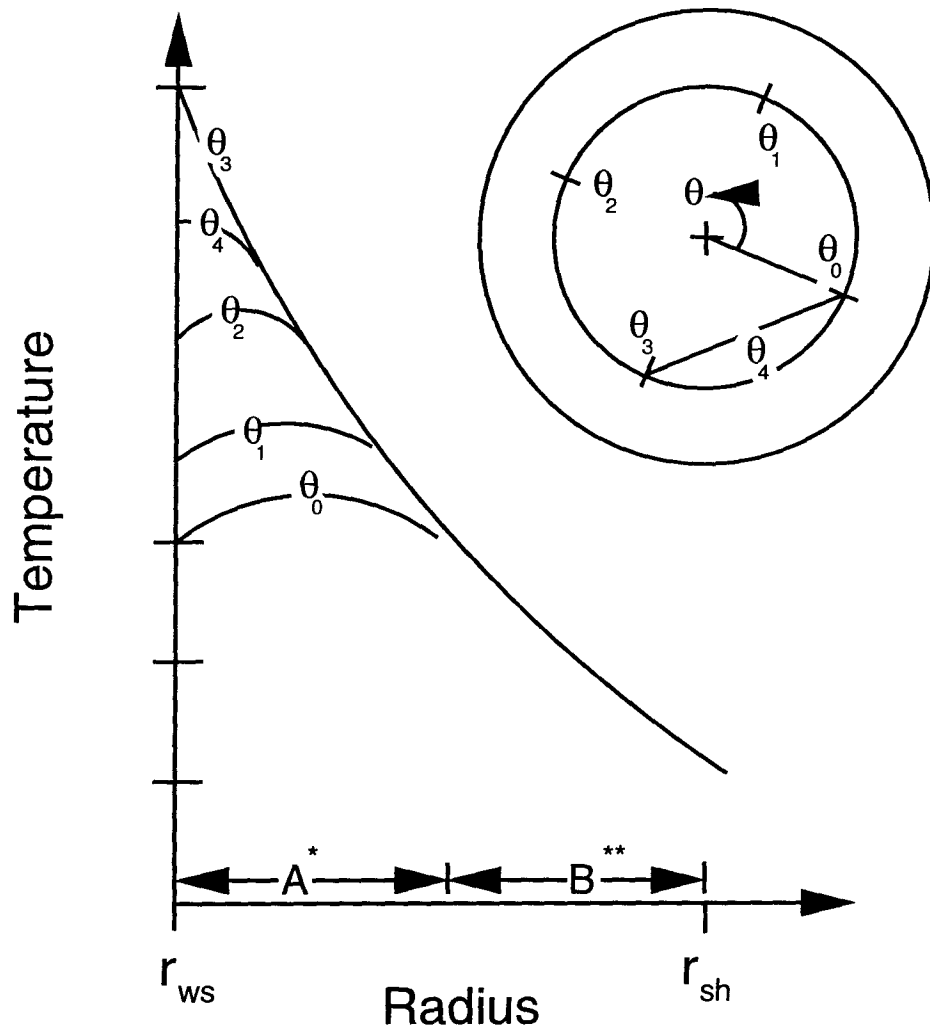


Figure 2.5 Random Continuous Network of Segregating Particles from (Savage, 1989).



- * A: Wall active layer
- ** B: Wall steady-state layer

Figure 2.6 Schematic of Expected Radial Temperature Profiles in Refractory Wall from Barr (1986).

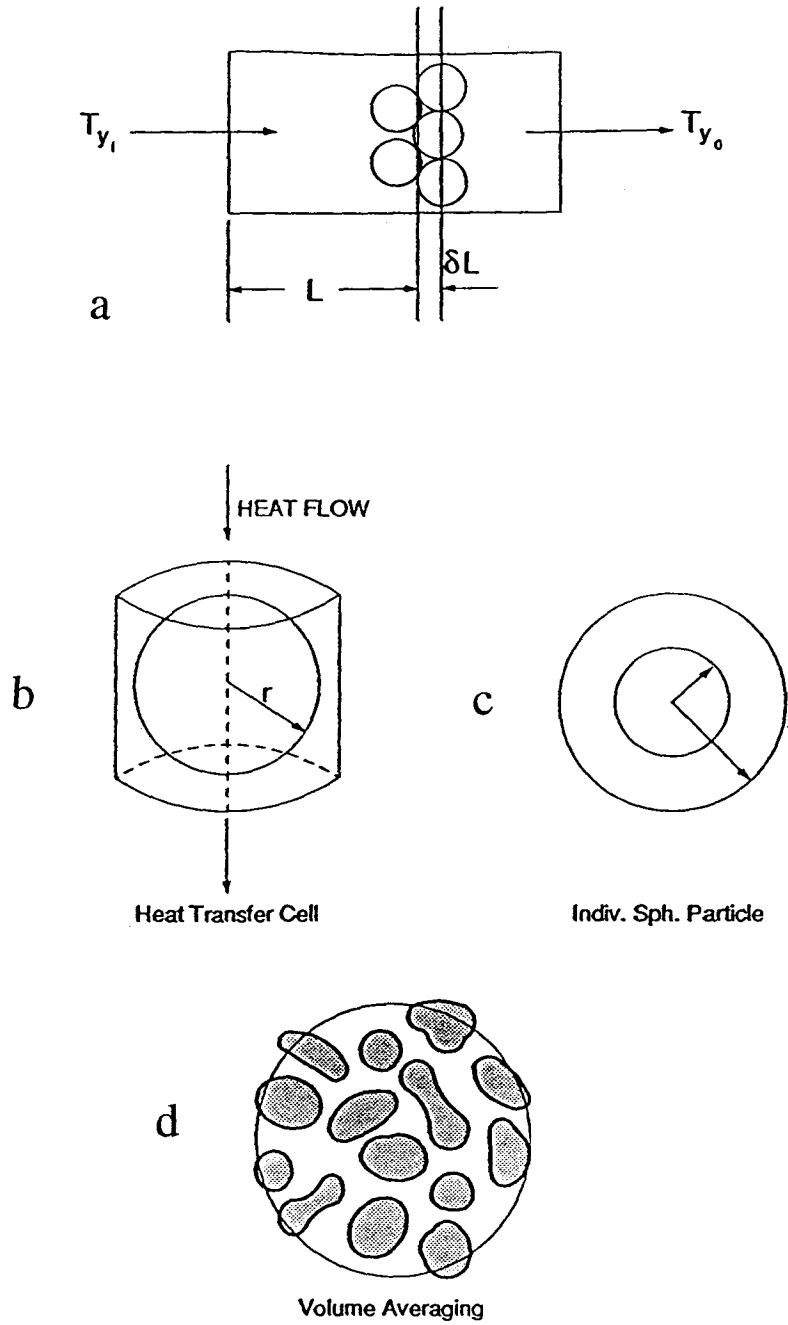


Figure 2.7 Packed Bed Models Formulation.

CHAPTER 3. OBJECTIVES AND SCOPE OF WORK

Based upon the discussions thus far, it can be said that at least some of the problems that plague industrial rotary kiln operations originate within the bed burden. Although existing kiln models may adequately represent conditions external to the bed they do not address conditions within, for example the flow of particles in the transverse plane. Because particle motion in the transverse plane controls other factors, for example the temperature field, segregation of particles, any significant improvement in our understanding and control of rotary kiln processing must grow from an improved understanding of transport processes in the transverse plane. The objective of the proposed research was therefore to develop an integrated model of the kiln bed for use in conjunction with existing models for the kiln freeboard. This integrated model consists of several modules:

- (i) A granular flow model for predicting the two-dimensional velocity field within the bed over the transverse plane of the kiln. Because of its importance to industrial kilns attention is focused on the rolling bed mode.
- (ii) A segregation model for predicting the preferential movement of particles within the bed over the transverse plane of the kiln. This comprises percolation of smaller particles into the bed and the rise of larger particles to the top surface.
- (iii) A heat transfer model for predicting the two-dimensional, steady state temperature field generated within the bed over the transverse plane of the kiln. This model incorporates the results from the flow model and the segregation model in order to calculate the advective component for heat transfer.

A necessary adjunct to the development of the mathematical model would be the generation of experimental data sufficient to validate the key results and assumptions. With this thought a necessary part of the objective was to, in addition to the existing pilot kiln, design and fabricate a sizable batch reactor to simulate the transverse bed motion.

CHAPTER 4. EXPERIMENTAL STUDY OF GRANULAR SHEAR FLOW IN THE TRANSVERSE PLANE

4.1 Introduction

In the preceding chapters the importance of the bed motion in energy distribution was stressed. Although the theories for granular shear flows are currently applied in chute flows and are receiving growing attention in other particulate flow applications, experimental work has generally been lacking (Savage, 1992). This is not to say that rotary kiln bed behavior experiments have been ignored, but rather it is the explanation of these experimental behaviors in the context of these theories that has been missing. As was mentioned earlier, the constitutive equations that have recently been developed for shear flows of granular materials have not yet been applied to kilns. As a result, earlier experiments have not gone beyond observations of the patterns that the bed material forms within the kiln and the relations between these patterns and easily measured operating parameters such as kiln speed and degree of fill. Very recently, however, Savage, using these granular flow theories, has attempted to model some of the experimental results for kiln behavior that have been reported in the literature, with some of these data dating as far back as the early sixties, for example the axial segregation patterns observed by Donald and Roseman (1962). All told, it can be said that, with the lack of suitable flow models, problems associated with transport phenomena in rotary kilns are still formidable.

It is the purpose of this chapter to explore (by way of experiment) the application of existing granular flow theory to the understanding of the flow of cohesionless materials in the rotary kiln. The main task is to carry out an experimental campaign that will make quantitative measurements of the field variables relevant to granular flow: e.g. velocity, granular temperature (the kinetic energy per unit mass in the random motion of particles or velocity fluctuations), and the solids concentration in the cross-sectional plane. These results will then attempt to explain the rheological behavior of the rotary kiln transport phenomena which will, in turn, justify the use of the constitutive

relations for granular flows developed by, e.g., Savage and Jeffery (1981), Lun, *et al.* (1984) etc., as a basis for the development of a flow model for the bed in a rotary kiln. With the above in mind, the objective of the experimental campaign may be stated as follows:

- (i) To study the general characteristics of the transport mechanisms that will later lead to the description of the appropriate mathematical models for the transport phenomena in rotary kilns.
- (ii) To collect the necessary data for the validation of the mathematical models that will be developed to predict the flow behavior.

4.2 Experimental Apparatus

The experimental facility employed for the flow measurements comprised a rotary drum of 1000 mm O.D. (964 mm I.D) and 1000 mm long which was designed specifically to study the flow behavior of granular material in the bed cross section. Figure 4.1 is a general overview of the apparatus. It consists of a steel cylinder driven by a 1/2 hp DC motor with a variable speed control. In order to prevent material slippage in the drum the smooth steel wall was roughened by a coating of Carboline 801 two-part epoxy paint which was then evenly sprinkled with coarse Ottawa sand having an average size of 3.2 mm in diameter. The drum was driven by a chain drive at the rear end and rested on four plastic rollers which were permanently secured to a steel frame. The rollers were arranged in such a way that any axial walk by the drum was only possible in the rear direction where a thrust bearing was secured to prevent such movement. In the front section of the drum a tempered glass panel of 15.86 mm thick with a 255 mm opening in the center was mounted to form an end-piece. The glass end-piece was secured by a flange and allowed a complete observation of the material flow in the drum; the center opening created an access for instrumentation. Loading and discharging of the drum were accomplished through the rear end center opening. The dimensions of the center opening in the glass end-piece as well as the rear access allowed drum loading up to 30% fill without material spilling over. The percent fills used in the experiments ranged between 3.3% and 29% depending on whether the drive system could

carry the torque. In view of this, limestone which has a relatively high density, was run at the lower range of the percent fill indicated. The rotational speeds of interest were in the range of 1 through 5 rpm which correspond to rotational Froude numbers ranging between 5.4×10^{-4} and 1.3×10^{-2} .

Following Savage (1979) and Ahn *et al.* (1991) the technique of measuring particle velocities by fibre optic probes was employed in the current study. Hence high speed photography, which has become almost universally associated with rotary kiln studies (notwithstanding the difficulties associated with image digitization and, in particular, the inaccuracies encountered in the measurement of turbulent shear flows), was avoided. The MTI KD 300 Fotonic sensor, which is usually employed as a displacement transducer was used as a probe for velocity measurements. The Fotonic sensor contains a bundle of optical fibres half of which transmit light while the other half act as receivers. It operates by transmitting light through a fiber probe to a target surface. Light reflected from the target surface back through the probe is converted into an electrical signal which is proportional to the amount of gap of displacement between the probe face and the target surface. The instrument creates a response curve which graphically compares the amount of reflected light and the amount of displacement between the probe and the target surface. The probe configuration, fiber distribution, and theoretical response curves are schematically shown in Figure 4.2. The initial linear rise in the response curve, called the *front slope*, is extremely sensitive and is used for measurements in the microinch range. The apex, called the *optical peak*, provides the output signal sensitivity to light intensity variations required for inspection and comparison of surface conditions; it is also employed to calibrate each probe module in order to establish standard sensitivity independent of target reflectance. The *back slope* is the portion of the response curve descending from the apex and is used for measurements which require greater standoff distances and less critical sensitivity and resolution.

In order to employ the fibre optic probes for bulk velocity measurements a pair of the sensors was required to be mounted in the streamwise direction of the flow at a distance of about one or two particle diameters apart. In order to measure the velocity of particles the signals from the two

sensors were cross-correlated for time delay between them. With the time delay and the distance between the sensors known the velocity of individual particles passing the probe unit could be calculated. The mounting of the two sensors was facilitated by the arrangement shown in Figure 4.1 in which a holder was designed to set the sensors at a specified distance apart. The whole probe arrangement was mounted on a Mitutoyo series 572 digital ruler which was used to determine the vertical distance traversed by the probe tip. With this arrangement, the velocity profile as a function of depth could be determined at various stations along the axial distance of the drum. The cross correlation was performed with the help of an analog HP 3731A correlator and time delay peaks were either read directly from the scale on the screen of the correlator or through an X-Y plotter. A typical output of the cross-correlation function is shown in Figure 4.3. The velocity measurement was calibrated by mounting the probe arrangement over the wheel of a Struers polishing machine rotating at a known rate. The velocity measured with the probe having a distance of 5 mm between the sensors gave an error of within 0.1%. In order to calibrate the measurements made in the 0.964 m I.D drum polyethylene particles were stuck onto the outer flange of the rotating drum and the tangential velocity at the outer rim of the drum, which was measured with the probe unit, was compared with the theoretical value which is calculated as ωR , where R is the distance from the drum's centerline to the outer rim. Once calibration of the probe unit was achieved measurement of particle velocity both at the exposed surface and within the material itself was undertaken.

Initial attempts to acquire data by shooting through the glass end-piece of the drum were not successful because the glass acted as a reflector of light and transmitted energy to the optical fibres. Although this problem could have been corrected by the use of a filter, e.g. MTI KD LS-1A, it was deemed desirable to obtain velocities further into the drum which would remove the influence of the end-piece on particle flow. This would also allow insertion of the probe unit into the bed and measurements of velocity profile normal to the bed surface. In measuring the velocity of an underlying layer the particles that see the tip of the probes were not disturbed by probe insertion; rather, any disturbance was confined to the surface layers above the test position. With the probe

diameter of 3.25 mm and polyethylene pellets as bed material such disturbances were very small and did not propagate further into the bed. A measure of the depth of the active layer for the drum cross section automatically resulted from the depth velocity measurements as part of the experimental procedure. A series of velocity data were collected by (i) changing the sampling times and (ii) by simply repeating the experiments. With these data the mean velocity at any test position was calculated. The root mean square of the velocity was considered a measure of the velocity fluctuation in the streamwise direction and was computed from the variance of the mean velocity (Ahn *et al.*, 1991). Knowing the mean velocity at a given position, the component of the solids fraction in the flow direction, v_x , was determined. This was accomplished (with the help of an oscilloscope) by counting the number of particles that passed by the probe unit.

4.3 Materials Employed and Their Characterization

The materials used for the flow experiments were (i) Dupont high density polyethylene pellets; (ii) long grain rice and (iii) limestone. This selection of materials included both regularly shaped particles as well as particles of random shapes as occur in industrial kiln operations. Polyethylene pellets were selected partly because the particles' spherical shape lends itself to mathematical modelling and partly due to their light weight and widespread usage in other flow experiments, e.g. chute flows and, as a result, the wide reporting of their flow behavior in the literature. The second material, long grain rice, was chosen because it is clear and, although it deviates from sphericity, retains a regular shape; its application in kilns can be found in grain drying and handling. The third material was limestone and was chosen because of its importance in industrial operations such as calcination. Its irregular shape and relatively wide range of particle size distribution make it a good candidate in the study of a typical industrial material in motion. The relevant physical properties of the materials are presented in Table 4.1. The angle of repose of the materials was estimated as per Henein (1980) by measuring the maximum angle subtended by the material as the drum was rotated. The maximum angle is defined as that angle at which the particles at the exposed bed surface begin to yield. The angle of repose for the polyethylene pellets

was measured as 25° and that for the rice and limestone ranged between 32° and 35° depending on the speed of rotation of the drum. The coefficient of restitution of the materials is one of the most important properties for granular flow since the material's rheology is dominated by the physical contact between particles and between particles and the cylinder wall. The particle to particle coefficient of restitution could not be measured directly but an attempt was made to estimate this value for polyethylene pellets by bouncing the particles from a distance over a plastic surface (Sondergaard, *et al.* 1990); the coefficient of restitution of the material and the cylinder wall was roughly estimated in a similar manner. For purposes of comparison, the particle to particle coefficient of restitution for polystyrene and glass beads have been reported in the literature as 0.85 and 0.95 respectively (Johnson and Jackson, 1987).

4.4 Parameters Derived from the Data

An attempt was first made to observe some of the results from experiments performed by Henein *et al.* (1983a). Henein *et al.* had studied bed behavior diagrams and established the slipping, slumping, rolling, and cataracting modes and their transitional boundaries. The bed behavior study, as defined by Henein *et al.* (1983a) is simply observations of various types of bed motion. In the current work no attempt was made to link various bed motions to the operating variables, rather, visual observations were made with regard to the slipping, slumping, rolling, and cataracting. Within the range of the operational variables studied active layer thickness, bed expansion, and dynamic angle of repose were quantified. The active layer was quantified in terms of its shape, symmetry, and depth. Dilation within the active layer was quantified by determining the solid fraction there and comparing it with the plug flow region.

In analyzing the flow behavior some of the key parameters that characterize rheological behavior of granular solids, specifically the velocity parallel to the bed surface, the granular temperature, the solid fraction, and the active layer depth were computed. The objective of this exercise was to completely characterize material flow in the rotary kiln so as to compare the similarities that may exist between the rapidly flowing active layer and other granular flow systems.

For each test position in the active layer the mean value of the velocity was computed from instantaneous velocities of particles flowing past the probe unit, and the velocity fluctuation, u'^2 , was calculated from the variance (see, e.g., Ahn *et al.*, 1991). The root mean square of velocity fluctuation is a measure of the kinetic energy of particle collisions and hence represents the granular temperature, \tilde{T} . The average value of the bulk velocity for the entire active layer was calculated as

$$\bar{u}_\delta = \frac{\sum_{i=1}^{N_\delta} u_y(\Delta y)_i}{\sum_{i=1}^{N_\delta} (\Delta y)_i} \quad (4.1)$$

where the denominator is simply the depth of the active layer from the bed surface to the interface between the active layer and the plug flow region. N_δ is the number of data points taken in the active layer, and Δy is the distance between data points.

The solid fraction in the transverse plane has horizontal and vertical components (i.e two dimensional variable); the former, which is called *solids linear concentration* in the direction of the flow, v_x (Ahn *et al.*, 1990), could be measured. In order to determine the linear concentration, v_x , the number of particle passages per unit time recorded by one of the fibre optic probe was divided by the mean velocity at the test location to obtain characteristic particle spacing, C_{sp} , from which the solid fraction was calculated as $v_x = d_p C_{sp}$. The mean shear rate was calculated as $\Delta u / \delta$ where Δu is the local velocity difference between the surface and the active layer/plug flow interface and δ is the local active layer depth normal to the surface plane.

In order to obtain a 'global' verification of both the velocity measurements and the delineation of the active layer depth, the material balance in the transverse plane was checked by comparing the mass flow within the active layer to that in the plug flow region. This was accomplished by calculating the areas under the velocity curves in the two regions as follows:

$$\begin{aligned}
\rho_p v_{AL} \int_0^{\Delta} u dy &= \rho_p v_{PF} \omega \int_{R_i}^{R_o} r dr \\
&= \rho_p v_{PF} \omega (R_o^2 - R_i^2)
\end{aligned}
\tag{4.2}$$

where ρ_p is the particle density, v_{AL} and v_{PF} are, respectively, the solids fraction in the active layer and that in the plug flow region. Δ is the active layer depth at mid-chord; R_o and R_i are, respectively, the internal radius of the drum and the distance from the drum's centerline to the interface between the active layer and the plug flow region. All of the variables in Eq. 4.2 are taken from the experimental results. If the parameters are normalized such that the velocity is u/\bar{U} , the normal distance from the bed surface to a location in the active layer is y/Δ , and that in the plug flow region is y/H , then the mass flow rate in the active layer may also be given as;

$$Q \cong \rho_p v_{AL} \bar{U} H \int_0^{y/\Delta} \frac{u}{\bar{U}} d\left(\frac{y}{H}\right)
\tag{4.3}$$

where $\bar{U} = \omega R_o$ and H is the bed depth at mid-chord.

No quantitative estimation of the segregation patterns was made, however, the mixing/de-mixing behavior was observed when limestone was used as bed material and the salient features were noted for qualitative assessment.

4.5 Experimental Results and Discussion

Owing to the large number of experimental variables involved in the flow experiments and the resulting large volume of experimental data the presentation of the results and discussion will be carried out in a rather non-conventional format. Firstly, results and observations on the general flow behavior will be described as an overview. Secondly, detailed experimental discussion will follow where the material flow behavior will be discussed in light of the field variables that describe granular flow theory, e.g., the velocity, granular temperature, the dilation factor, and the stresses. For generality these results will be compared with other results from computer simulations and

experiments from the literature describing the flow of granules in other areas of applications, e.g., chutes, couette flows, etc. The purpose of this exercise is to relate flow in the rotary kiln to other types of flow and thereby determine the adequacy of using some of the granular flow theories in the literature to mathematically model the flow behavior in rotary kilns. Further discussion on instabilities and what is believed to be their origin will be presented in Appendix A1.

4.5.1 An Overview of the Experimental Results

The rotary performance of the drum was considered to be good and the inner wall coating provided enough wall friction to prevent premature slippage. The support table was kept horizontal thereby providing almost two-dimensional flow in the transverse plane. The validity of the experimental results was ascertained by three indicators: (i) comparison of measured and calculated velocity; (ii) flow visualization; (iii) material balance between the active layer and the plug flow region. Figure 4.4 shows the measured and calculated values for the point velocities for an empty cylinder. It is apparent that the agreement between the measured and calculated velocities is good given the fact that the cross correlator used for data collection is an analog machine and the peaks for time delay functions employed in the computation of the velocities were recorded and read on charts. It was anticipated that this agreement would weaken as a result of possible instabilities when the drum was loaded but no scatter was observed in the measured results and the agreement was still good. For most of the experiments minimum drum speed was kept at 2 rpm.

Polyethylene was run on all the percent fills (i.e., 3.3%, 8.5%, 15%, and 29%) and operated at drum speeds ranging between 1 and 5 rpm. Rice was loaded at 3.3, 8.5, and 10% fills and operated from 3 through 5 rpm. Attempts to run the rice at 2 rpm was unsuccessful; it required a considerable amount of energy to initiate motion even at 3.3% fill. For deeper beds slipping was observed at the start of the drum but this was short lived. Limestone was operated on all the rpm reported but its weight allowed loading only up to 8.5% fill because of insufficient torque

from the drive motor. When assessed on the bed behavior diagram developed by Henein (Figure 4.5) all of the tests indicated either a rolling bed (which was in fact the case) or, in a few instances, a cascading bed (not observed).

The effect of the end walls on material flow was clearly evident and significant; there was a distinct change of the material's dynamic angle of repose as the end walls lifted the particles near the walls to a higher elevation than the rest of the bed. This effect disappeared at an axial distance of about 10 cm from the end-piece which represents about 250 particle diameters. In order to quantify the effect of the glass end-piece on the flow, surface velocity measurements were made on the exposed bed surface at 5 cm and 22 cm from the glass, the latter location being well clear of any observable end effects. Figure 4.6 shows the result of the glass end-piece on the surface velocity measurements taken for polyethylene at 15% fill and 5 rpm. Based on the results from chute flow experiments (Ahn, *et al.* 1991) it might be expected that the end walls would retard the movement of the flow and thus reduce the surface velocity. The fact that the opposite effect occurred in the drum, i.e., surface velocities near the end-piece were significantly higher than at a distance, is attributable to the wall friction between the particles and the moving end-piece which elevated the material's angle of repose and increased the effect of gravity component on the material flow in this region. In all subsequent experiments, therefore, measurements were made at axial locations well away from end effects.

The parabolic nature of the surface velocity profiles shown in Figure 4.6 indicates that the particles accelerate rapidly from the apex up to a location around the mid-chord and then decelerate as a result of the impact of the rotating wall on the material at the base, as would be expected in a confined flow. The mid-chord velocity of 110 cm/s attained for this particular run condition represents over seven times the circumferential velocity of the drum wall. This indicates a very rapid flow of particles over the exposed bed surface. The parabolic nature of the surface velocity is in agreement with observations made by Singh (1978) who had also used polyethylene pellets in rotary kiln experiments. However, the symmetry in the profile was not consistent for all the

materials tested or even for the same material in different tests. The profiles can also be skewed by variations in bed depth (or percent fill) and drum speed. Figure 4.7 shows the surface velocity as a function of distance from the apex for polyethylene pellets at 3.3% fill and the same rotation rate as in the previous figure. The skewness in the profile indicates that particles can sometimes accelerate past the mid-chord. In Figure 4.8, which shows the measured surface velocity for rice grains at 10% fill and drum rotation rate of 5 rpm, it is worth noting that for this material acceleration and deceleration occur before mid-chord thereby creating two parabolas. The velocity of the first profile reached 55 cm/s with a sharp peak; the other at 30 cm/s showed a gradual change resulting in almost constant surface velocity. Visual observations indicated that when the grains are released they align themselves longitudinally in order to expend the minimum energy required to balance the mass flow. It appears that because of its shape the rice grain requires a considerable amount of energy to rearrange itself and therefore in the course of minimizing energy it piles up at the apex. This energy build-up is then released very rapidly like water falls. Similar bifurcation behavior was also observed for limestone. The rheological implications of this and other instabilities will be elucidated later in this chapter.

The profile for the active layer thickness was parabolic irrespective of the nature of the shape of the velocity profile thereby appearing like the shape of a boundary layer thickness in conventional fluid flow. Figure 4.9 depicts the profile for the active layer thickness for polyethylene at 8.5% fill and 2 rpm, and also for 15% fill and 3 rpm. A notable feature of Figure 4.9 is the symmetry about the mid-chord which prevailed in all run conditions despite the often asymmetric shape of surface velocity profile. For the polyethylene pellets the thickness of the active layer at mid-chord, as observed through the glass end-piece, was as high as 30% of the bed depth at mid-chord. Active layer depth for other materials was generally a little less than for the polyethylene. The extent of the active layer thickness can be expected to depend on the physical properties of the material which determine the shearability of the granules. Henein (1980) reported the thickness of the active layer for relatively deep beds to be about 10% of the bed

depth at mid-chord. The results reported in this work indicate that 10% is not an 'across the board' figure but, rather, depends on the material. It is worth mentioning that the actual thickness of the active layer cannot be found by looking through the glass end-piece as is done in most experiments; rather, it should be measured by depth probing or extrapolated from the result of the velocity measurement at various depth locations. The detailed results of the active layer thickness will be presented later in the chapter.

Velocity profiles at the mid-chord position and as a function of depth are shown in Figure 4.10 for polyethylene at 29% fill and at 1, 3 and 5 rpm. The velocity is normalized with the wall velocity (drum circumferential velocity) and the depth is normalized with the bed depth at initial loading. Figure 4.11 shows the particle count profiles for the same run conditions. These measurements were made by inserting the probes into the bed normal to the bed surface at the mid-chord position. Although the flow might be disturbed by the probe this did not occur because the probe actually measures light reflected from the particles beneath the tip location and no appreciable disturbance of these particles occurred. The accuracy of the velocity measurements can be deduced from the fact that the values obtained for the locations in the plug flow region are in agreement with the linear profile ωR_i . As is also seen from Figure 4.10, the linear curve extrapolates to the origin, as should be the case where correct measurements have been made without any flow interference. This also testifies to the fact that, although calibration was carried out on a rigid surface (particles were stuck onto the flange of the rotary drum) as opposed to the tumbling surface of the bed, the velocity measurements in the bed were still accurate within an experimental error of less than 1%. The shape of the velocity profile as a function of depth appears to be parabolic and is in agreement with that obtained by Savage (1979) for flow of polyethylene pellets on an inclined chute. This profile is typical of flows over rough surfaces. In mathematics the profile would be called *tractrix* (from Latin *tractum*, meaning drag). Upon close inspection it is evident that, except for the regions near the surface, and near the interface, the curve is essentially linear (see, Figure 4.10(b)). This linear profile implies a constant shear rate

($du/dy = \text{const}$) and can be considered as a uniform simple shear flow. Further discussions on the velocity profiles will be carried out later in this chapter. Perhaps the most difficult velocity measurement was at the location where $u \rightarrow 0$ i.e., near the interface between the active layer and the plug flow region. However, in order to extract information concerning the active layer depth from the velocity profile, the interface can be located by extrapolating the velocity or particle count to zero or by locating it as the point of intersection between the profiles for the active layer and that for the plug flow region. The velocity profiles as a function of depth measured at three separate surface locations are shown in Figure 4.12. It is apparent that the shapes of the velocity profiles are all the same irrespective of surface location; this finding will obviously aid the modelling of the flow in the active layer.

The granular temperature, a measure of the velocity fluctuation, and the linear concentration are shown respectively in Figures 4.13 (29% fill; 1 and 3 rpm) and 4.14 (15 and 29% fill; 3 and 5 rpm) for polyethylene pellets. As was described earlier, the granular temperature, like its counterpart in the kinetic theory of dense gases i.e., thermodynamic temperature, can either conduct away from the free surface to the bed or vice versa. The profile shown here indicates that there was a granular temperature gradient between the bed surface and the bulk bed and this is in agreement with the computer simulation of Zhang and Campbell (1992) for couette flow of granules. It can be seen that the granular temperature is high in the regions where there is a mean velocity gradient and therefore it is not surprising to see *granular conduction* into the bed burden. Notice that increasing the drum speed from 1 rpm to 3 rpm results in an order of magnitude increase in the granular temperature. The profile for the linear concentration presented in Figure 4.14 shows that there is also a gradient between the surface and the bulk bed, however, this value may be constant throughout the entire active layer in some of the experimental results. Material dilation in the direction normal to the bed surface was not very significant according to visual observations through the glass end-piece. This is not surprising for rolling bed behavior; material balance calculations using Eq. 4.2 showed that bed expansion in the normal direction for all the

runs did not exceed 5%.

4.5.2 A Detailed Discussion of the Experimental Results

Having now given an overview of the experimental observations some of the results can now be examined in more detail, particularly with respect to the rheological behavior of granular flows. As was mentioned earlier, only two particle flow characteristics were determined i.e., (i) the bulk velocity of particles at a location representing the mean value of the velocity within that vicinity, and (ii) particle count, which gives the number of particles per second. Figure 4.15 shows the results of the velocity profiles as a function of depth for the three materials from the 3.3 percent fill and 3 rpm run. Figure 4.16 also shows the particle count for the same run conditions. For clarity the bed surface and mid-chord plane are shown, respectively, with horizontal and vertical dotted lines. The circles in the bulk velocity results are the mean values of at least 5 velocity measurements each established from hundreds of sampling points taken by the cross correlator in estimating the time delay peak. Superimposed on the results are the fitting curves from correlation functions. The profiles in all three cases can be fitted to a parabolic function in y , the bed depth at the active layer, with a coefficient of correlation of over 98%. At the interface near the zero velocity line, the behavior can be considered to be an inflection. The active layer velocity profile resembles a typical drag problem and is in agreement with velocity profiles for granular material flowing down an inclined plane (see, e.g., Savage, 1979). Notice that the same trends are repeated in the results for particle count shown in Figure 4.16. The shaded point at coordinates $(-1,-1)$ in the plug flow region is a theoretical point with velocity ωR ; it is superimposed on the experimental results in order to validate the measured results. The other shaded point is the zero velocity found by extrapolating the two profiles to their point of intersection. As was mentioned before, the linear fit to the velocity profile in the plug flow region is an indication of valid measurements since the velocity in this region is directly proportional to the radius i.e., ωR_i . The normalized surface velocity, C_o , relates the surface velocity at mid-chord to the drum speed (i.e., $u_s = C_o \omega R_i$) and is presented in Tables 4.2 through 4.4 for all

the experimental runs. At a glance it would appear that the depth of the active layer, as estimated from the velocity profiles, is the same for all the materials at this run conditions. Although there are slight differences, all values were between 24 and 34% of the original bed depth. This result indicates that a considerable amount of the material is sheared at this run condition, which is not surprising considering the relatively shallow bed and resulting small overburden pressure. The profiles shown in Figure 4.15 are comparable with computer simulations of Zhang and Campbell (1992) for granular flow behavior in a couette flow where they employed the constitutive relations of Lun *et al.* (1984), described earlier in the literature review, in modelling the flow behavior.

By maintaining the same bed depth and increasing the drum speed it is expected that more material will shear or the magnitude of the active layer velocity will increase (or even both). From the entire results on velocity measurements it can be said that as the drum speed is increased the velocity profile tends from a parabolic *concave* shape (looking from the bed) toward a more linear profile, i.e., the flow behavior approaches that of a uniform simple shear flow. For deeper beds and at higher rotation rates the profile will revert to parabolic but this time with fuller profiles having a *convex* shape with vanishing shear stress at the free surface, analogous to open channel fluid flow. This condition is depicted in Figure 4.10 taken from the run with polyethylene at maximum loading. For materials having lower coefficient of restitution, e_p , and higher coefficient of friction, μ , e.g. rice and limestone, these changes are more significant and are observed even at lower bed depths. Figure 4.17 illustrates changes in the profile's shape for rice as a function of rotation rate. Again, these results are in agreement with the predictions made by Savage and Jeffery (1981) and also by Campbell and Brennen (1983) for gravity flow on an inclined plane using the constitutive relations developed for granular flows. The results show some levels of the changes that result when material moves from solid-like behavior to fluid-like behavior when it is sheared.

As can be seen in Figure 4.17, which shows the velocity profiles obtained for a relatively deeper 10% fill bed of rice grains at several rotation rates, the region near the free surface where

$du/dy \rightarrow 0$ is more than a couple of particle sizes deep and the depth increases with rotation rate. This same behavior was also observed for limestone. Thus a 'rigid' zone similar to a plastic sheet is formed near the upper surface of the bed which moves en-bloc without shearing. In order to understand such flow behavior it is necessary to consider the surface velocity, granular temperature, and linear concentration profiles together. Figures 4.18 and 4.19 show the flow properties at the surface for rice and limestone respectively. Because of the high friction coefficient the order-disorder behavior of the material as it discharges from the plug flow region to the active layer requires a lot of energy and therefore results in material build-up at the apex. At this point the granular temperature is low owing to the inelasticity of collisions. The first appearance of the 'fluidized' behavior as the material yields at the apex follows the Mohr-Coulomb failure criterion ($\tau_{xy} = \tau_{yy} \tan \xi$) where the normal stress is simply the overburden pressure, and is defined by the concentration of particles ($\int v dy$); ξ is the friction angle. Since the energy is not self-sustaining in granular materials it is transferred down as kinetic energy of the mean flow (with some, perhaps, converting into thermodynamic heat). Bearing in mind that in a field of rapid granular transport, the granular temperature plays the same role as thermodynamic temperature plays in kinetic theory of dense gases, it should be expected that the granular temperature is large at the regions where the material exhibits fluid-like behavior and low in the regions where the behavior is solid-like (Zhang and Campbell, 1992). The results shown in Figure 4.18 and 4.19 confirm this hypothesis with the granular temperature being dissipated in the flow direction (i.e., from the apex to the base). The mechanism by which granular heat is generated has been attributed to shear work on the control volume, i.e., defined as the product of the shear stress and the shear rate ($\tau_{xy} \times du/dy$) and as a result, a change in the granular temperature will occur only in the regions where there is a mean velocity gradient. At the base of the rapid fall therefore, the shear work goes to zero, but the stress ratio is not zero ($\tau_{xy}/\tau_{yy} = \tan \xi$), and therefore, $du/dy \rightarrow 0$, resulting in a low granular temperature. The fluid-like behavior, as a result, changes to solid-like behavior whereby a few particles at the surface form a non-shearable structure as was observed in the runs whose results are presented in Figure 4.17. As a result of inadequate

energy dissipation (inelastic dissipation) there is also the possibility of a multiple formation of surface velocity giving rise to periodic motion on the exposed bed surface as is shown in Figure 4.20.

The formation of multiple parabolic profiles mentioned above is attributed to instabilities which develop as a result of granular energy dissipation, a property which has a strong dependence on the solid fraction (concentration) and the coefficient of restitution of the material. Hence for the polyethylene pellets, except for very deep beds, single surface velocity profiles will always develop and this profile can be either symmetrical about the mid-chord plane or skewed (see, e.g., Figures 4.6 and 4.7). This behavior is attributable to the fact that polyethylene pellets are more dissipative compared with the rice grains and the limestone as a result of the material's higher coefficient of restitution. The collision inelasticity which gives rise to a pile of material at the apex for rice and limestone is relatively weaker in polyethylene (i.e., stronger elastic collision). Increasing the percent fill increases the chord length and hence the distance which particles will have to travel increases. For higher coefficient of restitution materials (e.g., polyethylene pellets) the flow on the exposed bed surface behaves in a similar manner to flow in chutes where the momentum is carried by gravity and rapid shearing due to near perfect elastic inter-particle collisions. Thus, the flow will accelerate rapidly up to a point and then will decelerate as it approaches the base. It is even possible that, for relatively deep beds, the flow would be fully developed by the time it gets to the mid-chord; i.e., before the boundary condition set by the rotating wall at the base has any effect on the flow. This finding is depicted in the results shown in Figure 4.21. It appears that the rotating wall effect is the source of the symmetry seen in the surface velocity profile for polyethylene. At slow flow, given no instabilities, there is the possibility that the rate at which the material is discharged into the active layer will equal that at which the wall at the base disperses it and this will result in a symmetrical parabolic profile depicting a mirror image boundary condition so expedient to modelling. On the other hand, at higher speeds or for deeper beds any inequalities will tend to skew this symmetry to the base.

Turning now to the measurements of the active layer depth, it can be said that except for attempts made by Gauthier (1991) the active layer thickness has not been thoroughly studied. Nevertheless, it is accepted in all kiln studies that the extent of particle mixing for both axial and radial directions depends on the layer thickness. Until recently the shape and the thickness of the active layer had only been observed through a glass end-piece but, as shown earlier, the actual depth cannot be estimated through the end-piece because of its effect on the flow. The experiments carried out in this study made it possible to determine with considerable accuracy the true value of the active layer depth well away from end effects. Figures 4.22 through 4.27 show the percent active layer depth at mid-chord plane for all the materials as a function of rotation rate as well as a function of percent fill. The percent active layer depth here is defined as the ratio of the distance between the exposed bed surface and the zero velocity line to the bed depth at initial loading. Experiments carried out elsewhere (Gauthier, 1991) had suggested that the active layer thickness increases with rotation rate and decreases with increased degree of fill and this was found to be true for all the materials tested here. Although the observed trends are in agreement with Gauthier's results (Gauthier, 1991) which employed high speed photography and tracer particles, the magnitudes of the results by Pershin (1988) and Gauthier (1991) are underestimated because of end effects. Although the results shown in Figures 4.22 through 4.27 are anticipated it is imperative to explain the origin of these trends in light of the rheological behavior of granular flows. In order to do so it is worthwhile to consider that in failure zones such as the one which the active layer represents the stress ratio is constant, following the Mohr-Coulomb yield criterion, i.e., $\tau_{xy}/\tau_{yy} = \tan \xi$. In the dilated state, termed the 'grain inertia regime' by Bagnold (1954), the shear stress is related to the velocity gradient in a manner analogous to Reynold's stresses in fluids, i.e., $\tau_{xy} \propto (d_p du/dy)^2$, therefore, increasing the rotation rate increases the shear stresses. In order to maintain the constancy established by $\tan \xi$, the normal stress must increase. As mentioned earlier, the normal stress is nothing but the overburden pressure which is the weight or the thickness

(for that matter) of the active layer. More material is expected to shear as a result of increased rotation rate. This analysis is not new in the studies of other granular flow applications (see, e.g., Johnson and Jackson, 1984; Campbell and Gong, 1986, etc).

The percent fill area as a function of chord length, L , can be represented by the ratio of the area of the fill segment to area of the cylinder cross section, i.e., (see, e.g., Ferron and Singh, 1991);

$$\% \text{ fill area} = \frac{1}{\pi} \{ \sin^{-1}(L/R) - L/R \sqrt{1 - (L/R)^2} \} \quad (4.5)$$

which is an asymptotic function shown in Figure 4.28. Hence, increasing the percent fill means that although more material goes into shearing, this time the amount of material sheared is distributed over a longer chord length and rather smaller increment in thickness; this results in the observed decrease in percent active layer depth. The decreasing percent active layer depth with increased percent fill is therefore related to geometrical definitions. Suffice to say that there is a limit to the amount of material that can be sheared as the drum speed is increased (at a specified degree of fill), which results in the asymptotic profiles seen in Figures 4.22 through 4.27. These asymptotes are even clearer in Gauthier's results because he used a drum of smaller diameter. In their couette shear flow experiments Johnson and Jackson (1987) showed that increasing the outer wall speed after a critical point could not force any more material to enter into the shear layer and values of up to 23% were reported for the shear depth. It is therefore not surprising to see a consistent increase in shear rate as a function of rotation rate and degree of fill. Figures 4.29 through 4.31 show the shear rate in the active layer for all the experimental runs.

In concluding this chapter it is essential to mention that the experimental observations were not restricted to those discussed above. As was mentioned earlier on, there were observed instabilities which created bifurcations in surface velocity profiles. There was also wave formation

(depending on the material used) in the axial direction, resulting from forced oscillations. It is believed that these instabilities play a vital role in axial segregation. The observed instabilities and the theoretical analysis of what is believed to be their origin are presented in Appendix A1.

4.6 Summary and Conclusions

Experiments on the continuous flow of granular material in the transverse plane of a rotating drum have been carried out with the objective of obtaining data for mathematical modelling and understanding the rheological behavior of granular material in rotary kilns. Granular materials employed varied widely in their physical properties, and included polyethylene pellets, long grain rice, and limestone. Optical fibre probes were used to measure mean depth as well as surface velocities, from which one component of the velocity fluctuations and the linear concentration of particles were computed. The rotary drum comprised a steel cylinder of 0.964 I.D (1 m O.D) and 1 m long having a glass end-piece with a center opening providing an access for flow measurements.

In light of the shape and the thickness of the active layer preliminary experiments were confined to the observation of the general behavior of material flow in the cross-section. It was found that the transition of particles from the plug flow region of the transverse plane, where material moves in rigid motion with the cylinder, to the active layer (the thin layer on the exposed bed surface), where particles are continuously shearing, does not only depend on the material angle of repose but also physical properties such as the coefficient of restitution of the material. Because the shear stress is comprised mainly of collisional elasticity it is observed that, for polyethylene pellets, the dynamic angle of repose is relatively low and the transition from potential energy in the plug flow region into kinetic energy in the active layer is easily accomplished. On the other hand, for low coefficient of restitution material, e.g. rice and limestone, the friction angle is relatively high and the energy dissipation is lower than that for polyethylene pellets. As a result, high potential energy is built up during the transition and is accompanied by material build-up prior to release into the active layer. Instabilities result with the possible formation of multiple dynamic angles of repose giving way to unsteady distribution of velocity at the exposed bed surface.

The depth of the active layer as well as the rheological characteristics such as granular temperature and dilation of this layer depend on the coefficient of restitution of the material. Granular temperature, which is a measure of kinetic energy, is high and the concentration is low in the region of high mean velocity. The shape of the active layer is parabolic irrespective of material used, but the thickness of it depends on the physical properties of the material and the operational parameters. The percent active layer depth ranged from 15% for limestone operated at 8.5% fill and 2 rpm to 37% for polyethylene pellets operated at 3.3% fill and 5 rpm. At a given material and a given degree of fill there is a monotonic increase in active layer thickness with increased rotation rate up to a point where more material declines to go into shearing. Also, for a given material and a given drum speed, increasing the degree of fill reduces the percent increase in active layer depth.

Because there is a limit to the amount of material that goes into shearing, there are variations in the shape of the velocity profile in the active layer. There is a linear dependency between the shear rate in the active layer and the drum speed; thus, for a given degree of fill, increasing the rotation rate results in increased shear rate and both the active layer velocity and the thickness increase in order to accomplish material balance. In the limit where no more material goes into shearing, increased shear rate results in changing the shape of the velocity profile from a parabolic *concave* to a linear profile, and further to a parabolic *convex* profile.

The surface velocity is parabolic and particles, after transferring from the plug flow region into the active layer, accelerate rapidly up to around mid-chord of the surface plane before decelerating. Besides inter-particle collision, gravity plays a major role in momentum transfer. Thus increasing the degree of fill provides a longer chord length for material to travel and for larger drums the velocity at the exposed bed surface will be fully developed by mid-chord. For deep beds (e.g., 29% fill polyethylene) surface velocities can reach as high as 4.5-7.5 times the drum speed, representing some 1.2 m/s of material flow at the exposed bed. Near the glass end-piece friction increases and particles there sustain a higher angle of repose than particles well away from

the end-piece. Although there is a retarding effect of the end-piece on particle velocity, the overall effect of increased angle of repose and gravity results in a slightly increased surface velocity. The active layer thickness is therefore smaller near the end walls than in the rest of the bed and, as a result, reported values in the current literature have been underestimated.

4.7 Tables and Figures

Table 4.1. Estimated Relevant Properties of Material Used in Flow Experiment

Material	Av. Particle Size ⁺	Particle Density	Static Angle of Repose	Coeff. of Restitution e_p	Coeff. Of Restitution e_w
	[<i>mm</i>]	[<i>kg/m</i> ³]	[°]	[-]	[-]
Polyethylene	$d_p = 3.63(\pm 0.02)$	960	25	0.85	0.7
Limestone	$d_p = 3.22(\pm 1.23)$	3730	35	0.60	0.5
Long Grain Rice	$L = 6.41(\pm 1.18)$ $W = 2.17(\pm 0.14)$ $Th = 1.62(\pm 0.08)$	1046	32	-	-

⁺ Standard errors are shown in bracket.

Table 4.2. Data on Flow Characteristics for Polyethylene Pellets

%Fill (Bed Depth Chord Length)	Rotational Speed	Tangential Speed ωR	Normalized Surface Velocity $C_o = u_s/\omega R$	Active Layer Depth	Shear Rate @ Active Layer du/dy
	[rpm]	[cm/s]	[-]	[%]	[1/s]
3.3 ($H = 7.5 \text{ cm}$ $2L = 50.0 \text{ cm}$)	2.054	10.349	2.474	28.571	12.173
	3.071	15.475	1.956	34.424	13.333
	4.134	20.848	1.878	36.735	16.000
	5.219	26.295	1.696	37.757	17.026
8.5 ($H = 13.5 \text{ cm}$ $2L = 65.0 \text{ cm}$)	1.875	9.446	4.173	27.040	10.253
	2.870	14.460	3.207	28.480	11.913
	3.975	20.027	2.859	29.697	12.500
	5.077	25.579	2.593	31.121	13.771
15.0 ($H = 20.0 \text{ cm}$ $2L = 75.0 \text{ cm}$)	2.135	10.755	4.266	23.571	8.647
	3.067	14.828	3.791	25.000	10.563
	4.112	20.715	3.442	26.290	13.669
	5.114	25.766	3.188	27.397	14.177
29.0 ($H = 32.0 \text{ cm}$ $2L = 90.0 \text{ cm}$)	0.915	4.610	7.500	14.286	6.563
	2.832	14.268	5.451	18.571	10.888
	5.148	25.940	4.494	18.571	17.474

Table 4.3. Data on Flow Characteristics for Rice Grains

%Fill Bed Depth Chord Length	Rotational Speed	Tangential Speed ωR	Normalized Surface Velocity $C_o = u_s/\omega R$	Active Layer Depth	Shear Rate @ Active Layer du/dy
	[rpm]	[cm/s]	[-]	[%]	[1/s]
3.3	3.082	15.529	2.016	33.000	13.445
($H = 7.5 \text{ cm}$	4.091	20.610	2.212	36.000	18.402
$2L = 50.0 \text{ cm}$)	5.150	25.944	1.832	38.600	19.203
8.5	3.017	15.200	1.931	27.140	7.969
($H = 13.5 \text{ cm}$	4.095	20.630	1.853	30.000	9.979
$2L = 65.0 \text{ cm}$)	5.166	26.030	1.626	31.670	10.194
10.0	3.000	15.113	1.778	25.714	6.857
($H = 15.0 \text{ cm}$	4.122	20.770	1.602	28.571	7.269
$2L = 70.0 \text{ cm}$)	5.201	26.205	1.291	30.000	6.589

Table 4.4. Data on Flow Characteristics for Limestone

%Fill Bed Depth Chord Length	Rotational Speed	Tangential Speed ωR	Normalized Surface Velocity $C_o = u_s/\omega R$	Active Layer Depth	Shear Rate @ Active Layer du/dy
	[rpm]	[cm/s]	[-]	[%]	[1/s]
3.3	2.000	10.064	2.207	21.200	15.762
<i>(H = 7.5 cm 2L = 50.0 cm)</i>	3.003	15.128	2.156	28.200	13.483
	4.096	20.635	2.114	29.380	15.484
	5.073	25.557	1.783	30.590	18.000
8.5	1.967	9.908	2.576	15.758	12.042
<i>(H = 13.5 cm 2L = 65.0 cm)</i>	3.068	15.460	2.639	22.424	14.042
	4.012	20.215	1.766	-	-

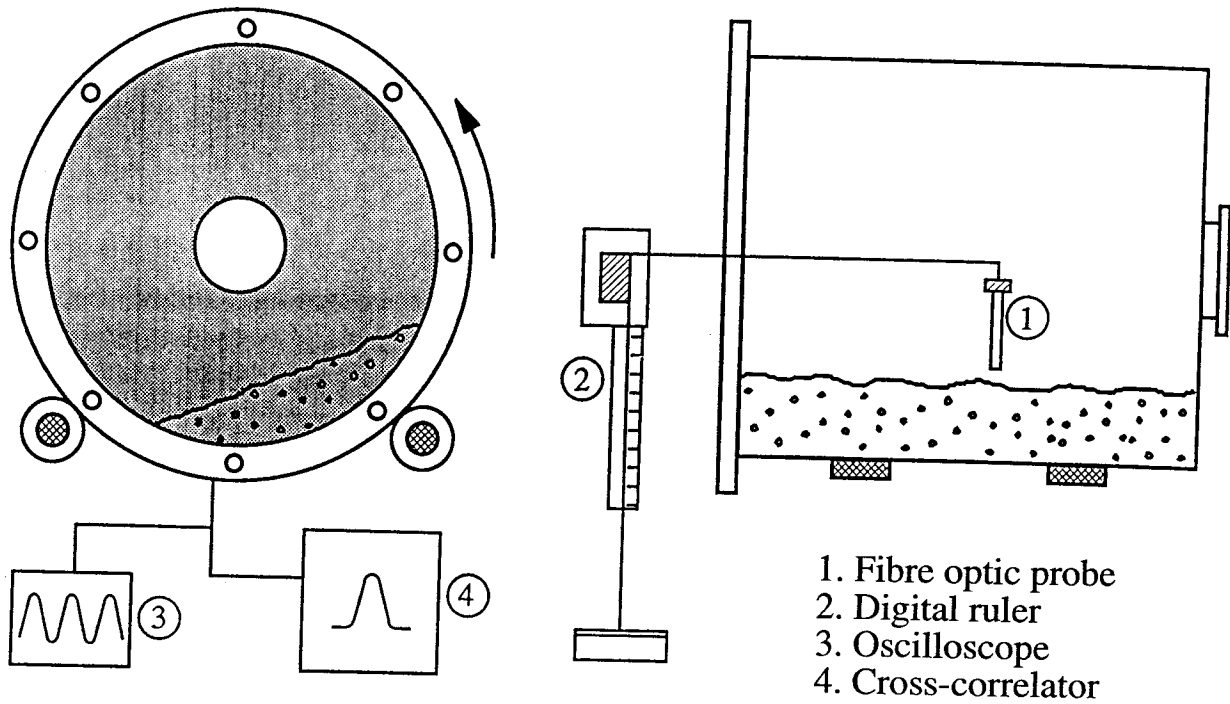


Figure 4.1. The Experimental Apparatus Showing Rotary Drum and Instrumentation for Velocity Measurements.

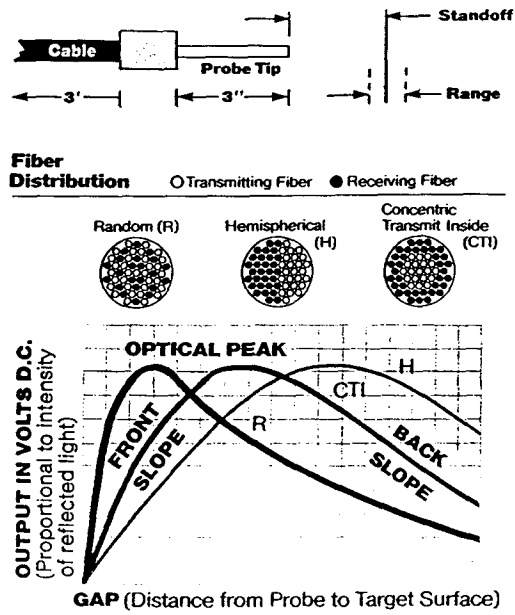


Figure 4.2. Optic Probe Tip, Fibre Orientation, and Theoretical Response Curves.



Figure 4.3. Typical Cross Correlation Curve for the Two Optical Fibre Probes Placed 5 mm Apart.

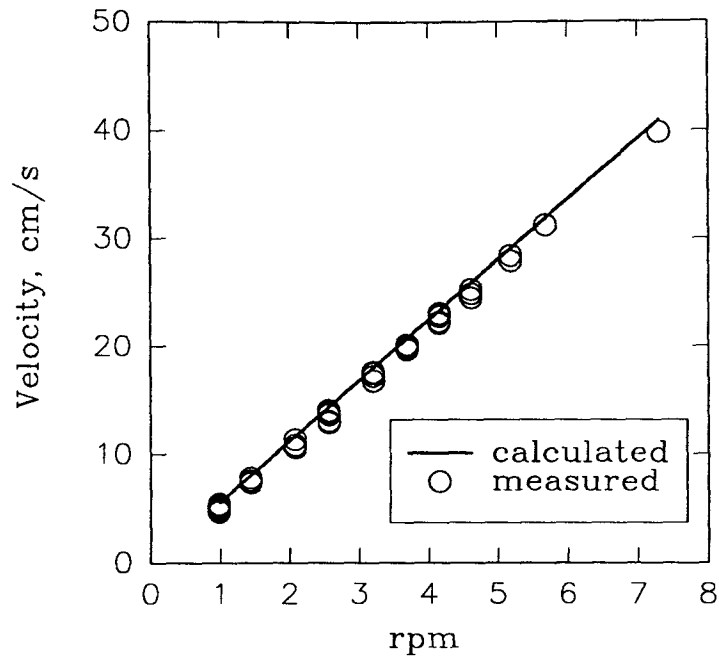


Figure 4.4. Velocity Calibration for Optical Fibre Probes Using Empty Drum; Calculated is the Tangential Velocity (ωR_o) for a Local Point on Flange.

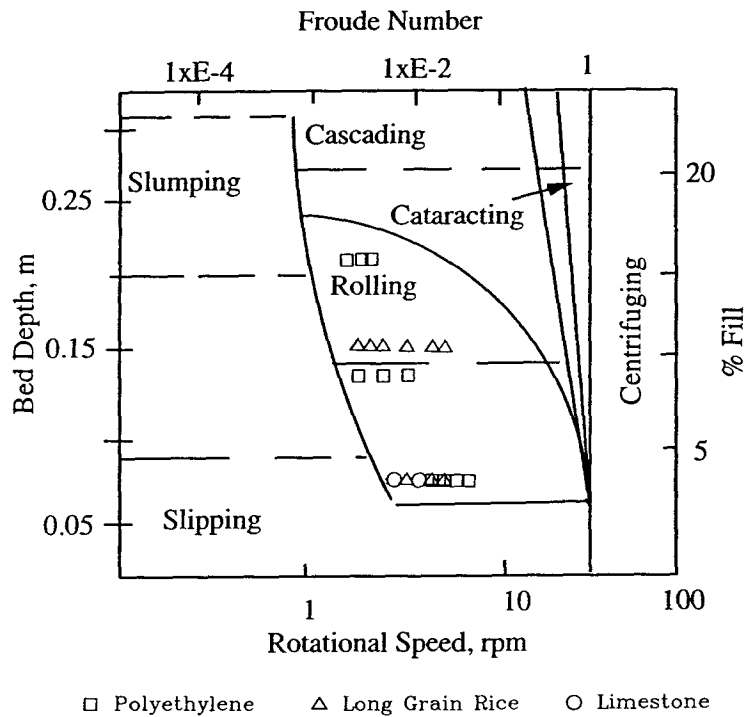


Figure 4.5. The Operational Modes for Present Experiment as per Bed Behavior Diagram of Henein *et al* (1983).

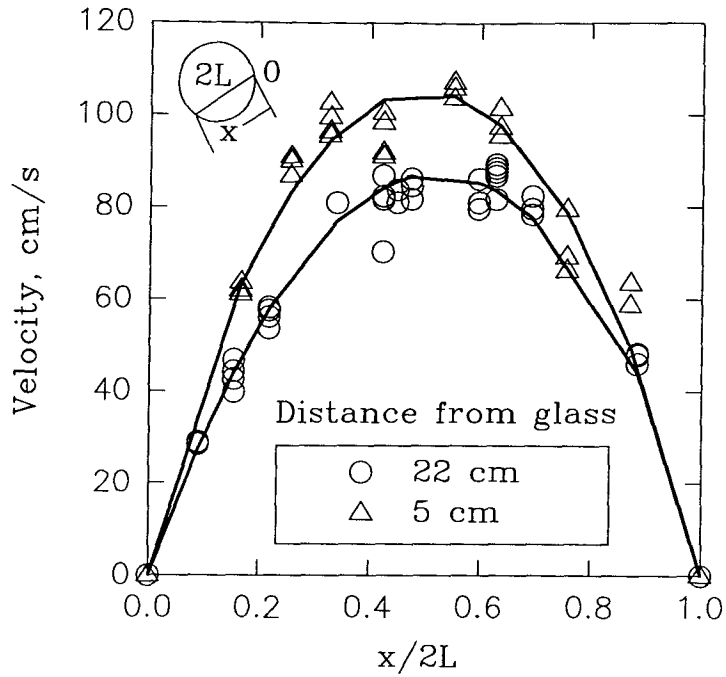


Figure 4.6. Bulk Velocity at the Exposed Bed Surface for Polyethylene Showing Effect of Glass End-piece (15% Fill and 5 rpm).

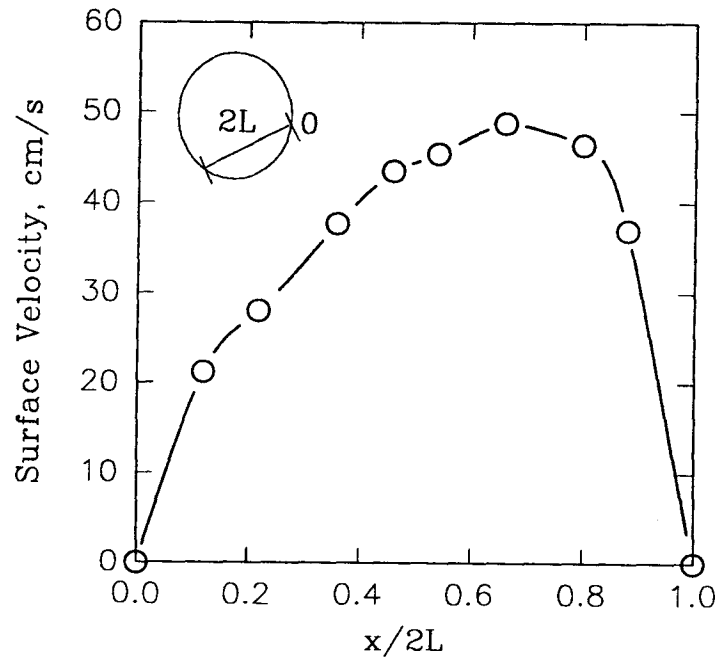


Figure 4.7. Bulk Velocity at the Exposed Bed Surface for Polyethylene Showing Skewness to Base of Transverse Plane: Drum run at 3.3% Fill and 5 rpm.

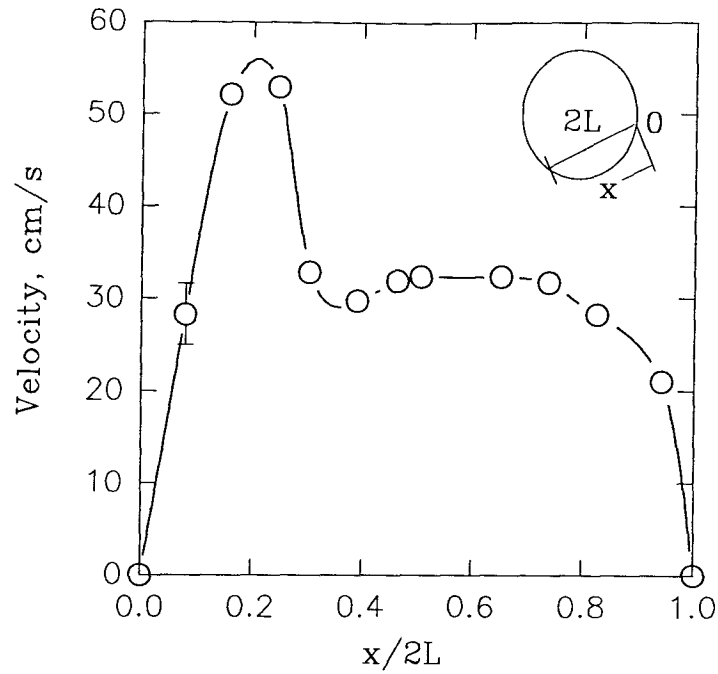


Figure 4.8. Bulk Velocity at the Exposed Bed Surface for Rice Grains Showing Two Parabolic Profile Resulting from Changes in Dynamic Angle of Repose: Drum run at 10% Fill and 5 rpm.

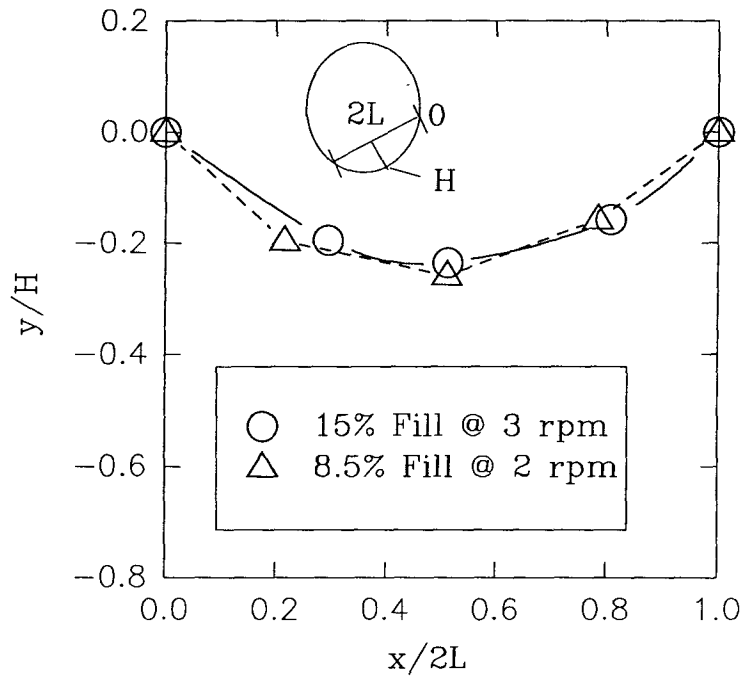


Figure 4.9. Shape of Active Layer for Polyethylene Pellets Showing Symmetry at Mid-chord.

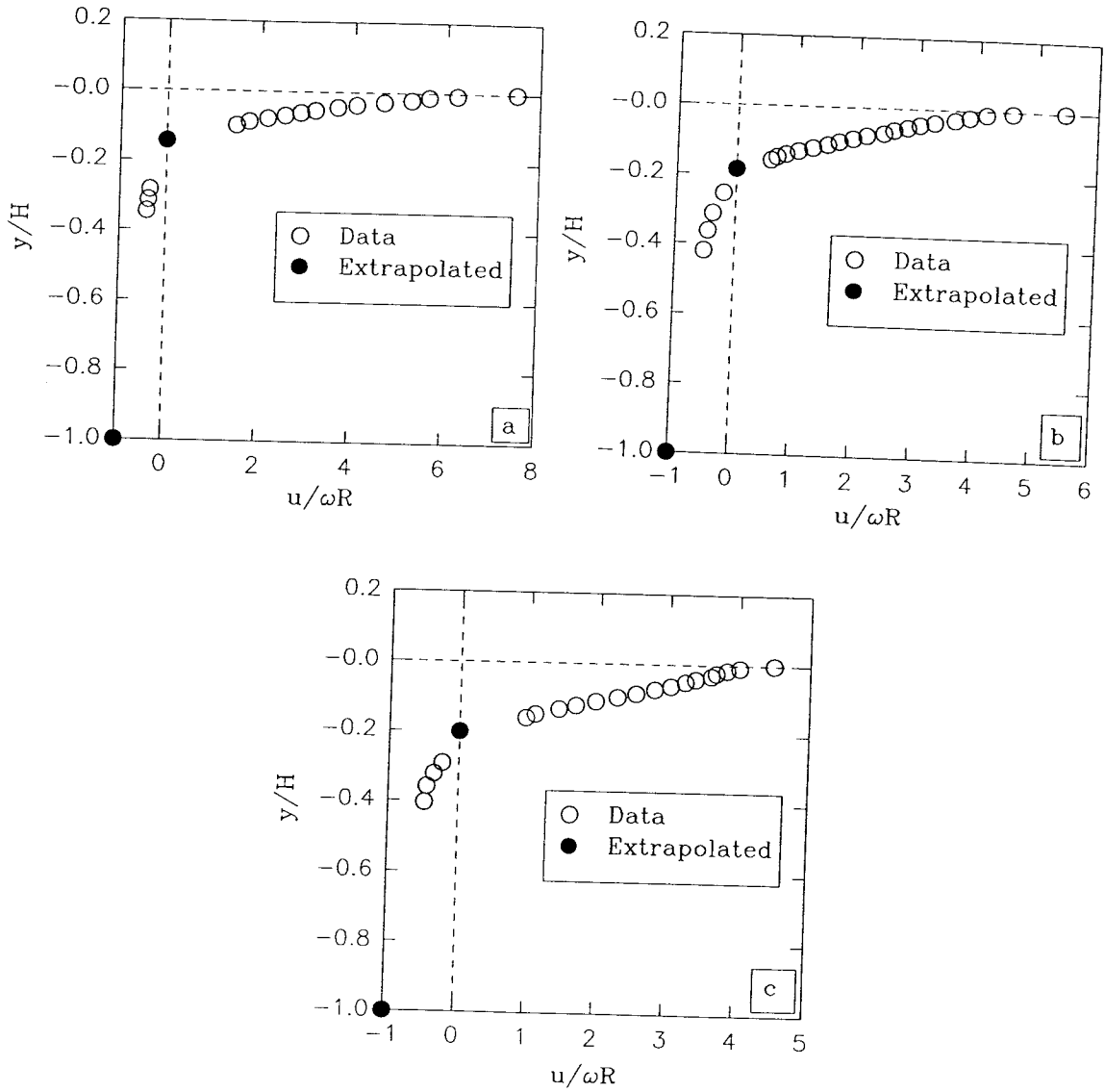


Figure 4.10. Bulk Velocity as Function of Depth and Rotational Speed Taken at Mid-chord Position; Shown here for Polyethylene Pellets at 29% Fill: a) 1 rpm, b) 3 rpm, and c) 5 rpm.

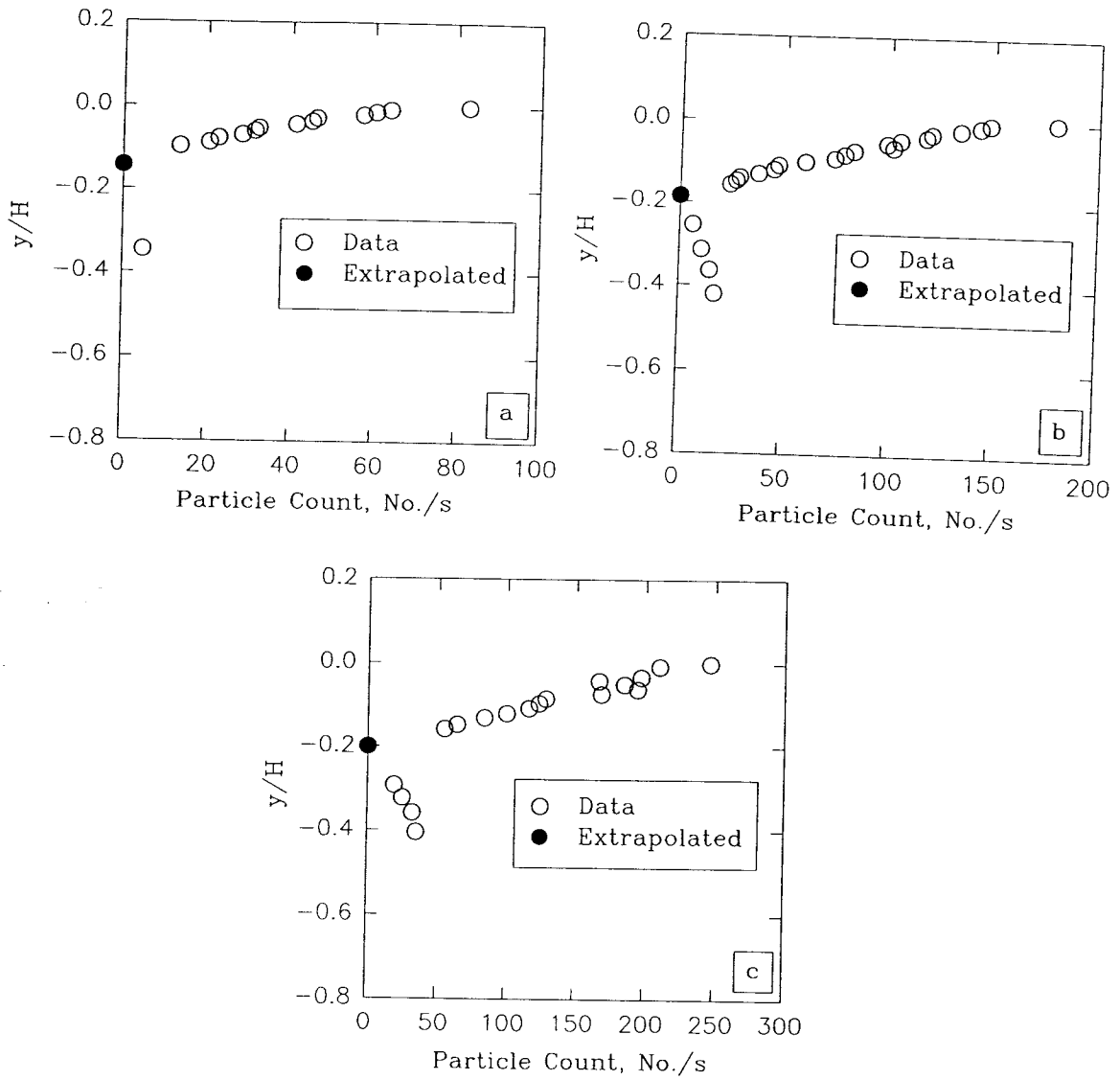


Figure 4.11. Particle Count as Function of Depth and Rotational Speed Taken at Mid-chord Position; Shown here for Polyethylene Pellets at 29% Fill: a) 1 rpm, b) 3 rpm, and c) 5 rpm.

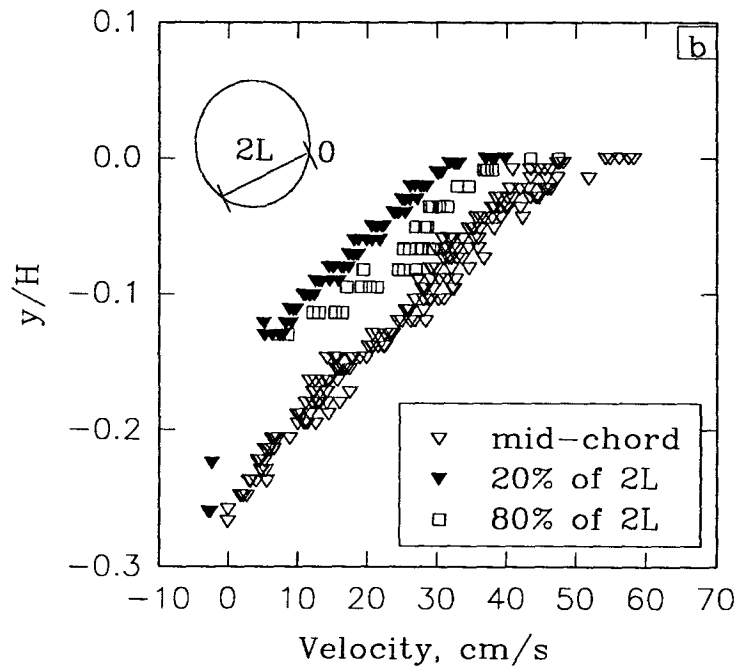
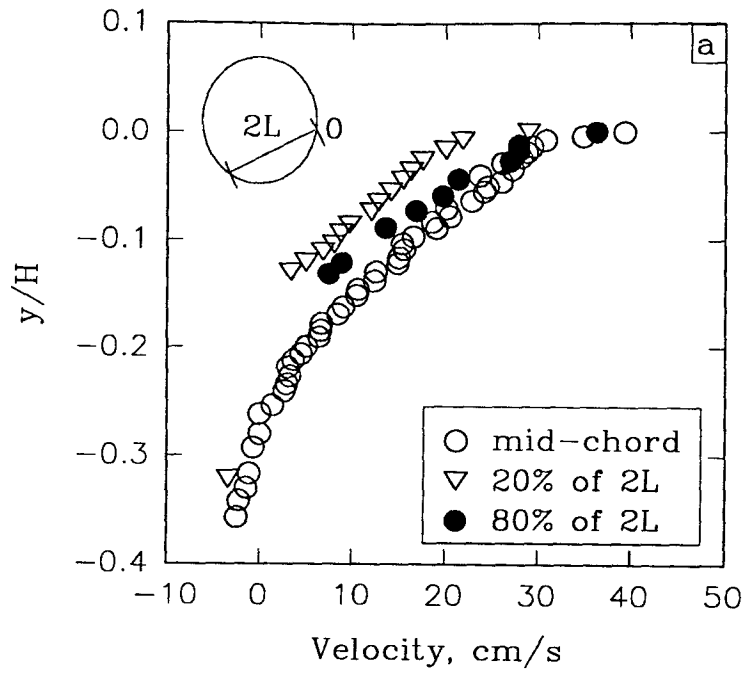


Figure 4.12. Bulk Velocity as Function of Depth at Different Surface Locations Showing Similarities in Profile Irrespective of Surface Location: a) Polyethylene Pellets at 8.5% Fill and 2 rpm, b) Polyethylene Pellets at 15% Fill and 3 rpm.

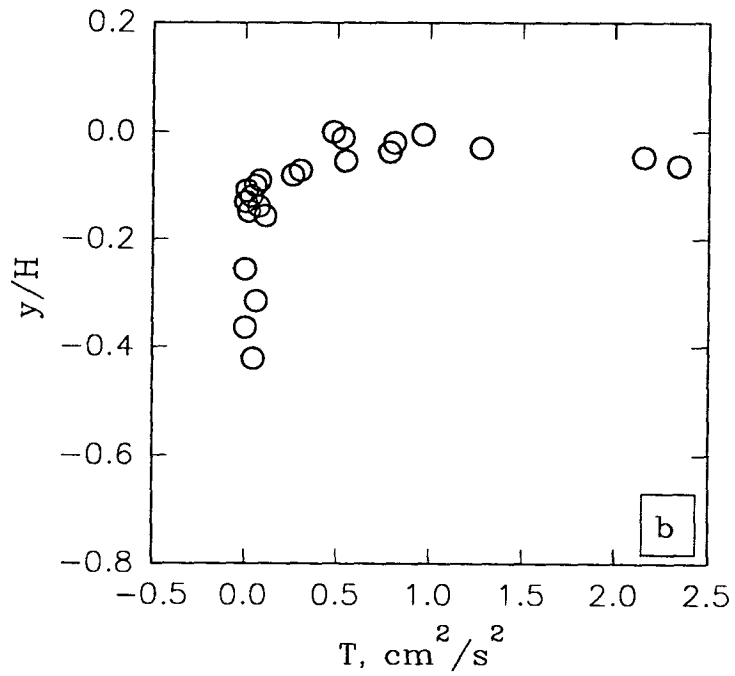
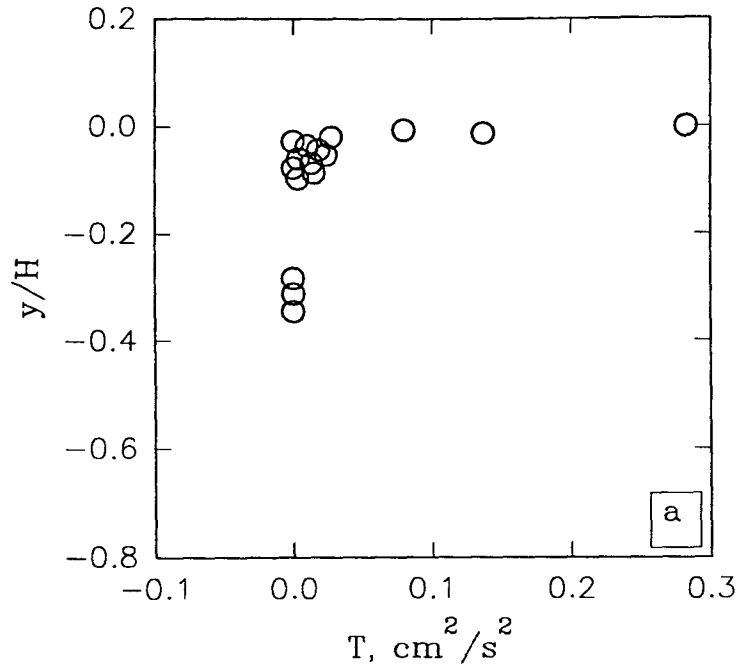


Figure 4.13. Granular Temperature as a Function of Depth; Shown here for Polyethylene Pellets at 29% Fill: a) 1 rpm, b) 3 rpm.

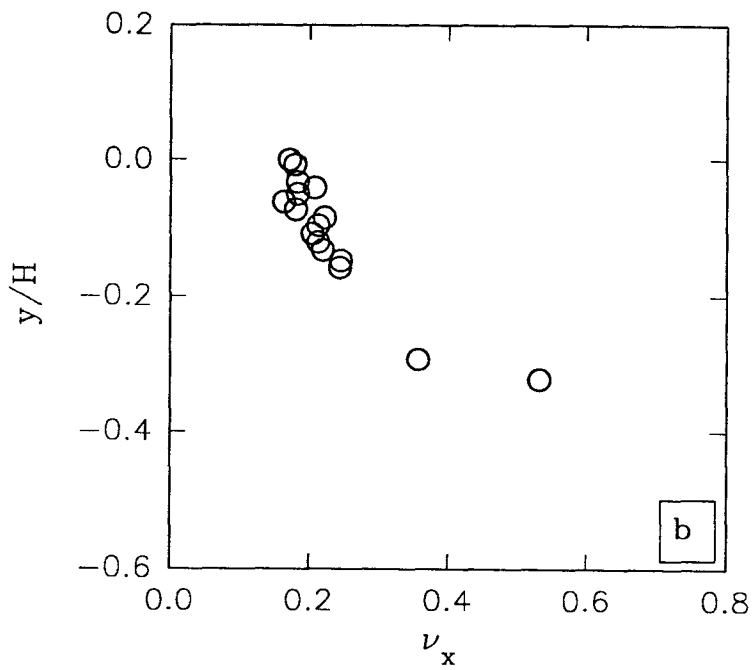
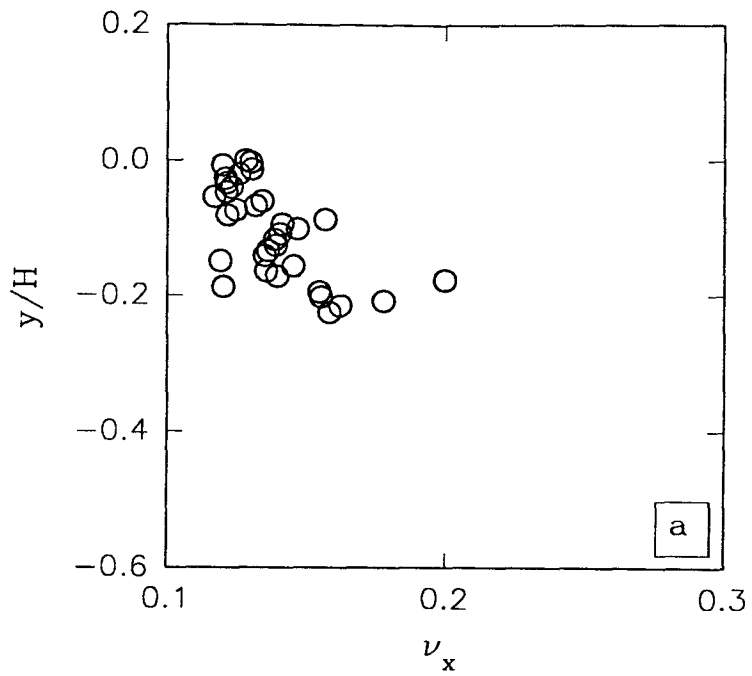


Figure 4.14. Linear Concentration as Function of Depth; Shown here for Polyethylene Pellets: a) 15% Fill and 3 rpm, b) 29% Fill and 5 rpm.

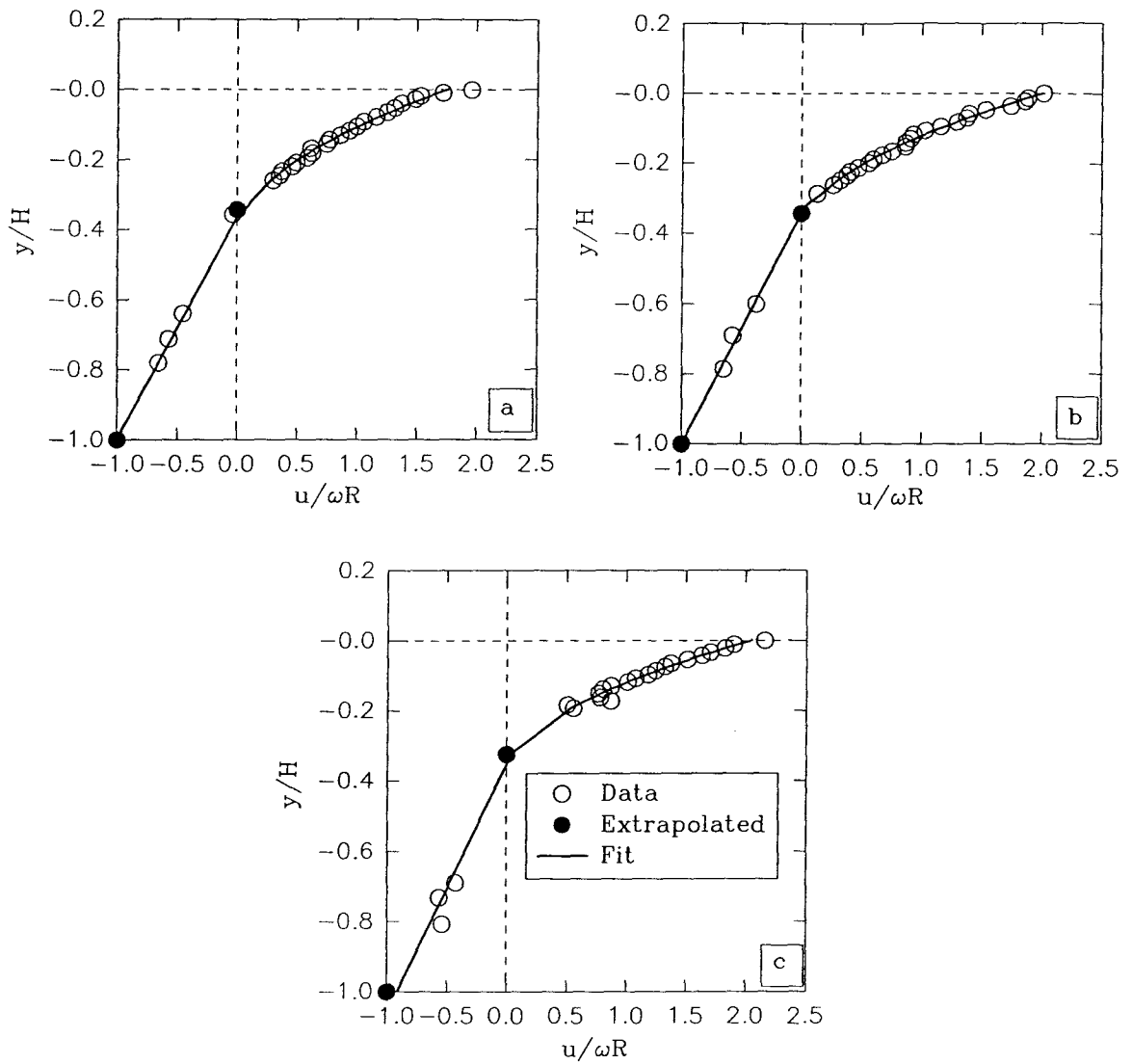


Figure 4.15. Bulk Velocity as Function of Depth for Different Material at Same Run Conditions; Shown here for 3.3% Fill: a) Polyethylene Pellets, b) Rice Grains, and c) Limestone.

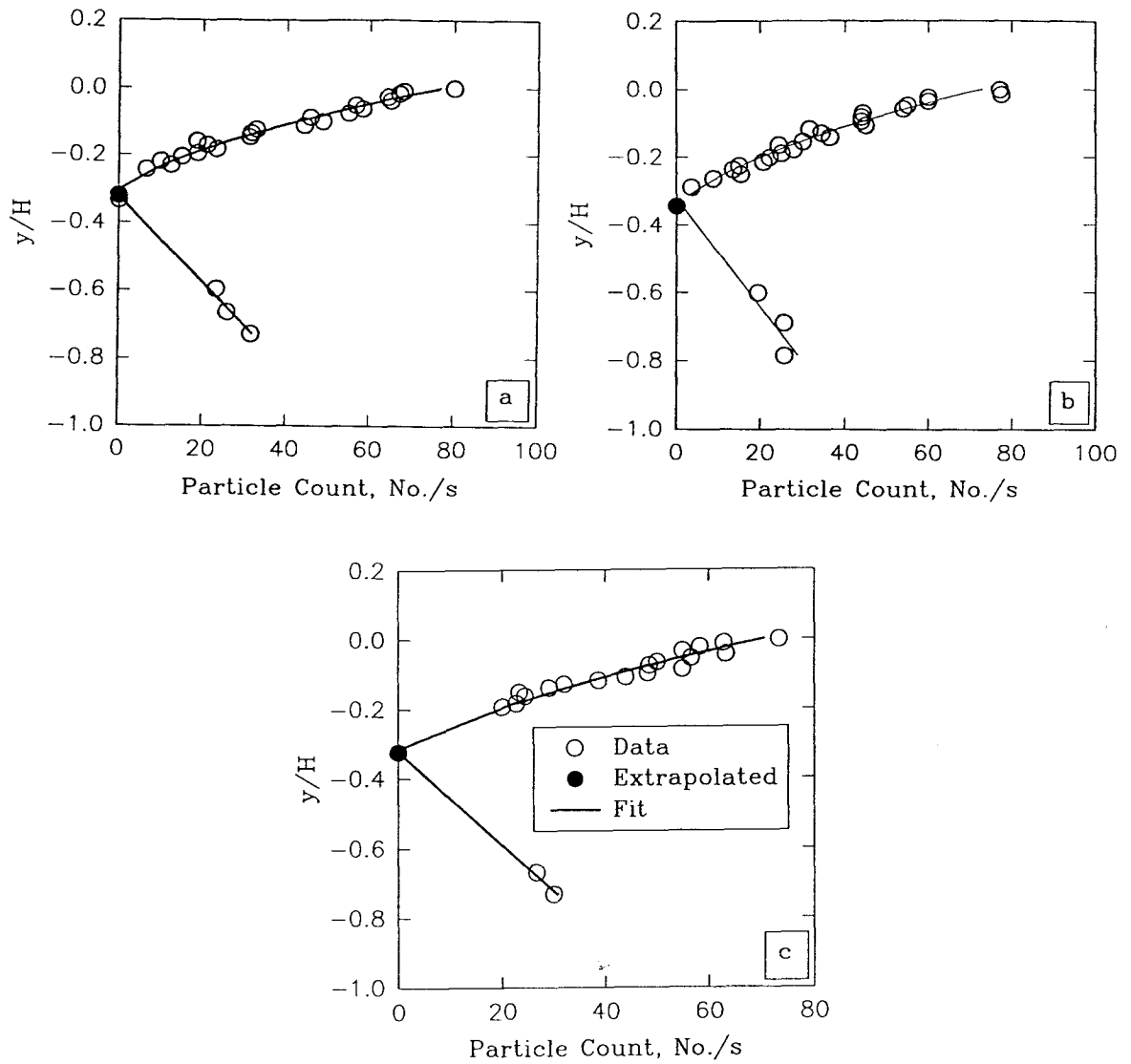


Figure 4.16. Particle Count as Function of Depth for Different Material at Same Run Conditions; Shown here for 3.3% Fill: a) Polyethylene Pellets, b) Rice Grains, and c) Limestone.

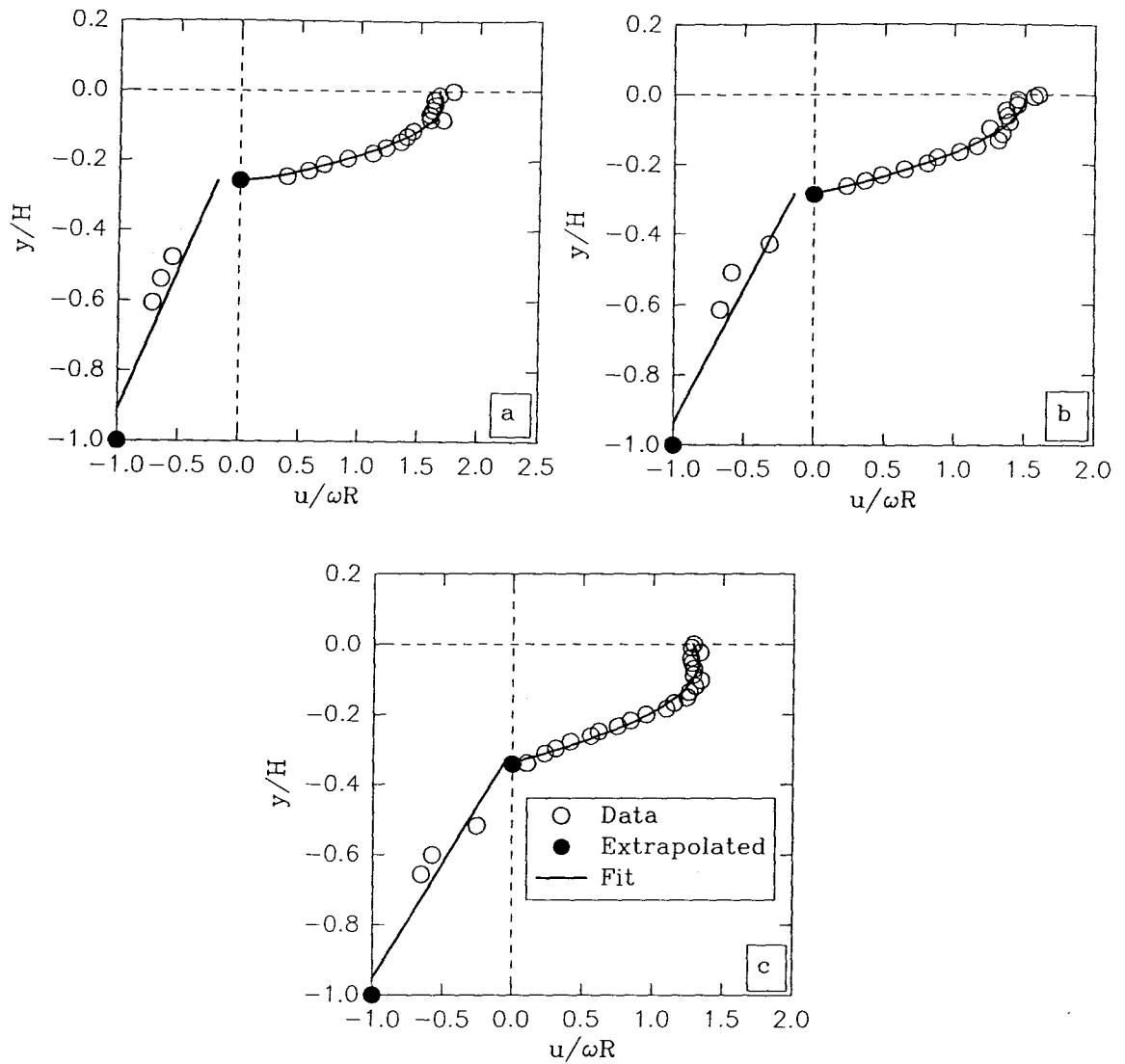


Figure 4.17. Bulk Velocity as Function of Depth Depicting Structure Formation at Free surface; Shown here for Rice Grains at 10% Fill: a) 3 rpm, b) 4 rpm, and c) 5 rpm.

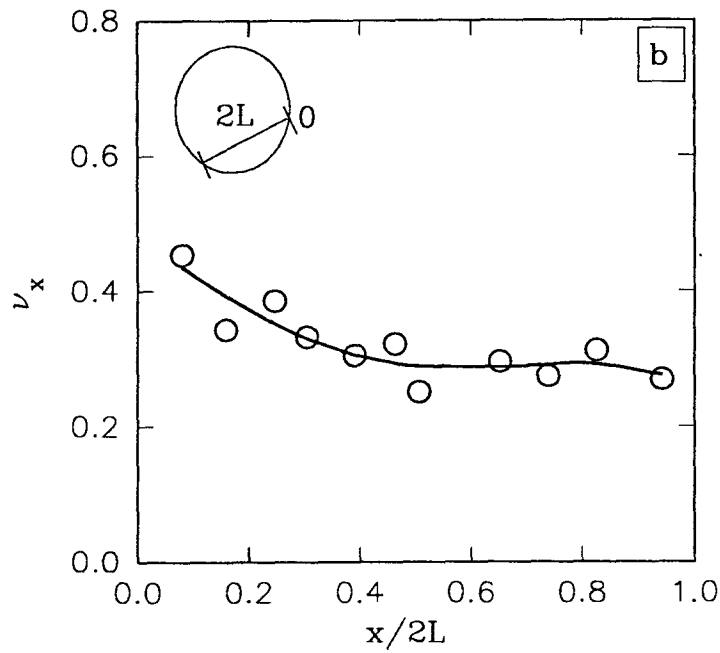
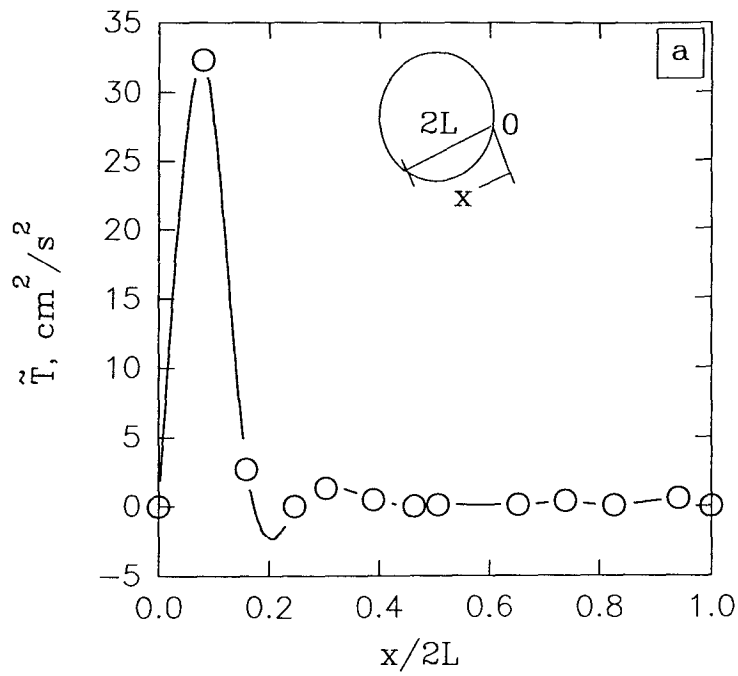


Figure 4.18. Flow Characteristics at the Exposed Bed Surface Shown for Rice Grains at 10% Fill and 5 rpm; a) Granular Temperature, b) Linear Concentration.

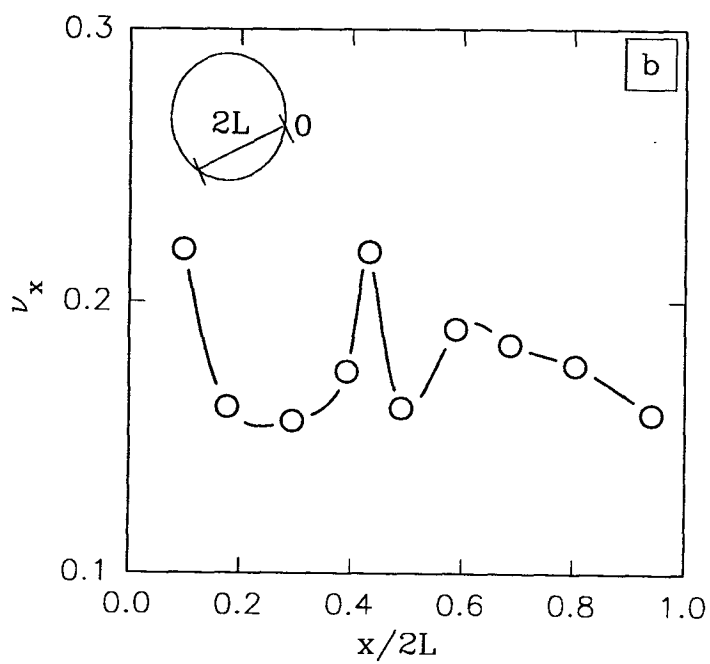
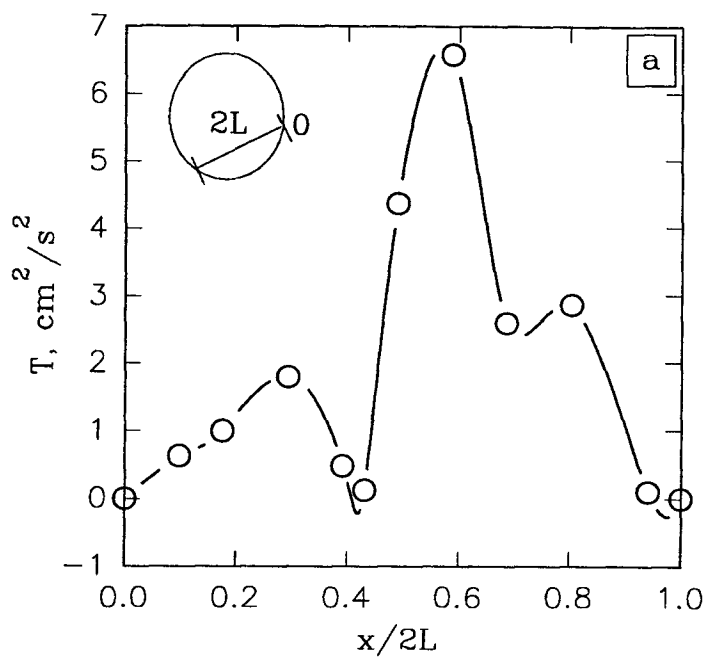


Figure 4.19. Flow Characteristics at the Exposed Bed Surface Shown for Limestone at 3.3% Fill and 2 rpm; a) Granular Temperature, b) Linear Concentration.

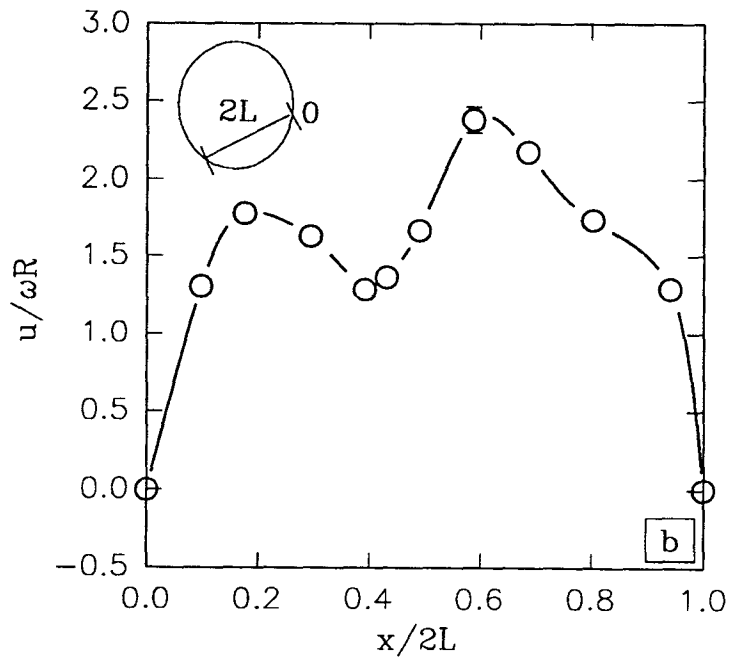
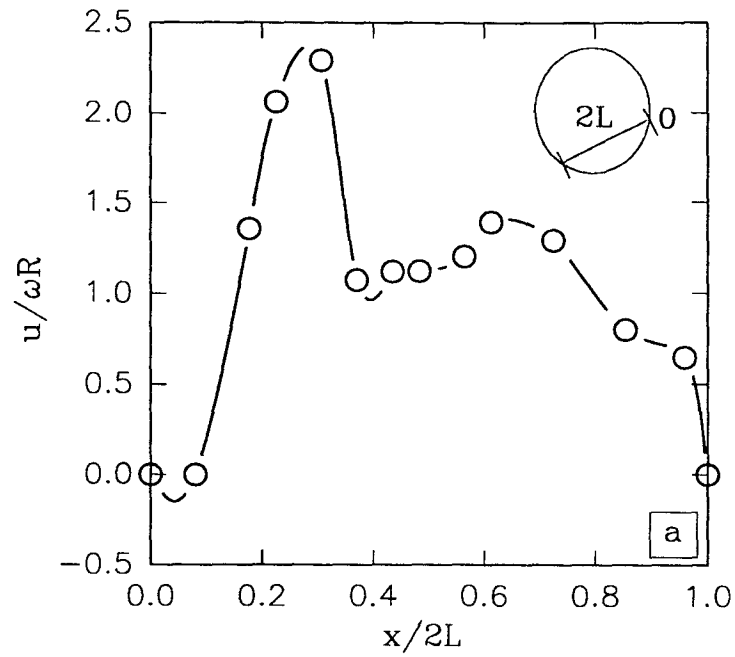


Figure 4.20. Surface Velocity as Function of Chord Length Showing the Formation of Periodic Profiles as a Result of Low Energy Dissipation or Low Coefficient of Restitution; a) Rice Grains at 8.5% Fill and 3 rpm, and b) Limestone at 3.3% Fill and 2 rpm.

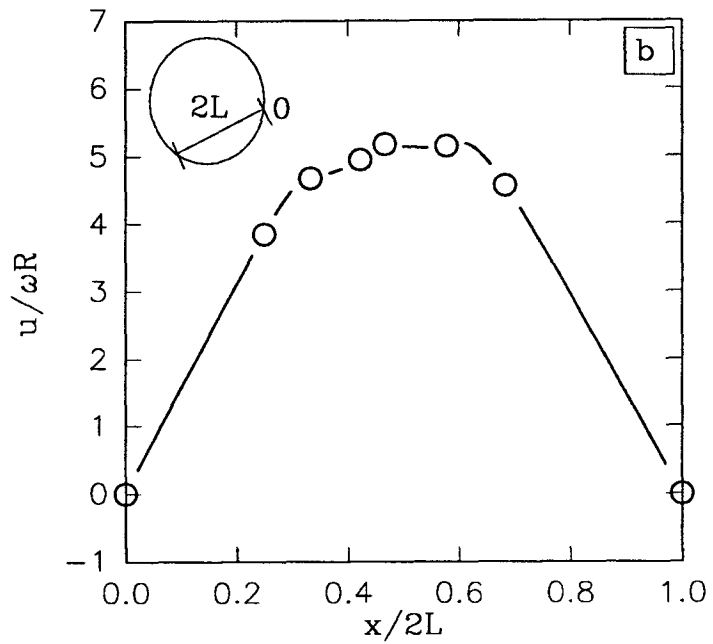
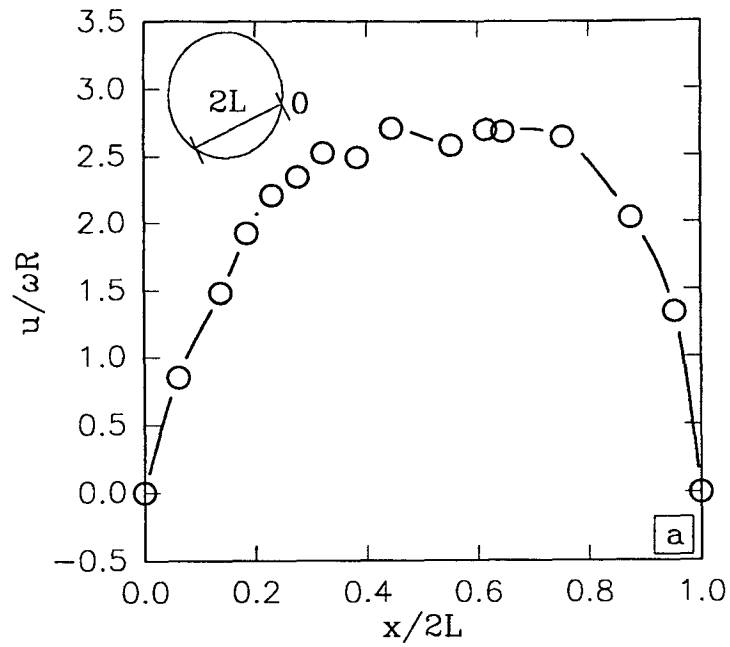


Figure 4.21. Surface Velocity as Function of Depth for Polyethylene Pellets Depicting Fully Developed Flow at Mid-chord; a) 8.5% Fill at 5 rpm, and b) 29% Fill at 3 rpm.

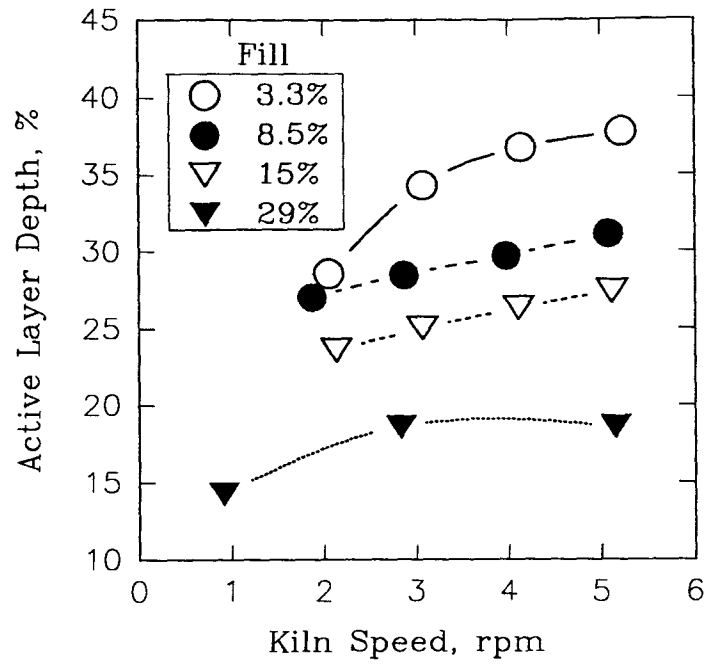


Figure 4.22. The Active Layer Depth as a Function of Cylinder Rotation shown for Polyethylene Pellets at 3.3, 8.5, 15, and 29% Fill.

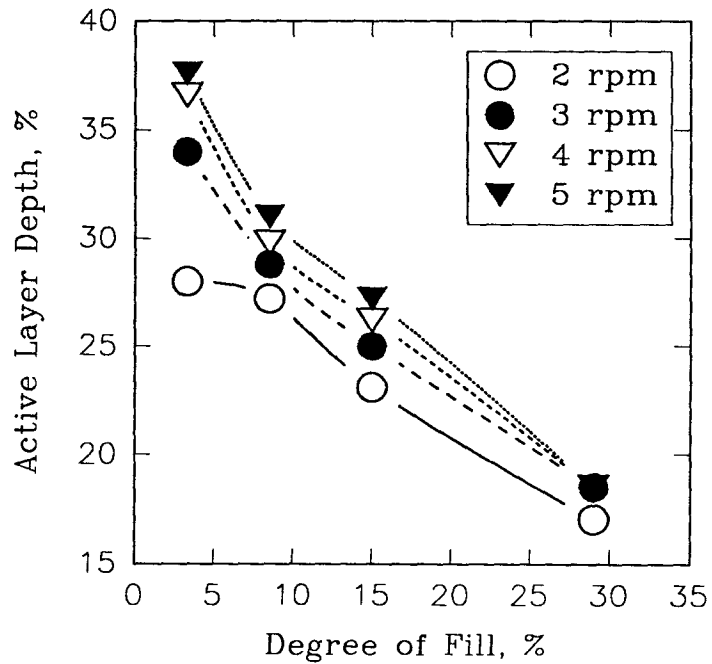


Figure 4.23. The Active Layer Depth as a Function of the Degree of Fill shown for Polyethylene Pellets at 2, 3, 4, and 5 rpm.

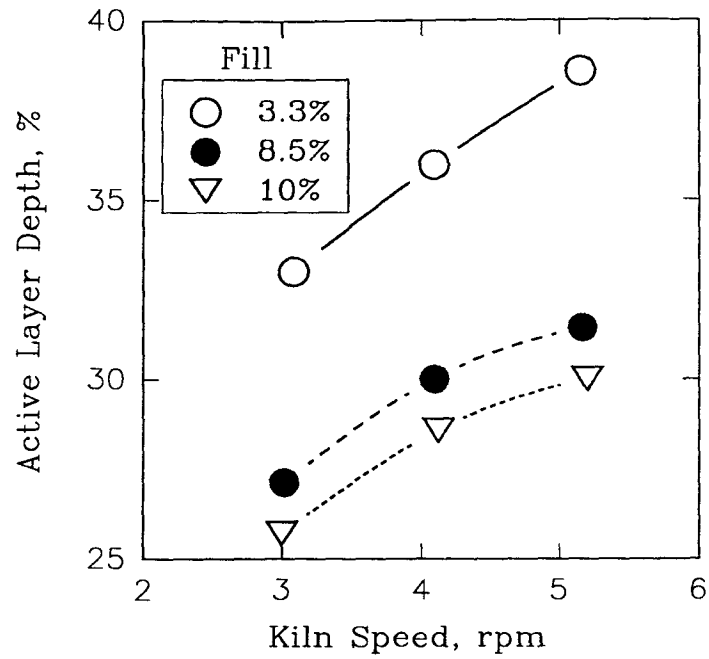


Figure 4.24. The Active Layer Depth as a Function of Cylinder Rotation shown for Rice Grains at 3.3, 8.5, and 10% Fill.

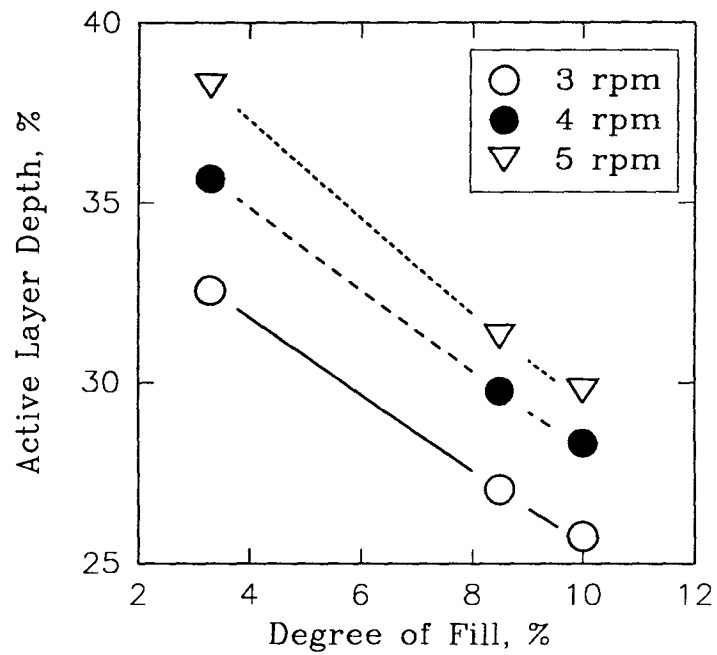


Figure 4.25. The Active Layer Depth as a Function of the Degree of Fill shown for Rice Grains at 3, 4, and 5 rpm.

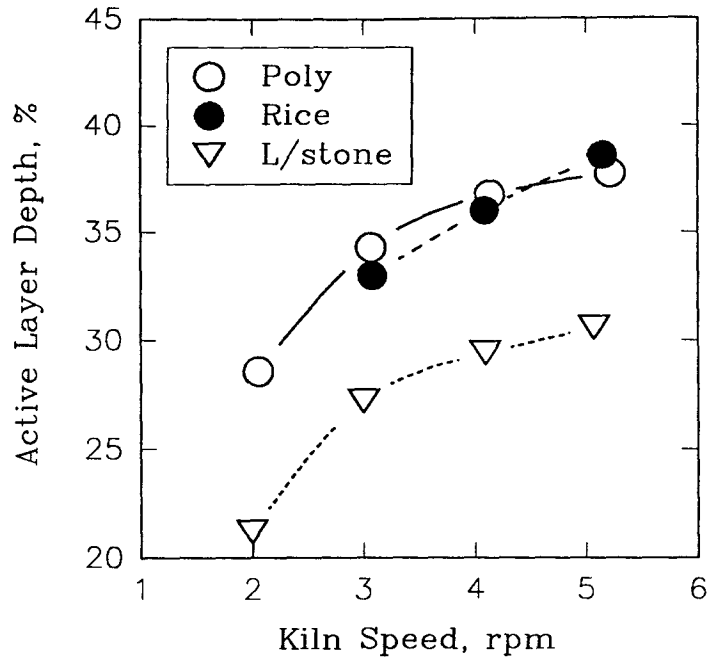


Figure 4.26. The Active Layer Depth as a Function of Cylinder Rotation shown for Polyethylene Pellets, Rice Grains, and Limestone all at 3.3% Fill.

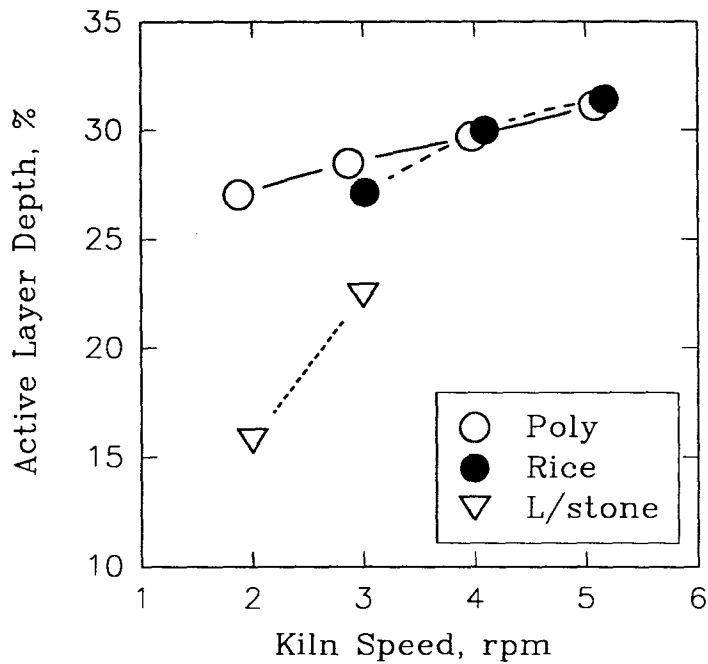


Figure 4.27. The Active Layer Depth as a Function of Cylinder Rotation shown for Polyethylene Pellets, Rice Grains, and Limestone all at 8.5% Fill.

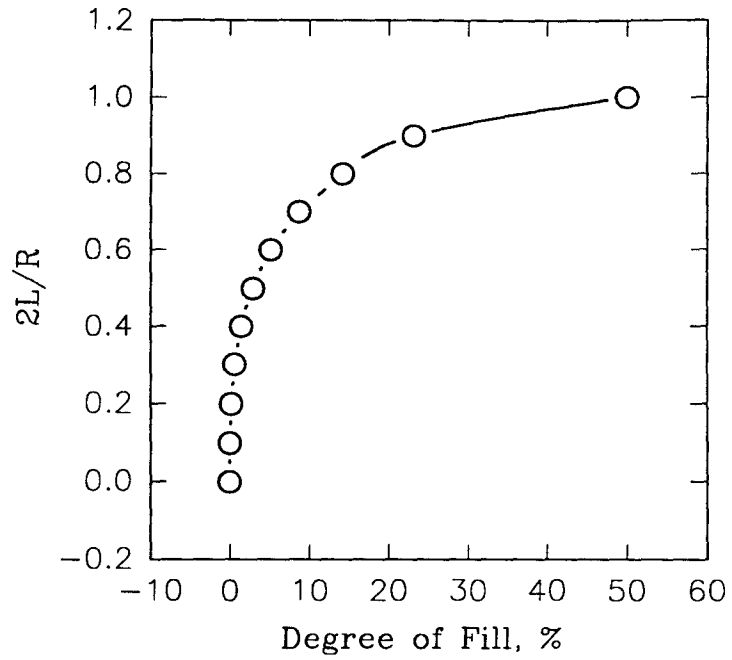


Figure 4.28. Relationship Between the Chord Length and the Degree of Fill.

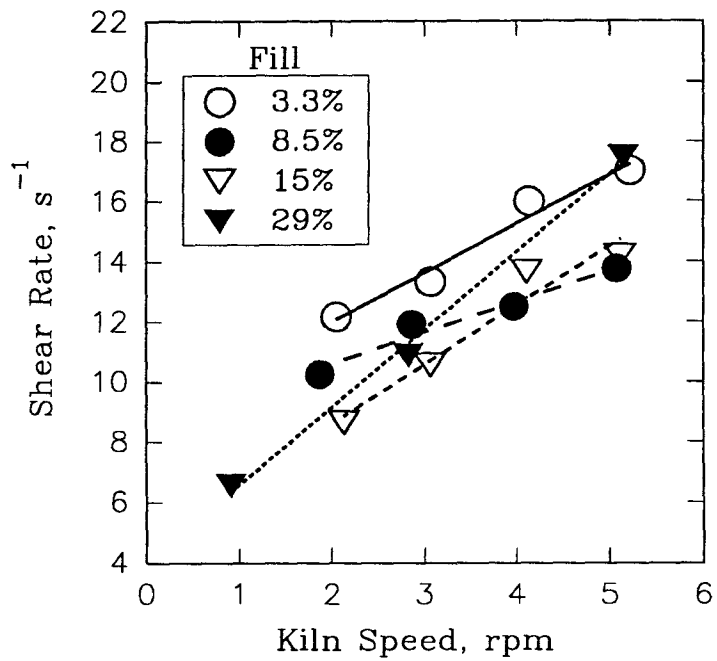


Figure 4.29. Shear Rate, du/dy , at the Active Layer for Polyethylene run at 3.3, 8.5, 15, and 29% Fill.

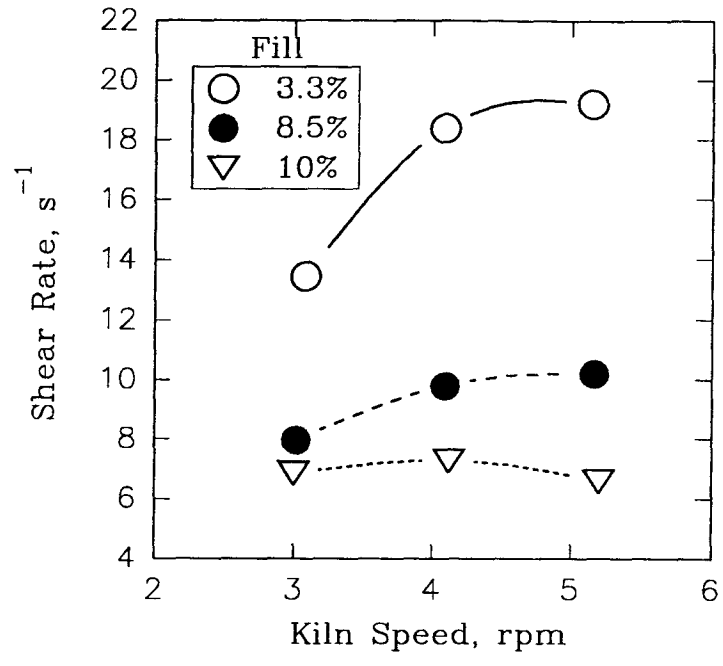


Figure 4.30. Shear Rate, du/dy , at the Active Layer for Rice run at 3.3, 8.5, and 10% Fill.

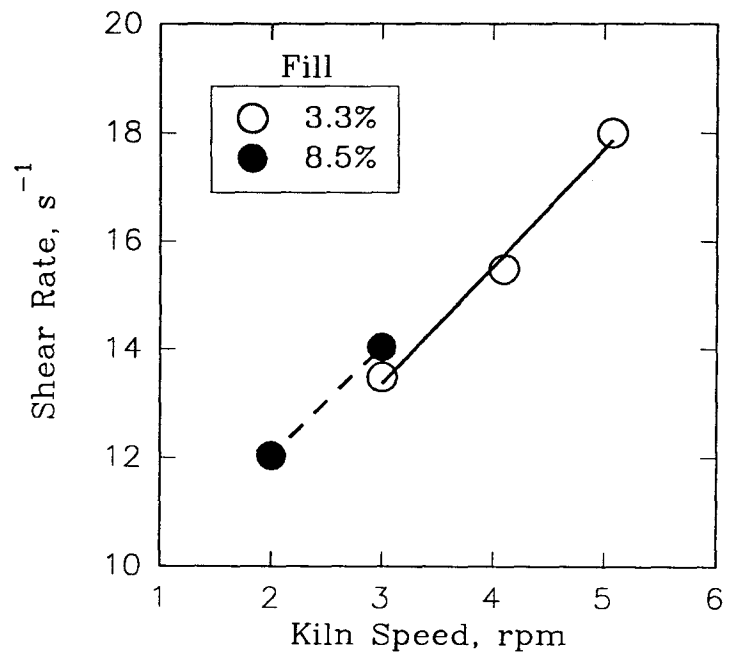


Figure 4.31. Shear Rate, du/dy , at the Active Layer for Limestone run at 3.3 and 8.5% Fill.

CHAPTER 5. MODELLING THE GRANULAR FLOW IN TRANSVERSE PLANE

5.1 Introduction

It was stated in the previous chapter that the objective of the flow experiments was to establish the basis for the development of a mathematical model which would predict the rheological behavior of material flow in the rotary kiln. Previous work on granular flow on inclined planes (e.g., chute flow) had suggested that the constitutive equations of Lun *et al.* (1984), developed for rapidly shearing (slightly inelastic) granular material and based on the analogy of kinetic theory of dense gases, were appropriate in interpreting the experimental results. Although other theories exist for example, plastic formulations (see, e.g., Mandl and Luque, 1970), they have not been widely tested for rapidly shearing granular flows. Having established the justification for doing so, the task is to find appropriate solutions to these equations by invoking the boundary conditions appropriate for the rotary kiln. The experimental results and observations provide the appropriate boundary conditions and also help in establishing the relevant assumptions in the flow calculations. In this chapter therefore, simple, yet adequate, solutions are sought for governing granular flow equations in order to predict the bed behavior in the transverse plane of the kiln.

5.2 Model Description

The domain for which a solution to the flow problem is sought is depicted in Figure 5.1. As shown in the figure two distinct regions, (i) the non-shearing (plug flow) region and (ii) the shearing region which forms the active layer near the bed surface, can be discerned by an interfacial boundary which is a few particles away from the zero velocity line. At this boundary particles are sustained by the dynamic angle of repose. In the plug flow region the particles rotate with the kiln as a rigid body and the strain rate in this region is zero. The flow of particles within the active layer near the upper bed surface is rather more complex since it involves all the aspects of granular flow discussed earlier. In this region the material can acquire any of the several modes described earlier i.e:

slumping, which is a slow flow occurring when the bed inclination just exceeds the static angle of repose of the material; rolling bed, for which the material is continuously sheared and the flow, as well as diffusion, is the result of inter particle collisions. Although equations for the mode-to-mode transitions will be discussed in the development of the model, attention will be focused on the rolling bed because of its importance to industrial kiln operation. For the rolling mode the plug flow region might be anticipated to behave as a rigid lattice of particles rotating with the kiln wall without slippage. This was confirmed by the experimental campaign; thus the velocity within the plug flow region is a linear function of radius and a solution for the flow field is therefore required only for the active layer near the upper surface of the bed. However, the location of the interface between this region and the active layer is not known *a priori* and one of the tasks of the flow model is to allow prediction of its position and hence to determine the active layer depth.

5.2.1 Simplifying Assumptions

The primary assumptions which were made during the development of the flow model were as follows:

- (i) The bed material consists of cohesionless particles which possess a relatively high coefficient of restitution. This assumption places important emphasis on the role of inter-particle collision on momentum transfer and permits the use of the equations of Lun *et al.* (1984).
- (ii) Particles are spherical, rigid, and slightly inelastic like the polyethylene pellets used in the experimental work.
- (iii) The bed motion is rolling and the active layer is considered to be thin relative to the bed depth (the ratio of the active layer depth at mid-chord to the chord length was less than 0.04 in the experiments). The granular temperature in the active layer is assumed constant in the radial direction of each bed surface position.

- (iv) The motion is essentially two-dimensional in the transverse plane since the transverse velocity is several orders of magnitude than the axial velocity. Also particle flux into the active layer at the right quadrant is assumed equal to particle flux into the plug flow region at the left quadrant and therefore only half of the two-dimensional domain is considered.
- (v) The particle ensemble behaves as a continuum and the flow properties e.g., solids concentration, are thus continuous functions of position.

5.2.2 Governing Equations for Momentum Conservation

As was seen in the previous chapters, the governing equations for the flow are similar to those derived for conventional fluids, for example the Navier Stokes equations for Newtonian isotropic material. However, in the latter instance flow properties such as viscosity are experimentally determined. In the case of dense gases and, by extension, granular flows, collisions between particles play a significant role in the exchange of both energy and momentum. Under these conditions kinetic energy conservation must also be considered along with momentum and mass. The governing equations for such granular flows are stated as (Lun *et al.*, 1984)

$$\frac{\partial \rho}{\partial t} + \nabla \cdot (\rho \mathbf{u}) = 0 \quad (5.1)$$

$$\rho \frac{D\mathbf{u}}{Dt} = \rho \mathbf{g} - \nabla \cdot \mathbf{P} \quad (5.2)$$

$$\frac{3}{2} \rho \frac{D\tilde{T}}{Dt} = -\nabla \cdot \mathbf{q}_{PT} - \mathbf{P} : \nabla \mathbf{u} - \gamma \quad (5.3)$$

where \mathbf{u} is the bulk velocity, $\rho = v\rho_p$ is the bulk density and v is the solids volume fraction. \mathbf{P} is the total stress tensor, which consists of both static and kinetic (streaming and collisions) components. The term \mathbf{q}_{PT} is the flux of pseudo-thermal energy defined by the kinetic energy definition of temperature, \tilde{T} , also known as granular temperature (see, Johnson and Jackson, 1988), while γ is the dissipation of pseudo-thermal energy due to inelastic collision of particles. The kinetic contribution of the stress tensor has been given as per Lun *et al.*, (1984) as

$$\begin{aligned} \mathbf{P} &= [\rho\tilde{T}(1+4\eta v g_o) - \eta\mu_b \nabla \cdot \mathbf{u}] \mathbf{I} \\ &\quad - \left\{ \frac{2\mu}{\eta(2-\eta)g_o} \left(1 + \frac{8}{5}\eta v g_o \right) \left[1 + \frac{8}{5}\eta(3\eta-2)v g_o \right] + \frac{6}{5}\mu_b \eta \right\} \mathbf{S} \end{aligned} \quad (5.4)$$

and has been derived by considering the pair distribution function in collision theory. In Eq. 5.4, \mathbf{S} is the deviatoric stress which is given by;

$$\mathbf{S} = \frac{1}{2}(\mathbf{u}_{i,j} + \mathbf{u}_{j,i}) - \frac{1}{3}\mathbf{u}_{k,k}\delta_{ij}$$

where δ_{ij} is the kronecker delta; i.e., $\delta_{i,j} = 1$ for $i = j$, $\delta_{i,j} = 0$ for $i \neq j$.

The flux of pseudo-thermal energy has also been given (Johnson and Jackson, 1988) as;

$$\begin{aligned} \mathbf{q}_{pT} &= -\frac{\lambda_i}{g_o} \left\{ \left(1 + \frac{12}{5}\eta v g_o \right) \left[1 + \frac{12}{5}\eta^2(4\eta-3)v g_o \right] \right. \\ &\quad \left. + \frac{64}{25\pi} (41-33\eta)(\eta v g_o)^2 \right\} \nabla \tilde{T} \\ &\quad - \frac{\lambda_i}{g_o} \left(1 + \frac{12}{5}\eta v g_o \right) \frac{12}{5}\eta(2\eta-1)(\eta-1) \frac{d}{dv} (v^2 g_o) \frac{\tilde{T}}{v} \nabla v \end{aligned}$$

The dissipation of energy due to inelastic collisions may be written (Johnson and Jackson, 1988) as;

$$\gamma = \frac{48}{\sqrt{\pi}} \eta(1-\eta) \rho_p \frac{v^2}{d_p} \tilde{T}^{3/2}$$

As was mentioned earlier, the constitutive equations are taken from Lun *et al.* (1984) and therefore the nomenclature is consistent with that work. Using the analogy of fluid flow, the various parameters in these constitutive equations can be defined as follows:

μ_b [= $256\mu v^2 g_o/5\pi$] is the bulk 'viscosity' for perfectly elastic particles;

$\eta\mu_b$, is the bulk 'viscosity' for inelastic particles;

λ [$= 75m\sqrt{\bar{T}}/\pi/64d_p^2$] is the granular conductivity;

λ_i [$= 8\lambda\eta(41 - 33\eta)$] is the granular conductivity for inelastic particles;

η [$= 1/2(1 + e_p)$] is the average value between the coefficient of restitution of the particle, e_p , and that of a perfectly elastic particle, $e_p = 1$;

μ [$= 5m\sqrt{\bar{T}}/\pi/16d_p^2$] is the shear viscosity, where m and d_p are, respectively, particle mass and diameter;

μ_i [$= \mu/\eta(2 - \eta)$] is the shear viscosity for inelastic particles;

g_o [$= 1/(1 - v/v_*)^{1/3}$] is a radial distribution function at contact during binary collision; it was given earlier in Eq. 2.4 as the dilation factor. In this term v_* is the maximum shearable solids volume fraction.

The objective in making the assumption that the active layer is thin relative to the bed depth, is to confine the domain for which a solution to the flow problem is sought to the active layer, thus avoiding the computational demands of solving for the already-known velocities in the plug flow region. The obvious choice was to develop approximate solutions analogous to those of other thin flows, i.e., of boundary layer flows. It was necessary, therefore, to normalize the governing equations according to the geometry of the kiln and to establish whether these equations could be reduced to parabolic equations similar to those for flow over a flat plate. The first step in this exercise was to recast Eq. 5.1 through 5.3 into primitive variables. This procedure is given in detail in Appendix A2. After doing so the steady-state continuity, momentum, and kinetic energy equations take on the forms:

$$\frac{\partial u}{\partial x} + \frac{\partial v}{\partial y} = 0 \quad (5.7)$$

$$\rho \left[u \frac{\partial u}{\partial x} + v \frac{\partial u}{\partial y} \right] = \rho g \sin \xi - \frac{\partial P_{xx}}{\partial x} - \frac{\partial P_{xy}}{\partial y} \quad (5.8)$$

$$\rho \left[u \frac{\partial v}{\partial x} + v \frac{\partial v}{\partial y} \right] = -\rho g \cos \xi - \frac{\partial P_{xy}}{\partial x} - \frac{\partial P_{yy}}{\partial y} \quad (5.9)$$

$$\rho \left[u \frac{\partial \tilde{T}}{\partial x} + v \frac{\partial \tilde{T}}{\partial y} \right] = - \left[\frac{\partial q}{\partial x} + \frac{\partial q}{\partial y} \right] - \left[P_{xx} \frac{\partial u}{\partial x} + P_{xy} \frac{\partial v}{\partial x} + P_{yx} \frac{\partial u}{\partial y} + P_{yy} \frac{\partial v}{\partial y} \right] - \gamma \quad (5.10)$$

Having obtained the equations of motion for the active layer the next step is to apply the simplification derived from thin flow assumption to these governing equations and solve for the velocity distribution in the active layer.

The first task is to normalize all variables in terms of characteristic dimensions as shown in Figure 5.2. The coordinates appropriate to the active layer may be defined in cartesian coordinates with field variables taken with respect to x and y where, from assumption (iv), $-L \leq x \leq L$ and $0 \leq y \leq -H$. These variables are Δ , the depth of the active layer at mid-chord of the free surface plane, and L is half of the mid-chord length. If the angle subtended by the boundary interface is the dynamic angle of repose, ξ , then $\tan \xi$ is the coefficient of dynamic friction and the stresses can be normalized with the gravity term as (see, e.g., Savage and Hutter, 1989);

$$\begin{aligned} (x, y) &= ([L]x^*, [\Delta]y^*) \\ (u, v) &= \left([(gL)^{1/2}]u^*, \left[\frac{\Delta}{L}(gL)^{1/2} \right]v^* \right) \\ (P_{xx}, P_{yy}, P_{xy}) &= [\rho g \cos \xi \Delta] (P_{xx}^*, P_{yy}^*, \tan \xi P_{xy}^*) \end{aligned} \quad (5.11)$$

Normalizing the continuity and the momentum equations and rendering $\Delta/L \rightarrow 0$ (see Appendix A3) the equations, indeed, reduce to boundary layer equations which, deleting the * from the non-dimensional terms have the form:

$$\frac{\partial u}{\partial x} + \frac{\partial v}{\partial y} = 0 \quad (5.12a)$$

$$u \frac{\partial u}{\partial x} + v \frac{\partial v}{\partial y} = \sin \xi - \sin \xi \frac{\partial P_{xy}}{\partial y} \quad (5.12b)$$

For this thin flow, the y-wise momentum equation becomes the overburden pressure;

$$\begin{aligned} \frac{\partial P_{yy}}{\partial y} &= 1 \\ P_{yy} &= \int_0^{\Delta} v dy \end{aligned} \quad (5.13)$$

It should be noted that so far as nothing is said about the stresses, which depend on the boundary conditions, Eqs. 5.12 are similar to those for flow over a flat plate developed by Prandtl (see, e.g., Schlichting, 1979). In order to solve for Eqs. 5.12 the continuity equation can be rearranged as;

$$v = - \int_0^y \left(\frac{\partial u}{\partial x} \right) dy \quad (5.14)$$

Substituting into the corresponding momentum equation, an approximate solution similar to that obtained by von Karman for flow over a flat plate can be sought (see, e.g., Schlichting, 1979). However, having demonstrated that the active layer flow can be mimicked by boundary layer equations, the objective was not to solve these equations directly but to re-establish the momentum integral equations, which would result from the above integration, through the control volume approach. Such an approach would, obviously, highlight the physical interpretation of the complex granular flow equations as they apply to the rotary kiln cross-section.

5.2.2.1 The Integral Equation for Momentum Conservation

So far the problem has been dealt with by stating the continuum equations for material flow and these equations have been reduced to parabolic equations involving unknown stresses by using the geometry of a rolling bed. It will now be shown that if the flow behaves as a continuum, then the same equations can be deduced by simply considering material and momentum balance over a control volume in the active layer of the bed such as that shown in Figure 5.3. By proceeding in a manner similar to that employed in deriving the von Karman equation for a developing boundary layer, the system of partial differential equations 5.12 can be reduced to the ordinary differential equation (see, Appendix A5 for a detailed derivation):

$$\rho \frac{d}{dx} \left(\int_0^H (u^2 - u_\delta u) dy \right) dx + \frac{du_\delta}{dx} \left(\int_0^H \rho u dy \right) dx = \Sigma F_x \quad (5.15)$$

It can be readily shown that Eq. 5.15 can also be obtained by substituting Eq. 5.14 into the continuity and momentum equations directly and integrating by parts. It should be emphasized that, provided no statement is made about the stresses or the net forces acting on the control volume, the net momentum equation is the same as that governing fluid flow e.g., Blasius problem (Schlichting, 1979). In Eq. 5.15, u_δ , the velocity at the transition from the active layer to the plug flow, is a function of radius only ($u_\delta = \omega r$) but the radius for this transition requires knowledge of the active layer depth, δ_x , at that distance, x , from the apex. From the geometry in Figure 5.3 it can be shown that

$$\begin{aligned} r^2 &= (L-x)^2 + (OB + \delta_x)^2 \\ \cos\theta &= \frac{(OB + \delta_x)}{r} \end{aligned}$$

where OB is the distance from the kiln's center-line to the bed surface. These geometrical relationships will introduce non-linearities in Eq. 5.15 and an iteration procedure would be

required in order to solve for the active layer depth. Having now derived the momentum conservation (Eq. 5.15) in the active layer the next step is to proceed with the evaluation of the force terms.

The forces acting on the control volume are shown in Figure 5.4. These consist of a gravity force (body force) and the forces that are generated by the stresses described earlier. The net force is equal to

$$-\tau_w dx + \sigma_N dx + \rho g dx \quad (5.16)$$

where σ_N is the overburden pressure and is given as

$$\sigma_N = P_{yy} + P_{xx}$$

The top face of the control volume being considered to be a free surface and the shear stress is therefore zero (plane A-A in Figure 5.3). The normal stress at this surface is due to the forces exerted by the freeboard gas. If there is no significant saltation of particles on the free surface then the normal stress at this plane is also zero. By equating the net momentum to the net force, the integral momentum equation becomes,

$$\rho \frac{d}{dx} \left(\int_0^\delta (u^2 - u_\delta u) dy \right) + \frac{du_\delta}{dx} \int_0^\delta \rho u dy = -\tau_w + P_{xx} dy + \rho g \sin \xi \quad (5.17)$$

The second term on the left of Eq 5.17 would, in fluid flow, equal the hydrostatic pressure according to Bernoulli's equation. For granular flow on an incline this term is equivalent to the driving force parallel to the inclined plane and hence may be equated to the overburden pressure in the x-direction i.e.,

$$\frac{du_\delta}{dx} \int_0^\delta \rho u dy = P_{xx} \quad (5.18)$$

Assembling the results obtained thus far yields the expression

$$\rho \frac{d}{dx} \int_0^{\delta} (u^2 - u_{\delta} u) dy = \rho g \sin \xi - \tau_w \quad (5.19)$$

The final task before proceeding with its solution is to derive an appropriate expression for the shear stress acting over the bottom surface of the control volume, τ_w .

The shear stress is a combination of static and kinetic and the extent of each contribution would be determined by the operational parameters i.e., the rotational speed, degree of fill, etc. The various modes of bed behavior can therefore be related to the stresses acting on the material within the depth of the active layer. These modes can be mathematically described as follows;

(i) *Slumping Bed*. When the rotation and/or collision of particles are constrained and if $\partial u / \partial y > 0$ then the shear stress is static and is simply given as

$$\tau_w = \rho g \cos \xi \tan \phi \quad (5.20)$$

where ϕ is the static angle of repose. This situation occurs for slumping bed behavior where the active layer of the bed material is not shearing by inter-particle collision (see, e.g., Henein *et al.*, 1981). The corresponding momentum equation is given as;

$$\begin{aligned} \rho \frac{d}{dx} \int_0^{\delta} (u^2 - u_{\delta} u) dy &= \rho g \sin \xi - \rho g \cos \xi \tan \phi \\ &= g \cos \xi (\tan \xi - \tan \phi) \end{aligned} \quad (5.21)$$

Thus, if $\xi > \phi$, the flow is accelerated, while, if $\xi < \phi$, the flow is damped. When $\xi = \phi$, it can be said that the flow is indeterminate (Kanatani, 1979). Suffice to say that damped flow is the mode for slipping bed behavior.

(ii) *Rolling Bed*. From the flow experiments discussed earlier, it can be said that the rolling bed is the situation where the kinetic stress is the driving force for material flow i.e., when the bed is in the rolling mode the material in the active layer shears continuously. In this case all the aspects of granular flow come into play and the shear stress is deduced from the constitutive

equations described earlier. Many forms of the shear stress expressions exist in the literature, however, they are all variants of the equation first proposed by Bagnold (1954) which is given as

$$\tau_w = -c_i \rho_p \left(d_p \frac{du}{dy} \right)^2$$

where c_i is the Bagnold's constant (see, e.g., Campbell and Gong, 1986). The stress/strain rate relationship employed in this work is that derived by Lun *et al.* (1984) through the analogy of kinetic theory of dense gases;

$$\tau_w = C' \frac{du}{dy}$$

where the 'apparent' viscosity, C' , is a function of the dilation, $C' = f(\rho_p, d_p, e_p, v, \tilde{T})$ as determined in Appendix A4. This apparent viscosity is related to the properties of the bed according to (see, Appendix A4 for detailed derivation of C')

$$C' = -\rho_p d_p g_2(v) \tilde{T}^{1/2} \quad (5.22)$$

where $g_2(v)$ is a term relating the viscosity to flow properties such as the coefficient of restitution of the particles, $\eta = (1 + e_p)/2$, solids fraction, v , and is derived in Appendix A4 as

$$g_2(v) = \frac{5\sqrt{\pi}}{96} \left[\frac{1}{\eta(2-\eta)g_o} + \frac{8}{5}(3\eta-1) \frac{v}{(2-\eta)} + \frac{64}{25} \left\{ \frac{\eta(3\eta-1)}{(2-\eta)} + \frac{12}{\pi} \right\} v^2 g_o \right] \quad (5.23)$$

Inserting this result for the shear stress in Eq. 5.19 the momentum conservation equation takes on its final form:

$$\frac{d}{dx} \rho \int_0^{\delta} (u^2 - u_{\delta} u) dy = \rho g \sin \xi + g_2(v) \rho_p d_p \tilde{T}^{1/2} \frac{du}{dy} \quad (5.24)$$

Notice that this equation involves the shear rate, du/dy , in the active layer, the particle dilation of the bed, the granular temperature, and gravity, all of which are granular flow characteristics and were previously discussed in the experimental results. The equation points to the fact that boundary layer analogy can be combined with the constitutive equations of Lun *et al.* (1984) to arrive at a single analytical model which can be used to predict the depth and velocity of the active layer. It should be mentioned that although the kinetic energy equation has been avoided in the derivation of the momentum equations, its solution is required in order to obtain the granular temperature for Eq. 5.24. As will soon be shown, in this particular case, a corrector-predictor technique may be used to estimate \tilde{T} in order to simplify the calculations.

5.2.3 Solution of the Momentum Equation in the Active Layer of the Bed

Equations 5.21 and 5.24 represent the integro-differential equations for the bulk material flow in the bed active layer. However, in order to proceed further a 'suitable' form for the velocity profile is required. In choosing this suitable velocity function, it is necessary to account for the boundary conditions (i) at the free surface, (ii) at the interface between the active and the plug flow region of the bed, and also to satisfy the requirement of continuity at the point where the solution in the active layer is joined to the plug flow solution. However, before proceeding with a choice for velocity profile, it is first necessary to consider the material balance for the bed section being considered.

The schematic shown in Figure 5.5 depicts material mass balance at an arbitrary x-position in the free surface plane. As pointed out in Chapter 4, a basic constraint on any 'solution' to the flow problem is that the mass flow in the active layer must equal the mass flow in the plug flow region, i.e.,

$$\dot{m}_{AL} = \dot{m}_{PF}$$

or, when stated mathematically,

$$\rho_{AL} \int_0^{\delta_x} u_{AL}(x, y) dy = \rho_{PF} \int_{r_x}^R u_{PF}(r) dr$$

Recognizing that the bulk density is simply the particle density times the solid fraction ($\rho = \rho_p v$), and that, within the plug flow region $u = \omega r$, this equation simplifies to (dropping the subscript *AL* for velocity in the active layer)

$$v_{AL} \int_0^{\delta} u dy = v_{PF} \int_{r_x}^R \omega r dr \quad (5.26)$$

which after integration of the right hand side, gives

$$v_{AL} \int_0^{\delta} u dy = 0.5 v_{PF} \omega \left[R^2 - \left(\frac{H + \delta_x}{\cos \theta} \right)^2 \right] \quad (5.27)$$

where $u = u_{AL}(x, y) = f(y)$ is the active layer velocity function which includes the actual active layer depth. At mid-chord, the global material balance for the entire cross-section is satisfied and since the subtended angle there (i.e., θ) goes to zero, Eq. 5.27 reduces to

$$v_{AL} \int_0^{\Delta} u dy = 0.5 v_{PF} \omega [R^2 - (H + \Delta)^2] \quad (5.28)$$

In solving for the active layer depth and velocity using Eq. 5.24 there are two possible constraints that may be used to terminate the iteration, i.e., either by ensuring that the mass flow in the active layer is balanced at each x-position from the apex, using Eq. 5.27, or by ensuring that global mass in the active layer is balanced at mid-chord using Eq. 5.28.

5.2.3.1 Velocity Profile in the Active Layer

Application of integral methods for solving boundary layer flows involves fitting the velocity profile to a polynomial form,

$$u = a_0 + a_1y + \dots + a_ny^n \quad (5.29)$$

where the degree, n , depends upon the number of conditions imposed on the profile by physical considerations, typically for example stress or velocities at the boundaries. However, the experimental results indicated that a parabolic profile would be sufficient to describe the shape of the velocity profile in the active layer and hence only three conditions can be imposed on the profile. The points at which these three conditions would be applicable are selected to be (i) the free surface, (ii) the yield line which lies between the active layer and the plug flow region where deformation of material occurs, and (iii) the zero velocity line which lies between (i) and (ii) as a result of particle flow reversal.

Free Surface Boundary Condition. Following the fluid flow analogy, the most obvious choice for a free surface boundary condition is to allow the shear stresses to vanish and thus force the shear rate to zero (i.e., $du/dy = 0$). Although this condition has been used in chute flow calculations (see, e.g., Savage, 1979; Campbell and Brenen, 1985; etc) it forces the velocity profile to a shape which is not always consistent with the experimental results, a condition imposed by the infinite size of particles; i.e., the continuum assumption breaks down. Therefore the boundary condition imposed at the free surface was not that of null shear stress, which was inconsistent with the experimental results, but rather the velocity itself as measured in the rotary apparatus. As was seen in the experimental results, the free surface velocity depends on the chord length since it is the maximum distance which a particle can travel at a certain fixed speed imposed either by the kiln rotation or by gravity (free fall). Qualitatively, the surface velocity for a bed of material with a given particle size will depend on three parameters i.e., the speed of rotation, the kiln size, and the degree of fill. The most reliable way to establish this relationship is to utilize the experimental results, from which a correlation was derived relating the surface velocity to kiln speed and fill i.e., $u_s = C_o \omega R$, where the constant of proportionality, C_o , must be related to the degree of fill and the rotational speed of the kiln, i.e., $C_o = f(\%Fill, \omega)$. The

relationship between C_o , at mid-chord, and kiln speed with degree of fill as a parameter is shown for polyethylene and rice grains in Figures 5.6. In order to establish a mathematical relationship for use as a boundary condition, the data was fitted to the form,

$$C_o = A_1 \omega^b p^c \quad (5.30)$$

where the coefficients A_1 , b , and c were recovered by a three parameter minimization technique (see, e.g., Boateng *et al.*, 1990). The relationship between the experimental and the calculated values using the above equation is shown in Figure 5.7 for polyethylene pellets, with the linear relationship indicating a good fit.

Conditions at the Interface Between Plug Flow and Active Layer. These involve the location of the zero velocity line and the yield line shown in Figure 5.3. At the yield line, continuity of flow in both the active layer and the plug flow region requires that $u = u_\delta$. The relationship between α and δ (see, Figure 5.3) i.e., the respective distances from the bed surface to the zero velocity line and the yield line may be established by considering the Coulomb yield criterion, $\sigma_s = \sigma_{yy} \tan \phi$. Since $\tan \phi$ is constant, the ratio between the shear and normal stresses at the interface must also be constant. Because the normal stress is the weight of the overlying burden, the number of particles that the material can sustain between the zero line and the yield line depends on the packing and must, therefore, be related to the degree of fill. Hence, the ratio α/δ represents the yield criterion and must be a constant which is related to the percent fill. Experimental observations show that this is indeed true and can be used to establish the two boundary conditions; this argument is analogous to boundary layer flows where the layer depth is usually related to a certain percentage of the free stream. Gauthier (1991) gave a value of $\alpha = 0.75\delta$ for a small batch reactor using Ottawa sand as bed material. However, experiments carried out in the present work show that when larger particle size ranges are employed, the value will lie between 0.7 and 0.9 depending on the degree of fill. Figure 5.8 shows the ratio α/δ calculated from observations through the glass end-piece in the experiments carried out in

the rotary apparatus reported in chapter 4. Although there is a considerable amount of scatter in the plot, which is, partly attributable to the end-piece effects, a quantitative measure of the range which this ratio lies can still be established from these observations.

Inclusion of these constraints into the parabolic velocity profile provides an analytical expression for the profile (see, Appendix A6 for detailed derivation):

$$\frac{u}{u_\delta} = \kappa + \frac{\kappa\alpha^2 - \kappa\delta^2 + \alpha}{\alpha\delta^2 - \alpha^2\delta} y + \frac{\kappa - \kappa\alpha - \alpha}{\alpha\delta^2 - \alpha^2\delta} y^2 \quad (5.31)$$

where κ is the ratio between the velocity parallel to the bed surface, u_x ($C_o\omega R$), and u_δ (ωr_x) i.e., $\kappa = C_o R/r_x$. The velocity profiles for the range of values of α/δ , shown in Figure 5.8, may be given as:

$$\frac{u}{u_\delta} = \kappa + a_1 \left(\frac{y}{\delta} \right) - a_2 \left(\frac{y}{\delta} \right)^2 \quad (5.32)$$

with the coefficients presented in Table 5.2.

The velocity profiles obtained using Eq. 32 depend on the values selected for κ as shown in Figure 5.9. It can be seen that the shapes of the profile are similar to those obtained from the experimental results. For low values of κ i.e., for low bed surface velocity, the profile (see, Figure 5.9(a)) will take the form of a parabolic *concave* at $\alpha/\delta = 0.75$, then it becomes a linear profile at $\alpha/\delta = 0.85$, and then becomes parabolic *convex* at $\alpha/\delta = 0.9$. However, when the value of κ is doubled (Figure 5.9(b)) all the profiles take the form of a parabolic concave. Notice that all the shapes of the velocity profiles encountered in the experiments are captured here using the three boundary conditions.

5.2.3.2 Density and Granular Temperature Profiles

It must be pointed out that the momentum conservation equation (Eq. 5.24), which forms the analytical model for the active layer flow, does not only require a velocity profile for its

solution but it also requires density and granular temperature profiles. The density profile for the bed active layer will differ from that in the plug flow region because of material dilation. In the plug flow region the solids volume concentration, v , can be assumed constant and equal to the maximum shearable solids concentration, v_* . The numerical value of v_* depends on the material packing which, in turn, depends upon the material properties and particle shape. For close packing of spherical particles, the value can be as high as 0.7. However for most practical situations it ranges between 0.59 and 0.62 (Savage, 1989). In the bed active layer, the solids fraction is not always constant but may vary from that of the plug flow ($\approx v_{PF}$) at the interface to a very small quantity, v_o , at the free surface, as was determined for one of its components (the linear concentration profile) in the experimental results. The actual value for the solids fraction should, therefore, be determined as part of the solution of the granular flow equations because of its interdependency with the granular temperature. For the present application a linear solids concentration profile should be adequate because of the thinness of the active layer. Such an approach has been employed before in the calculations of sedimentation transport in ocean beds (Hanes and Bowen, 1985) which bears some similarities with the present problem. Assuming a linear profile, the solids concentration profile can be given as;

$$\frac{v - v_*}{v_* - v_o} = -\frac{y}{\delta}$$

$$v = v_* - \frac{y}{\delta}(v_* - v_o) \quad (5.33)$$

Again, v_* is the at rest solids concentration which should equal the packing in the plug flow region. Ideally, however, v_o is determined by matching the stress generated by the bed surface velocity and that due to the flow of freeboard gas. For sedimentation transport where vigorous saltation of particles occurs due to turbulent ocean flow, the value has been shown to range between 0.05 and 0.16 (Hanes and Inman, 1985). In the rotary kiln situation, such vigorous saltation of particles is not observed and the value of v_o is expected to be high for a rolling bed.

Based on the experimental data, the dilation in the active layer was not more than 5% over that in the plug flow region and employing a constant value for volume (solids) concentration in the flow calculation should result in little error.

Now, with respect to the granular temperature, the experimental results indicate that there is some granular conduction into the bed as is evident from the gradient in the profile shown in Figure 4.13. Although the profile follows the same parabolic behavior as the velocity profile, it is very difficult to establish boundary conditions for the granular temperature. Although this is done in chute flow calculations, the arguments put forward to explain the granular temperature behavior at the free surfaces may not be sufficient for the explanation of its behavior in rotary kilns. For purpose of this work, which is aimed at approximate solution to the problem, it will be assumed that the granular temperature is isotropic for the entire depth at any x-position. As can be seen from the experimental results on the one-component measured, this approximation should be sufficient for the present calculation. Values of granular temperature must, however, be computed as part of the solution of the flow problem and, as will be shown, can be found by an iterative procedure.

5.2.3.3 The Analytical Expression Developed for the Thickness of the Active Layer

Substitution of the velocity profile (Eq. 5.32) into the momentum conservation equation (the left hand side of Eq. 5.24) and carrying out the integration yields the result

$$\begin{aligned} \frac{d}{dx} \rho \int_0^{\delta} (u^2 - u_{\delta} u) dy &= \rho \frac{d}{dx} \left[\{ (\kappa^2 - \kappa) + \frac{1}{2} (2\kappa a_1' - a_1') + \frac{1}{3} (a_1'^2 - 2\kappa a_2' + a_2') \right. \\ &\quad \left. - \frac{1}{4} (2a_1' a_2') + \frac{1}{5} (a_2'^2) \} \delta \right] u_{\delta}^2 \end{aligned} \quad (5.34)$$

Substituting this result into Eq. 5.24 yields

$$\rho \frac{d}{dx} [(b_o + b_1 \kappa + b_2 \kappa^2) \delta] u_{\delta}^2 = \rho g \sin \xi + \rho_p d_p g_2(v) \bar{T}^{1/2} \frac{du}{dy} \quad (5.35)$$

where the coefficients, b_i , are the results generated when the terms in a_i' are expanded for the various values of the ratio α/δ . Again by recognizing that $\rho = \rho_p v_{AL}$, Eq. 5.35 becomes

$$\begin{aligned} \frac{d}{dx} [(b_o + b_1 \kappa + b_2 \kappa^2) \delta] u_\delta^2 &= g \sin \xi + d_p \frac{g_2(v)}{v_{AL}} \tilde{T}^{1/2} \frac{u_\delta}{\delta} \\ &= \frac{g \sin \xi}{u_\delta^2} + d_p \frac{g_2(v) \tilde{T}^{1/2}}{v_{AL} \delta u_\delta} \end{aligned} \quad (5.36)$$

In this equation, u_δ is a function of active layer depth, δ , i.e., (dropping the subscript, x)

$$u_\delta = \omega r \cos \theta$$

where

$$r = \frac{(H + \delta)}{\cos \theta}$$

which means that the velocity at the active layer depth is given by

$$u_\delta = -\omega(H + \delta)$$

Although u_δ is a function of δ , the variables in Eq. 5.36 may be separated as if the right hand side were constant which is consistent with boundary layer fluid flow solution (see, e.g., Schlichting, 1979). In a numerical solution, u_δ can be computed with a previous value of δ and then be updated. By carrying out the separation of the variables, Eq. 5.36 becomes;

$$\int_0^\delta [(b_o + b_1 \kappa + b_2 \kappa^2) \delta] d\delta = \int_0^x \left[\frac{g \sin \xi}{u_\delta^2} \delta + d_p \frac{g_2(v) \tilde{T}^{1/2}}{v_{AL} u_\delta} \right] dx \quad (5.37)$$

When a boundary condition, $\delta = 0$ @ $x = 0$, is employed at the apex (origin of flow calculation), the final form of the integral equation becomes;

$$\frac{1}{2}(b_o + b_1\kappa + b_2\kappa^2)\delta^2 - \frac{g \sin \xi}{u_\delta^2} \delta x - d_p \frac{g_2(v)\tilde{T}^{1/2}}{V_{AL}u_\delta} x = 0 \quad (5.38)$$

This is the quadratic equation required for the prediction of the active layer depth which, in turn, is substituted into the velocity profile to obtain the velocity distribution in the two-dimensional domain shown in Figure 5.10.

5.2.3.4 Numerical Solution for the Momentum Equation

The velocity determination requires the prediction of the active layer depth using Eq. 5.38 at any x-position along the bed surface and substituting this value into the velocity profile in order to determine the velocity parallel to the bed surface as a function of bed depth. The local velocity normal to the bed surface is then established by solving the continuity equation given in Eq. 5.1. Solving for δ_x also requires the granular temperature, which is found by iteration. The value of the granular temperature obtained after convergence is an average quantity for each x-position in the active layer. The flow chart employed for the calculation is given in Figure 5.11. The procedure follows the sequence whereby (i) the average granular temperature for the entire depth at any x-position is estimated; with this value $g_2(v)$ is computed; (ii) Eq. 5.38 is solved for a first approximation of δ_x by neglecting the quadratic term; (iii) with the value of δ_x , u_δ is computed and Eq. 5.38 solved for actual value of δ_x ; (iv) knowing δ_x , the velocity profile is computed, from which follows the calculation of the mass flow for the active layer at the x-position. This mass flow is compared with that in the plug flow region at the same location using Eq. 5.26 and this procedure is repeated using an improved estimate of the granular temperature if the mass flow for the active layer does not balance the mass flow in the plug flow region. Otherwise, the solution is advanced to the next x-position until mid-chord.

The stability of the solution procedure just described depends on the choice of the granular temperature needed to initiate the solution. As was seen in the experimental result, there is an order of magnitude increase in the granular temperature for each increase in kiln speed and therefore instabilities are likely to be developed when a solution for successive kiln speeds is

required. Nevertheless, this problem is easily rectified by a good initial guess for the granular temperature and the choice of the mass balance convergence criterion. In order to use small convergence criteria, which are required for low granular temperatures (i.e., for low kiln speeds), small nodal sizes are required. For the results to be presented for the experimental apparatus, 24 nodes were used between the apex and the mid-chord for all the kiln speeds solved and the convergence criterion (the percent difference between the mass flows in the active layer and the plug flow region) was set as 0.1%.

5.3 Model Validation from the Experimental Results

The flow model was validated by comparing the velocity calculations with the values measured for the active layer in the 1 m O.D (96.4 cm I.D) rotary drum. Figures 5.12 through 5.14 show results obtained during the validation procedure. The material in this sequence is polyethylene pellets which was chosen because its physical properties are better known than those of the rest of the materials used in the experiments. The coefficient of restitution for the material is relatively high and the material has also been used in validating granular flow theories applied to chutes (Savage, 1979). Figures 5.12(a) through 5.12(c) compare the velocity predictions, at mid-chord, for 29% fill and three different speeds of rotation whereas Figures 5.13(a) through 5.13(d) are for 15% fill and four different rotational speeds. The results indicate a generally good fit to the experimental data, especially for 15% fill condition. The difference in the predicted and measured velocities found in the results for the very deep 29% fill can, perhaps, be attributed to the effect of the granular temperature. It might be recalled that the model assumes $d\tilde{T}/dy$ to be zero ensuring that the granular temperature is constant at each x-position in the active layer. This assumption is not consistent with the experimental results and, therefore, discrepancies are anticipated at higher degrees of fill and higher kiln speeds where the granular temperature can make a considerable difference. Nonetheless, for an approximate solution, the predictions are considered to be good. It is interesting to note the accuracy with which the shapes of the velocity profiles are predicted just by choosing the relationship between the zero velocity line and the yield line.

Although precise values are not known, the coefficient of restitution for both the rice grains and the limestone are low compared with polyethylene. Nevertheless, comparisons are made between measured and predicted velocities using these materials as well. Figure 5.14 shows the predicted and measured velocities as function of depth, at mid-chord, for rice grains in the 1 m O.D drum operated at 3 rpm. Figure 5.14(a) shows the results for 8.5% fill while 5.14(b) shows the result for 10% fill. Also shown in Figure 5.15 are the results using limestone at (a) 3.3% fill and 2 rpm and (b) 8.5% fill at 2 rpm. It can be seen from these results that, with respect to predicting the gradients of the profiles, the accuracy of the predictions are comparable to those obtained for the polyethylene pellets. The magnitudes of the predicted velocities compare well with the experimental data, despite the fact that the coefficient of restitution for these materials was rather poorly measured. As will be shown this leads to the conclusion that the coefficient of restitution of the material does not directly influence the velocity field but rather influences the granular temperature and, consequently, the kinetic diffusion. Therefore the flow field is determined primarily by the boundary condition and, in particular, by the operational conditions i.e., the degree of fill and rotation rate.

The predicted active layer depth and the corresponding measured values at mid-chord are presented in Table 5.4 for all the experimental data on polyethylene. Also presented are the results from the equilibrium model of Pershin (1988) which is based on the equilibrium of energy between the plug flow region and the active layer. The explicit mathematical expressions used in Pershin's model are based on results of experiments that were carried out at relatively high rotational speeds ($\omega \geq 0.2\omega_{cr}$); this corresponds to rotating the 1 m O.D drum used in the current experiments at 15 rpm and beyond. Nonetheless, it is the only model existing in the literature that may be used to predict active layer depth and must therefore be reported despite differences in experimental campaigns. In light of this, the comparison made with Pershin's model is only qualitative. Figure 5.16 shows the model prediction of active layer depth using the experimental conditions of Gauthier (1991) for mesh 40 sand (≈ 0.42 mm diameter particles). The drum dimension for this work was

36.8 cm I.D and the depth predictions made by Gauthier, shown in the figure, are based on his empirical relations established for the active layer depth as a function of kiln speed and degree of fill. It is worth pointing out that, like Pershin (1988), Gauthier had carried out the measurements by filming the flow behavior through a glass end-piece. As might be recalled from the experiments described in Chapter 4, estimating the flow behavior through the glass end-piece is not recommended because of the end effects; this may explain the marked differences between their results and that of the current work. In the present work the active layer depth, as observed through the end-piece, was consistently 20-30% less than that determined by depth probing away from the end-piece. In addition, the surface velocity adjacent to the end-piece (see, e.g., Figure 4.6) was consistently greater than the rest of the bed due to changes in angle of repose; therefore, for the same kiln speed material balance requires that the depth be thinner at the glass end-piece.

5.4 Application of the Flow Model

Having established the validity of the model, the next step was to generate velocity profiles and characterize the flow for three drum sizes; 0.41 m which applies to the UBC pilot kiln, 1.0 m which applies to the experimental apparatus and 2.5 m which is typical of an industrial kiln operation. The results of this work are now described.

Velocity Profiles. The velocity profiles as function of depth at various positions on the exposed bed surface are presented in Figures 5.17 and 5.18 at respective kiln speeds of 2 and 5 rpm and for the three kiln sizes. It can be noted that the particles at the surface accelerate up to about 40% of the chord length beyond which the flow may be deemed developed. However, the velocity below the surface at this same location may not be fully developed since new material is constantly introduced into the active layer from the plug flow region. As a result, material balance requires that the active layer depth must increase so, therefore, the profile becomes fuller and tends towards uniform shear flow behavior. The velocity profiles at mid-chord are shown in Figure 5.19 for rotational speeds ranging from 1.5 through 5 rpm. Notice that the shape of the profile changes from approximately linear to parabolic with increased rotational speed. This is because of the rapid

increase in shear rate at the expense of the increased active layer depth. It can be seen from the results that, at 2 rpm (Figure 5.17), the surface velocity at mid-chord changes from 15 cm/s for the 0.4 m I.D drum to 40 cm/s for the 1 m I.D drum and increases to about 100 cm/s for the industrial size drum. At 5 rpm (Figure 5.18), the respective velocities are 40 cm/s, 75 cm/s, and 200 cm/s. It can be deduced that the velocity increases at about the same rate as the scale-up of the drum diameter given the same operational conditions. This is attributed to the fact that for the same operational conditions the exposed bed surface boundary condition, C_o , is constant and since $C_o = u_s/\omega R$, the surface velocity must have a one-to-one relationship with the drum size. Until kiln size is included as a parameter in determining C_o , the effect of scale-up on surface velocity can only be considered one-to-one. Material balance in the cross-section requires that this must, indeed, be true because, as shown in Figure 5.20, the active layer depth is but a weak function of operational conditions. The results shown in Figure 5.20 are consistent with the experimental results reported in Chapter 4 and indicate that, for the same degree of fill, the active layer thickness grows up to a limit with increased rotational rate. Couette granular flow models (Johnson and Jackson, 1987) also show that there is a critical speed when more material will decline to go into the shear region.

Granular Temperature and Kinetic Diffusion. Before discussing the results of the granular temperature it is necessary to draw attention to some of the granular flow characteristics as they are defined in the literature and in Appendix A4. It might be recalled that the flux of fluctuating energy in the normal direction, q_y , is given as (Appendix A4)

$$q_y = -\rho_p d_p \left(g_3(v, \epsilon_p) \tilde{T}^{1/2} \frac{d\tilde{T}}{dy} + g_4(v, \epsilon_p) \tilde{T}^{1/2} \frac{dv}{dy} \right) \quad (5.39)$$

By assuming average values for the granular temperature and the volume concentration in each surface position, the normal gradients in these field variables have been forced to go to zero (i.e., isotropic in y) and, as Eq. 5.39 implies, the flux in the normal direction will vanish in the model. Therefore, Figure 5.21 shows the variation of the granular temperature in the direction of the flow. As is seen here and, as in the case of the experimental results shown in Chapter 4, the granular

temperature can be seen to increase rapidly at the onset of flow and then dissipate in the flow direction. As was pointed out earlier, in the experimental section, the granular temperature is the result of kinetic energy associated with increased mean flow and only minor fluctuations are to be expected near the mid-chord. It is also to be expected that the granular temperature will increase with kiln speed as shown in Figure 5.22. The self diffusion coefficient (for equally sized particles) follows the trends in the granular temperature directly. It might be recalled from Eq. 4.18 that the diffusion coefficient is inversely proportional to the coefficient of restitution of particles and solids concentration, but directly proportional to the granular temperature. Therefore, for the same material and constant solids concentration, diffusion is expected to increase with increased granular temperature or kiln speed. The forgoing results therefore show that the model can correctly predict the trends of the diffusion coefficient in the active layer.

The Effect of Material Physical Properties on Flow Characteristics. The experimental results presented in Chapter 4 indicated that, for the rolling bed (which is the focus of the present work), dilation of the bed in the active layer does not exceed 5% of that in the plug flow region. On this basis a constant value of the solids fraction was assumed in the model for the entire active layer. This assumption does not seriously hamper the calculation of bulk velocity in the active layer. However the flow characteristics are dependent on the extent of dilation and it is important to determine the effects of changing the solids concentration on flow characteristics. Other physical properties which may influence the flow characteristics are particle size, the coefficient of restitution of particles, and the angle of repose, the latter being the major factor which determines the coefficient of friction and the stiffness coefficient. The effect of these various physical properties on flow within the bed was therefore explored using the model in order to establish the importance of each parameter in determining particle flow.

(i) *Solids Concentration.* The solids concentration (volume fraction) might be expected to significantly influence flow characteristics; this is because the volume fraction is a measure of dilation and hence, the state of fluidization or expansion of the bed burden. As is depicted in Figure

5.23, as the dilation of the bed increases, the quantity of the material entering the sheared region (i.e., active layer) also increases. Figure 5.23(a) shows that the shear rate will decrease with increased dilation because of the increase in the depth of the shear layer as can be seen in Figure 5.23(b). Thus, as shown in Figure 5.23(c) the overall result is to increase diffusion by several orders of magnitude.

(ii) *Coefficient of Restitution*. Figure 5.24 shows that the coefficient of restitution has an order of magnitude effect on the granular temperature and, for that matter, diffusion. When the coefficient of restitution of the particles is increased the granular temperature tends to decrease. However the coefficient of restitution has almost no effect on the shear rate; i.e., on active layer depth or velocity in the active layer. The dependence of the flow behavior on coefficient of restitution can be explained by considering the Jeffrey-Savage parameter, a ratio of normal to shear stress, which can be expressed in terms of material properties as (Ahn, *et al.*, 1992)

$$d_p(du/dy)/\tilde{T}^{1/2} = g_1(v)/g_2(v) \tan \phi \quad (5.40)$$

From Table A.3 in Appendix A4 it can be seen that, for most of the terms in the series, $g_2(v)$ is inversely proportional to $\eta (= (1 + e_p)/2)$, while $g_1(v)$ is directly proportional to the coefficient of restitution. This means that, for a constant shear rate, as the coefficient of restitution of the material increases, the granular temperature must decrease. Hence if the kiln speed is maintained constant, then the material that exhibits low elastic collision must have enhanced mass diffusion in the active layer of the rotary kiln. This is consistent with Eq. 4.18 (Savage, 1993).

(iii) *Angle of Repose*. The influence of the angle of repose on bed behavior is similar to that of the coefficient of restitution. This is because the two properties are related in particle flow behavior. Material with high coefficient of restitution will not sustain a high angle of repose and vice versa. The effects of the angle of repose on the flow are presented in Figure 5.25. It was established from the same result that particle size does not have any appreciable effect on the flow. Although this

seems surprising, the constitutive relations for granular flow indicate that, although particle size plays a role in determining the shear stress, the velocity fluctuations are determined by the dilation of the material and the coefficient of restitution.

5.5 Model Prediction for Flow in the Transverse Plane

To this stage the focus has been on the development of means for predicting conditions in the active layer as well as the extent of the active layer. The procedure for doing so was to note the relative thinness of the active layer (compared to the plug flow region) and develop flow expressions based on this analogy with other thin flows. One major practical application of the flow model is the development of the complete flow field in the transverse plane which can then be incorporated into existing thermal models but (finally) dispensing with the well mixed assumption. Therefore the model was used to calculate the velocity field as shown in Figure 5.26. This was carried out by re-meshing the entire cross-section to include the plug flow region. Because the velocity in the plug flow region is easily determined once its domain is known, the prediction of the active layer depth is fundamental to determining the velocity components for the plug flow region. In the active layer, the y-wise components of the velocity vector, although small, were computed using a backward difference formulation of the continuity equation. The resultant flow field for the bed cross-section which is presented in Figure 5.26 is for the pilot kiln at 12% fill and operated at 2 rpm. Notice the continuous feeding of material from the plug flow region into the active layer and vice versa. After emerging from the plug flow region near the apex, an individual particle will travel downward in the stream of particles which form the active layer. Because of kinetic diffusion it may sink or rise and may end up in a location in the plug flow region different from where it started. Because the active layer velocity is about three or four times greater than that in the plug flow region, mixing effects are confined to this region. However, if fine or denser particles are used as tracers then the velocity distribution shown in Figure 5.26 will help to determine the extent to which the tracers will travel before percolating down. These scenarios will be the subject of the next chapter. Lastly, beside advective heat transfer which can be calculated

through knowledge of the flow field, mass transfer 'enhanced' thermal conductivity can be computed as $\rho c_p D$ where D , the kinetic diffusion, is computed from the granular temperature given by the flow model.

5.6 Summary and Conclusions

A mathematical model for the prediction of the velocity field in the transverse plane of a rotary kiln has been constructed. The model is based on the assumption of a continuum and draws on theories derived for granular flows. These theories are analogous to the theories of kinetic energy of dense gases. In developing the model, theoretical constitutive equations developed by Lun *et al.* (1984) have been employed as the governing equations and, as a result, the kinetic energy equation has been considered as part of the solution of the flow model. Because the flow of material in the cross-section of the kiln is confined, inertia terms of the momentum equations could not be neglected. Owing to the fact that the active layer is thin relative to the kiln dimensions and also due to the fact that plug flow velocity is known when the active layer depth is predicted, 'exact' numerical solutions to the governing equations for the entire bed cross-section were avoided and approximate solutions were therefore sought. The active layer was considered analogous to boundary layer flow and such approximations were made to effect a solution of the velocity field. The stress-strain rate relationships from existing granular flow theories were incorporated into the developed boundary layer equations.

Experimental results showed that the velocity profiles in the active layer could be described as parabolic and therefore three boundary conditions were invoked to characterize this profile. One of the three boundary conditions, i.e. the free surface velocity, was established from the experimental data after revealing that the shear stress there does not always go to zero. As a result the surface velocity was determined as a function of the kiln speed, geometry, and degree of fill. The two other boundary conditions were related to yield stress and were established by considering the ratio of the depth of the zero velocity line and that of the yield line.

The resulting integro-momentum equation was solved to obtain the active layer depth as a function of exposed bed surface location. The solution procedure required an iteration of the granular temperature with the convergence criterion established by the material balance between the active layer and the plug flow region at the exposed bed surface location of interest. The ensemble average velocity results predicted by the model are in agreement with experimental results. The model has been used to demonstrate the marked effect of solids concentration on flow characteristics. Having validated the model, it was run using the geometry and operating conditions of the UBC pilot kiln in order to determine the velocity distribution in the transverse plane which, until now, has not been quantitatively estimated. The results provide an opportunity, for the first time, to estimate the advective component of sensible energy distribution in the cross-sectional plane. Other prominent features of the model include the ability to predict the granular temperature which is, in turn, used to predict kinetic diffusion in the transverse plane.

5.7 Tables and Figures

Table 5.1 Parameter Estimation for Surface Velocity, $C_o = A\omega^a p^b$

Parameter	Value	St. Dev. $\times 10^{-2}$
A	0.897	5.211
a	-0.324	2.257
b	0.409	2.160

Table 5.2. Coefficients Resulting from Velocity Profile

α/δ	a_1'	a_2'
0.75	$3.0 - 2.333\kappa$	$4.0 - 1.333\kappa$
0.80	$4.0 - 2.250\kappa$	$5.0 - 1.250\kappa$
0.85	$5.67 - 2.177\kappa$	$6.67 - 1.177\kappa$
0.90	$9.0 - 2.111\kappa$	$10.0 - 1.111\kappa$

Table 5.3. Coefficients Resulting from Integro-Momentum Equation

α/δ	b_o	b_1	b_2
0.750	0.170	0.422	0.033
0.800	0.177	1.875	0.000
0.850	0.093	6.768	-0.601
0.900	0.833	-0.487	-0.593

Table 5.4. Model Validation for Active Layer Depth

Degree of Fill	Rotational Speed	AL Depth Experimental	AL Depth Predicted	Pershin's Model
%	rpm	%	%	%
3.3	2.054	28.571	33.238	8.327
	3.071	34.424	34.553	8.921
	4.134	36.735	35.476	10.104
	5.219	37.757	36.171	11.865
8.5	1.875	27.040	30.575	6.215
	2.870	28.480	32.148	6.639
	3.975	29.697	33.306	7.905
	5.077	31.121	34.148	8.745
15.0	2.135	23.571	28.184	4.566
	3.067	25.000	29.674	4.897
	4.112	26.290	30.856	5.890
	5.114	27.397	31.716	6.549
29.0	0.915	16.923	20.093	2.531
	2.832	18.571	25.242	3.034
	5.148	18.571	27.969	4.289

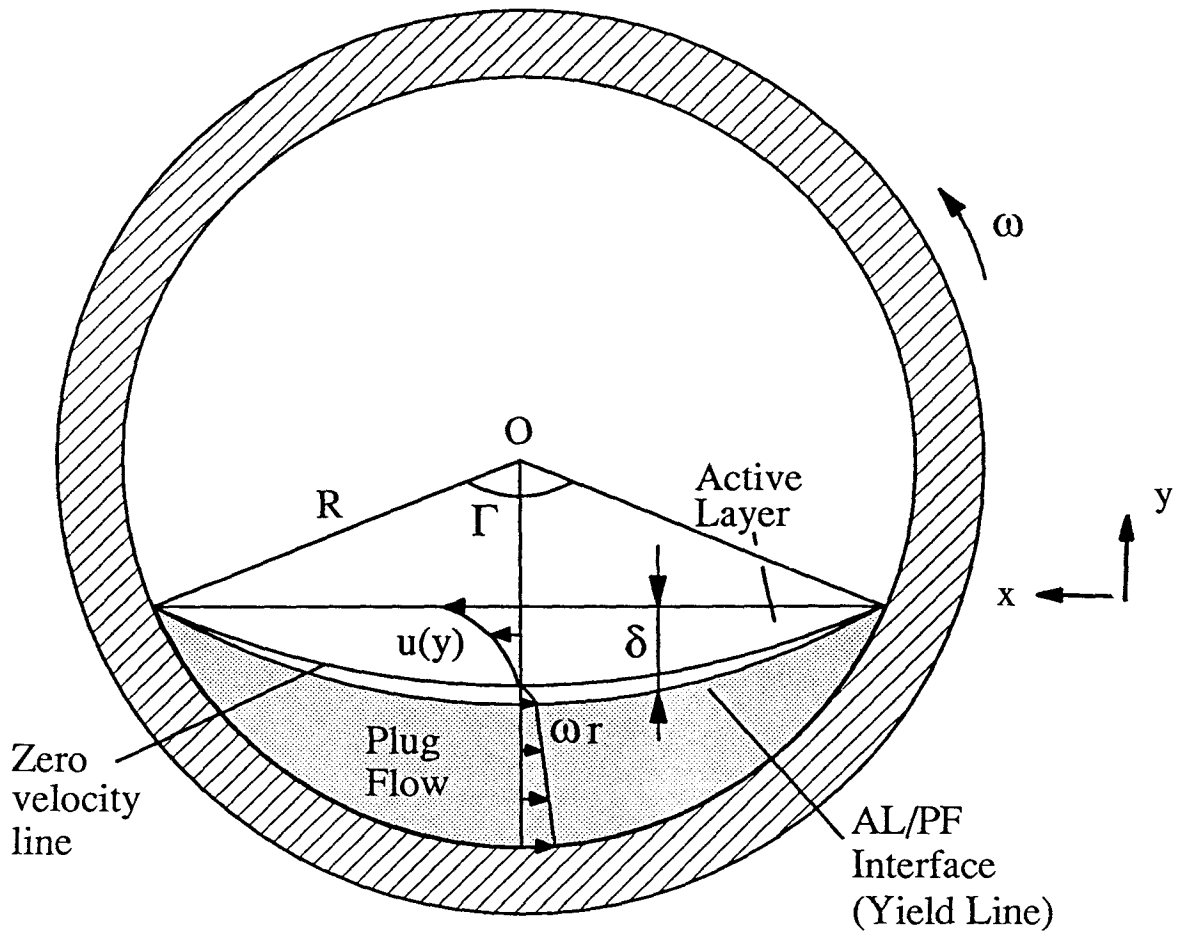


Figure 5.1. Schematic of Kiln Cross-section Showing the Domain of the Flow Problem.

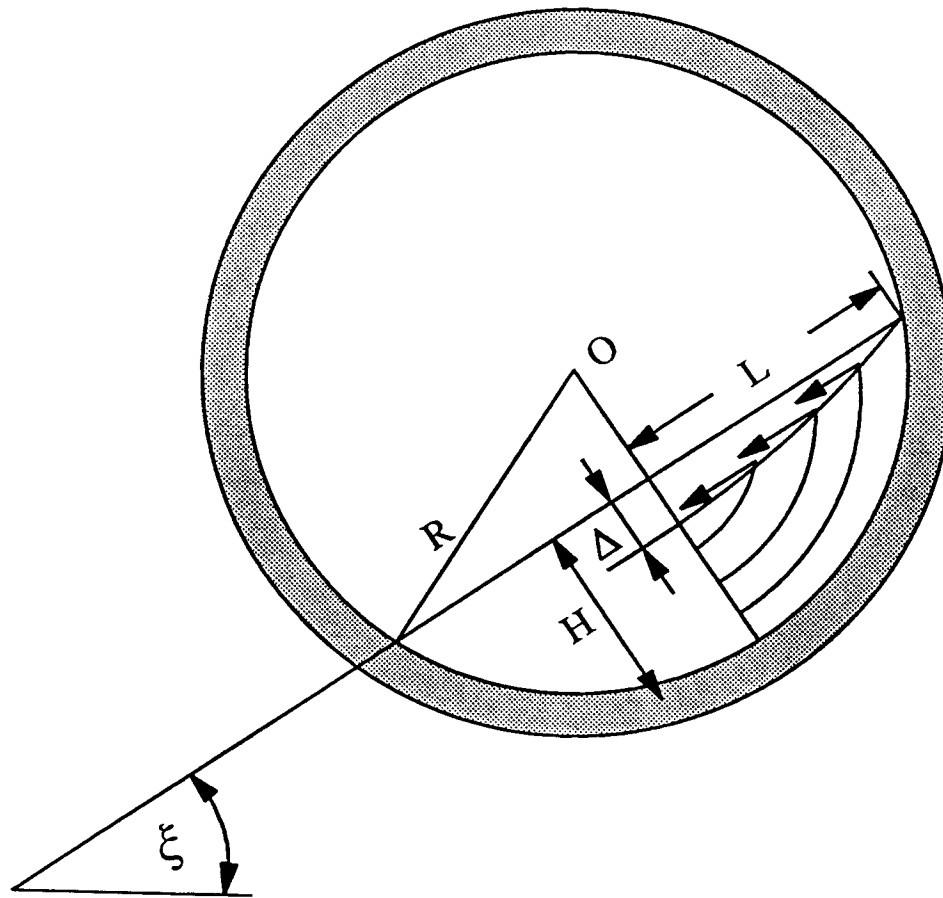
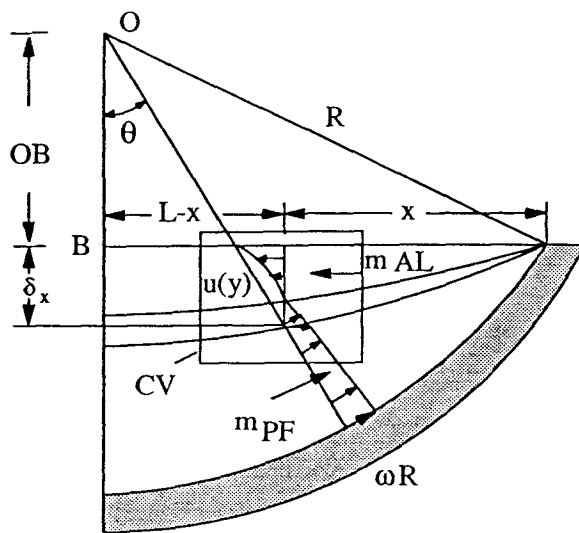


Figure 5.2. Schematic Showing Scaling Variables Employed in Normalizing Governing Equations.



CONTROL VOLUME

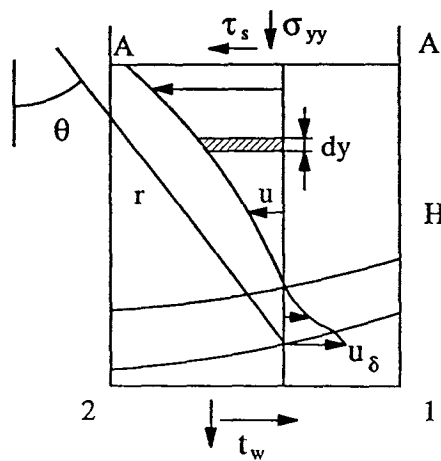


Figure 5.3. Schematic of the Control Volume Used in Deriving Integro-Momentum Equations.

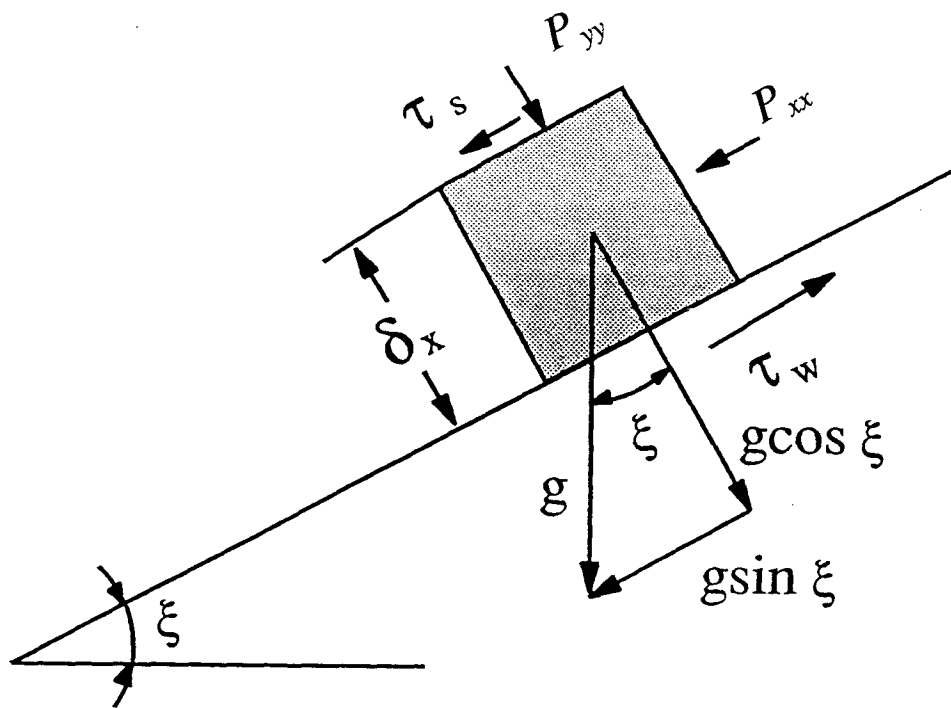


Figure 5.4. Schematic Showing Normal and Shear Stresses Acting on a Control Volume of Granular Material.

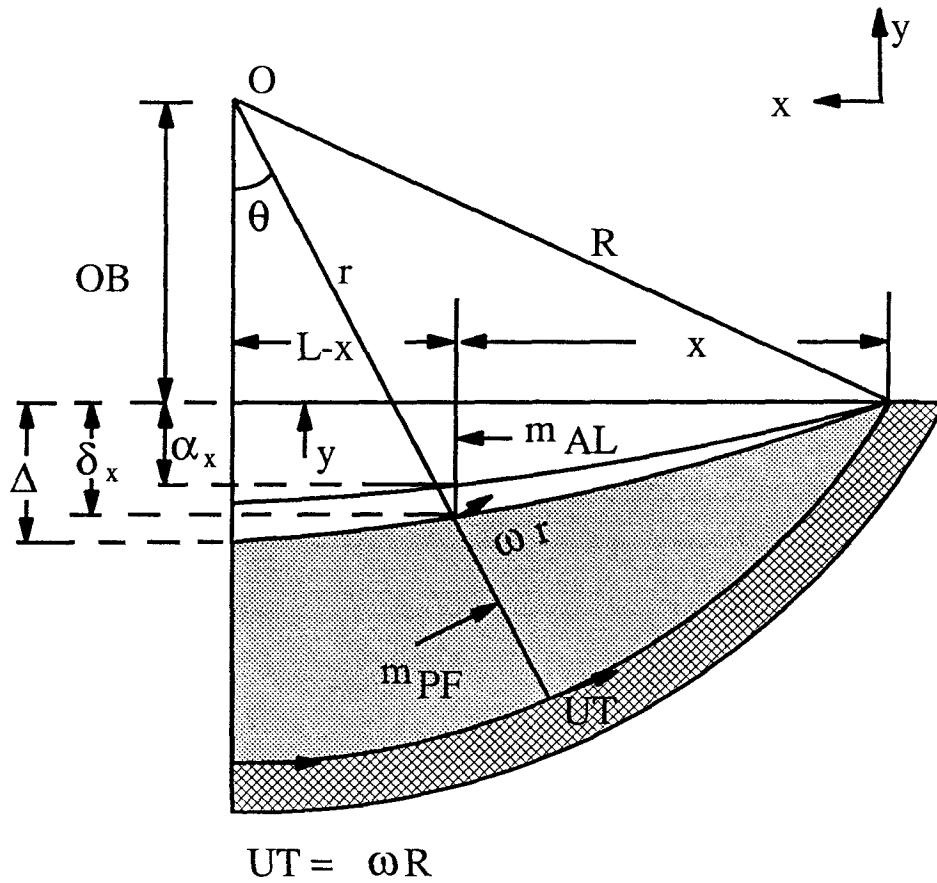


Figure 5.5. Schematic of Kiln Cross-section Showing the Calculation of Material Balance Between Active Layer and Plug Flow Region.

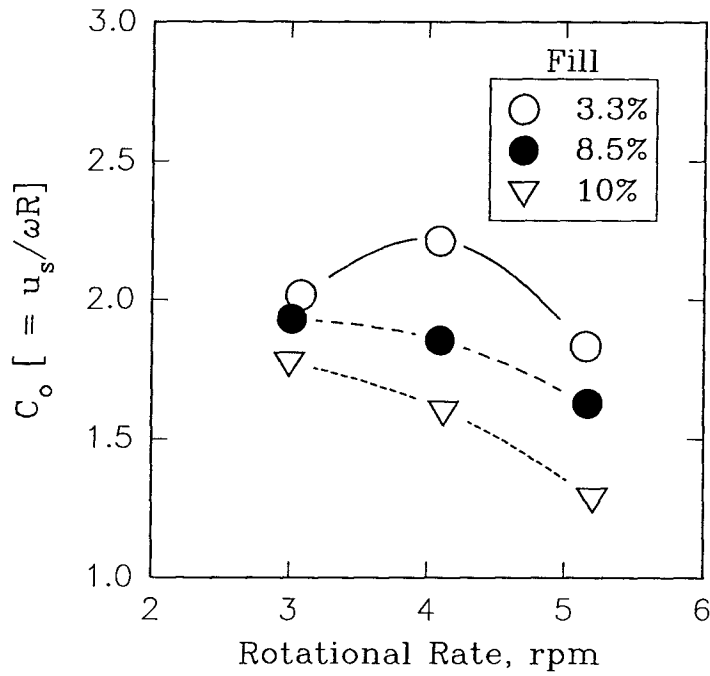
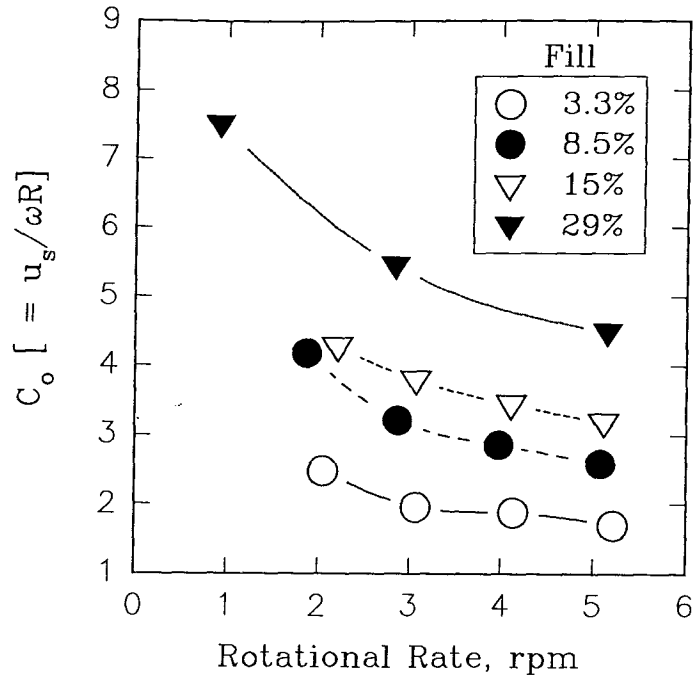


Figure 5.6. Experimental Normalized Surface Velocity ($C_o = u_s/\omega R$) Shown as Function of Kiln Speed. (a) Polyethylene Pellets and (b) Rice Grains

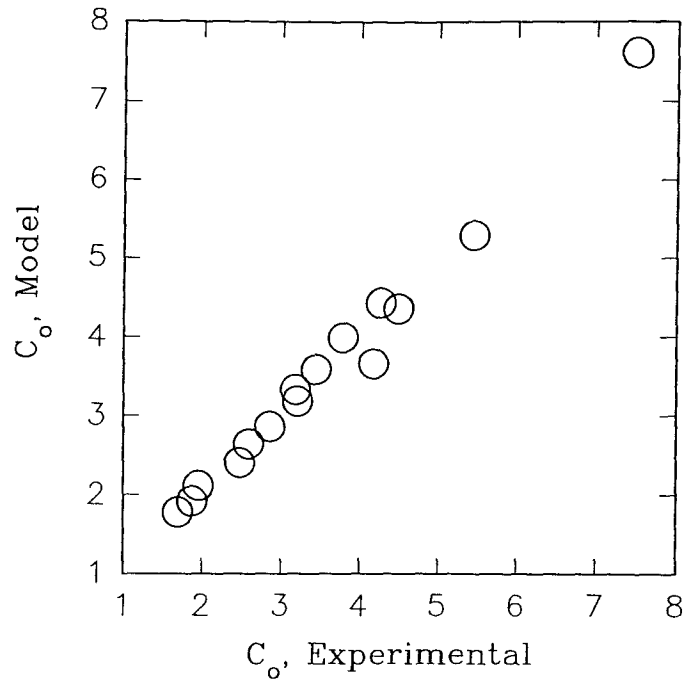


Figure 5.7. Comparison of Experimental and Model Fit for Normalized Surface Velocity.

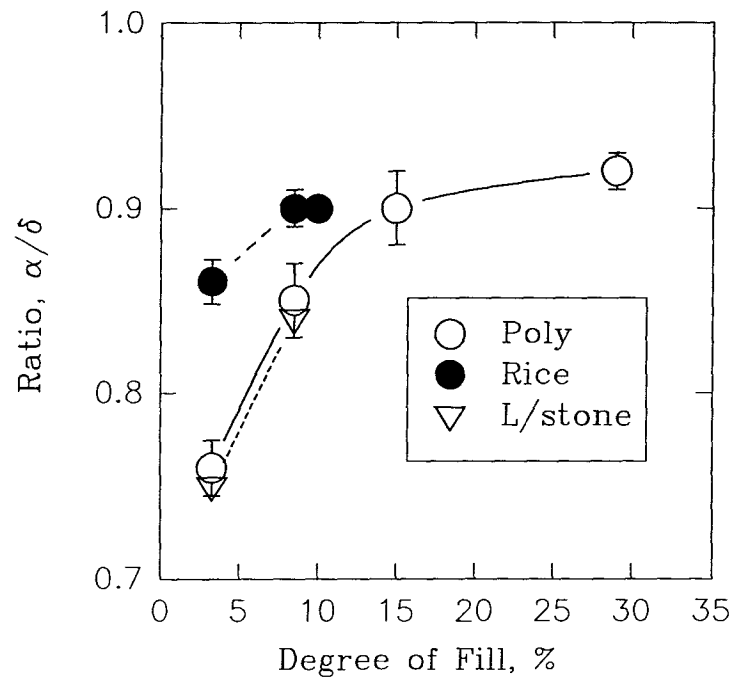


Figure 5.8. The Ratio of the Depth of the Zero Velocity Line to the Depth of the Yield Line (Experimental Observations Through Glass End-piece).

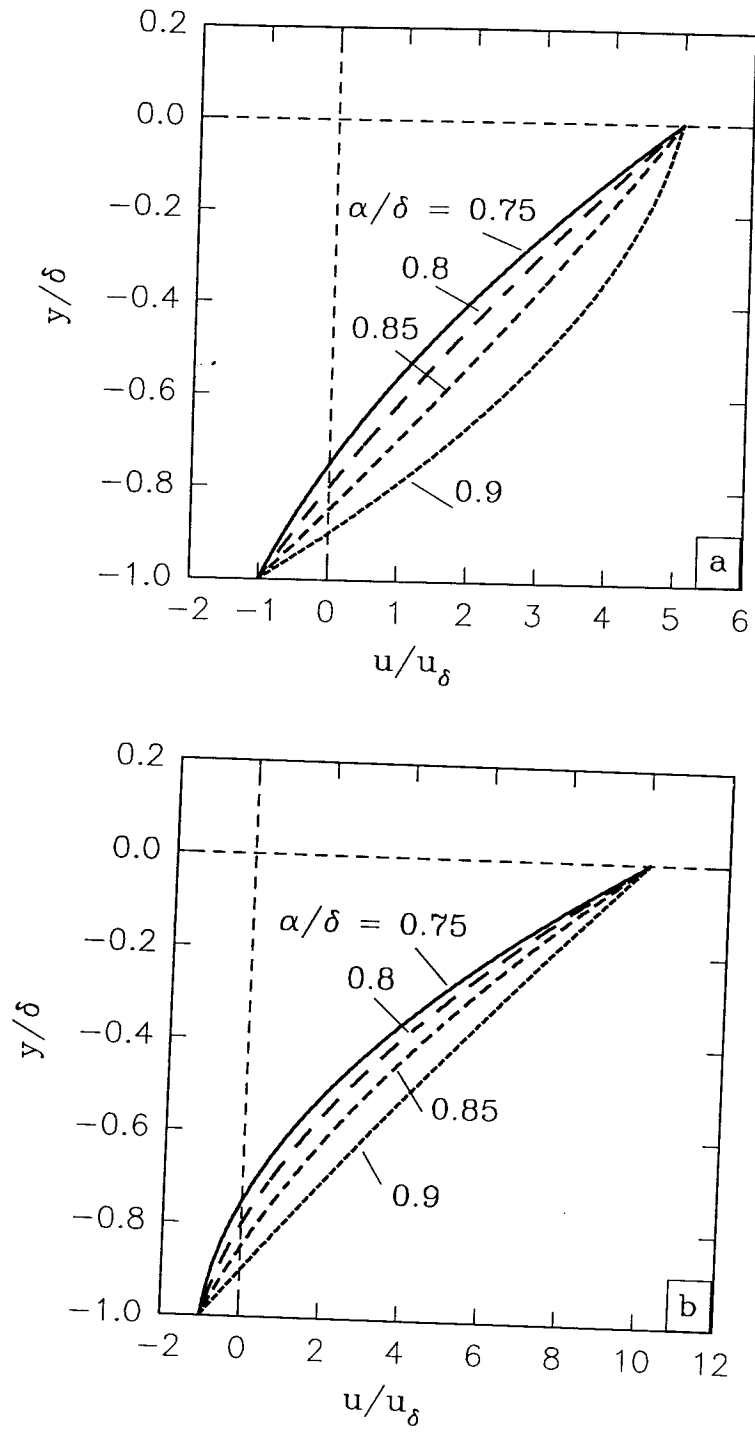


Figure 5.9. Arbitrary Velocity Profiles Showing the Effect of the Boundary Conditions Imposed on Flow Model. Family of Profiles for (a) $\kappa = 5$; (b) $\kappa = 10$

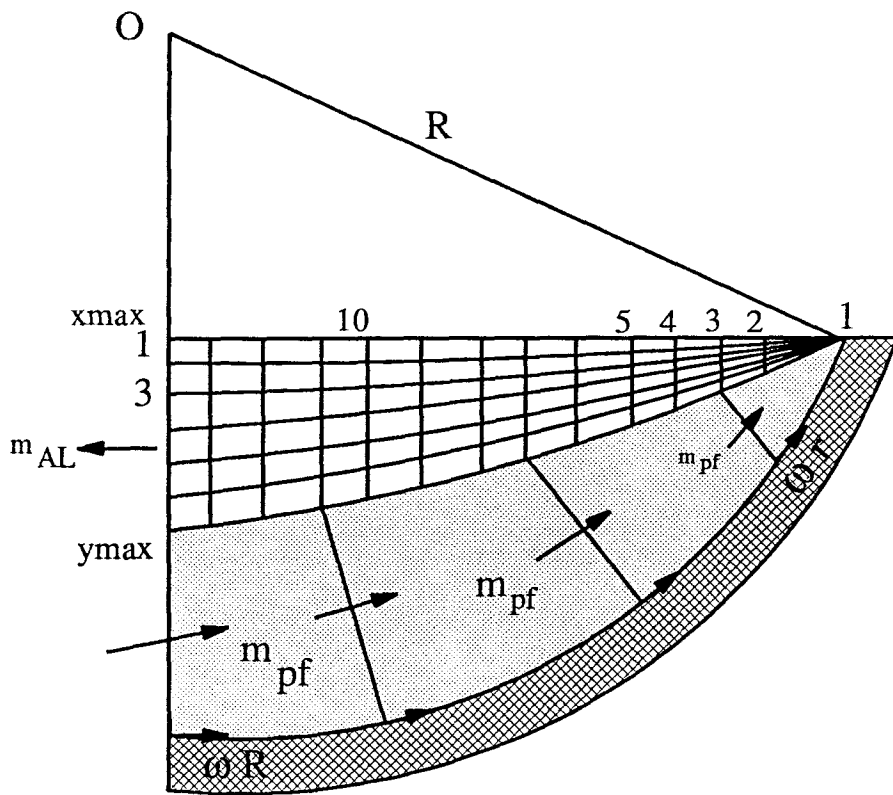


Figure 5.10. Schematic of Kiln Cross-section Showing the Mesh Used in Computing Resultant Boundary Layer Equation.

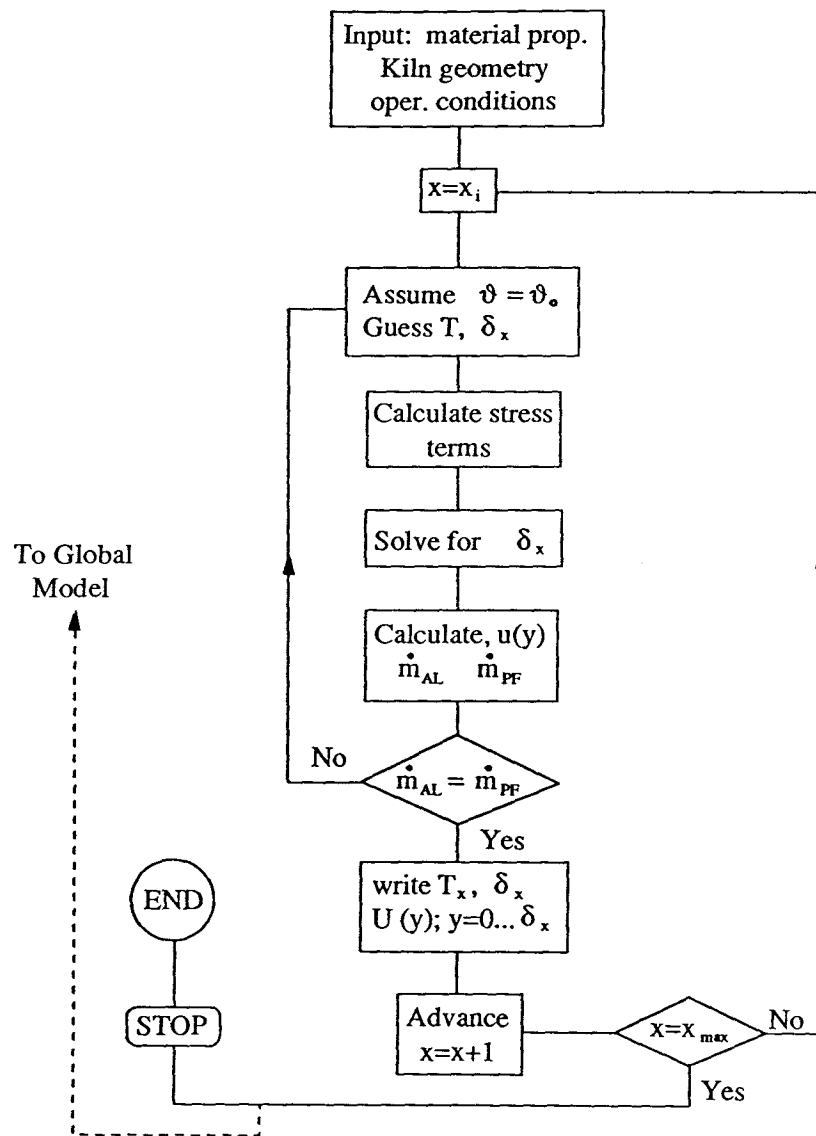


Figure 5.11. The Flow Chart for the Prediction of the Active Layer Depth and Velocity.

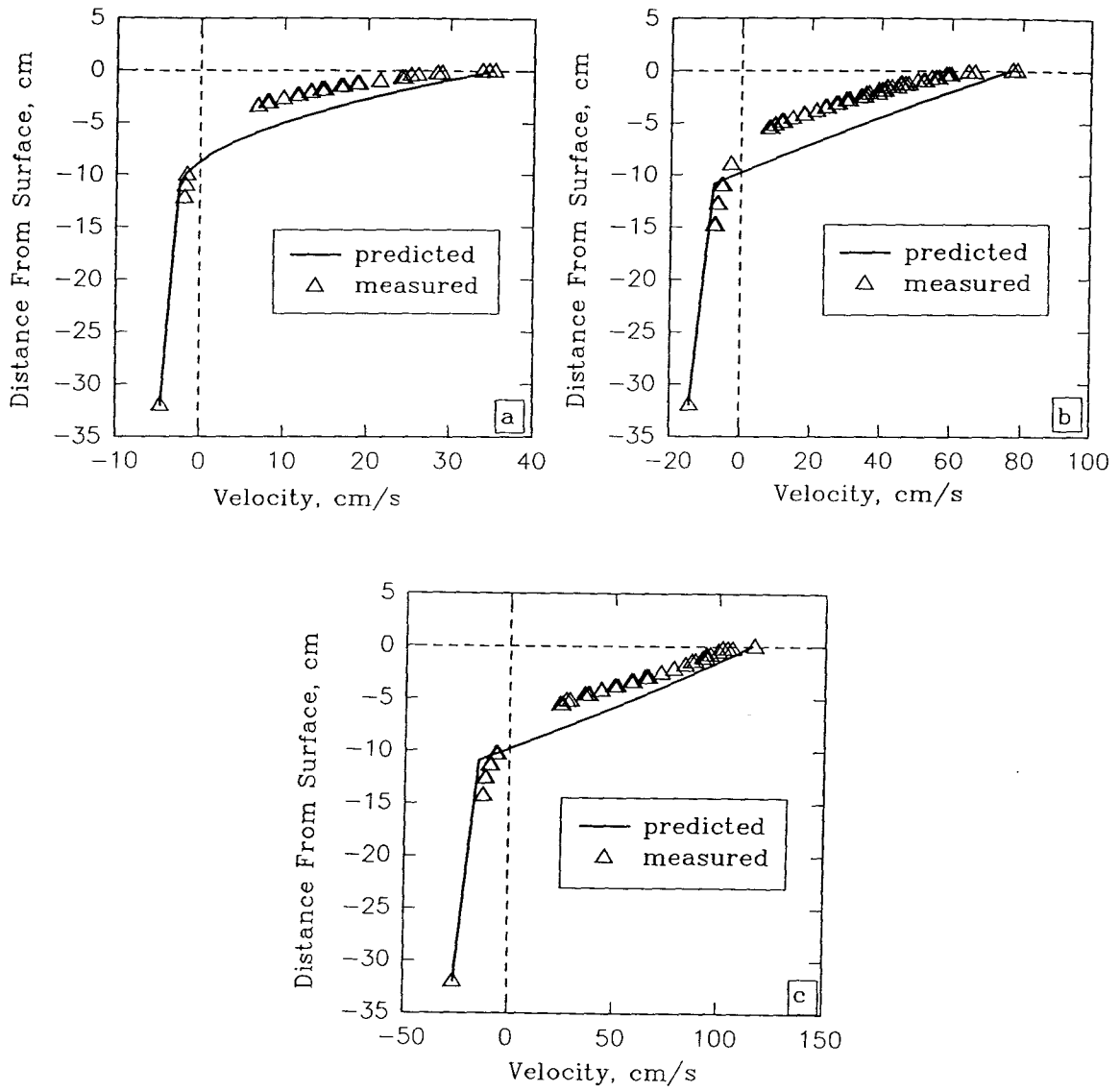


Figure 5.12. Predicted and Measured Velocity as Function of Depth at Mid-Chord with Polyethylene in the 1 m I.D Rotary Drum Filled at 29%. (a) 1 rpm; (b) 3 rpm; (c) 5 rpm.

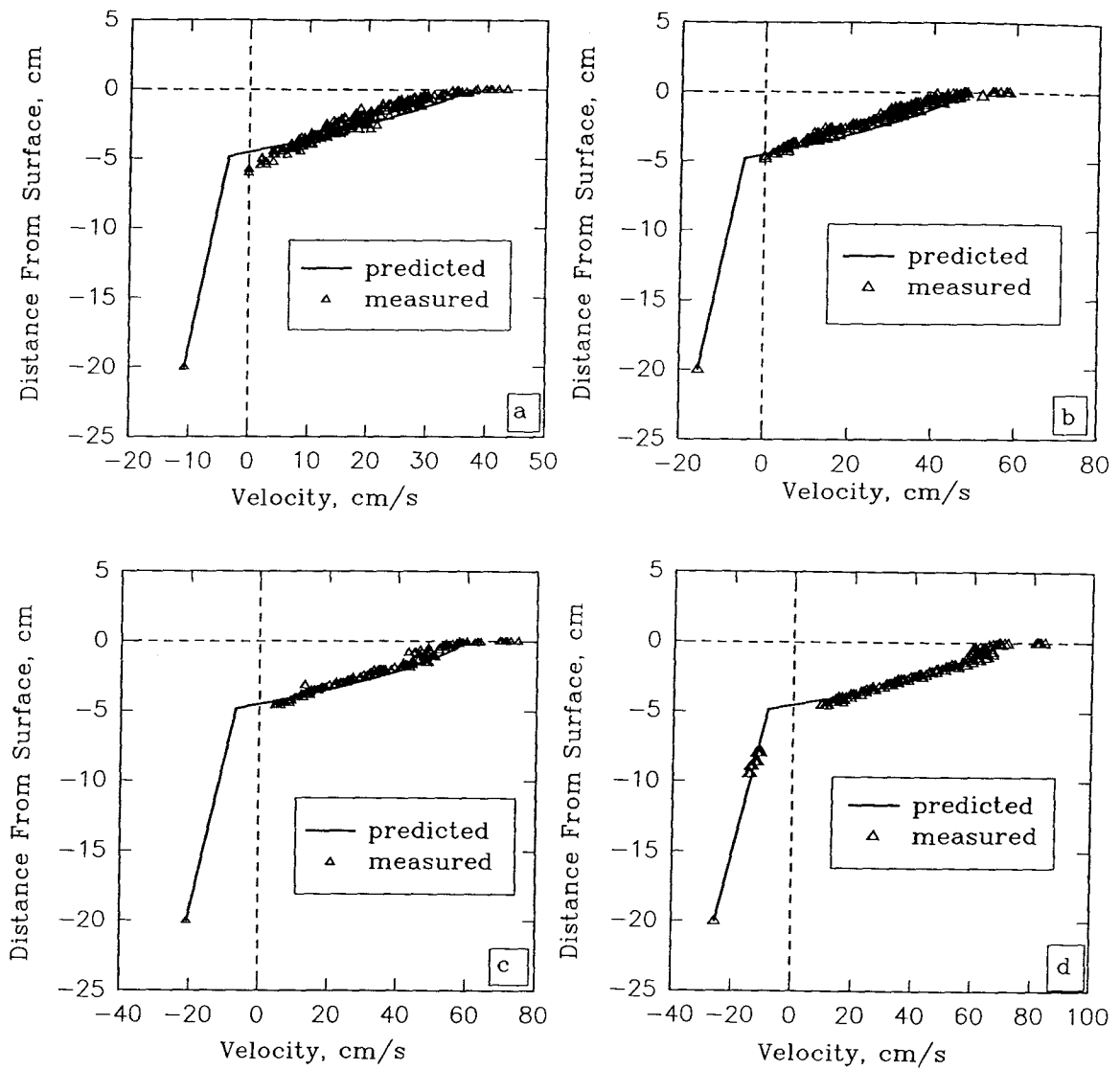


Figure 5.13. Predicted and Measured Velocity as Function of Depth at Mid-Chord with Polyethylene in the 1 m I.D Rotary Drum Filled at 15%. (a) 2 rpm; (b) 3 rpm; (c) 4 rpm; (d) 5 rpm.

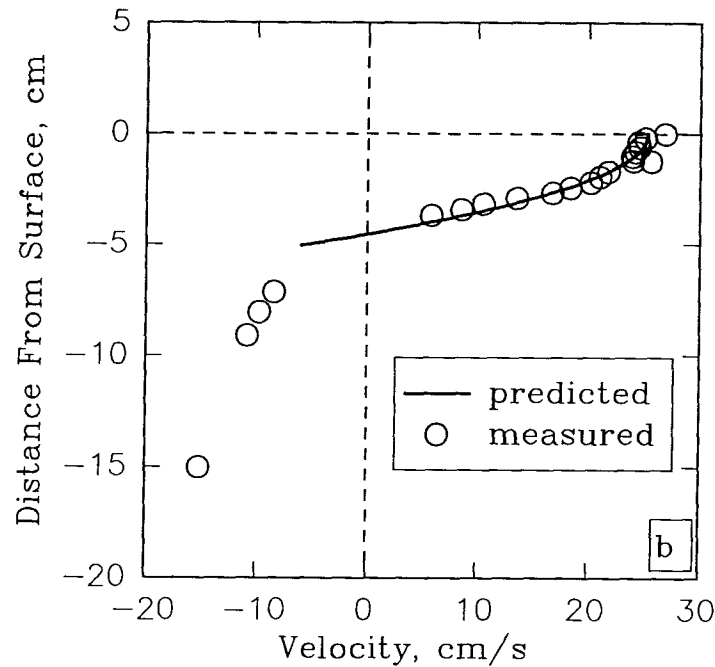
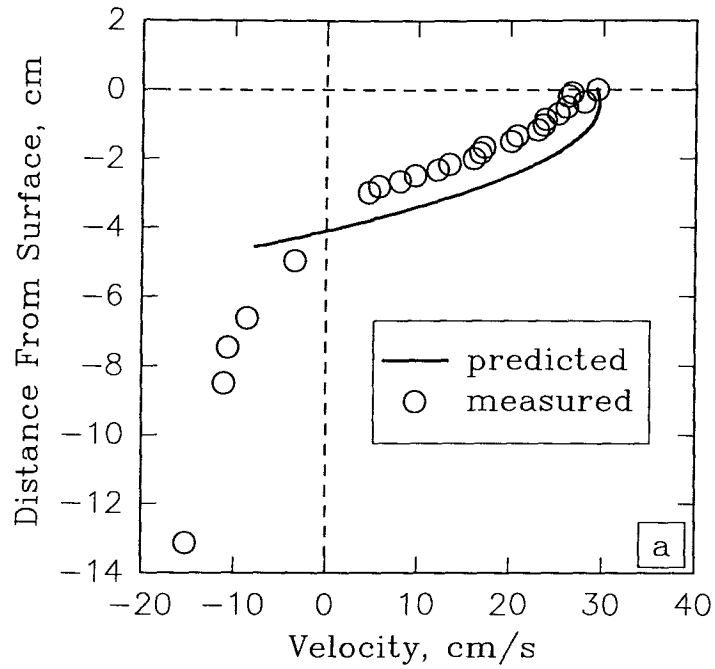


Figure 5.14. Predicted and Measured Velocity as Function of Depth at Mid-Chord with Rice Grains in the 1 m I.D Rotary Drum Filled at 3 rpm. (a) 8.5% Fill; (b) 10% Fill.

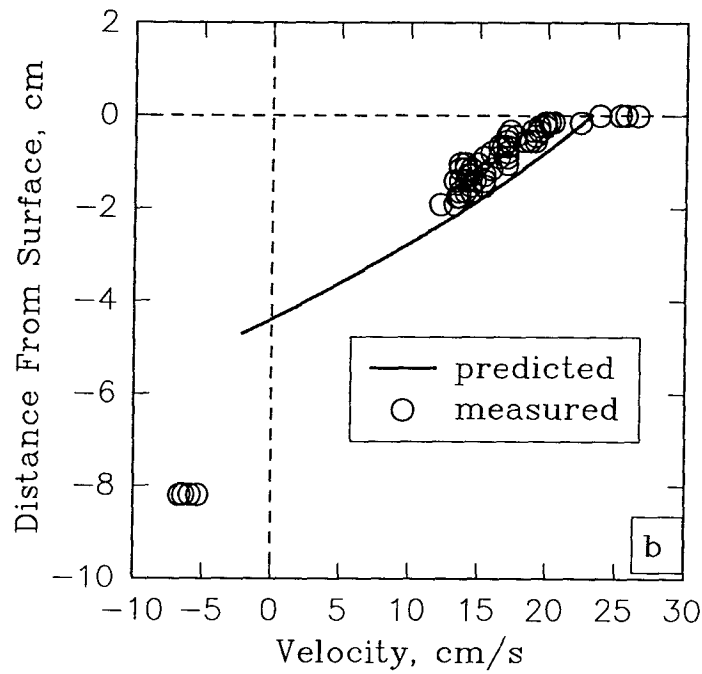
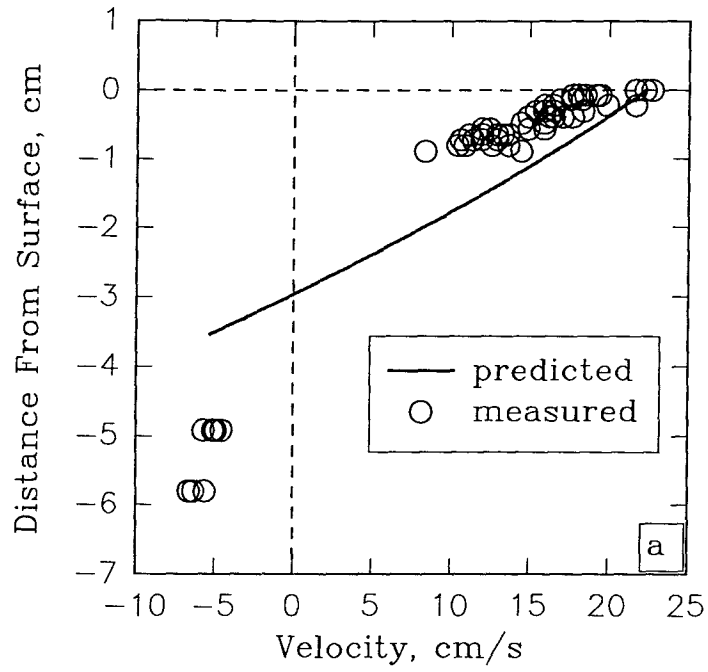


Figure 5.15. Predicted and Measured Velocity as Function of Depth at Mid-Chord with Limestone in the 1 m I.D Rotary Drum Filled at 3 rpm. (a) 3.3% Fill; (b) 8.5% Fill.

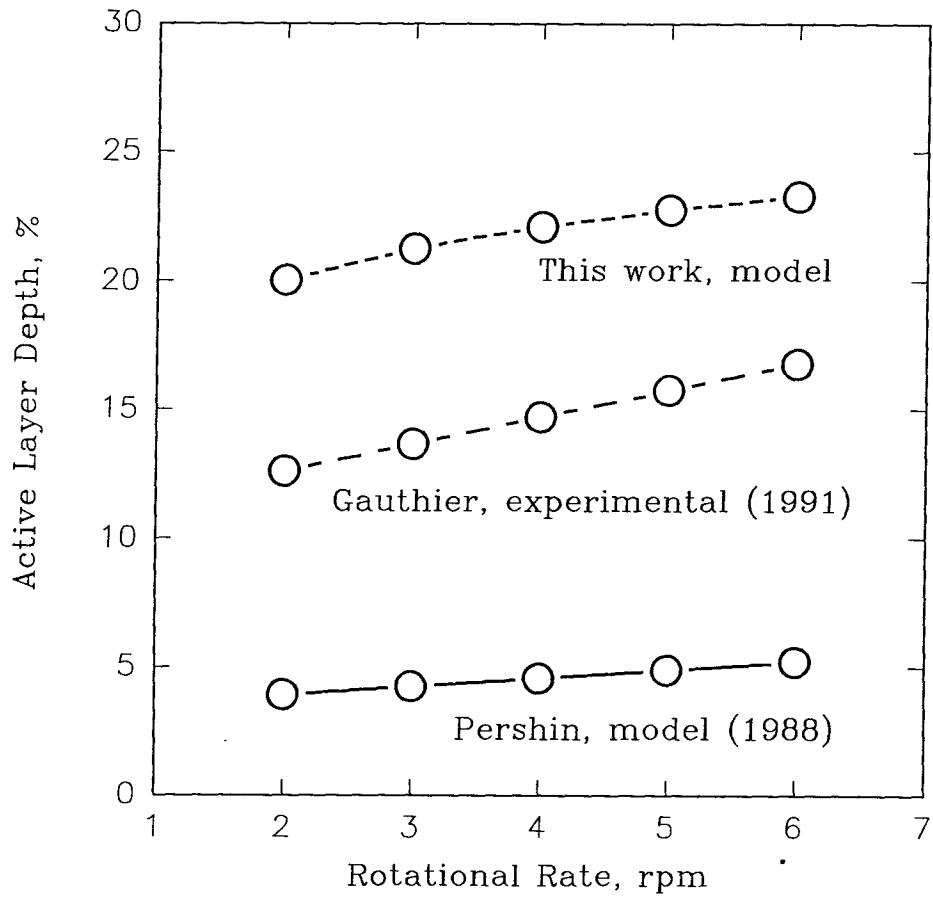


Figure 5.16. Qualitative Comparison of Various Active Layer Depth Estimations.

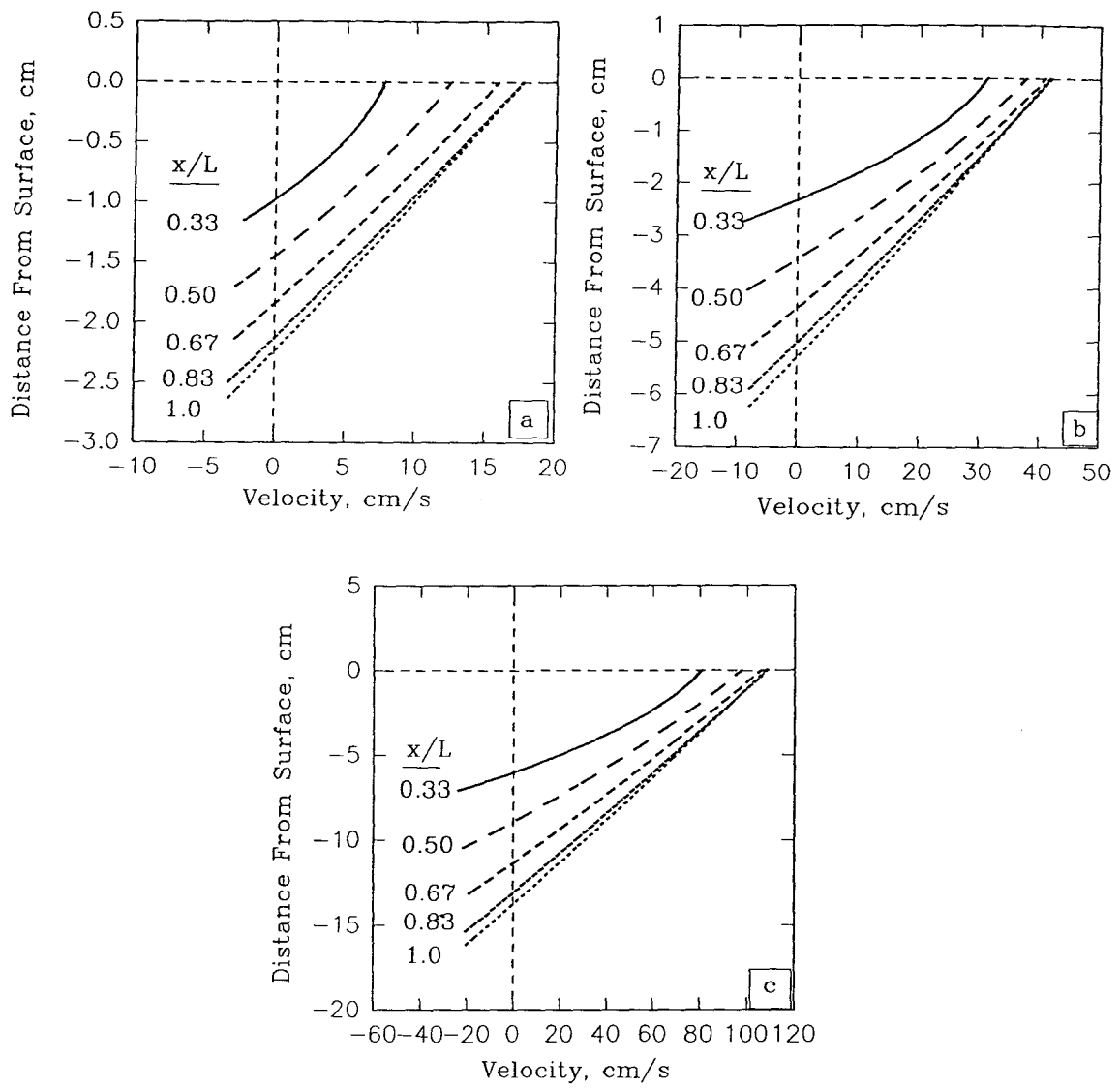


Figure 5.17. Model Prediction for Velocity in the Active Layer as a Function of Distance from Apex with Operational Conditions of 2 rpm and 12% Fill: (a) 0.41 m I.D Pilot Kiln; (b) 1 m I.D Drum; (c) 2.5 m I.D kiln.

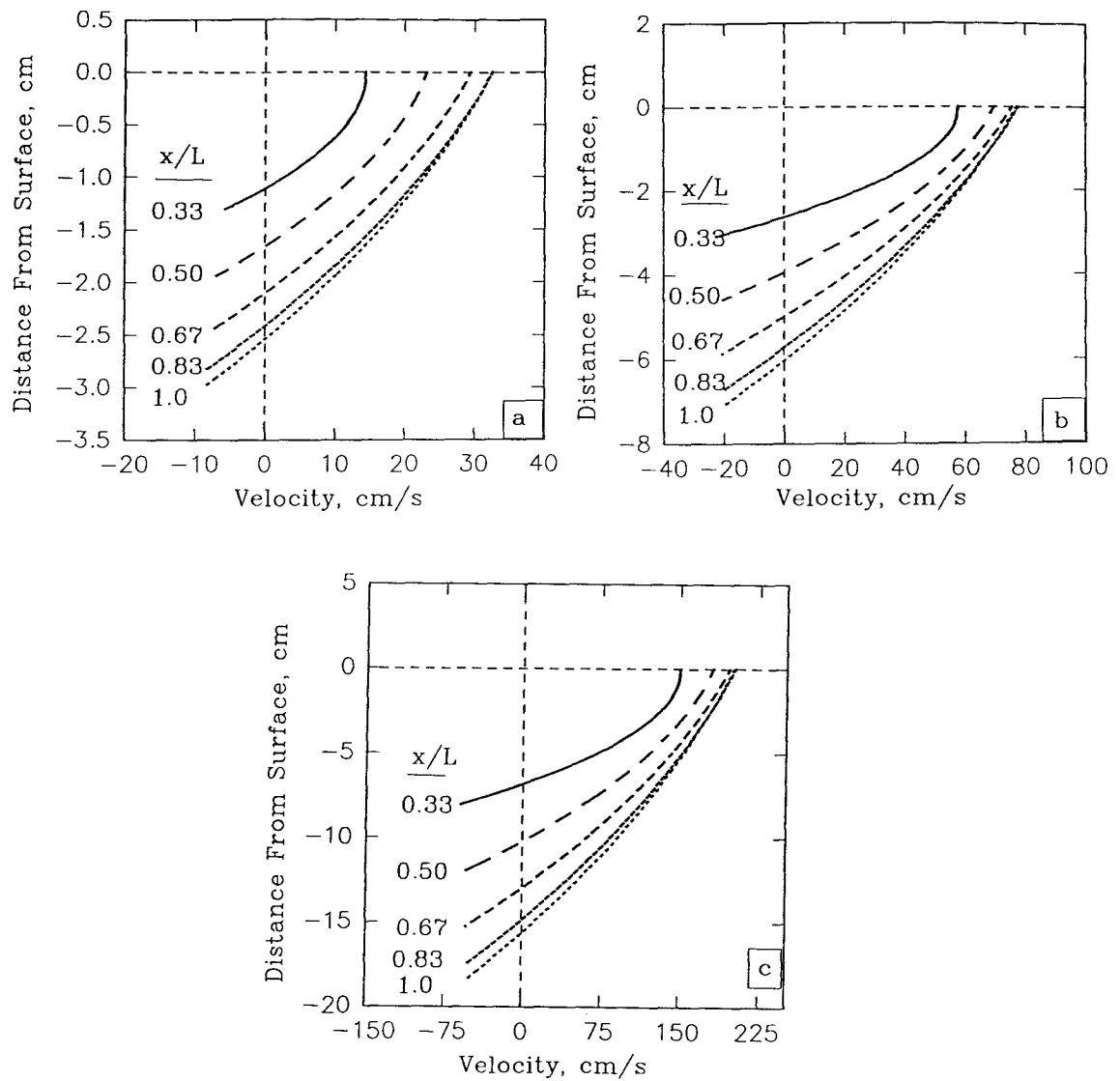


Figure 5.18. Model Prediction for Velocity in the Active Layer as a Function of Distance from Apex with Operational Conditions of 5 rpm and 12% Fill: (a) 0.41 m I.D Pilot Kiln; (b) 1 m I.D Drum; (c) 2.5 m I.D kiln.

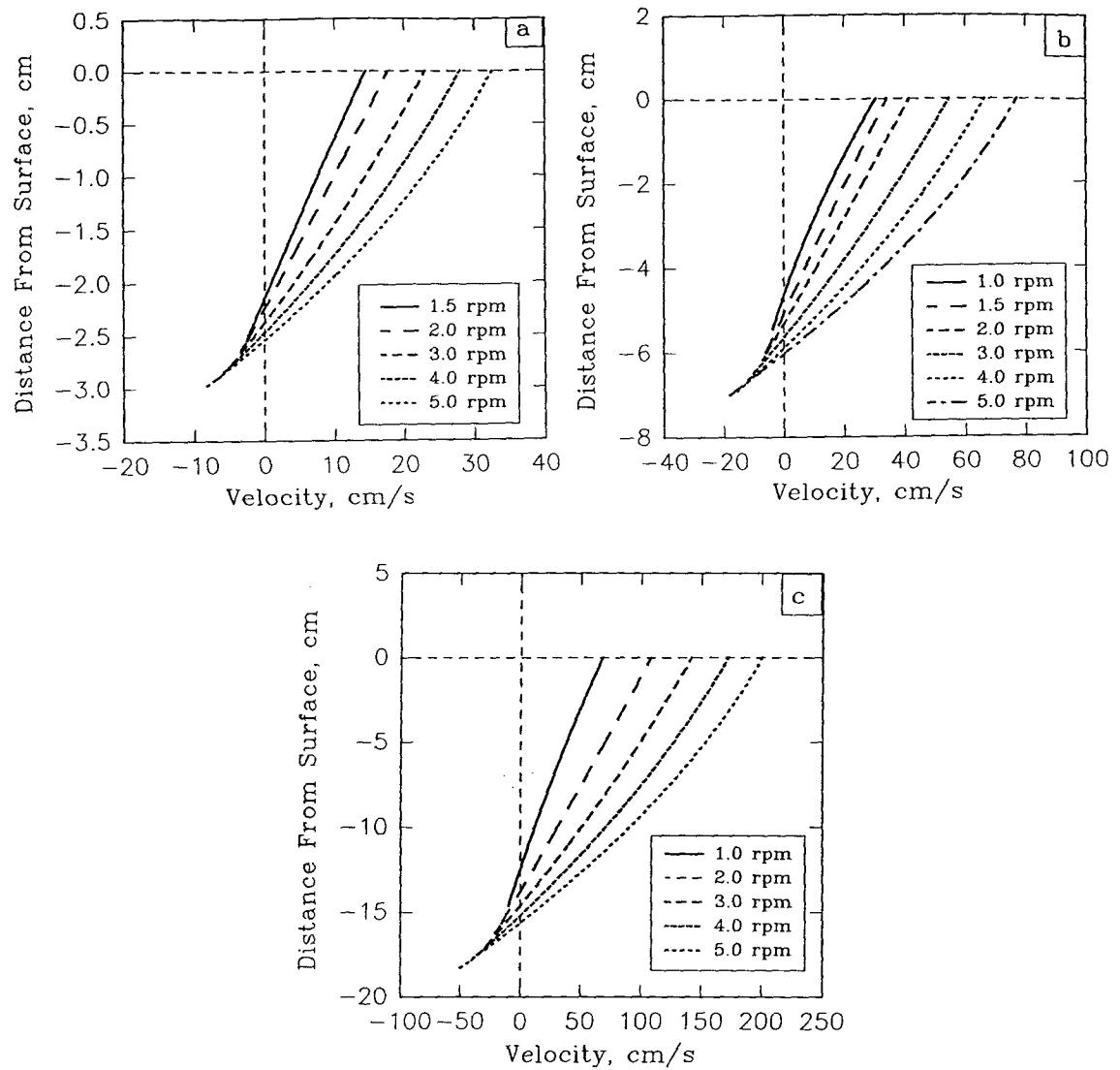


Figure 5.19. Predicted Velocity Profiles at Mid-Chord as a Function of Kiln Rotation Rate: (a) 0.41 m I.D Pilot Kiln; (b) 1 m I.D Rotary Drum; (c) 2.5 m I.D Industrial Kiln.

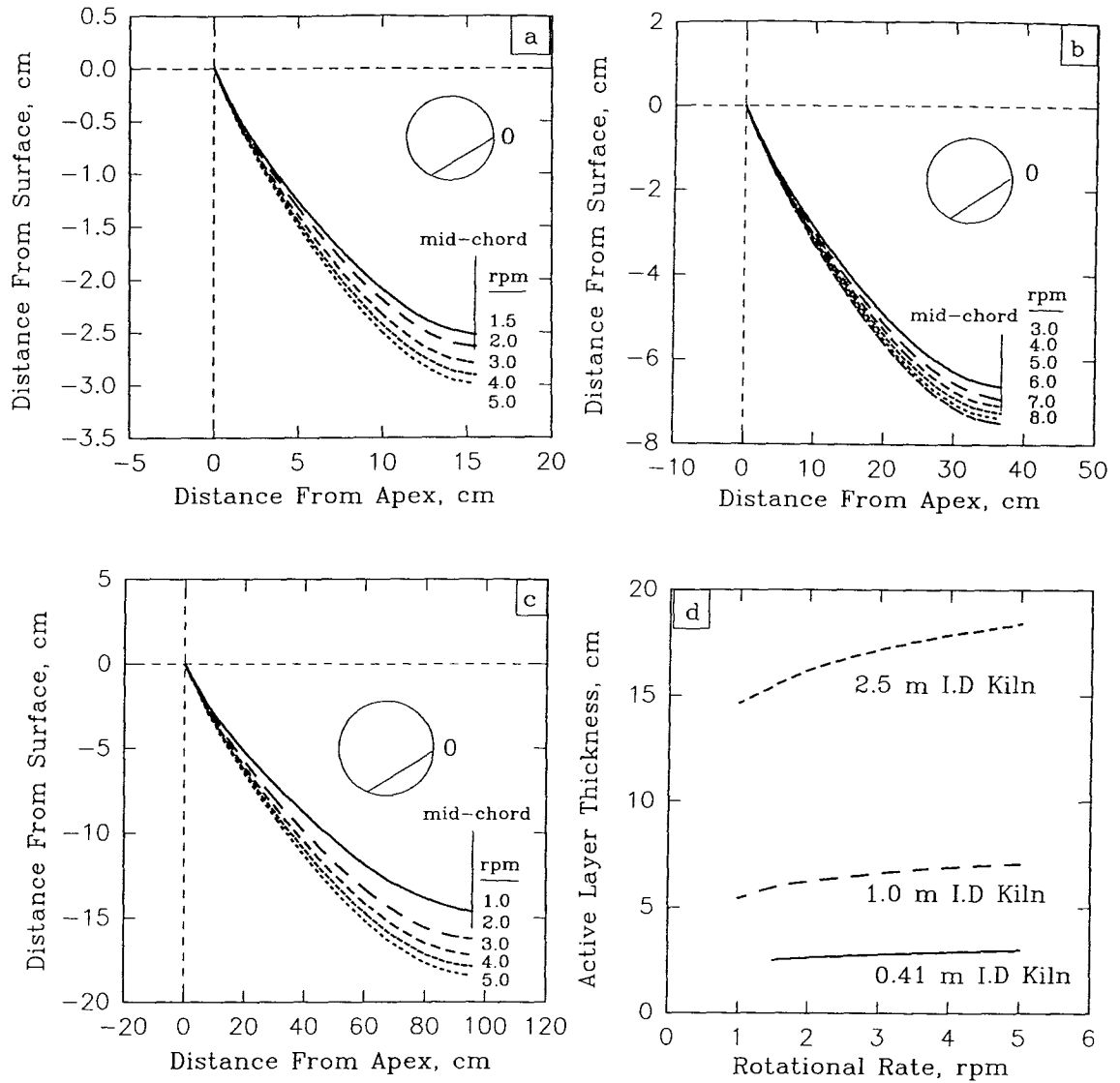


Figure 5.20. Predicted Active Layer Depth as a Function of Kiln Rotation Rate: (a) 0.41 m I.D Pilot Kiln; (b) 1 m I.D Rotary Drum; (c) 2.5 m I.D Industrial Kiln; (d) Active Layer Thickness as Function of Rotational Rate.

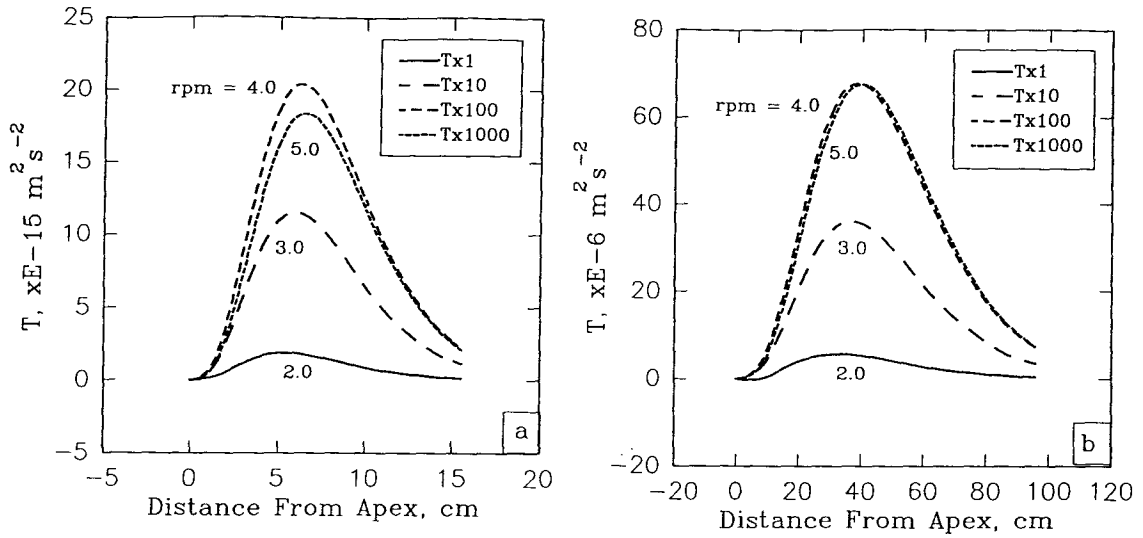


Figure 5.21. Predicted Granular Temperature as a Function of Kiln Rotation Rate: (a) 0.41 m I.D Pilot Kiln at 12% Fill; (b) 2.5 m I.D Industrial Kiln at 12% Fill.

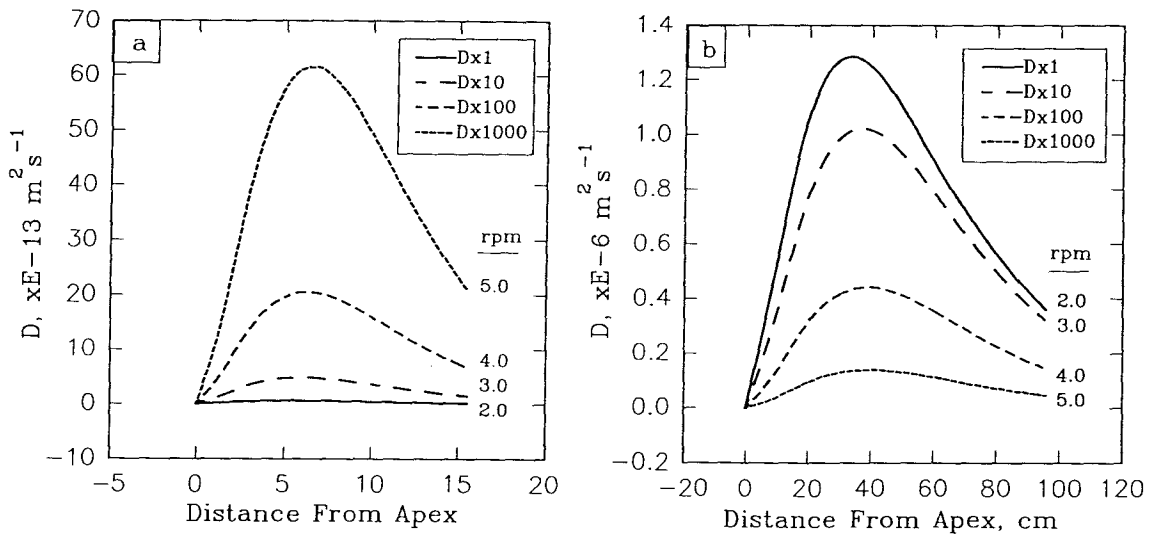


Figure 5.22. Predicted Kinetic Diffusion Coefficient as a Function of Kiln Rotation Rate: (a) 0.41 m I.D Pilot Kiln at 12% Fill; (b) 2.5 m I.D Industrial Kiln at 12% Fill.

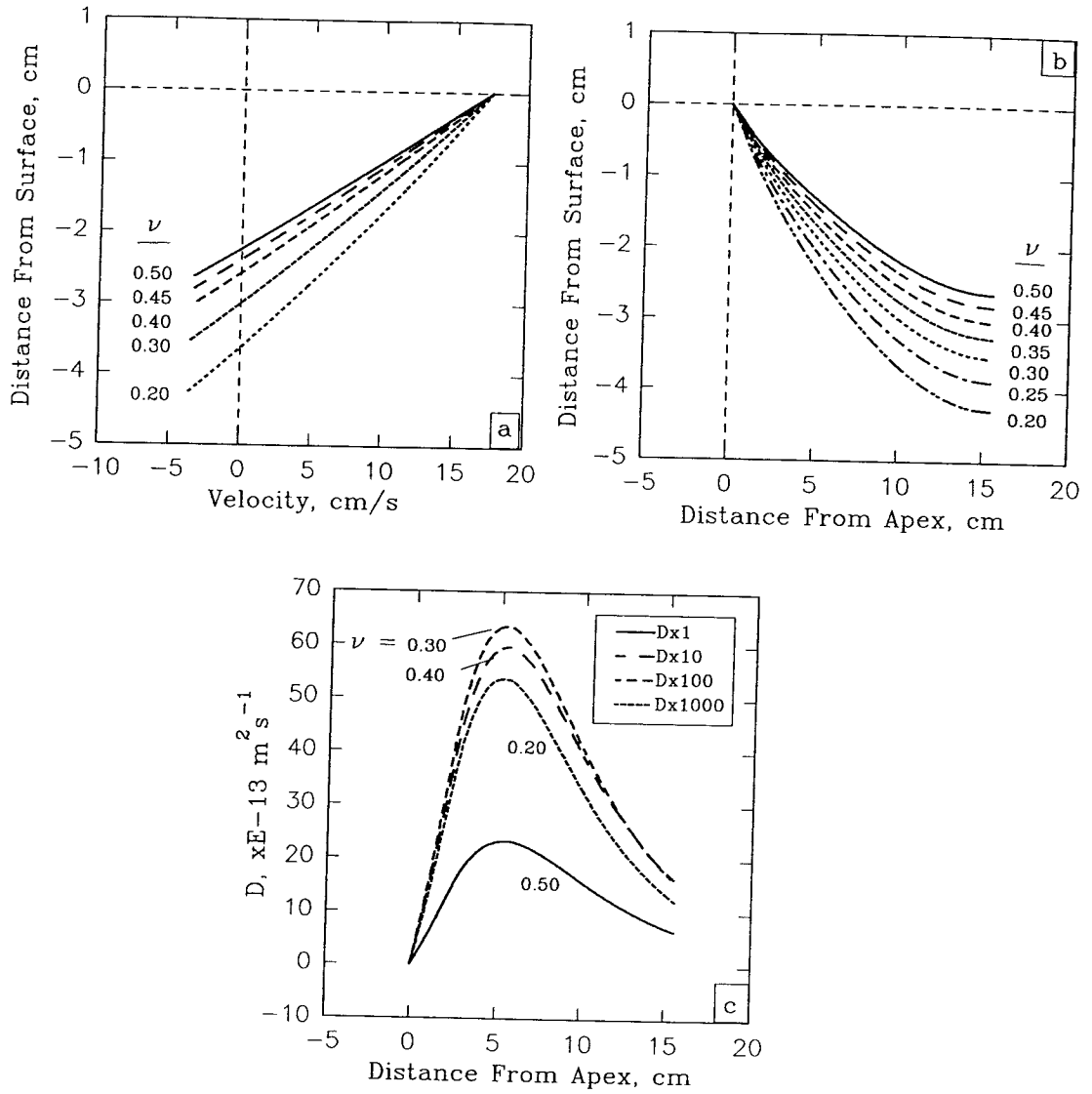


Figure 5.23. Effect of Solids Concentration on Flow Characteristics for Pilot Kiln at 12% Fill run at 2 rpm: (a) Effect on Velocity; (b) Effect on Active Layer Depth; (c) Effect on Diffusion.

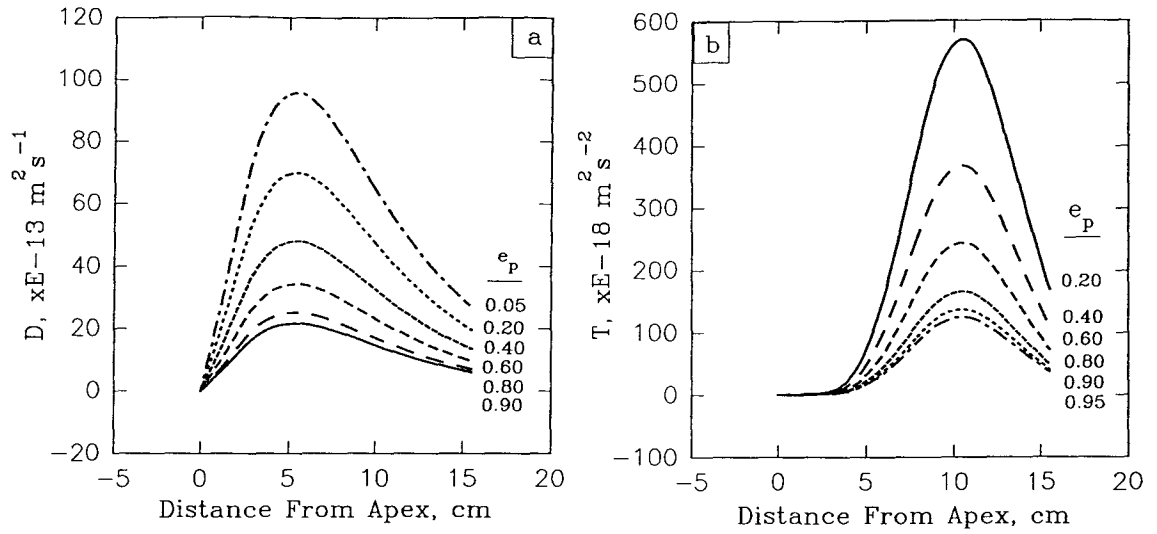


Figure 5.24. Effect of Particle Coefficient of Restitution on Flow Characteristics for Pilot Kiln at 12% Fill run at 2 rpm: (a) Effect on Diffusion; (b) Effect on Granular Temperature.

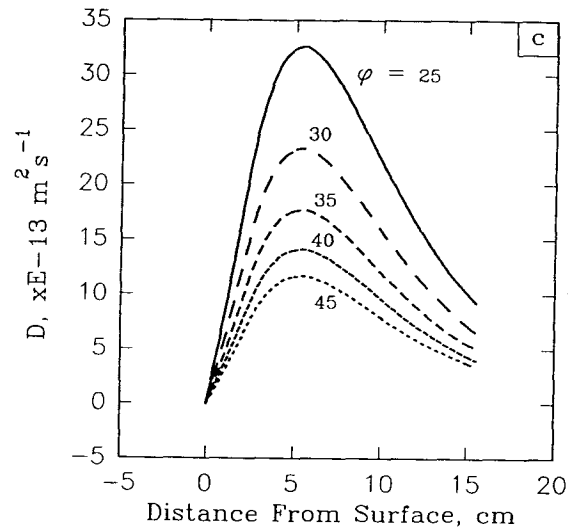


Figure 5.25. Effect of Static Angle of Repose on the Diffusion Coefficient for 0.41 m I.D Pilot Kiln Filled at 12% and Operated at 2 rpm.

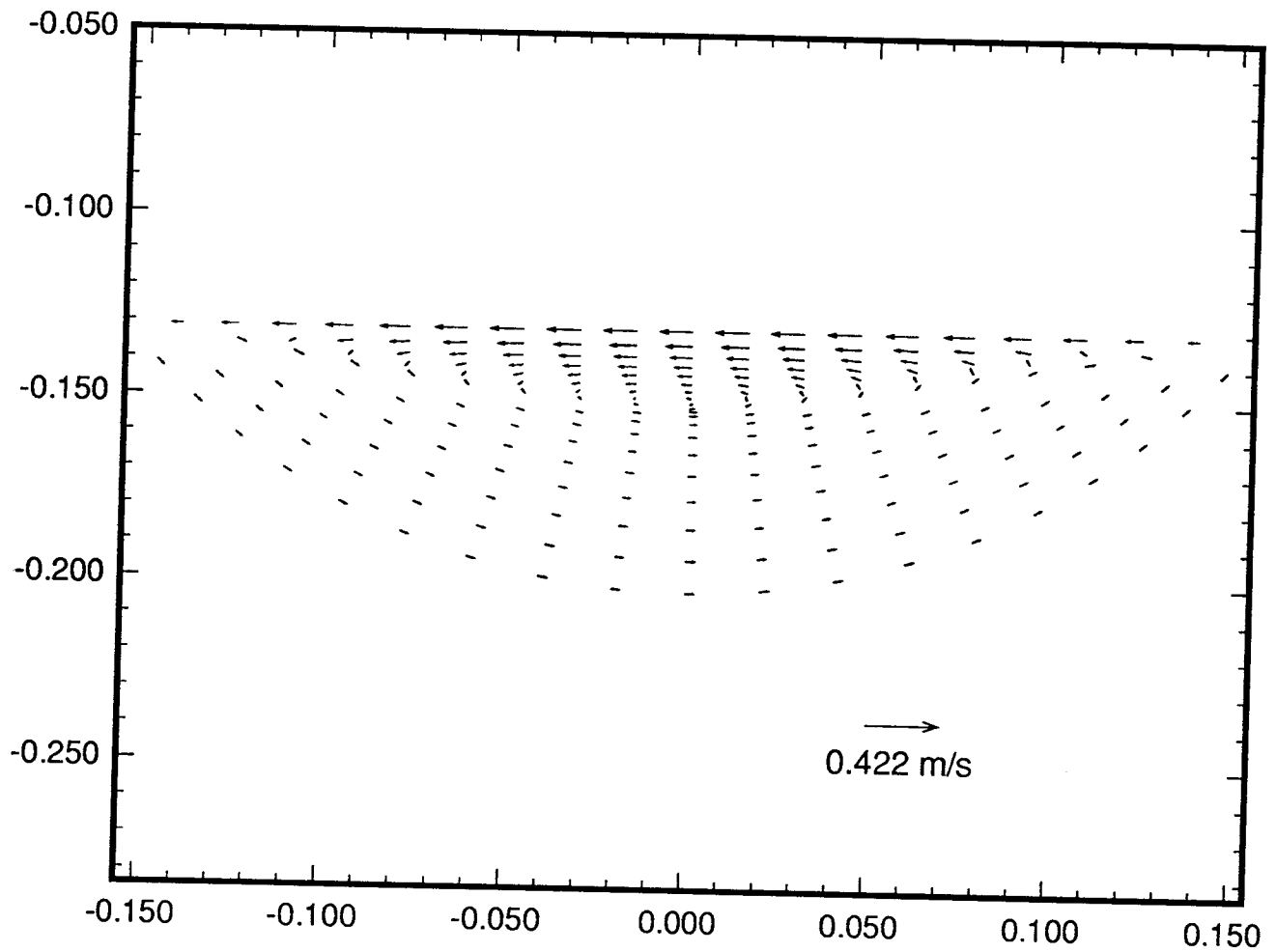


Figure 5.26. Velocity Predictions for a Cross-section of the 0.41 m I.D Pilot Kiln at 12% Fill and 2 rpm.

CHAPTER 6. MODELLING OF PARTICLE MIXING AND SEGREGATION IN THE TRANSVERSE PLANE

6.1 Introduction

It is evident both from the rotary kiln literature and operator experience that thorough mixing of particles in the transverse plane of a rotary kiln is fundamental to achieving uniform heating or cooling of the charge and, ultimately, to the generation of a homogeneous product. This good mixing assumes particles are evenly sized which effectively means that (statistically) exposure to freeboard will be same. Unfortunately, when significant variation in particle sizing occurs, superimposed on this mixing will be the tendency of small particles in the active layer to sieve downwards through the matrix of larger particles. Thus, the bed motion tends to concentrate finer material within the core (see, Figure 1.4), and material within the core, because it has very little chance of reaching the exposed bed surface for direct heat transfer from the freeboard, tends to a lower temperature than the surrounding material. Thus segregation can counteract advective transport of energy and thus promote temperature gradients within the bed. As was said earlier, the net effect is not necessarily negative, and for a process such as limestone calcination where smaller particles react faster than larger ones (at the same temperature) segregation of fines to the cooler core may be essential to obtaining uniform calcination of all particles. This suggests that particle size distribution in the feed material might be optimized, which points out the need for developing our predictive capabilities for the material mixing and segregation.

The objective of this chapter is to construct a mathematical model that will describe the phenomenon of segregation and to predict the extent and dimensions of the segregated core. It is worth pointing out that, although segregation in drum mixers is a well known phenomenon and has been characterized in many ways, quantitative prediction of the composition of the core has been lacking. Fan *et al.* (1970) reviewed over 30 forms of mixing indices that have appeared in the literature to characterize particulate mixing and segregation in drum mixers. Most of these characterization parameters are probabilistic or statistical in nature and, although often helpful,

tend to conceal the details of the phenomenon and yield little information on, for example, the effect of material properties on flow and hence on segregation. Scaling factors are also difficult to evaluate without a good grasp of the physical phenomena which drive segregation.

The segregation model developed in the present work considers a binary mixture of small and large particles in the continuously shearing active layer of the kiln bed. Continuum equations are employed to describe the mixing and segregation rates in the transverse plane of the bed which result from both particle percolation and diffusional mixing. The diffusion coefficients and the convective terms for material concentration in the continuum equations are obtained from the granular flow model described in Chapter 5. The percolation velocities are calculated using existing models which relate percolation to the probability of void formation in the shear plane. The segregation model is applied in order to predict the size and extent of the segregated core as well as to show the effect of segregation on material mixing and on the effective thermal conductivity of the bed. Model predictions for segregation rate in the radial direction are compared to experimental results and the adequacy of the model will be discussed.

6.2 The Model Developed for Segregation within the Bed

In the granular flow experiments described in Chapter 4 no quantitative measurements were made to estimate mixing and segregation. However, the salient features of segregation were observed qualitatively, both through the introduction of fine particles of the same material into the bed as well as the introduction of different material into the bed. The segregation process as observed in the experiments was similar to that described in the literature and confirmed that percolation is the primary cause of segregation in the rotary kiln. A review of the literature pertaining to segregation of the bed material in rotary kilns leads to the following conclusions:

- (i) From a condition of uniform mixing of particles within the bed, radial segregation proceeds very rapidly and is fully implemented within 2 to 10 kiln revolutions (see, e.g, Rogers and Clements, 1971; Pollard and Henein, 1989). The mechanism of segregation can therefore be considered as a steady-state problem.

- (ii) The segregation process is continuous and there is a constant discharge of fines from the plug flow region into the active layer. This discharge of fines occurs in the upper part of the bed toward the apex and is followed by percolation normal to the bed surface as material is sheared in the active layer.
- (iii) The 'kidney' (or 'tongue') formed by the segregated core does not consist entirely of fine material but also contains some small amounts of coarse particles (there are concentration gradients even in the core).
- (iv) The bulk velocity distribution in the active layer does not change with addition of fines and the bed behavior (e.g., rolling, slumping, etc.) remains unchanged with fines (Henein, 1980).
- (v) The percolation velocity of fine particles depends on the size of the voids formed in an underlying layer; these voids are formed in a random manner (Savage, 1988).
- (vi) For particles below some critical size, spontaneous percolation may also occur in the plug flow region thereby resulting in a possible collection of fines near the bed/wall interface (Bridgwater and Ingram, 1971).
- (vii) Downward movement of segregating particles in the active layer is compensated by an equal volumetric upward movement of bulk particles in the active layer (*squeeze expulsion mechanism*, Savage, 1988).

Based on this information a credible mathematical model would be one which accounts for the mass conservation of the sinking and/or floating particles in a control volume and whose analysis can be restricted to the active layer since, in view of (vi) above, the probability of fines moving through the plug flow region is very low relative to dilated shearing flow in the active layer. The plug flow region can therefore be assumed impermeable and serving only as the circulation path by which particles are fed back to the active layer. By this assumption, spontaneous percolation is precluded in the model. The situation to model is shown schematically in Figure

6.1. For convenience, the coordinate system used here is consistent with that in the flow model where a cartesian system is allocated to the active layer such that $0 \leq x \leq 2L$ where $2L$ is the chord length, and the origin is at the apex of the bed.

In the present work, only a simple binary system of two particle sizes, each of the same density, will be considered. Since the calculation domain is restricted to the active layer, the fine particles are assumed to be larger than the critical size which causes spontaneous percolation. This occurs when the diameter ratio of the small to large particles exceeds the critical value, which, for closely packed bed, has been given as (Savage, 1988);

$$\bar{\sigma} = \frac{d_{ps}}{d_{pL}} \leq 0.1547 \quad (6.1)$$

where d_{ps} and d_{pL} are, respectively, the sizes of the small and large particles for the binary system. By choosing the size ratio to be greater than the critical value it is implicitly assumed that percolation will occur only when the voids formed are larger than the smaller size particle, d_{ps} , of the binary mixture. For a continuously shearing active layer of the rotary kiln it will be further assumed that void formation is a random occurrence and follows a probability law. For generality the model is developed by adapting the terminology employed by Gibilaro and Rowe (1974) for fluidized-bed segregation whereby sinking particles, either due to size or density differences, are called 'jetsam' and floating particles are called 'flotsam'. The model is derived on a volume balance basis and the concentration terms refer to volumetric fraction of jetsam in a given volume of solids. The relationship between the volume fraction jetsam concentration and the number of particles in the control volume can, therefore, be expressed as;

$$C_j = v \frac{\bar{\eta}\bar{\sigma}^3}{1 + \bar{\eta}\bar{\sigma}^3} \quad (6.2)$$

where v is the solids concentration, $\bar{\eta}$ is the particle number ratio, n_j/n_F , with n_j and n_F being the respective jetsam and flotsam number particles. This relation is developed in Appendix A7 for jetsam loading of the kiln.

Following on with the continuum assumption, the control volume required for the material balance is that shown in Figure 6.2. The equilibrium concentration of jetsam within the control volume depends on the interaction of three components; i.e., (i) convection (drift) caused by the bulk velocity, (ii) diffusion-like mixing, and (iii) segregation associated with movement through voids. The rate at which jetsam is spread over the cross section is mathematically depicted in Figure 6.3. Of the three mechanisms shown, segregation is the only one that distinguishes jetsam from flotsam and it depends on the percolation of jetsam into the underlying layer and subsequent displacement of flotsam from the underlying layer as a compensation. This compensation is what is termed the 'squeeze expulsion' mechanism (Savage, 1988). Because the upward flow of material that compensates percolation of jetsam may itself contain jetsam, the rate of jetsam concentration due to the segregation mechanism is represented by a non-linear concentration gradient.

6.2.1 The Governing Equations for Segregation

The governing equations for mixing and segregation are derived by considering an equilibrium balance of material for the control volume shown in Figure 6.3. Firstly, particles drift into the control volume by convection as a result of the bulk velocity in the active layer. The rate of jetsam dispersion in and out of the control volume may be represented, respectively, as $AuC_{J(x,y)}$ and $AuC_{J(x+dx,y)}$, where A is the area normal to the bulk flow, and u is the bulk velocity. The rate of diffusional mixing is proportional to the concentration gradient and the effect of this component in the x-wise direction of the active layer may be neglected relative to the large advection term. The rate of diffusion-like mixing at each x-position in the active layer is therefore given as $-\bar{r}(\partial C_J/\partial y)$, where \bar{r} is the proportionality constant equal to the product of the diffusion coefficient and the participating area in the control volume, i.e. $D_y A [m^2/s] [m^2]$. The rate of segregation for

jetsam particles is given by a non-linear quantity, $\bar{k}C_J(1 - C_J)$, where \bar{k} is the product of the area and the percolation velocity, i.e., $A v_p [m^3/s]$. By employing the Taylor series expansion the rates of jetsam outflow from the control volume may be expressed as:

(i) Bulk Flow;

$$Au(y)C_{J_{l_x+dx}} = Au(y) \left[C_{J_{l_x}} + \frac{\partial}{\partial x}(C_J)dx + \frac{\partial^2}{\partial x^2}(C_J)dx^2 + \dots \right] \quad (6.3)$$

(ii) Diffusion;

$$-r \frac{\partial C_J}{\partial y} \Big|_{l_y-dy,x} = -r \left[\frac{\partial C_J}{\partial y} \Big|_{l_y,x} - \frac{\partial}{\partial y} \left(\frac{\partial C_J}{\partial y} \right) dy + \dots \right] \quad (6.4)$$

(iii) Segregation;

$$\bar{k}C_{J_{l_y+dy,x}} [1 - C_{J_{l_y,x}}] = \bar{k} [1 - C_{J_{l_y,x}}] \left[C_{J_{l_y,x}} + \frac{\partial}{\partial y}(C_J)dy + \dots \right] \quad (6.5a)$$

$$\bar{k}C_{J_{l_y,x}} [1 - C_{J_{l_y-dy,x}}] = \bar{k}C_{J_{l_y,x}} \left[1 - \left\{ C_{J_{l_y,x}} - \frac{\partial}{\partial y}(C_J)dy + \dots \right\} \right] \quad (6.5b)$$

By expanding the terms given in Eqs. 6.3 through 6.5 and substituting the rate of jetsam inflow of particles for the control volume, the net change of jetsam concentrations becomes;

$$D_y \frac{\partial^2 C_J}{\partial y^2} dx dy dz + v_p (1 - 2C_J) \frac{\partial C_J}{\partial y} dx dy dz = u(y) \frac{\partial C_J}{\partial x} dx dy dz \quad (6.6)$$

and the differential equation describing the movement of jetsam concentration in the active layer may be written as;

$$D_y \frac{\partial^2 C_J}{\partial y^2} + v_p (1 - 2C_J) \frac{\partial C_J}{\partial y} - u(y) \frac{\partial C_J}{\partial x} = 0 \quad (6.7)$$

In arriving at Eq. 6.7, the boundary layer condition whereby $u_x \gg u_y$ has been imposed; the y-component of the species convection term has been ignored and thus the vertical movement of jetsam occurs only by percolation or diffusion.

The diffusion flux in the active layer occurs as a result of particle collision in the continuously shearing active layer. The diffusion coefficient and the bulk velocity are determined by the flow model detailed in Chapter 5. D_y is the kinetic diffusivity which had been computed from the granular temperature as (Savage, 1993);

$$D_y = \frac{d_p \sqrt{\pi \tilde{T}}}{8(e_p + 1) v g_o(v)} \quad (6.8)$$

As well, $u(y)$ is the velocity profile for the active layer which is obtained from the flow model described in Chapter 5. At this point the percolation velocity is the only remaining unknown component required for the solution of the segregation problem. In order to determine this velocity, the model developed by Savage (1988) for segregation in inclined chute flow was adapted. The model considers the probability for formation of a void in an underlying layer with a size sufficient to capture the smaller particles within the overlying layer. The net percolation velocity for the smaller particles in the neighborhood was determined by Savage (1988) to be

$$v_p = d_{ps} \left(\frac{du}{dy} \right) \frac{1}{(1 + \eta \sigma^3)} (v_{ps} - v_{pL}) \quad (6.9)$$

with the percolation velocities for smaller (jetsam), v_{ps} , and larger (flotsam) particles, v_{pL} , being given by the following equations:

$$v_{ps} = d_{pL} \left(\frac{du}{dy} \right) G(\bar{\eta}, \bar{\sigma}) \left[\bar{E} - E_m + 1 + \frac{(1 + \bar{\eta})\bar{\sigma}}{(1 + \bar{\eta}\bar{\sigma})} \right] \exp \left[\frac{(1 + \bar{\eta})\bar{\sigma}/(1 + \bar{\eta}) - E_m}{\bar{E} - E_m} \right] \quad (6.10)$$

$$v_{pL} = d_{pL} \left(\frac{du}{dy} \right) G(\bar{\eta}, \bar{\sigma}) \left[\bar{E} - E_m + 1 + \frac{(1 + \bar{\eta})}{(1 + \bar{\eta}\bar{\sigma})} \right] \exp \left[-\frac{(1 + \bar{\eta})/(1 + \bar{\eta}) - E_m}{\bar{E} - E_m} \right] \quad (6.11)$$

The function $G(\bar{\eta}, \bar{\sigma})$, in Eqs. 6.10 and 6.11, relates the packing of particles around a void to particle size ratio $\bar{\sigma}$, and particle number ratio $\bar{\eta}$, and is given by the expression;

$$G(\bar{\eta}, \bar{\sigma}) = \frac{4k_{LT}^2(M/N)(1 + \bar{\eta}\bar{\sigma})}{\pi(1 + \bar{\eta}) \{ (1 + \bar{\eta})[1 + \bar{\eta}\bar{\sigma}^2]/(1 + \bar{\eta}\bar{\sigma})^2 + (\bar{E}^2)/(k_{AV})(M/N) \}} \quad (6.12)$$

where \bar{E} is the mean void diameter ratio and E_m is the minimum possible void diameter ratio when spontaneous percolation occurs. M is the total number of voids in the neighborhood, N is the total number of particles in the same region, and k_{AV} is the ratio of the mean voids sphere projected area to the mean projected total area. All the terminology in the forgoing equations is consistent with that of Savage (1988). The parameters M/N , E_m , and k_{AV} are constants which depend on particle packing, and for which appropriate values can be chosen for the particle assembly. For example, for the closest packing of spherical particles these values are $M/N = 2$, $E_m = 0.1547$, and $k_{AV} = 0.466$ while for a simple cubic array they are, respectively, 1.0, 0.414, and 0.63 (Savage, 1988). The parameter k_{LT} in Eq. 6.12 depends on the geometry of the grid chosen for the control volume and is defined as $\delta y = k_{LT}\bar{D}$ (see, e.g., Savage, 1988), which is the mean particle diameter in the neighborhood. The number of particles per unit area i.e., the number density, is computed as a function of the voids area ratio, e_A , as;

$$N_p = \frac{(1 + \bar{\eta})}{A_s(1 + e_A)(1 + \bar{\eta}\bar{\sigma}^2)} \quad (6.13)$$

In the application of such a model to the rotary kiln, it must be pointed out that, as a result of jetsam segregation, the values for M/N , E_m , and k_{AV} are susceptible to changes because of rearrangement of the particle ensemble. Nevertheless, it is possible to alter these constants dynamically with respect to both time and space (e.g. for each kiln revolution or material turn over in the cross section). With the altered values of the constants the solid fraction for the segregated core may be computed with the following relationship (Savage, 1988);

$$v = \frac{2(1 + \bar{\eta})(1 + \bar{\eta}\bar{\sigma}^3)}{3k_{LT}(1 + e_A)(1 + \bar{\eta}\bar{\sigma}^2)(1 + \bar{\eta}\bar{\sigma})} \quad (6.14)$$

It should be recalled that, although a constant value of the solids concentration had been employed in the granular flow model, Eq. 6.14 provides a means of determining changes in void fraction due to segregation.

6.2.2 Boundary Conditions

The calculation domain for jetsam segregation and the percolation process is shown in Figure 6.1. Owing to kiln rotation, an initially well mixed binary mixture will follow a specific path in the plug flow region until it crosses the yield line into the active layer. For the active layer, material enters from the plug flow region with a given jetsam concentration and then travels down the incline plane in a streaming flow. During this journey, jetsam particles sink when the voids in the underlying layer are large enough for the particles to percolate. If this does not occur they will pass the yield line again and recirculate. The plug flow region serves only as an 'escalator' and within this region particles do not mix or percolate unless small enough to undergo spontaneous percolation; a condition which is precluded from the model. The percolation process in the active layer is repeated for each material turn over, and as the jetsam content in the core increases, fines will no longer be visible at the exposed bed surface. Henein (1980) had observed that the only time fine particles are observed at the top of the bed is when the vessel is loaded with 40-50% fines. The boundary conditions for Eq. 6.7 will, therefore, depend on the operation of the kiln. For a dilute mixture of jetsam particles, for example, the boundary conditions will be as follows;

$$@ \quad x = 0 \quad C_J = C_{J0} \quad (6.15a)$$

$$@ \quad y = 0 \quad C_J = 0 \quad (6.15b)$$

$$@ \quad y = \delta_x \quad C_J(1 - C_J) = 0 \quad (6.15c)$$

where C_{j0} is the influx of jetsam particles at the apex (bed/wall boundary). Condition (b) indicates that, at the free surface, there are no jetsam particles as all the fines in such a dilute mixture will percolate to the core region, whereas condition (c) is the result of the non-linear concentration term which will render pure jetsam ($C_j = 1$) at any boundary where particles are finally settled (see, e.g., Gibilaro and Rowe, 1974). It is assumed that this latter boundary condition can be applied at the interface between the active layer and the plug flow region, thus rendering the yield line impermeable to flotsam/jetsam percolation. Nevertheless, the percolation process described above allows particles at the interface to be replaced by those 'escalated' by the plug flow and, as a result, the most appropriate boundary condition for the interface will be

$$\frac{\partial C_j(x, \delta_x)}{\partial y} = 0 \quad (6.15d)$$

and this was adopted in the model.

6.2.3 Solution of the Segregation Equation

The basic expression describing segregation, Eq. 6.7, with the appropriate boundary conditions, can be solved when the bulk velocity, the percolation velocity, and the diffusion coefficients are all determined *a priori*. The solution of the differential equation can be achieved by considering the problem in terms of several particular cases.

(i) *Strongly Segregating System (Case I)*. For a strongly segregated binary mixture of different size particles the diffusion of jetsam particles in the vertical plane can be ignored. This situation will pertain to a very dilute mixture where $\bar{\eta} \rightarrow 0$ and from Eq. 6.2, although the gradient does not go to zero, infers that $C_j \rightarrow 0$. The differential equation for segregation thus becomes;

$$v_p \frac{\partial C_j}{\partial y} - u_x(y) \frac{\partial C_j}{\partial x} = 0 \quad (6.16)$$

with boundary conditions given in Eq. 6.15. It can be pointed out that Eq. 6.16 is the same as that employed to describe segregation in chute flows and can be solved analytically by the method of characteristics (see, e.g., Bridgwater, 1985; Savage, 1988). The characteristic solution would normally involve choosing a characteristic value, s say, such that

$$\frac{dy}{ds} = v_p \quad (6.16a)$$

$$\frac{dx}{ds} = -u(y) \quad (6.16b)$$

Substituting Eq. 6.16(b) into 6.16(a) gives

$$-u(y)dy = v_p dx \quad (6.16c)$$

Recalling that the velocity profile for bulk flow in the active layer was given in the flow model by the parabolic equation;

$$\frac{u(y)}{u_\delta} = \kappa + a_1' \left(\frac{y}{\delta} \right) - a_2' \left(\frac{y}{\delta} \right)^2$$

this result can be substituted into Eq. 6.16(c) which, after integration, gives

$$\kappa y + a_1' \frac{y^2}{\delta} - a_2' \frac{y^3}{\delta^2} = -v_p x + B_1 \quad (6.16d)$$

if the integration constant, B_1 , is set to zero, the result is given as;

$$\kappa y + \frac{a_1'}{\delta} y^2 - \frac{a_2'}{\delta^2} y^3 + v_p x = 0 \quad (6.16e)$$

The solution of Eq. 6.16(e) at various x positions will yield the characteristic lines for equal jetsam concentration in the active layer.

(ii) *Radial Mixing (Case II)*. When the system contains mono-sized particles (i.e., particles are identified only by color differences) of uniform density, the percolation term in the differential equation can be ignored and the problem reduces to that of diffusional mixing with drift. In this case, $C_J = C$ (color) and the resulting differential equation may be given by;

$$D_y \frac{\partial^2 C}{\partial y^2} - u_x(y) \frac{\partial C}{\partial x} = 0 \quad (6.17)$$

which is the linear diffusion problem of Graetz (see, e.g., Arpaci, 1966). Analytical solutions to Eq. 6.17 exist for several boundary conditions. By employing the boundary condition discussed above, i.e.,

$$\begin{aligned} C(0, y) &= C_{J0} \\ \frac{\partial C(x, \delta_x)}{\partial y} &= 0 \\ C(x, 0) &= 0 \end{aligned}$$

the solution for the diffusional mixing may be given as (Arpaci, 1966);

$$\frac{C(x, y)}{C_{J0}} = \frac{2}{\delta_x} \sum_{n=0}^{\infty} \frac{(-1)^n}{\lambda_n} \exp[-\lambda_n^2 x / 2s] \cos \lambda_n y$$

where $s = u/2D$ and

$$\lambda_n = \frac{(2n+1)\pi}{2\delta_x}, \quad n = 0, 1, 2, \dots,$$

(iii) *Mixing and Segregation (Case III)*. This is the complete solution to the mixing and segregation problem and it describes the movement of jetsam particles by the mechanism of mixing as well as segregation. The differential equation, as was given earlier, is;

$$D_y \frac{\partial^2 C_J}{\partial y^2} + v_p(1 - 2C_J) \frac{\partial C_J}{\partial y} - u(y) \frac{\partial C_J}{\partial x} = 0 \quad (6.18)$$

Although Eq. 6.18 is non-linear, solutions can be found by functional transformation (see, e.g. Ames, 1965). Analytical methods leading to the solution of the equation are given in Appendix A8. The concentration of jetsam particles in the active layer is given by this solution as;

$$C_j(x, y) = \frac{1}{2} \left[1 - 2 \frac{D_y}{v_p} \frac{\partial}{\partial y} (\ln \tilde{Q}) \right] \quad (6.19)$$

where \tilde{Q} represents the solution for the special case given above for diffusional mixing (Case II).

6.2.4 Numerical Solution of the Governing Equations

In solving the governing equations by analytical methods advantage may be taken of the symmetry of the problem as was employed in the flow model earlier in Chapter 5. Although the analytical methods suggested provide one avenue of approach to the problem, factors such as geometry preclude their ultimate exploitation for various reasons e.g., a recirculation term is required to furnish jetsam particles from the plug flow region into the active layer as was shown in Figure 6.1. Therefore, in the present work, the derivative terms in the governing equations were replaced by finite difference approximations and the resulting algebraic equations solved numerically. The discretized equations employed are as follows (see, e.g., Anderson, *et al.* 1984):

(i) Eq. 6.16:

$$C_{i,j} = \frac{1}{[v_p/\Delta y_j + u_{i-1,j}/\Delta x]} \left\{ \frac{v_p}{\Delta y_j} C_{i,j-1} + \frac{u_{i-1,j}}{\Delta x} C_{i-1,j} \right\} \quad (6.20)$$

(ii) Eq. 6.17:

$$\begin{aligned}
& - \left\{ \frac{2D_i}{[\Delta y_{j-1} + \Delta y_{j+1}] \Delta y_{j-1}} \frac{1}{\Delta y_{j-1}} + \frac{2D_i}{[\Delta y_{j-1} + \Delta y_{j+1}] \Delta y_{j+1}} \frac{1}{\Delta y_{j+1}} + \frac{u_{i,j}}{\Delta x} \right\} C_{i,j} \\
& + \left\{ \frac{2D_i}{[\Delta y_{j-1} + \Delta y_{j+1}] \Delta y_{j-1}} \frac{1}{\Delta y_{j-1}} \right\} C_{i,j-1} + \left\{ \frac{2D_i}{[\Delta y_{j-1} + \Delta y_{j+1}] \Delta y_{j+1}} \frac{1}{\Delta y_{j+1}} \right\} C_{i,j+1} \\
& = - \frac{u_{i,j}}{\Delta x} C_{i+1,j}
\end{aligned} \tag{6.21}$$

(iii) Eq. 6.18 is solved numerically either by linearizing the non-linear term and discretizing the resulting equation or by discretizing Eq. 6.19 as an extension of the mixing problem. In the former case, the resulting equation is;

$$C_{i,j} = \frac{1}{[2A_1 + A_2 + A_3]} \{A_1 C_{i,j+1} + A_1 C_{i,j-1} + A_3 C_{i,j-1} + A_2 C_{i-1,j} - dC^2 dy\} \tag{6.22}$$

where,

$$\begin{aligned}
A_1 &= D_i / \Delta y_j \\
A_2 &= u_{i,j} / \Delta x \\
A_3 &= v_{i,j} / \Delta y_j
\end{aligned}$$

The non-linear term, $\partial C^2 / \partial y$, is discretized as;

$$\begin{aligned}
\frac{\partial C^2}{\partial y} &= \frac{[C_{i,j} + C_{i,j-1}]^2 - [C_{i,j+1} + C_{i,j}]^2}{4\Delta y_j} \\
&+ \frac{\gamma |C_{i,j} + C_{i,j-1}| (C_{i,j} - C_{i,j-1}) - \gamma |C_{i,j+1} + C_{i,j}| (C_{i,j+1} - C_{i,j})}{4\Delta y_j}
\end{aligned} \tag{6.23}$$

As in the case of fluid flow, Eq. 6.22 requires the appropriate upwinding and as a result Eq. 6.23 represents upstream donor cell differencing whereby $\gamma = 1$ gives a full upstream effect. For $\gamma = 0$, the equation becomes numerically unstable (see, e.g., Anderson *et al.*, 1984).

It might be noted in the preceding development that Eq. 6.20 is an explicit algebraic formulation because of the parabolic nature of the differential equation. Thus, once the mixture concentration at the apex is given, the jetsam concentration along the chord length can be computed by marching down the incline. Eq. 6.21 is the algebraic form of a one-dimensional diffusion/convection equation (Graetz problem) and may be solved numerically using the Tri-diagonal Method Algorithm (TDMA) (see, e.g., Anderson, *et al.*, 1984). Eq. 6.22 is an implicit algebraic equation for the calculation of two-dimensional jetsam concentration in the cross-section; it may be solved by an iterative procedure for example the Gauss Siedel method, whereby the non-linear term, which is expressed by Eq. 6.23, is computed using previous values of $C_{i,j}$. In all the scenarios, a solution technique is employed whereby a set of calculations is carried out by marching from the apex to the base. The solution of this set of calculation represents the concentration of jetsam particles for a single pass or material turn over in the cross section. Because there is no diffusion in the plug flow region particles are allowed to drift (or recirculate) from the lower section of the plug flow/active layer interface to the upper section interface. The second set of calculations for the next pass is initiated with the convected concentration as initial condition (boundary condition). The calculation is repeated until the overall jetsam concentration in the cross section equals the jetsam loading. Because the bed material circulates for about 3 or 4 times per each kiln revolution, this approach allows for the estimation of the number of revolutions required to accomplish complete mixing or complete segregation. The solution method, therefore, represents a pseudo-transient solution in a two-dimensional plane.

6.3 Validation of the Segregation Model

As was said earlier in the chapter, the objective of the segregation model was to determine the extent and dimensions of the segregated core and, as a result, estimate the jetsam concentration gradient. Because the mixing and segregation experiments carried out in the current work were qualitative only, validation of the model was carried out against the experimental data of Henein (1980). In this work, a 40 cm I.D drum loaded with a prescribed jetsam concentration was rotated

for some desired number of times and then stopped. The bed was then sectioned using discs which were inserted normal to the drum axis. In each section fines concentrations were measured beginning from the apex to the base by sieving and weighing, or by simply counting, thereby mapping out a one-dimensional representation of jetsam concentration as a function of chord length. In order to convert the two-dimensional model result developed in the present work into the one-dimensional representation in Henein's experiment, the jetsam concentration for all radial nodes at each x-location was averaged using the formula

$$C_{J_{x,av}} = \frac{\sum_{j=1}^{jmax} C_{J_{i,j}} A_{i,j}}{\sum_{j=1}^{jmax} A_{i,j}} \quad (6.24)$$

Figures 6.4 through 6.7 show the predicted and measured radial segregation patterns determined for the case of a strongly segregated system (Case I above). It can be said that the predictions show good agreement with measured results despite the differences in the loading. It is worth pointing out that measurements in Figures 6.4 and 6.5 were taken from different axial locations of the same experimental run, hence although initial jetsam loading in the entire drum is the same, jetsam loading in each axial section (between discs) are different because of axial movement. The model predictions are based on relatively low values of the jetsam loading reported for the sections and justified the case scenario of a strongly segregated system (Case I). It might also be noted that the ratio of the fine particle diameter to the coarse particle diameter used in the experiment was about 0.125 which is below the threshold mark at which spontaneous percolation could occur. The experimental results suggest that fines must have sifted through the matrix of the plug flow region down to the kiln wall as evidenced by the small but non-zero jetsam concentration reported at the apex. Since the model precludes spontaneous percolation, the boundary conditions for the analytical solution require that jetsam concentration at the apex be zero. Therefore, the differences between measured and predicted results are partly attributed to spontaneous percolation.

6.3.1 Application of Segregation Model

One of the first applications of the segregation model was for the calculation of particle concentration profiles at mid-chord plane of a 0.41 m drum (comparable to the UBC pilot kiln facility). Because Case II is for complete mixing, no further discussion on this scenario is carried out. Solutions were developed for the remaining case scenarios (Cases I and III) described previously for segregation, and the plausibility of each situation examined. The results of these calculations are depicted in Figures 6.8 through 6.10 for the respective jetsam loadings of 20%, 30% and 50%, using polyethylene as the bed material. Notice the difference between a strongly segregated system (Case I) and combined mixing and segregation (Case III). The result shows that if diffusion is present then it will tend to spread jetsam concentration by moving fines towards the top; and when percolation ceases (Case II) the bed will be well mixed. Figure 6.10 shows that, perhaps, the boundary condition imposed at the top (i.e., $C_j = 0$) is not applicable to higher jetsam loading since the profile is forced to zero at the free surface. As was mentioned earlier, Henein (1980) had observed that fines begin to appear on top of the bed at jetsam loadings of 40%. Nonetheless, the profiles show that, for higher jetsam loading, the strongly segregated solution (Case I) is clearly no longer applicable rather; Case III must give a more reasonable result, but in order to apply it the surface boundary condition must be changed and the constraint that $C_j = 0$ must be removed.

Figures 6.11 and 6.12 show the radial profiles at mid-plane for polyethylene at various jetsam loadings for the entire bed depth with thickness, H . Notice the symmetry between the concentration gradient in the active layer and that in the plug flow region for Case I (Figure 6.11). This is the result of the 'escalator' role played by the plug flow region as was depicted in Figure 6.1. This symmetry is distorted when Case III was used (Figure 6.12) due to the effect of the diffusion term in the governing equations which tends to spread jetsam in the radial direction of the active layer (active layer mixing). The effect of kiln speed on segregation (Case I and III) is shown in Figures 6.13 and 6.14. For both cases there is very little effect of kiln speed on the

concentration profiles. This is not surprising because the model seeks a steady state solution and the result must converge to the jetsam loading. Prior to convergence, i.e. for each material turn over in the kiln which coincides with each calculation (not reported), the jetsam concentration gradients will be different and will depend on kiln speed.

Figures 6.15 and 6.16 are stacked bar chart representations of the radial segregation profiles as a function of positions and chord length for Case I and Case III respectively, for the 0.41 m I.D drum (pilot kiln) at 2 rpm, 12% fill polyethylene pellets, and three jetsam loadings (i.e., 10%, 20%, and 30%). Notice the shape of the profiles depicting the segregated core dubbed 'the tongue.' In order to show the segregated core in two-dimensional representation, contours of concentration gradients were plotted for the pilot kiln using limestone (Figures 6.17 and 6.18) and polyethylene pellets (Figures 6.19 and 6.20). As can be seen the 'tongue' is even more clearly shown in these contour plots. Figure 6.17 is the profile of concentration gradients predicted with Case I using the run conditions of Henein (1980); the same condition as predicted by Case III (i.e., allowing diffusion component) is shown in Figure 6.18. Figures 6.19 and 6.20 are similar results but run on polyethylene pellets for 20% jetsam loading using the pilot kiln at 2 rpm and 12% fill.

In order to examine the segregation patterns which are likely to occur in industrial kilns the model was run for the hypothetical 2.5 m I.D kiln employed for the granular flow model. Figure 6.21 predicts the radial concentration as a function of surface position as one moves from the apex to the base and provides a comparison between predictions at the pilot scale (where measurements were made) and industrial scale. As seen from the results, the smaller kiln tends to concentrate the fines to the center of the kiln more than the larger kiln. In other words, the distribution of jetsam in the larger kiln tends to skew more to the apex, depicting a more defined segregated tongue. The segregated tongue in the industrial size kiln is shown in the contour plots presented in Figure 6.22 for 2 and 5 rpm. The reason for the difference in jetsam distribution in

the two kilns may be attributed to the fact that, for the same degree of fill, the chord length in the industrial kiln is over five times longer than that of the pilot kiln and, as a result, most of the percolation process occurs between the apex and the mid-chord.

6.3.2 Discussion of Mixing Through Density Compensation

It is evident from the forgoing results that the bed would be 'well mixed' either when jetsam particles are not present ($C_J = 0$) or when the net percolation velocity of these fine particles is zero ($v_p = 0$). Since the former case is unrealistic, it will not be considered further. However if the latter case could be explored then practical industrial problems might be addressed. It is acknowledged that (Alonso, *et al.*, 1991) if the mixture contains some denser particles, these will percolate together with the fine particles as jetsam. Since larger particles (of same density) are flotsam, percolation may be prevented by introducing the denser materials as large particles into a mixture containing both size and density differences. Such weight compensation methods of minimizing free surface segregation have been discussed by Alonso, *et al.* (1991). The model developed in the present work is used to explore the appropriate size and density ratio which will combine to eliminate the percolation velocity in order to achieve a well mixed bed. Eq. 6.9 shows that this can only be accomplished by either setting the shear rate to zero (no shearing in the active layer) or making $v_{ps} = v_{pL}$. The only option is the latter case since the former can not be accomplished in a continuously shearing active layer. Therefore, for flotsam particles to behave as jetsam, the following condition for the flux of particles between layers must be satisfied

$$v_{pJ}\rho_J = v_{pF}\rho_F \quad (6.25)$$

Substitution of Eq. 6.10 and 6.11 into Eq. 6.25 (see Appendix A9 for details) gives the density ratios for which flotsam particles will sink as a function of the size ratio in a mixture of a dilute system. This relationship is presented in Figure 6.23 for two packing conditions, i.e., for closest packing and for a simple cubic array. As it can be seen, for a size ratio of flotsam to jetsam ranging between 1.5 and 2.0 the density ratio of the flotsam to jetsam particles at which the flotsam will

behave as jetsam would range between 7 and 8 for closest packing; it increases exponentially high at higher size ratios. This result indicates that eliminating size segregation by density compensation may not be practically feasible in most industrial operations except, perhaps, in incineration of solid waste where size and density differences are widely spread. Thus the only options in dealing with radial segregation in kilns would appear to be either removal of jetsam from the system (not practical) or take advantage of segregation. For example, as will be shown in the next Chapter, by loading low heat capacity materials as fines in order to achieve a homogeneous product. This can best be accomplished through an improved predictive capability for segregation.

6.4 Summary and Conclusions

Complete mixing of particles in the transverse plane of a rotary kiln is fundamental to the uniform heating or cooling of the charge and, ultimately, to the generation of a homogeneous product. However, differences in particle size and density result in a de-mixing process whereby smaller or denser particles segregate to form an inner core or kidney of segregated material which may never reach the bed surface to be exposed to freeboard temperatures. An analytical model has been developed which relates particle segregation rates to primary operating parameters such as kiln diameter, bed depth and rotational speed.

The model considers a binary mixture of small and large particles in the continuously shearing active region of the kiln bed. Continuum equations have been employed to describe the mixing and segregation rates in the transverse plane of the bed which result from both particle percolation and diffusional mixing. The diffusion coefficients and the convective terms for material concentration in the continuum equations have been obtained from a continuum granular flow model developed for this application. The percolation velocities are generated using existing models which relate percolation to the probability of void formation in the shear plane.

Model predictions are in good agreement with experimental results of Henein (1980); and it can be applied to predict the size and extent of the segregated core as well as to show effect of segregation on material mixing. The model has been used in establishing that elimination of size segregation by weight compensation, as described by Alonso *et al.* (1991), is possible but not practicable for industrial kilns. It may also be used to make estimation of the effective thermal conductivity of the bed.

6.5 Figures

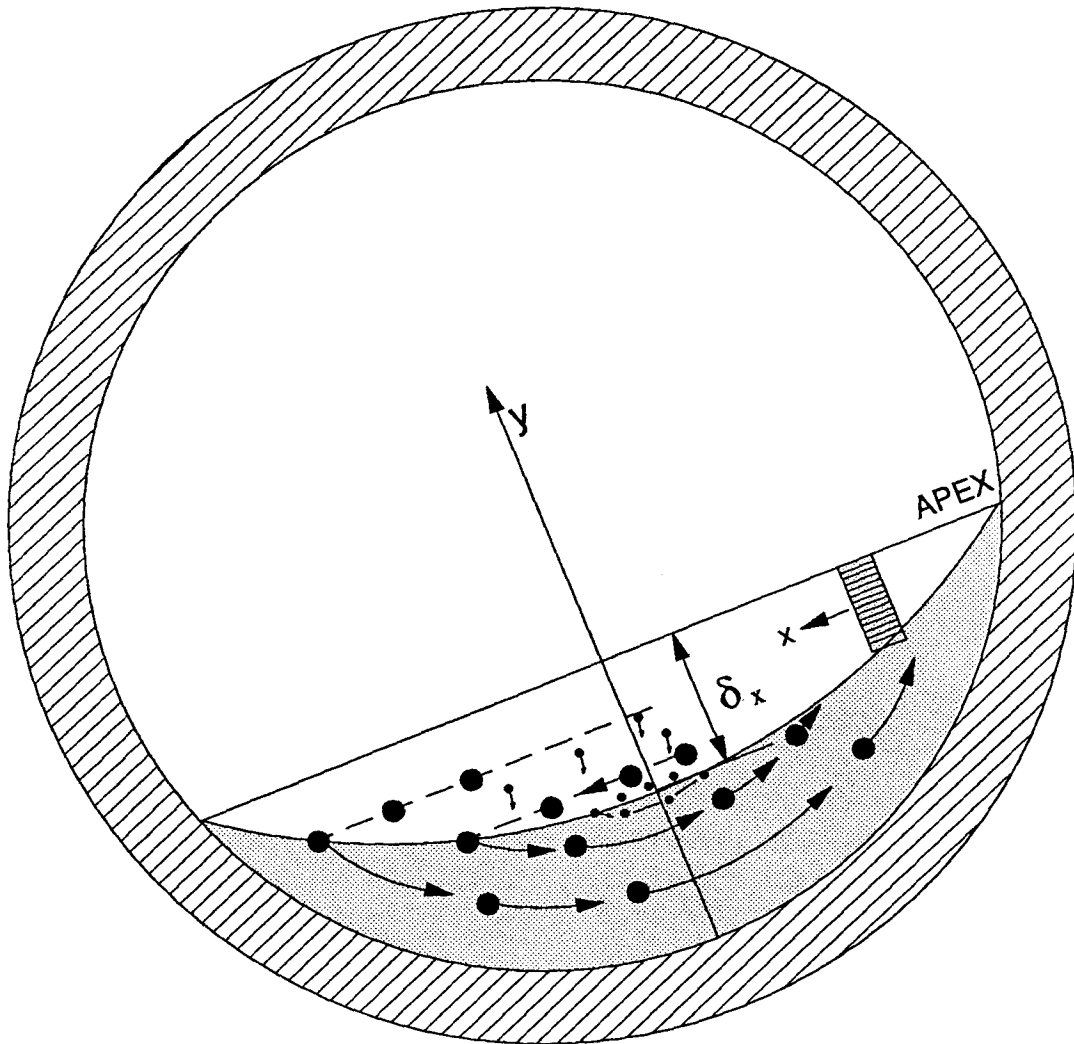


Figure 6.1. The mechanism of Percolation and the Calculation Domain for the Segregation Problem.

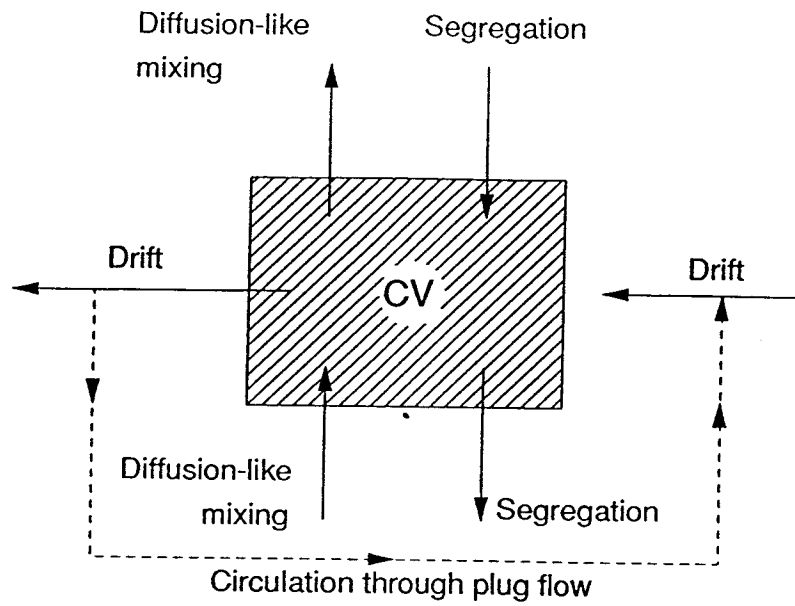


Figure 6.2. Control Volume for the Material Conservation in the Active Layer.

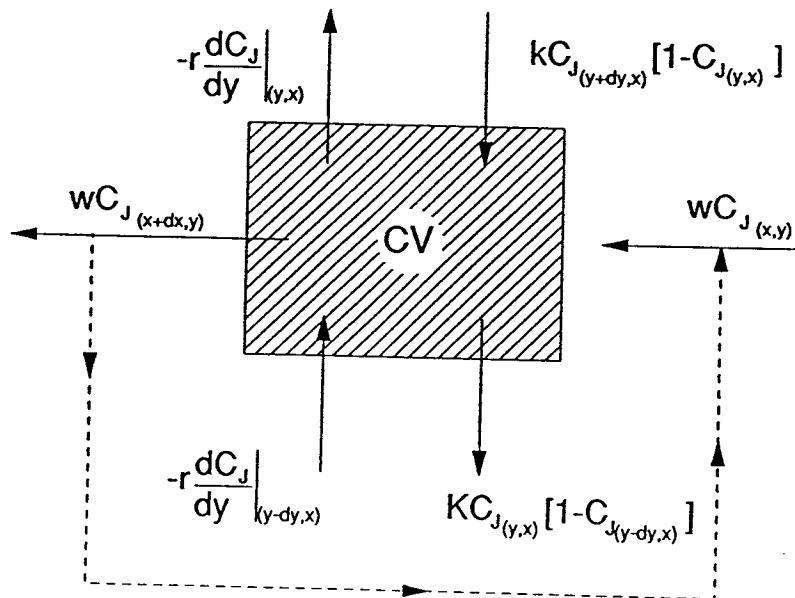


Figure 6.3. Mathematical Description for Material Balance in Control Volume; the Convective Flux, $w = Au(y)$, the Diffusion Flux, $r = D_y A$, and the Segregation Flux, $k = v_p A$.

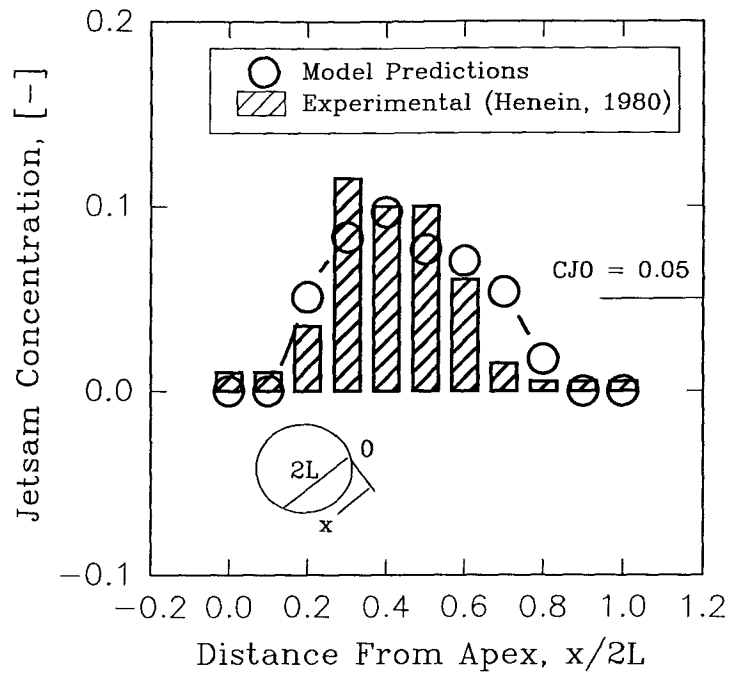


Figure 6.4. Predicted and Measured Profiles for Jetsam Concentration for a 40 cm Drum: Limestone, 3.11 rpm, 16% Fill. $d_{pF}/d_{pJ} = 8$, ($d_{pF} = 4.2mm$).

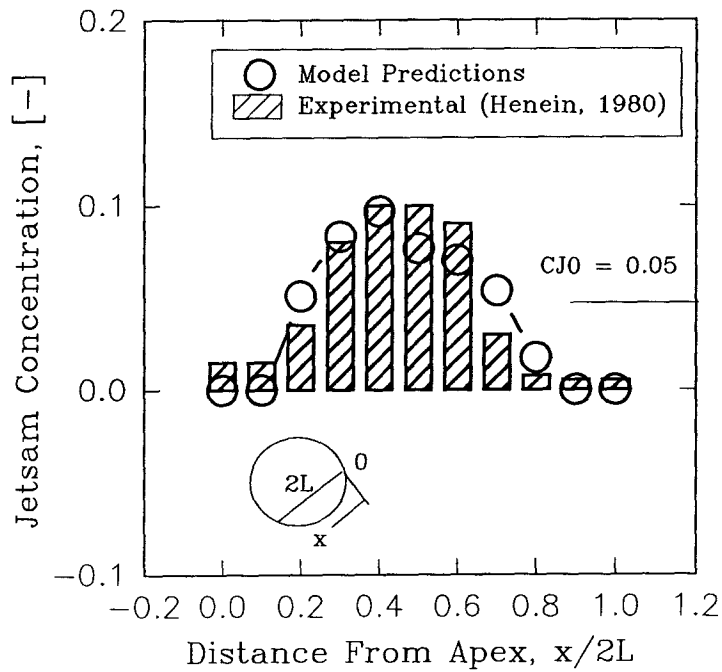


Figure 6.5. Predicted and Measured Profiles for Jetsam Concentration for a 40 cm Drum: Limestone at 3.11 rpm, 16% Fill. $d_{pF}/d_{pJ} = 8$, ($d_{pF} = 4.2mm$).

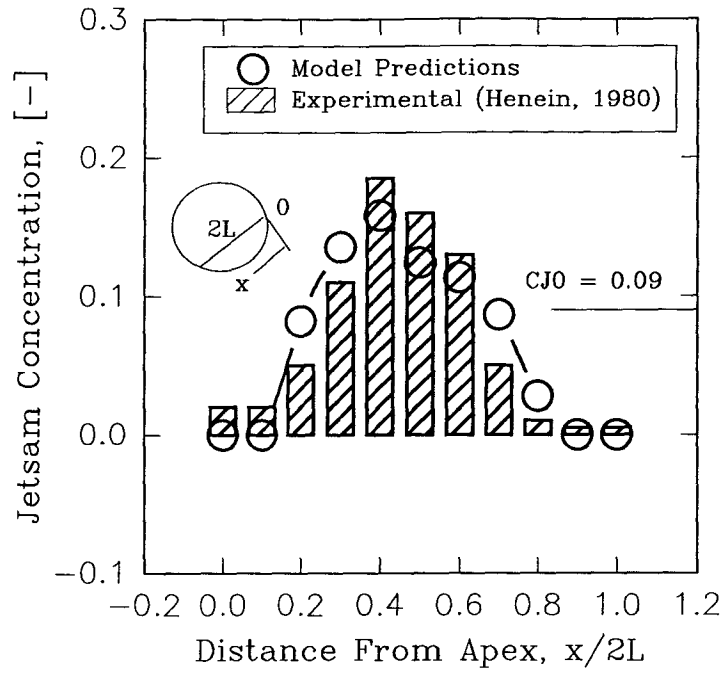


Figure 6.6. Predicted and Measured Profiles for Jetsam Concentration for a 40 cm Drum: Limestone at 3.11 rpm, 16% Fill. $d_{pF}/d_{pJ} = 8$, ($d_{pF} = 4.2mm$).

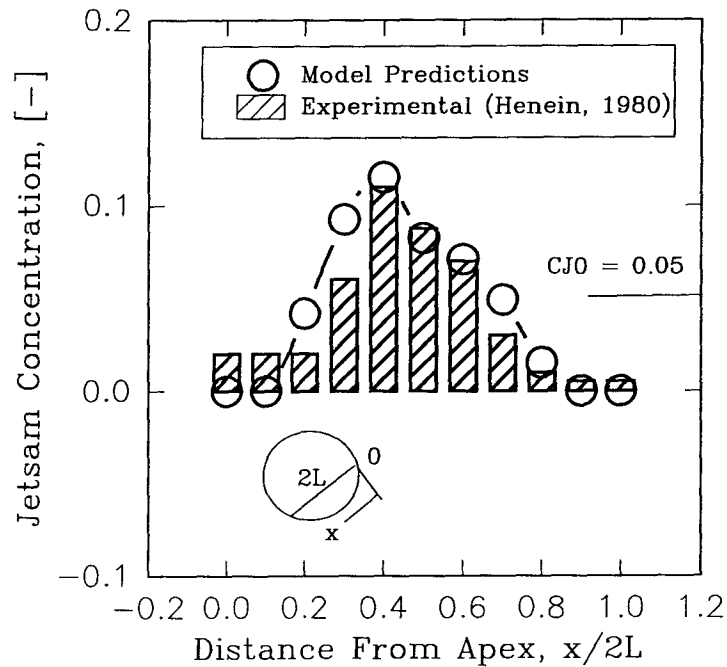


Figure 6.7. Predicted and Measured Profiles for Jetsam Concentration for a 40 cm Drum: Limestone at 3.19 rpm, 14% Fill. $d_{pF}/d_{pJ} = 8$, ($d_{pF} = 4.2mm$).

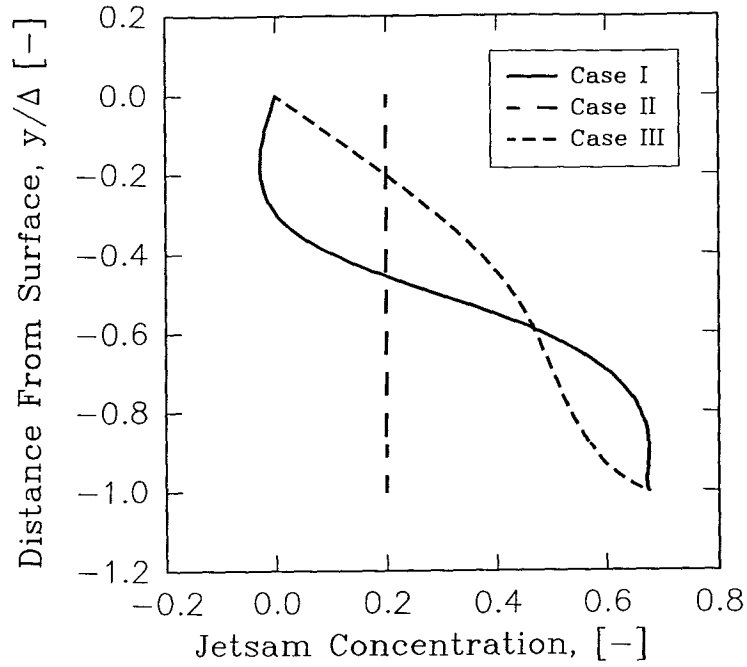


Figure 6.8. Predicted Jetsam Concentration in the Active Layer at the Mid-chord Position for the Three Cases Described in the Text: 0.41 m drum, 2 rpm, 12% Fill; Polyethylene Pellets, $CJ_0 = 0.2$, $d_{pF}/d_{pJ} = 2$.

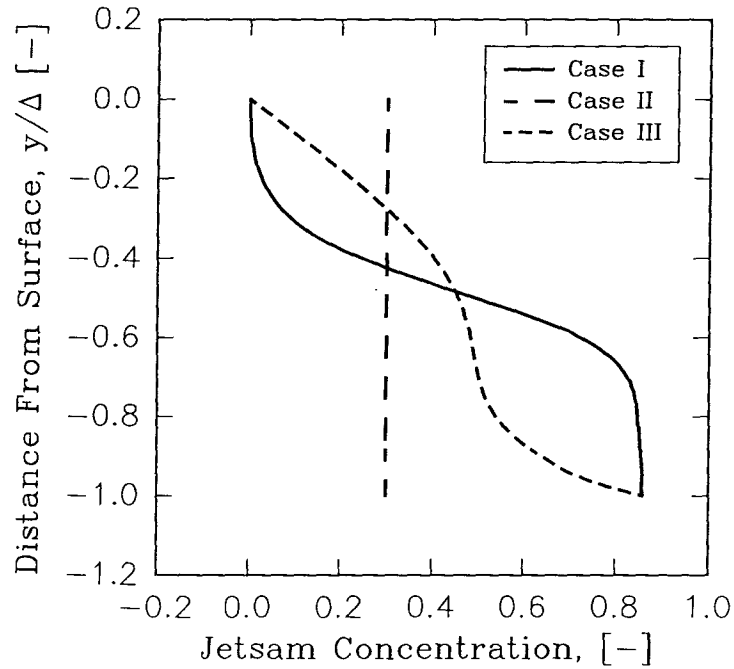


Figure 6.9. Predicted Jetsam Concentration in the Active Layer at the Mid-chord Position for the Three Cases Described in the Text: 0.41 m drum, 2 rpm, 12% Fill; Polyethylene Pellets, $CJ_0 = 0.3$, $d_{pF}/d_{pJ} = 2$.

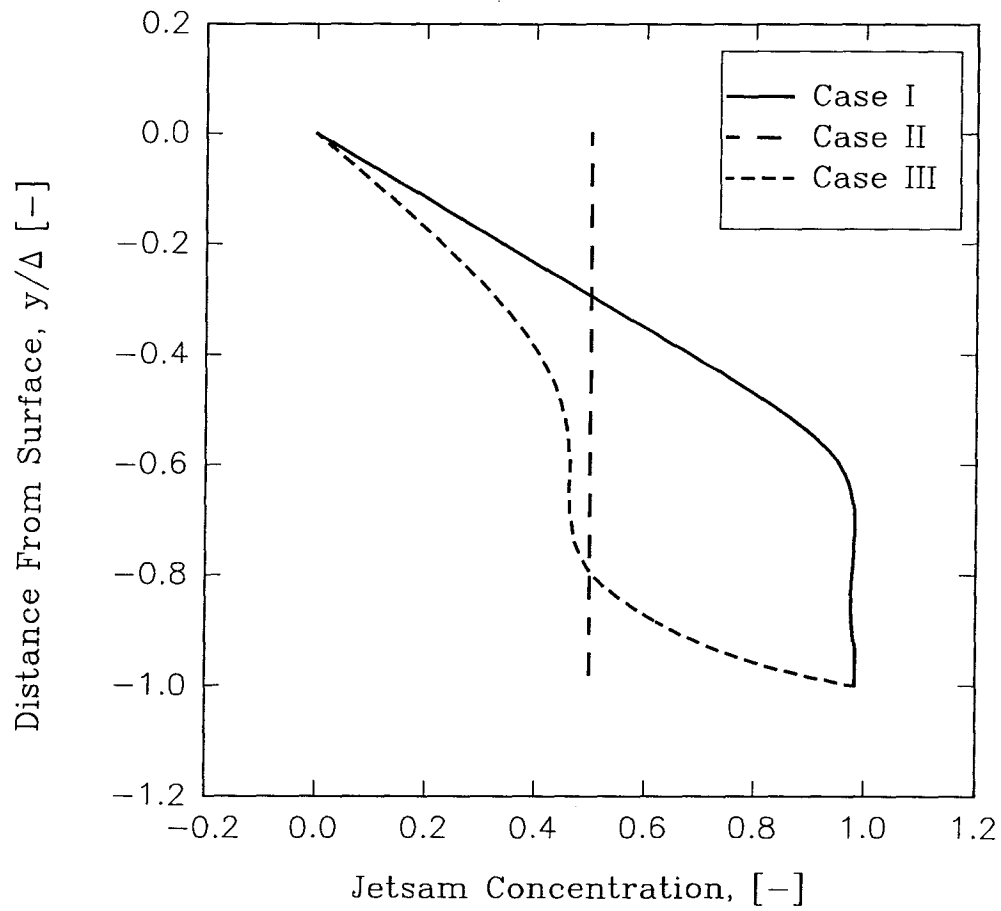


Figure 6.10. Predicted Jetsam Concentration in the Active Layer at the Mid-chord Position for the Three Cases Described in the Text: 0.41 m drum, 2 rpm, 12% Fill; Polyethylene Pellets, $CJ_0 = 0.5$, $d_{pf}/d_{pj} = 2$.

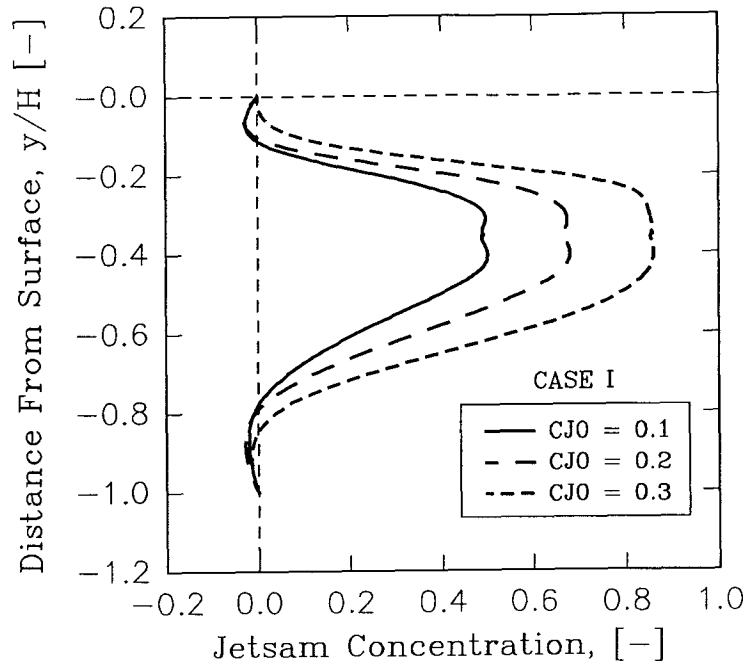


Figure 6.11. Predicted Jetsam Concentration in both Active Layer and Plug Flow Region Shown at the Mid-chord Position for Various Jetsam Loadings.

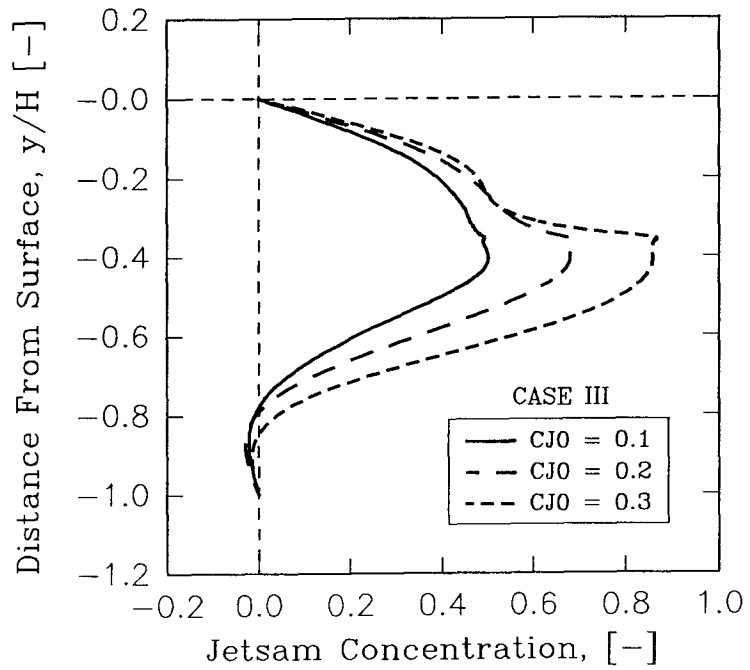


Figure 6.12. Predicted Jetsam Concentration in both Active Layer and Plug Flow Region Shown at the Mid-chord Position for Various Jetsam Loadings.

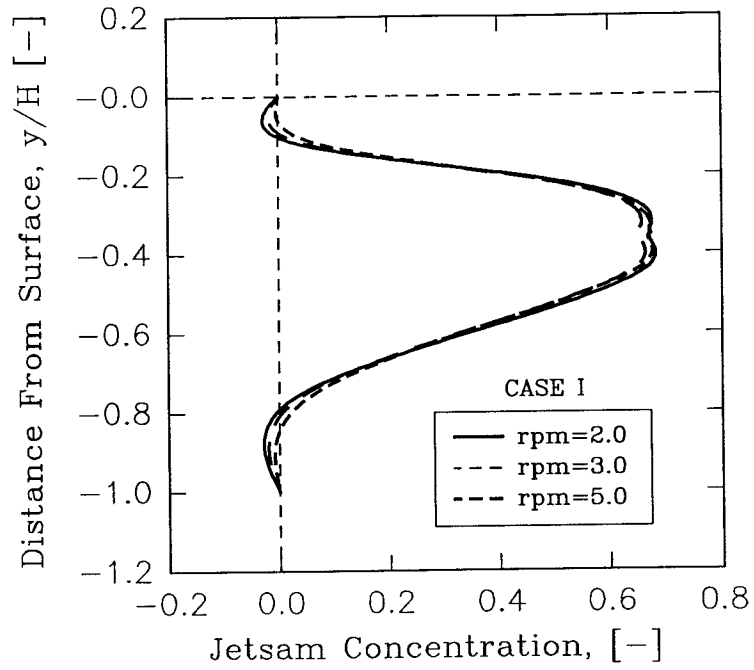


Figure 6.13. Predicted Jetsam Concentration in both Active Layer and Plug Flow Region as a Function of rpm at Mid-chord Position for Case I.

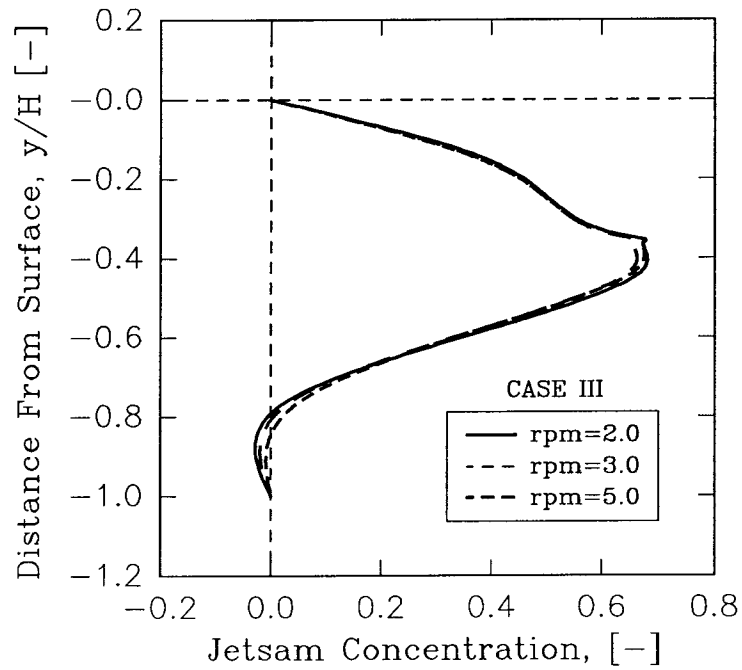


Figure 6.14. Predicted Jetsam Concentration in both Active Layer and Plug Flow Region as a Function of rpm at Mid-chord Position for Case III.

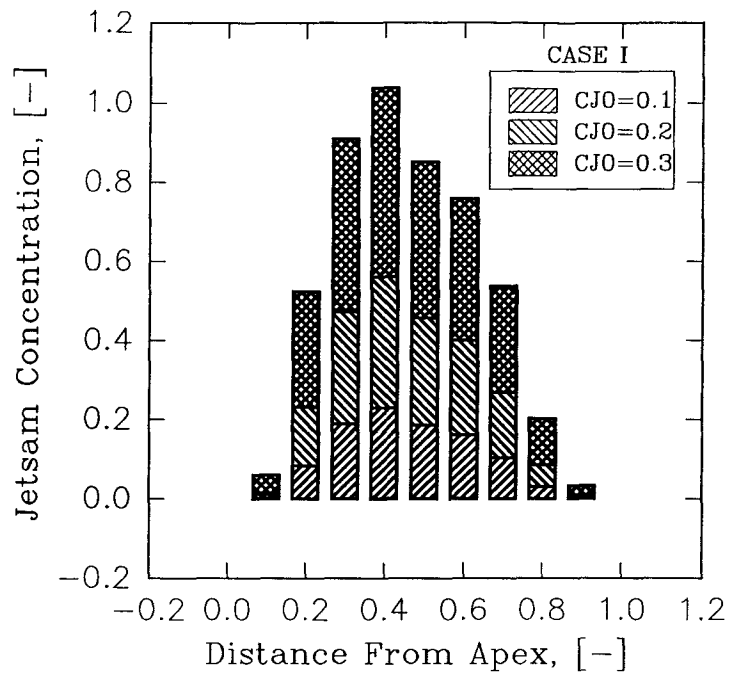


Figure 6.15. Predicted Jetsam Concentration Profile as a Function of Chord Length (Case I): 0.41 m Drum.

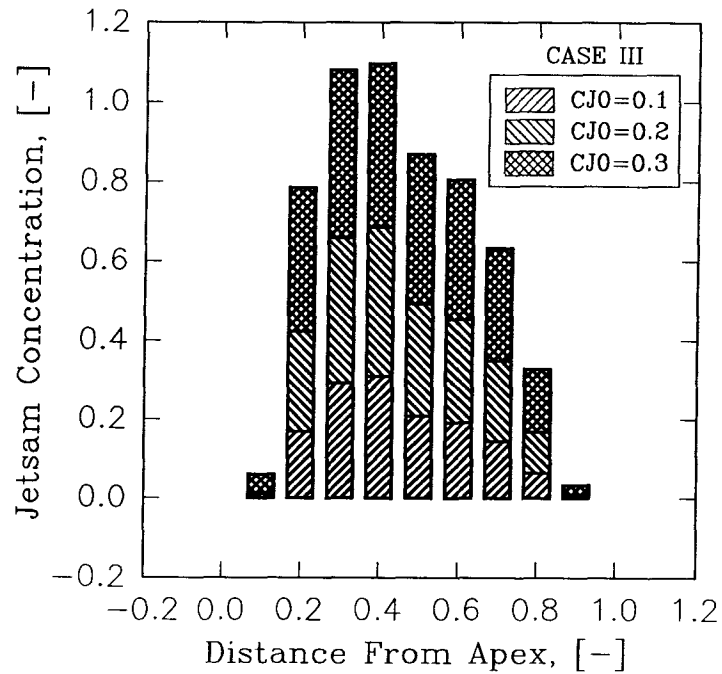


Figure 6.16. Predicted Jetsam Concentration Profile as a Function of Chord Length (Case III): 0.41 m Drum.

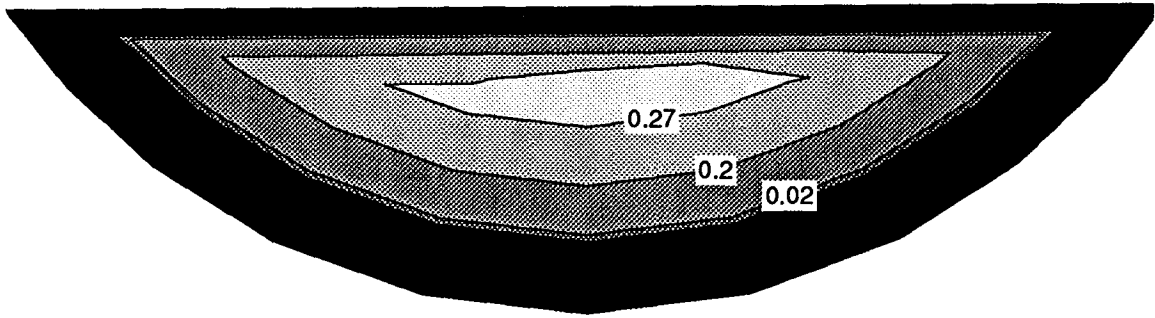


Figure 6.17. Contour Plots of Jetsam Concentration for Case I Predictions Using Operational Conditions of Henein (1980); Jetsam Loading at 9%; Limestone.

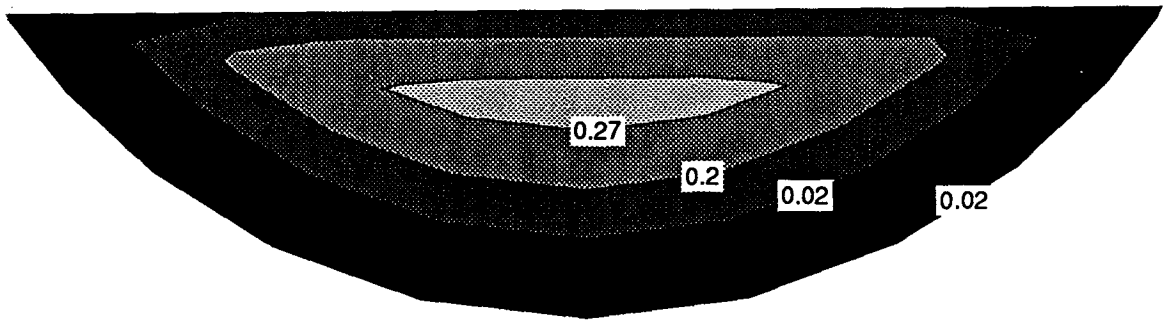


Figure 6.18. Contour Plots of Jetsam Concentration for Case III Predictions Using Operational Conditions of Henein (1980); Jetsam Loading at 9%, Limestone.

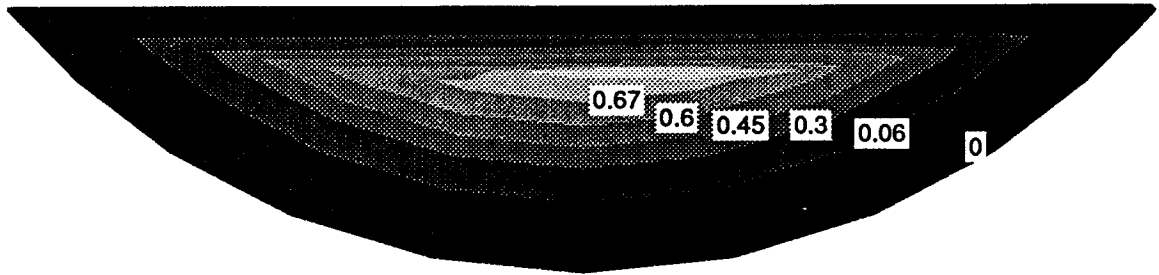


Figure 6.19. Contour Plots of Jetsam Concentration for Case I: 0.41 m Drum; 2 rpm, 12% Fill; Jetsam Loading at 20%; Polyethylene.

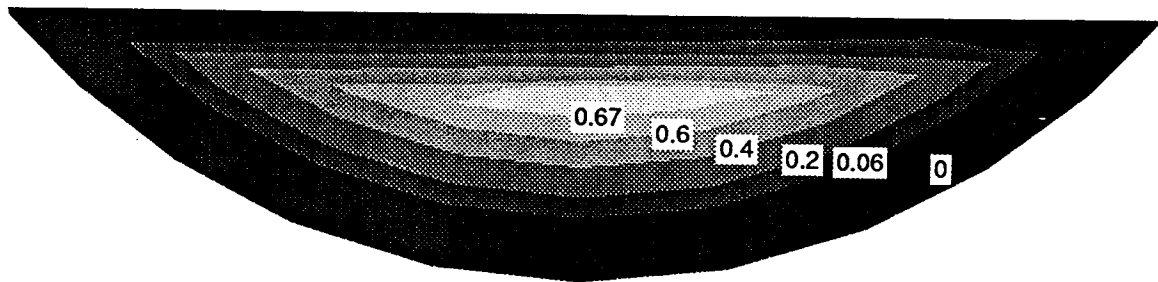


Figure 6.20. Contour Plots of Jetsam Concentration for Case III: 0.41 m Drum; 2 rpm, 12% Fill; Jetsam Loading at 20%; Polyethylene.

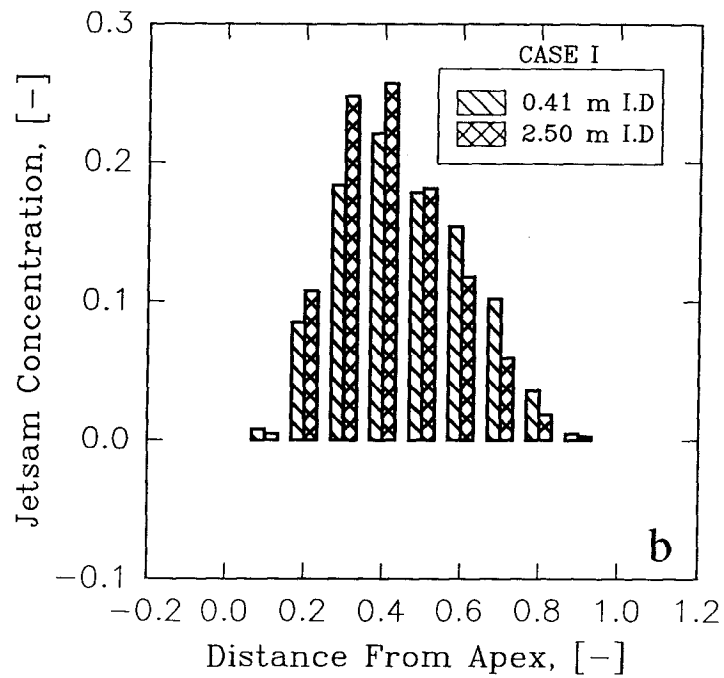
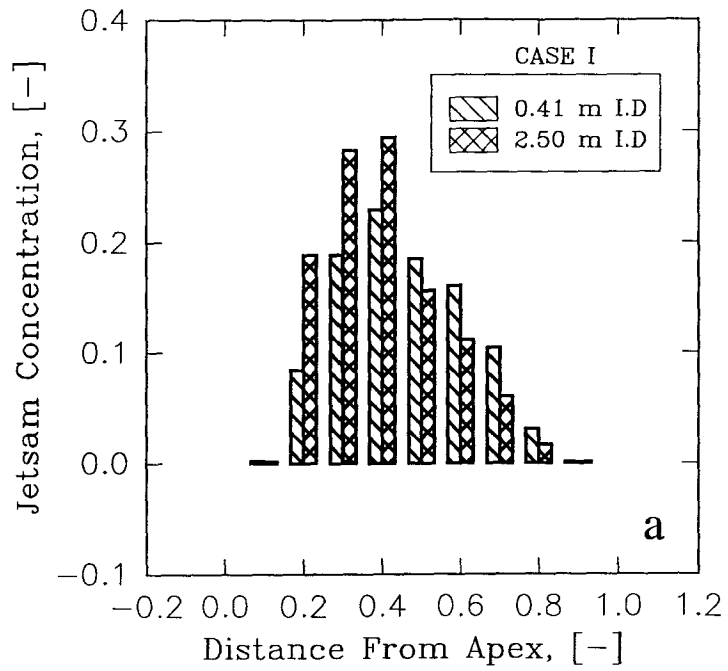
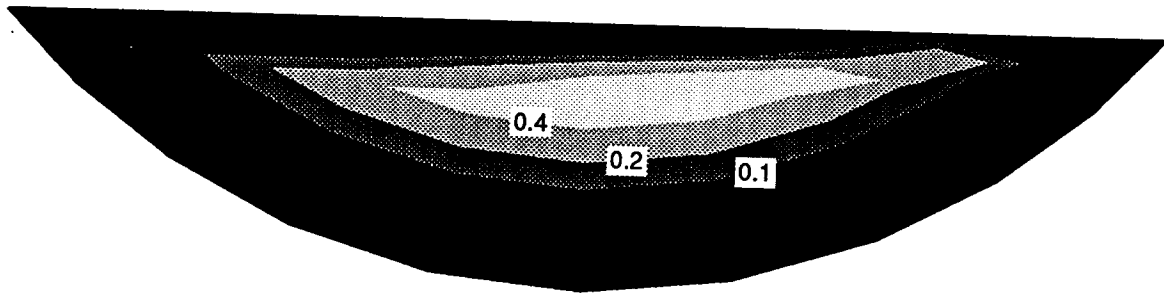
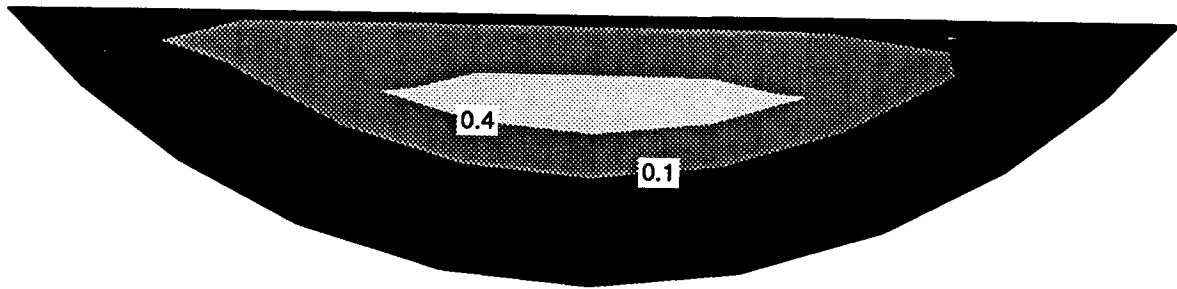


Figure 6.21. Comparison of Predictions for Jetsam Concentration in a 0.41 m Drum and a 2.5 m Drum at 12% Fill and Jetsam Loadings of 10%: (a) 2 rpm; (b) 5 rpm.



a



b

Figure 6.22. Contour Plots of Jetsam Concentration in a 2.5 m Drum at 12% Fill and Jetsam Loading of 10%: (a) 2 rpm; (b) 5 rpm.

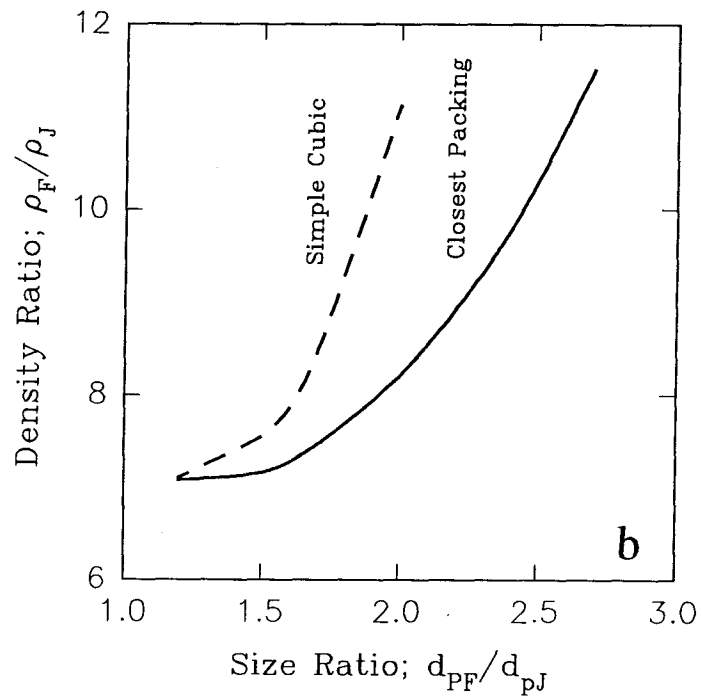
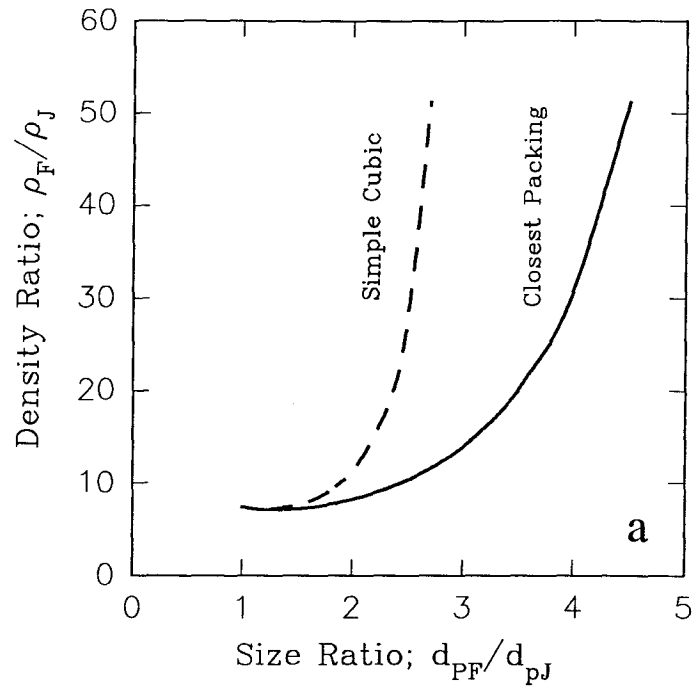


Figure 6.23. Density Compensation of Particle Size Segregation Showing Density Ratio Required for Flotsam to Behave as Jetsam in a Mixture with Specified Size Ratio: (a) Larger size Ratios; (b) Detailed at Smaller Size Ratio.

CHAPTER 7. HEAT TRANSFER PROCESSES IN ROTARY KILNS

7.1 Introduction

In the preceding chapters the flow behavior of the bed material as well as mixing and segregation within the bed have been described. From the viewpoint of rotary kiln operation these phenomena will affect heat transfer within the bed through their effect on advective energy transport. It is only natural, therefore, that having solved for the velocity and described the mixing and segregation of the bed material, the results should be applied to the modelling of heat transfer. The objective of this chapter, therefore, is to describe the development of a thermal model for a transverse section of bed material and incorporate this two-dimensional representation of the bed into a conventional one-dimensional, plug flow type thermal model for the rotary kiln. The resultant quasi-three-dimensional thermal model is used to examine the role of the various mechanisms for heat transfer within the cross-section, for example the regenerative action of the wall and the effect of the bed active layer on the redistribution of energy within the bed.

7.2 Description of the Thermal Model

The quasi-three-dimensional model developed in the current work comprises both an axial model (one-dimensional) and a cross-sectional model (two-dimensional). The former is used to independently determine the one-dimensional axial temperature profiles for the freeboard gas and the bulk bed. It is implicitly assumed that the details of the energy redistribution that occurs within the bed do not significantly influence heat transfer between the bed and the freeboard. As part of the procedure for calculating these axial temperature profiles, the surface heat flux to the bed is determined and this becomes the thermal boundary condition employed to drive the cross-sectional model. In doing so, the bed temperature gradient computed from the axial model is used as a sink term representing rate of energy removal due to the material flow in the axial direction. The one-dimensional bed temperature is also employed as a check on the mass-averaged temperature which is estimated from the bed cross-sectional model. The two-dimensional model is employed to determine the thermal condition of the bed material and the kiln wall over successive transverse

sections (or slices) of the kiln and incorporates both the flow and segregation models developed in the previous section. The interaction of the heat transfer model with other models in the global set-up for heat and mass transport calculations in the rotary kiln is depicted in Figure 7.1.

7.2.1 The One-dimensional Thermal Model Applied to the Bed and Freeboard

Various models for the rotary kiln (see, e.g., Sass, 1967; Tscheng and Watkinson, 1978; Barr *et al.*, 1989; etc.) have the capability of predicting 'average' conditions within both the bed and the freeboard as functions of axial position. The thermal component of these one-dimensional models can be derived by considering the transverse slice, shown in Figure 7.2(a), which divides the section into separate control volumes of freeboard gas and bed material. Under steady-state conditions energy conservation for any control volume requires that

$$\dot{Q}_{NET} = \sum(\dot{n}H)_{out} - \sum(\dot{n}H)_{in} \quad (7.1)$$

If conditions in the freeboard and bed are each assumed to be uniform in the transverse plane (the plug flow assumption), application of Eq. 7.1 to the control volume of freeboard gas and bed material, respectively, yields a pair of ordinary differential equations relating axial gradients of temperature and composition to the net rates of heat transfer for each control volume,

$$\dot{Q}_g = \sum_{i=1}^{N_g} \left[\dot{n}_{gi} c_{p_{gi}} \frac{dT_g}{dz} + H_i \frac{d\dot{n}_i}{dz} \right] \quad (7.2a)$$

$$\dot{Q}_b = \sum_{j=1}^{N_b} \left[\dot{n}_{bj} c_{p_{bj}} \frac{dT_b}{dz} + H_j \frac{d\dot{n}_j}{dz} \right] \quad (7.2b)$$

where N represents the total number of species in each region and T is the average or bulk temperature at that axial position.

In the absence of any chemical reaction or phase transformations these equations simplify to

$$\sum \dot{m}_g c_{p_g} \frac{dT_g}{dz} = Q_{g \rightarrow ew} + Q_{g \rightarrow eb} \quad (7.3a)$$

$$\sum \dot{m}_b c_{p_b} \frac{dT_b}{dz} = Q_{g \rightarrow eb} + Q_{ew \rightarrow eb} + Q_{cw \rightarrow cb} \quad (7.3b)$$

where the various heat transfer paths are shown in Figure 7.2(b). One additional condition which must be met is that no net energy accumulation can occur within the wall which yields an auxiliary condition

$$Q_{g \rightarrow ew} + Q_{eb \rightarrow ew} + Q_{cb \rightarrow cw} = Q_{shell} \quad (7.3c)$$

The system of equations (7.3) can be solved for successive axial positions by any of variety of techniques (e.g., Runge Kutta) provided that the various heat transfer terms are characterized in terms of the local gas, bed and wall temperatures. Thus, by starting at either end of the kiln, a complete solution of the thermal problem can be developed. It is chiefly the methodology employed in evaluating the heat transfer terms which distinguishes the various one-dimensional models.

Heat transfer at the interfacial surfaces is complex and involves radiation, convection and, at the covered bed/covered wall interface, conduction as well. Although a heat transfer coefficient can be allocated to each transport path shown in Figure 7.3 (Gorog *et al.*, 1983) this should not obscure the difficulty associated with realistic determination of values for these coefficients. As mentioned earlier, in the present work the one-dimensional model is required only to produce a framework from which to operate the two-dimensional thermal model for the bed and therefore existing models are used to evaluate heat transfer at the interfaces. In the freeboard, the model developed by Barr (1986) is utilized to develop coefficients for radiative heat transfer, i.e., $h_{r,g \rightarrow ew}$, $h_{r,g \rightarrow eb}$, $h_{r,eb \rightarrow ew}$, $h_{r,ew \rightarrow ew}$. Convection to the exposed wall and exposed bed may be calculated as per Gorog *et al.* (1983);

$$h_{c,ew} = 0.036 \frac{k_g}{D_k} Re^{0.8} Pr^{0.33} \left(\frac{D_k}{L_k} \right)^{0.055} \quad (7.4)$$

$$h_{c,eb} = 0.4 G_g^{0.62} \quad (7.5)$$

$$G_g = \frac{\dot{m}_g \times 3600}{A_g} \quad \left[\frac{kg}{m^2 \cdot hr} \right]$$

In applying these expressions the hydraulic diameter and transverse area of the freeboard must be utilized in evaluating the dimensionless grouping and mass flux terms. At the covered wall/covered bed interface Schlunder's model (Schlunder, 1984) is employed which, although perhaps inappropriately complex for the purpose of the present work, takes into account such factors as single particle heat transfer coefficient, wall-to-bed radiation, solid-to-solid heat conduction, and the continuum heat conduction through the gas gap between the bed and the wall surface.

Since there is no intent to restrict the work to non-reactive conditions in the bed and freeboard, Eq. 7.3 can be expanded to include the reactive terms, which are originally present in Eq. 7.2, to yield the system;

$$(\sum n_i c_{pi}) \frac{dT_g}{dz} = h_{ew} A_{ew} (T_g - T_w) + h_{eb} A_{eb} (T_g - T_b) + \sum \gamma_i A_g \quad (7.6a)$$

$$(\sum n_j c_{pj}) \frac{dT_b}{dz} = h_{eb} A_{eb} (T_b - T_g) + h_{cw} A_{cw} (T_b - T_w) + \sum \gamma_j A_b \quad (7.6b)$$

where T_b and T_w are the average temperature over the interfacial surfaces and γ are the production rates for various species involved in either chemical reactions, for example freeboard combustion, or phase changes (such as evaporation of free moisture) each to be determined by the appropriate kinetic expressions. Since mass must also be conserved for the control volumes of the bed and freeboard, a system of ordinary differential equations representing the mass balance also results

from these same kinetic expressions; for example the calcination reaction for limestone



generates the inter related mass balance expressions

$$\frac{d\dot{n}_{CaCO_3}}{dz} = -\frac{d\dot{n}_{CaO}}{dz} = \left(\frac{d\dot{n}_{CO_2}}{dz} \right)_{freeboard} \quad (7.8)$$

where

$$\begin{aligned} \frac{d\dot{n}_{CaCO_3}}{dz} &= \gamma_{CaCO_3} A_b \\ &= R \exp(E/RT) \end{aligned} \quad (7.9)$$

In developing the global solution for the kiln model the complete system of ordinary differential equations (i.e., the two energy balance equations, the mass balance equations, and the auxiliary energy condition for the wall) must be solved simultaneously.

7.2.2 The Two-dimensional Model Developed for the Bed

Although useful results have been obtained from one-dimensional models, the assumption that conditions will be uniform across any transverse section of the bed material will hold only for a well mixed bed. Since segregation is known to occur within the bed, a two-dimensional model provides an opportunity to examine the effects on kiln performance of 'de-mixing' within the bed. As seen earlier, segregation in the transverse plane is driven by the bed motion established by the rotation of the kiln but, since no adequate model for this motion has previously appeared, attempts to predict conditions within the bed in two or even three dimensions have been rare.

As was seen earlier, the rolling bed mode, which is preferred in most kiln operations, comprises two distinct regions i.e: the thinner active layer at the region near the surface, and the relatively thicker plug flow region near the covered wall (see, Figure 1.4 of Chapter 1). Because

of improved mixing during rolling, it is considered as the mode of operation for the thermal model. Heat transfer within the active layer occurs by conduction (diffusion) and advection (convection). Since flow within the active layer is primarily parallel to the top surface, a cartesian coordinate system was attached to this region for the heat transfer calculations. In order to simplify the analysis, the bed was assumed to consist of a single inert component and to behave as a continuum. Energy conservation for a control volume in the active layer, such as that shown in Figure 7.4(a), requires that

$$\frac{\partial}{\partial x} \left(k_{eff} \frac{\partial T}{\partial x} \right) - \rho c_p U_x \frac{\partial T}{\partial x} + \frac{\partial}{\partial y} \left(k_{eff} \frac{\partial T}{\partial y} \right) - \rho c_p U_y \frac{\partial T}{\partial y} + \dot{m}_b c_{pb} \frac{dT_{ba}}{dz} = 0 \quad (7.10)$$

It is further assumed that mixing is sufficient to ensure that, within the active layer, the temperature gradient in the axial direction of the kiln (i.e., dT_{ba}/dz in this expression) is uniform. Since transverse mixing is at least two orders of magnitude more effective than axial mixing (Barr, 1986) this latter condition appears justified. The last term in Eq. 7.10, which includes the axial gradients of temperature in the active layer, accounts for the removal of energy from the control volume by axial bed flow. It is assumed that all particles within the active layer advance axially at the same rate and that, because the plug flow region behaves as a rigid body, this axial advance occurs only within the active layer. Thus the mass flux \dot{m}_b in Eq. 7.10 is set by the kiln feed rate and the transverse area of the active layer, $\dot{m} = \dot{M}/A_{AL}$.

In contrast to the active layer, the plug flow region is relatively deep and, since it rotates as a rigid body about the kiln axis, a cylindrical coordinate system was applied in this region as well as for the wall itself. Energy conservation for any control volume in the plug flow region and the wall, such as shown in Figure 7.4(b), requires that

$$\frac{\partial}{\partial r} \left(k_{pf} \frac{\partial T}{\partial r} \right) + \frac{1}{r} \frac{\partial}{\partial \theta} \left(k_{pf} \frac{\partial T}{r \partial \theta} \right) - \rho c_{p, pf} \omega r \frac{\partial T}{r \partial \theta} = 0 \quad (7.11a)$$

$$\frac{\partial}{\partial r} \left(k_w \frac{\partial T}{\partial r} \right) + \frac{1}{r} \frac{\partial}{\partial \theta} \left(k_w \frac{\partial T}{r \partial \theta} \right) - \rho c_{p, w} \omega r \frac{\partial T}{r \partial \theta} = 0 \quad (7.11b)$$

where the first two terms constitute the radial and transverse conduction respectively, and the third term represents the movement of energy through the control volume due to the rotation of the kiln. Since the bed particles are assumed to advance axially only in the active layer, Eq. 7.11(a) does not include any term for energy transport in the axial direction, it being implicitly assumed that axial conduction in the plug flow region will be negligible.

The effective thermal conductivity was calculated by combining correlations of Diessler and Eian (1952) with an inter-particle radiation model by Schotte (1960) which was given earlier as

$$k_{be}^r = \frac{1 - e_o}{1/k_s + 1/4\sigma e d_p T^3} + e_o 4\sigma e d_p T^3 \quad \text{cf (2.28)}$$

Because of the mixing in the active layer the effective heat conductance there is greatly enhanced by the granular temperature (a measure of the velocity fluctuations) which results from inter-particle collisions. The effective thermal conductivity in the active layer is therefore modified by a factor relating the mass transfer to heat diffusion in the active layer, i.e.,

$$k_{eff}' = k_{eff} + \rho c_p D_y \quad (7.12)$$

where D_y is the mass diffusion coefficient calculated in the flow model using the granular temperature.

7.2.3 The Combined Axial and Cross-sectional: The Quasi- Three-Dimensional Model for the Bed

It was mentioned in the opening discussion that the objective of the current work was to examine the role of bed motion in the transverse plane in determining the distribution of energy within the bed. In order to apply this understanding over the entire length of the kiln the two-dimensional model developed for the bed was combined with a conventional one-dimensional axial model for the kiln to derive a quasi-three-dimensional model for the bed

material. Although a rigorous three-dimensional formulation of the problem is easily accomplished, the extreme aspect ratio of most kilns; i.e. length to diameter ratios $\approx 25:1$, makes the solution of the resulting equations somewhat impractical unless the aspect ratios of the nodal structure is distorted to such an extent that much of the rigor in the axial direction is lost. The impetus for the development of the quasi-three-dimensional model was the need to significantly improve our capability for predicting conditions within the bed while maintaining relatively modest demands on computing capability. In the development of the model two approaches may be considered:

(i) Synchronous solution of the individual formulations. With this method the heat transfer problem external to the bed might be determined using current values of the freeboard gas temperature and mean bed temperature. This would be accomplished in the same manner as Barr (1986) in which a transient one-dimensional model of the wall was employed to ensure closure of the energy balance over the cross-section, or alternatively, using a two-dimensional, steady-state formulation of the wall problem. Once the net rate of heat transfer to the bed is determined (including the flux distribution to the covered wall surface) the axial gradients of the freeboard gas and mean bed temperatures would be available for use in advancing these temperatures to the next axial position by solving Eq. 7.6. Before doing so the axial temperature gradient in the bed could be used to obtain a solution for Eq. 7.10 and 7.11(a) and hence determine the temperature distribution within the bed at the current axial position.

(ii) Asynchronous solution of the one and two-dimensional problem. The approach employed in the current work was to develop the one-dimensional solution over the entire kiln length before returning to the charge end to expand the axial bed temperature profile into the transverse plane. Implicit in doing so is the assumption that, at any axial position, heat transfer in the transverse plane (within the bed) will not significantly alter the freeboard, bed and wall. In the case of the pilot kiln, which will soon be shown, this seems justified. In the current work the axial temperature profiles for the freeboard gas, bed, and wall were developed using the one-dimensional model.

The gas temperature and axial gradient of the bed temperature are then employed to drive the transverse model of the bed and kiln wall at a series of axial kiln positions and thus determine, for each position, the temperature field in the bed and wall material. It should be pointed out at this stage that the two-dimensional model employs only the freeboard gas temperature and the axial gradient of bed temperature (both of which may be supplied either from experimental data or the one-dimensional model) at a given axial location in order to calculate the bed and wall temperatures at that axial position. Thus a check on the model can be made by comparing the computed bed and wall temperatures with either the measured values or, once the one-dimensional model has been verified, with values obtained from the latter.

7.2.4 Solution Procedure

As was pointed out earlier, the axial temperature profiles can be developed beginning from either end of the kiln by means of Eq. 7.3 and 7.6. However, because most kilns operate with counter-current flow, a shooting method (Tscheng, 1978) must be employed since, when starting at the charge end, the material temperature is known but the gas temperature is unknown. The calculations in the current work are made for an inert bed medium and the freeboard gas is assumed to consist of carbon dioxide and water vapor as the only combustion products. The thermal properties of the gas, as well as the calculation of the gray gas emissivities and absorptivities required for computing the radiative boundary conditions are based on these two gas constituents. Again, the exit gas temperature and composition are needed to initiate solution (for example, the Runge Kutta solution procedure) and again, a shooting method may be employed. However, exit gas parameters are measurable and input data from experiments will avoid the shooting method (which can destabilize the calculation as a result of the number of unknowns involved).

The numerical technique employed for the solution of the governing bed/wall equations for the cross-section was the finite difference method described for convective-diffusion equations (Patanker, 1980); the general form being:

$$\rho U \frac{\partial T}{\partial x_j} - \frac{\partial}{\partial x} \left(\Gamma \frac{\partial T}{\partial x_j} \right) = S \quad (7.13)$$

where S is the source term and Γ is the effective mass flux which can be given as;

$$\Gamma = \frac{k_{eff}}{c_p} \left[\frac{kg}{m \cdot s} \right]$$

Eq. 7.13 may be re-arranged to be

$$\frac{\partial}{\partial x_j} \left(\rho U T - \Gamma \frac{\partial T}{\partial x_j} \right) = S \quad (7.14)$$

where the term in the bracket, represented by J_i , is the sum of the convection and diffusion fluxes.

By introducing the continuity equation into the above equations the general algebraic form of the discretized differential equations for the bed and wall become;

$$A_p T_{i,j} = A_E T_{i+1,j} + A_W T_{i-1,j} + A_N T_{i,j-1} + A_S T_{i,j+1} - \dot{m} c_p \frac{dT_b}{dz} \quad (7.15)$$

where the coefficients A are given as;

$$\begin{aligned} A_E &= D_e A |P_e| + [-F_e, 0] \\ A_W &= D_w A |P_w| + [F_w, 0] \\ A_N &= D_n A |P_n| + [-F_n, 0] \\ A_S &= D_s A |P_s| + [F_s, 0] \\ A_p &= A_E + A_W + A_N + A_S \end{aligned} \quad (7.16)$$

The heat diffusion, D , and the convection, F , fluxes are:

$$\begin{aligned}
D_e &= \frac{\Gamma \Delta y}{(\delta x)_e} & F_e &= (\rho U_x)_{i+1,j} \Delta y \\
D_w &= \frac{\Gamma \Delta y}{(\delta x)_w} & F_w &= (\rho U_x)_{i-1,j} \Delta y \\
D_n &= \frac{\Gamma \Delta y}{(\delta y)_n} & F_n &= (\rho U_y)_{i,j+1} \Delta x \\
D_s &= \frac{\Gamma \Delta y}{(\delta y)_s} \left[\frac{kg}{m \cdot s} \right] & F_s &= (\rho U_y)_{i,j-1} \Delta x \left[\frac{kg}{m \cdot s} \right]
\end{aligned} \tag{7.17}$$

and the Peclet numbers given as follows:

$$\begin{aligned}
P_e &= \frac{F_e}{D_e} ; P_w = \frac{F_w}{D_w} ; \text{ etc} \\
&= \frac{kg}{m \cdot s} / \frac{kg}{m \cdot s}
\end{aligned} \tag{7.18}$$

Within the model, the function $A|P|$ is represented by a power law scheme as (Patanker, 1980)

$$A(|P|) = [0, (1 - 0.1 |P|^5)] \tag{7.19}$$

where the term in the square bracket represents the greater of the two quantities. Because of the inclusion of the source term, $\dot{m} c_p dT/dz$ in Eq. 7.15, Eq. 7.16, which represents the coefficients of the discretized equation, is multiplied by c_p so as to obtain the desired units, i.e.,

$$A_E = \frac{kg}{m \cdot s} \cdot \frac{J}{kg \cdot K} = \frac{W}{mK}$$

For the plug flow region and the refractory wall the discretized equations are the same as for the active region of the bed except that, as shown in Figure 7.4(b), they are in cylindrical coordinates. For the radial direction, only the conduction component is considered and the coefficient of the algebraic (discretized) equation is equal to, for example,

$$\begin{aligned}
A_s &= \frac{k_w \cdot r\theta}{\Delta R} \\
&= \frac{W}{m^\circ C} \cdot \frac{m}{m} \left[\frac{W}{m^\circ C} \right]
\end{aligned}$$

Here, also, all units are consistent with that of the term $\dot{m}c_p dT/dz$.

The mesh employed for the cross-sectional model is shown in Figure 7.5. Rectangular grids are used for most of the nodes except at the interface between the plug flow and the active layer where triangular nodes automatically emerge as a result of the merging of the two coordinate systems; such nodes are considered as half of the rectangular nodes in the calculation of the nodal areas. Higher density mesh is employed in the active layer of the bed and in the active region of the refractory wall where temperature cycling is expected to occur as a result of kiln rotation. Although the specific depth of the wall active region is not known *a priori*, temperature measurements by Barr (1986) suggest that this region does not exceed about 10% of the wall thickness. Although this value is used in establishing the mesh, the actual depth is found from the results of the numerical calculation. Sensitivity analysis on the mesh for the pilot kiln, whose geometry will soon be described, indicated that 15 exposed bed surface nodes were sufficient to produce consistent results. Hence, 21 surface nodes were used in all the thermal calculations. Outside the active wall region, the steady-state one-dimensional conduction can be applied:

$$Q_{ss} = 2\pi k_w \frac{T_{w_r} - T_{w_r + \Delta r}}{\ln[(r + \Delta r)/r]} \quad (7.20)$$

This arrangement speeds up the numerical calculation which is, otherwise, slow because of the slow thermal response of the wall. The Gauss Siedel iteration method was employed to solve the system of algebraic equations with the convergence criterion set as;

$$|T_{ij}^n - T_{ij}^{n+1}|_{\max} < 10^{-5} \quad (7.21)$$

The solution requires an under-relaxation technique because of the numerous non-linear temperature dependent terms.

7.3 Experimental

Temperature data for model verification were obtained from the 0.41 m I.D by 5.5 m long pilot rotary kiln located at the University of British Columbia. The facility, which has been described by Barr *et al.* (1991), is well instrumented with 66 thermocouples for determining temperatures throughout the freeboard gas, bed material and refractory wall. The pilot kiln trials made by Barr (1986) using inert Ottawa sand as bed material and natural gas to fire the kiln were used for validation of the current work. In Barr's trials, burner conditions were adjusted to produce a short intense flame, thus ensuring inert conditions in the freeboard over most of the kiln length. Peripheral air jets surrounding the burner were employed to satisfy the entrainment requirements of the enclosed jet system and thus eliminate any significant recirculatory flow in the hot end.

The experimental program consisted of two parts, the first being a conventional series of trials whereby axial temperature profiles were obtained for the freeboard gas and bed material under prescribed steady-state conditions, as described by Barr *et al.* (1991). Energy losses through the refractory wall as well as the regenerative action of the inside refractory surface were determined from these trials. In the conventional kiln trials (*trial 1* and *trial 2*) the bed temperatures were measured with thermocouples that rotate with the kiln wall and so sweep through the bed and the freeboard gas during each kiln revolution. Although Barr (1986) has developed a theoretical correction, which is based on the response time of the thermocouples, in order to obtain steady-state bed temperatures from the bed transient response, this correction is more accurate for deep beds where the time required for data acquisition is likely to coincide with the thermocouple response time. For shallow beds the measured temperatures still remain in transient conditions. Other trials were therefore carried out using a new method of obtaining bed temperatures whereby a tube, such as one shown in Figure 7.6, was inserted along the center-line of the kiln from the cold end. Although physical constraints prevented insertion along the entire kiln length, the measured bed

temperatures using the new method were deemed to better represent true bed temperatures and were therefore used to correct the bed temperatures in the conventional trials. The experimental run conditions used in validating the mathematical models are shown in Table 7.2.

7.4 Validation of the Thermal Model

As mentioned earlier, the current work followed the asynchronous solution of the one and two-dimensional problems. Model validation is, therefore, carried out by first comparing the one-dimensional model with axial profiles for the freeboard gas, mean bed temperature, and mean wall temperature from the pilot kiln trials. Having validated the one-dimensional model, the heat fluxes determined for the interfaces which will be used in the two-dimensional calculations as boundary conditions, are discussed. In order to validate the two-dimensional model, one-dimensional profiles are deduced from the cross-sectional temperature distribution for the wall and the bed which are, in turn, compared with either the already validated one-dimensional profiles or the original pilot kiln data. Other validation work includes the wall thermal gradients, steady-state wall temperature gradients, and the bed/wall temperature gradients established when the kiln is stopped. This last condition was used to assess the validity of the continuum assumption for the bed material.

7.4.1 Validation of the One-dimensional Model

The one-dimensional model was tested against two inert bed trials (*trial 1* and *trial 2* of Barr (1989)). Input variables for the model were the inlet bed temperature which was set at 50°C and the exit gas temperature (gas temperature at feed end) which was obtained from the experimental data. By using a known exit gas temperature to initiate the computation, the shooting method described earlier for solving the system of equations was avoided. The model computes the mean bed temperature, mean freeboard gas temperature, and the wall surface temperature as functions of axial position along the kiln. Figures 7.7(a) and 7.7(b) provide a comparison of predicted and measured temperature profiles for *trial 1* and *trial 2* respectively. Agreement between the measured and predicted values was generally good for any gas, bed and wall

temperatures. There is some discrepancy in the bed temperatures near the charge end which may be attributable to uncertain entrance conditions. However, such discrepancies are typical of heat transfer in open tubes where ambient conditions are likely to influence heat exchange at the entrance. Further down the kiln, Ottawa sand undergoes heating during its journey along the kiln as a result of energy exchange with the freeboard gas and the refractory wall. As the material approaches the exit end of the kiln, the temperature difference between the bed and the wall gets smaller.

The radiative heat transfer interactions as predicted by Barr's radiation sub-model (one clear plus two gray gases, Barr (1986)) and used in the energy balances at each axial position are shown in the form of heat transfer coefficients (or fluxes) in Figures 7.8(a) and 7.8(b) for *trial 1* and *trial 2* respectively. It can be seen from these plots that, except for the gas to exposed wall component, there is an increase in heat transfer coefficients as a function of axial position. The net heat flux from gas to exposed wall increases up to about a third of the kiln length and decreases sharply as the radiative interactions among various surfaces intensify. The contribution of the gas convection heat transfer was less than 2% in all cases.

7.4.2 Validation of the Cross-Sectional Model

The initial step in verifying the cross-sectional model was to compare the bed and wall temperatures obtained from this model (using the experimental values of T_g and dT_{ba}/dz as described earlier) against the pilot kiln data. The steady-state one-dimensional profiles shown in Figure 7.7 or the measured values are used to validate the two-dimensional results. However, in order to do so the mass averaged bed temperature for each cross-section, along with the arithmetic average surface wall temperature, must be calculated from the two-dimensional temperature distribution at each axial position. Figures 7.9(a) and 7.9(b) provide a comparison between the measured bed and wall surface temperature profiles and those predicted by the model (using the measured gas temperatures as input data). Although the predictions are quite satisfactory, it was anticipated that the converted two-dimensional results into one-dimensional profiles cannot

reproduce the measured temperatures as accurately as the one-dimensional model. Nevertheless, the largest temperature difference between the model predictions and experiments does not exceed 50°C which is within limits of experimental error at elevated temperatures. The temperature profiles through the kiln wall as predicted by the two-dimensional model are validated with experimental results in Figures 7.10(a) and 7.10(b) for *trial 1* and *trial 2* at three different axial locations (i.e., three freeboard gas temperatures). Also, in Figure 7.11, the resultant wall steady-state heat losses are presented. As seen from the plots, model predictions are in good agreement with experiment and therefore lend some confidence to the predictions for the temperature distribution in the bed which generated these results.

In an effort to verify the continuity assumption imposed on the granular bed medium, the two-dimensional model was run for the condition of no kiln rotation (pilot kiln *trial 5*) and the results obtained were validated with measured temperature gradients. The results of this work are shown in Figure 7.12. Using the sub-model of Schotte (1960) the bed thermal conductivity was predicted as 0.111 W/mK, while the measured value (estimated from the measured bed temperatures) was determined as 0.13 W/mK. The good agreement between the model predictions and experiments verifies that the model is fundamentally correct prior to rotation and validates the assumption that the bed can be considered as a continuum with effective thermal conductivity. It also provides the opportunity to check how sensitive the convective (advective) components would be in distributing energy in the bed.

Having established the validity of the two-dimensional model it is important to describe the effect of the flow on the temperature distribution before proceeding with a discussion of the heat transfer interactions in the entire cross-section. The effect of the flow field on temperature distribution can be established by sensitivity analysis of the various flow factors on the two-dimensional model. These factors include the x-wise and the y-wise velocity components in the active layer, the mass diffusion coefficient resulting from granular temperature, and, in the case of a segregating bed, the percolation velocity of jetsam concentration in the active layer.

For purposes of discussion the flow characteristics may be placed in two categories with respect to what constitutes (i) a 'mixed bed,' and (ii) a 'segregated bed.' It might be recalled that, since the active layer flow is primarily parallel to the top surface of the bed, a cartesian coordinate system was attached to that region and, assuming that the x-wise velocity component dominated the flow field, the boundary layer flow model was employed to calculate the velocity there. The y-wise velocity component was estimated by satisfying the continuity equation after the bulk velocity in the x-wise direction had been calculated. It is therefore important to check how sensitive the y-wise velocity vector is in the thermal model.

(i) *The mixed bed.* For this condition the bed motion is assumed to be in the rolling mode and therefore the model implements all the flow results obtained from the granular flow model. The particle size used in the model is assumed uniform and spherical and the diameter is taken as an average of the size range used in the experiment which is 0.569 mm for fine Ottawa sand, and 2.25 mm for coarse Ottawa sand (Table 7.1). The x-wise and the y-wise velocity components, as well as the enhanced thermal conductivity given in Eq. 7.12, are employed in the calculations for the 'mixed bed.' Figure 7.13 and 7.14 show contour plots of the temperature distribution within the bed cross-section for *trial 1* at local freeboard gas temperatures of 631°C and 804°C respectively. Also shown in Figures 7.15 and 7.16 are contour plots established for *trial 2* at freeboard gas temperatures of 701°C, and 953°C. Notice from the result of the 1.5 rpm trials that, because of the effect of the y-wise velocity component and insufficient mixing, a slight temperature gradient is established between the active layer and the rest of the bed. Also, as a result of the regenerative action of the wall, the bed temperature at the wall is slightly higher than the rest of the bed. It is worth mentioning that these results are those that were validated with experiments in Figure 7.9. However, when the model was run by increasing the kiln speed from 1.5 rpm to 3 rpm the gradient between the bed surface and the rest of the bed was reduced from 30°C to 12°C and a further increase from 3 rpm to 5 rpm made the bed virtually isothermal. Similar trends can be seen in Figures 7.15 and 7.16 for *trial 2*, except that the gradients between

the top surface and the rest of the bed are relatively greater than those in *trial 1*. The increased gradient is attributed to the decrease in particle size in *trial 2* (from 2.25 to 0.569 mm in diameter). It might be recalled from the flow model that the velocity is virtually independent of particle size, however, the effective thermal conductivity is a strong function of particle size. Figure 7.17 shows the enhanced bed effective thermal conductivity as function of freeboard gas temperature for the two run conditions at a kiln speed of 1.5 rpm. As can be seen from the plots, although the gas temperatures for *trial 2* are higher than that in *trial 1*, the thermal conductivity is lower because of the decreased particle size. The isothermal bed that result from increased kiln speed is due to the increased y-wise velocity component and increased thermal conductivity. As might be recalled, the self diffusion coefficient in the active layer increases an order of magnitude with an increase in kiln speed (the diffusion coefficient increases 10 times per each increase in kiln speed) and so the effective thermal conductivity is enhanced in the same order of magnitude as well.

The 'mixed bed' was tested by setting the y-wise component velocity to zero; the temperature contours that resulted are presented in Figure 7.18. The justification of setting the y-wise velocity component to zero is to assess its strength in comparison with the self diffusion component. Notice that temperature profiles are formed based on the particle circulation paths and that the gradient between the top surface and the rest of the bed for 1.5 rpm is about the same as that for Figure 7.13. Also the bed tends to isothermal conditions as the kiln speed is increased (Figure 7.18(b)) due to the enhanced thermal conductivity or increased diffusion. However, although the contours appear to represent what is expected of material circulation in a rotary kiln, the bed temperatures that result from these calculations are about 90°C higher than measured values. Also, the average bed temperature is about 100°C higher than the covered wall temperature which makes the results not credible. Besides, there cannot be diffusion without y-wise velocity vector so therefore, for a rolling bed, the y-wise velocity component cannot be zero.

(ii) *The segregated bed.* In order to establish the criteria that result in temperature nonuniformities in a segregated bed it was assumed that the bed comprises a binary mixture so that the segregation

model could be incorporated into the two-dimensional thermal model. Because the effective thermal conductivity is a function of particle size, its magnitude will depend upon the concentration gradient at each node and is therefore calculated as

$$C_j(i,j)k_{eff} |_{d_{p_s}} + [1 - C_j(i,j)]k_{eff} |_{d_{p_L}} \quad (7.22)$$

The thermal model was run with the y-wise component equated to the percolation velocity of jetsam particles. The results obtained by running the model under these conditions are shown in Figure 7.19 for a local freeboard gas temperature of 804°C and a jetsam loading of 20%. As can be seen, temperature gradients are established in the same manner as the 'mixed bed' except that the bed temperatures are relatively higher and the bed does not become isothermal with increased rpm. Also, the region with the lowest temperature does not coincide with the segregated core as has been observed in experiments with wide variation of particle size. Calcination profiles for a strongly segregated limestone bed (Watkinson, 1993) show that the fine particles are not fully calcined. Since observations and also the segregation model show that the fines tend to concentrate at the core, the region with the lowest temperature should coincide with the core. The run conditions just described cannot, therefore, represent a condition of a segregated bed. One possibility is that, the y-wise velocity component should vanish once the bed is completely segregated, since there should be no y-wise velocity component without diffusion. Therefore the model was re-run by setting the y-wise velocity component to zero and the results are shown in Figure 7.20. It is evident from this figure that, for these assumed conditions, the region with the lowest temperature (*cooler spot*) coincides with the segregated core as anticipated in a strongly segregated rotary kiln bed.

From the forgoing sensitivity analyses for mixed and segregated beds, it can be concluded that, whenever the bed is considered mixed (e.g., rolling) and the particle size is fairly uniform, the thermal model must incorporate both x-wise and y-wise velocity vectors into the calculations as advective components of energy. Also the bed effective thermal conductivity must be enhanced

by the self diffusion coefficient. Otherwise, for a strongly segregated bed where diffusion is negligible (see segregation model) the y-wise component of the velocity vector must vanish and so does not enter into the thermal model calculations. Before the effect of segregation on bed temperature distribution at more elevated temperatures is discussed, it is important to discuss the heat transfer interactions in the cross-section using the validated results from the 'mixed bed' conditions at 1.5 rpm.

7.4.3 Heat Transfer Rates within Kiln Cross-section

The heat transfer rates at the boundary surfaces for mixed bed are shown in Figures 7.21(a) and 7.21(b) for *trial 1* and *trial 2* respectively. Superimposed on the graph is the freeboard gas temperature used as data to operate the bed thermal model. These plots indicate that, except at the entrance region, there is a progressive increase in all the interacting heat transfer mechanisms with increased T_g . Although the trends are the same for both *trial 1* and *trial 2*, the magnitudes of the heat transfer rates are higher in *trial 2* than in *trial 1* as a result of generally higher gas temperatures. It might be noted that Q_{eb} , the rate of heat transfer to the exposed bed surface, tends to decrease with axial distance from the charge end for *trial 1*. The equality, $Q_{w-net} = Q_{sh}$, testifies to the fact that the convergence criterion used in terminating the thermal model calculation (i.e., nodal temperature difference criterion) was adequate. The exposed wall heat transfer coefficient depends on the radiative exchange between the exposed wall and the freeboard gas, Q_{g-ew} , the exchange between the exposed wall and exposed wall itself, Q_{ew-ew} , and the exchange between the exposed wall and exposed bed, Q_{ew-eb} . The exposed wall heat transfer coefficients as function of radial position and selected freeboard gas temperatures are shown in Figures 7.22(a) and 7.22(b) for *trial 1* and *trial 2* respectively. These were obtained from a radiation sub-model of Barr *et al.*, (1989). It can be seen that the heat transfer coefficient, which comprises over 98% radiative component, increases as the wall moves from the covered wall exit and reaches a maximum as it reaches the middle of the second quadrant; it will then decrease sharply up to the 90° line (meridian). This trend is repeated in the next quadrant but this time with decreased magnitude.

At a modest fill of 12% in this instance, the exposed bed occupies a total of two and a half quadrants and the view factor results in periodic changes in h_{ew} . What can also be deduced from the plots is the effect of T_g on the magnitude of the exposed wall heat transfer coefficient; i.e., h_{ew} increases with increased freeboard gas temperature. The predicted regenerative action of the wall is depicted in Figure 7.23 which shows the temperature variation at the inside face (Figure 7.23a) and the temperature profiles through the wall (Figure 7.23b). From Figure 7.23(a) model predictions show that the wall will pick up energy from the freeboard gas and will give it to the bed at the covered wall as the kiln rotates. This means that before the bed temperature becomes isothermal the material at the wall will always have a higher temperature than the rest of the bed except, perhaps, the top surface which interacts with the freeboard gas. Model results shown in Figure 7.23(b) indicate that, besides the regenerative effect, the thickness of the wall active region can be predicted. From the figure, this thickness can be estimated as about 8% of the total wall thickness which agrees with Barr's observations (Barr, 1986).

7.4.4 Effect of Segregation on Bed Temperature Distribution

As was established from the sensitivity analysis described earlier, radial segregation will tend to generate a cooler region which coincides with segregated core of fine particles. This means that, for example in limestone calcination, either the fine particles may not fully calcine or the larger ones at the peripheral region may be over-burned at a specified freeboard gas temperature. In other processes, e.g., incineration of solid waste and cement clinkering, there is the possibility that the charge will contain materials of varied density. Density differences also result in segregation. These are the areas where the thermal model can be used to control temperature nonuniformities which accompany segregation. The only means of determining bed temperature in industrial kilns, at the moment, is through the use of a pyrometer which, usually, overlooks the bed surface only and will not detect core temperature. The kiln operator will, therefore, not know whether the core materials are fully calcined or not until the material is discharged. Here is a typical case where the thermal model may be applied to establish the bed

temperature distribution at a particular axial position and thus assess the quality and energy problems that may arise as a result of segregation. In the discussion to follow, an analysis of the effect of segregation on bed temperature distribution is carried out using the pilot kiln operated at 1.5 rpm and 12% fill, with jetsam loading set at 20% fines. In order to set the basis for comparison, Figures 7.24(a) through 7.24(c) present mixed bed results at a local freeboard gas temperature of 1000°C and Figures 7.25 through 7.28 present the results of bed temperature distribution for segregated bed with local gas temperatures ranging between 1000°C and 1200°C (color plots are shown as *plate*). As can be seen from Figure 7.25, the model predicts that at $T_g = 1000^\circ\text{C}$ the core temperature will be 700°C while the surface temperature will be 835°C, which is about the threshold temperature for limestone calcination. In comparison, the mixed bed (Figure 7.24(a)) core temperature will be 810°C. Under these conditions the particles at the core of segregated bed tends to react at a significantly lower rate than in the hotter peripheral region. If the kiln operator, upon noticing under-calcined fine particles, decides to increase the gas temperature (the obvious and usual practice), he will have to decide by how much the gas temperature should be increased. If he increases the gas temperature to 1200°C, predictions show that the core will be at 910°C and the peripheral region will be about 1000°C; thus either the larger particles are likely to be over burned, or unnecessary energy usage will result. The model indicates that for the present operational conditions the optimum gas temperature would be between 1050 and 1100°C. In the case of density differences, for example during solid waste incineration, the particle size of the feed can be controlled by using the model to decide jetsam loading so that the material with low heat capacity will be fed as fines in order to accomplish uniform burning.

7.5 Summary and Conclusions

The temperature distribution within the bed of a rotary kiln has been investigated by means of a mathematical model which incorporates all the transport phenomena within the bed and the freeboard as well. The two-dimensional thermal model combines with existing one-dimensional

plug flow type thermal model to predict the freeboard gas and the bed temperatures as a function of axial position. The predicted freeboard gas temperatures and the axial gradients are, in turn, used as data to predict detailed temperature distribution within any transverse slice of the kiln. This combination of the one-dimensional and the cross-sectional models results in a quasi-three-dimensional rotary kiln model which is capable of predicting conditions within the bed without the rigor of the very complex freeboard gas modeling. The results from the model are in agreement with temperature measurements of Barr *et al.* (1989) carried out in a 0.41 m I.D pilot kiln.

The thermal model developed for the bed cross-section assumes the bed material to behave as a continuum with effective thermal conductivity which depends on particle size, and incorporates advection components of energy due to material flow in the cross-section. The thermal model allows for the assessment of the effect of granular flow on energy redistribution and the effect of particle segregation on temperature nonuniformities.

For a mixed bed condition, which is a condition of a rolling bed with uniform particle size, the velocity field that results from kiln rotation, as well as self diffusion, enhance the effective thermal conductivity of the bed and promotes temperature uniformity. The temperature gradients within the bed, for a moderate fill of 12% Ottawa sand in the pilot kiln, at all local freeboard gas temperatures (600-1200°C), do not exceed 30°C for kiln rotational speed of 1.5 rpm. Because of strong diffusion effects, the bed tends to virtually isothermal conditions at higher kiln speeds.

For a segregated bed, which is a condition with marked particle size differences, and also for a condition whereby the flow field suppresses diffusion (e.g., slumping bed mode), temperature nonuniformities exist within the bed. Introduction of 20% fines into the charge for the pilot kiln at the same run conditions as the mixed bed, results in temperature gradients of about 100°C, with the cooler region coinciding with the segregated core.

Other essential features of the thermal model include the ability to produce accurate temperature distribution of the refractory wall, provide knowledge on the regenerative action of the wall, as well as freeboard gas/ bed heat transfer interactions. The thermal model can be a useful tool to control product quality in industrial kilns.

Table 7.1. Relevant Physical Properties

Property	Sand (Fine)	Sand (Coarse)	Limestone	Refractory
k W/mK	0.268	0.268	0.692	0.400
ρ_{bulk} kg/m ³	1520	1460	1680	1334
ρ_p kg/m ³	2627	2627	-	-
C_p @ 700K KJ/KgK	1.085	1.085	1.137	1.0-1.2
@ 1000K	1.160	1.160	1.298	1.1-1.3
@ 1300K	1.195	1.195	1.452	1.2-1.4
Particle size, mm	0.297-0.841	1.14-3.36	1.0-3.36	N/A

Table 7.2. Run Conditions for Pilot Kiln Trials Used in Model Validation.

Trial	Gas Flow	Air Flow Prim/Sec	Feed Material/ Rate	Fill	Kiln Speed	Comments
		l/s	kg/s	%	rpm	
1*	1.97	17.4/43.0	CS/62.0	12	1.5	HT/HF
2*	2.53	18.8/43.0	FS/64.0	12	1.5	HT/HF
3	1.97	17.4/43.0	LS/90.0	27	1.0	LT/LF
4	1.97	17.4/43.0	LS/190.0	27	2.0	LT/LF
5	1.41	-	LS/190.0	27	0	LT/LF
CS - Coarse sand		FS - Fine sand		LS - Limestone		
LT - Low temperature		LF - Low flow		* - Barr (1986)		

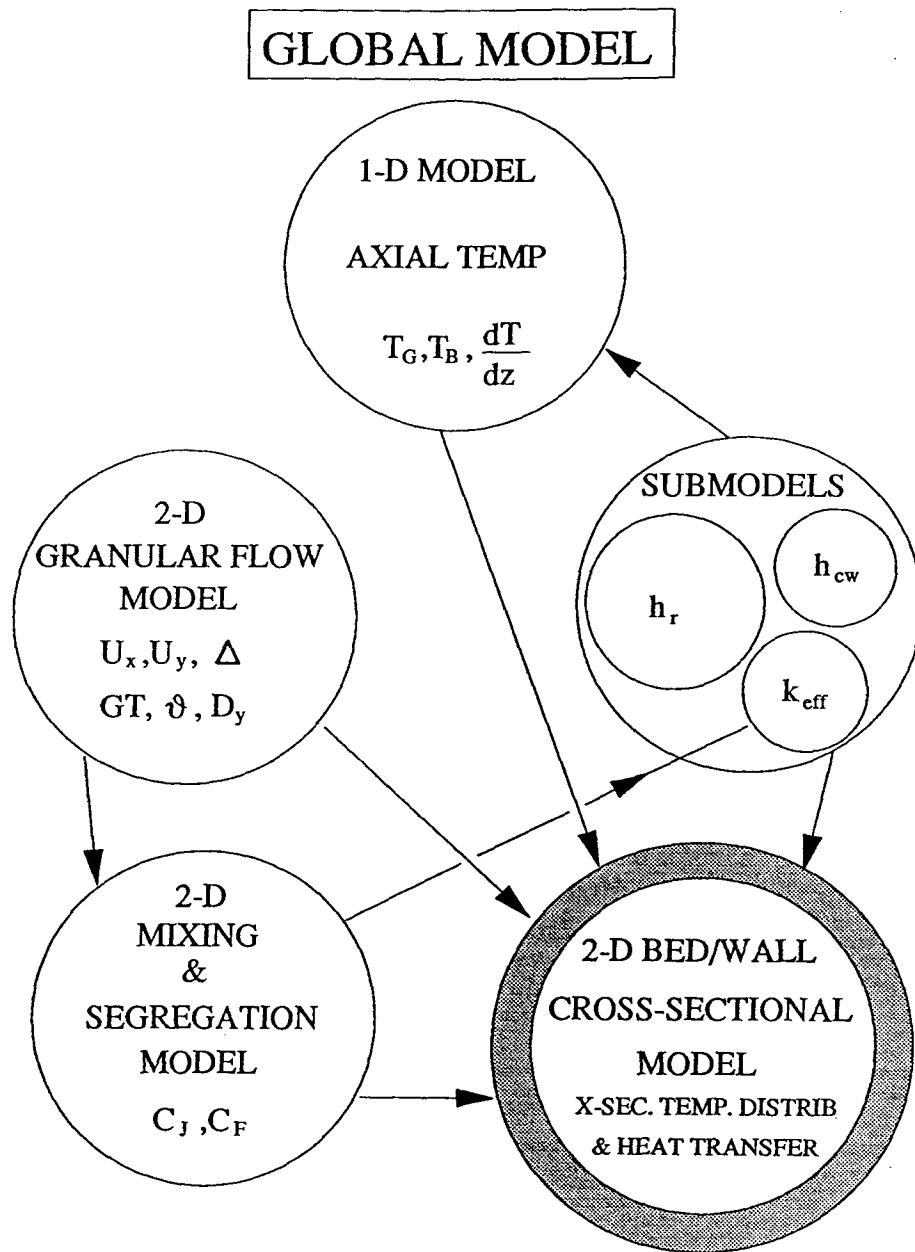


Figure 7.1. Global Model Layout

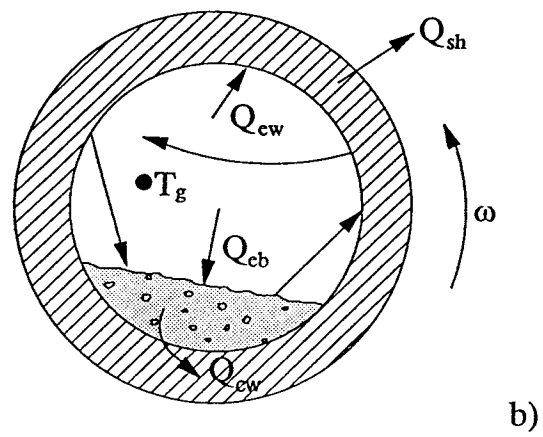
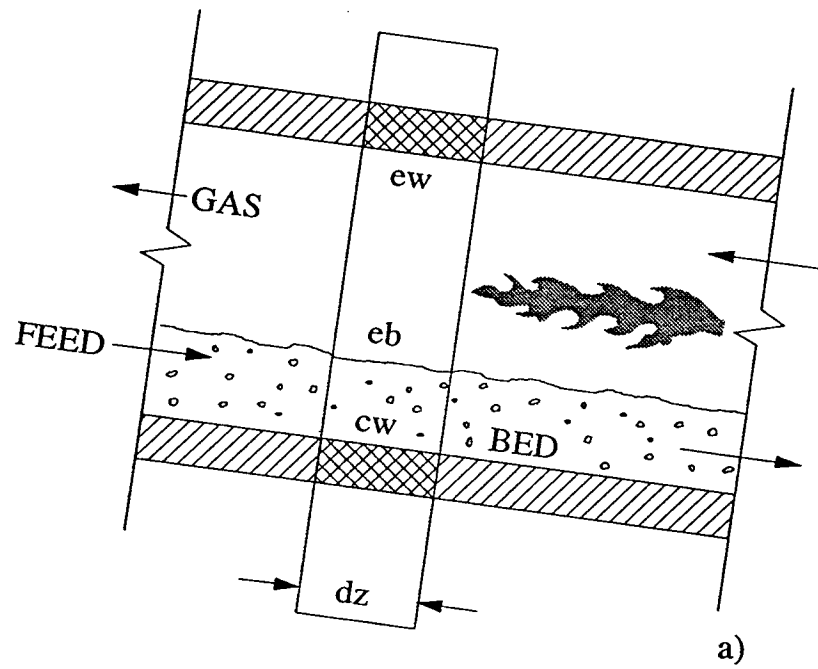


Figure 7.2. Axial and Transverse Slice of Rotary Kiln

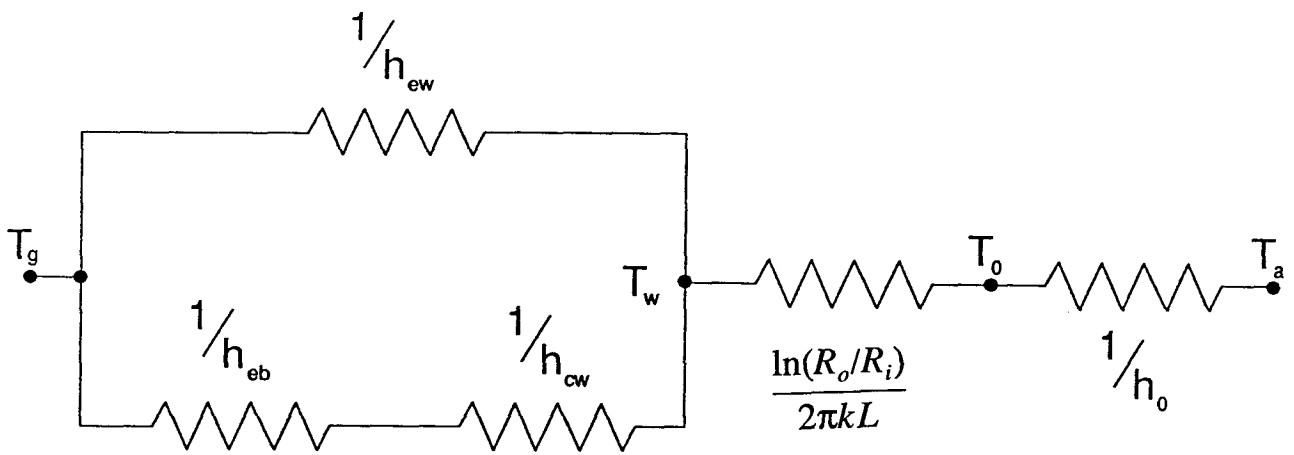


Figure 7.3. Heat Transport Paths and their Thermal Resistance Network

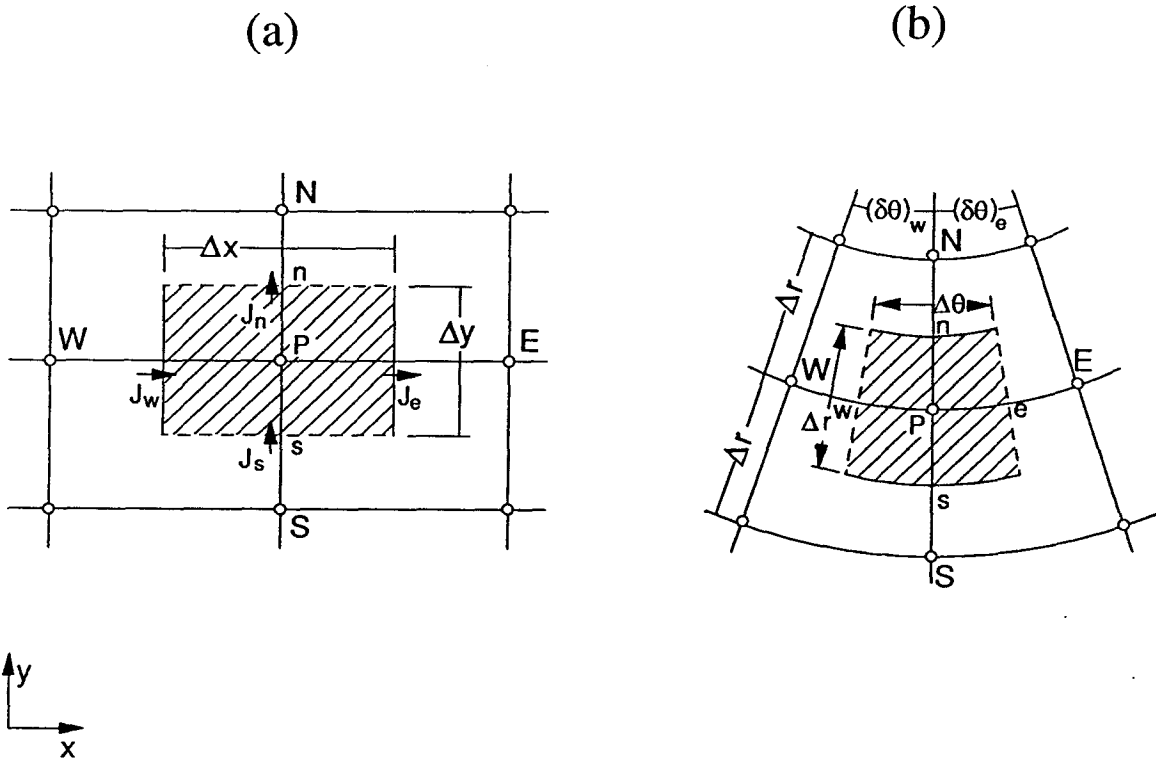


Figure 7.4. Control Volume for Heat Transfer Calculation; (a) Active Layer, (b) Plug Flow Region and Refractory Wall.

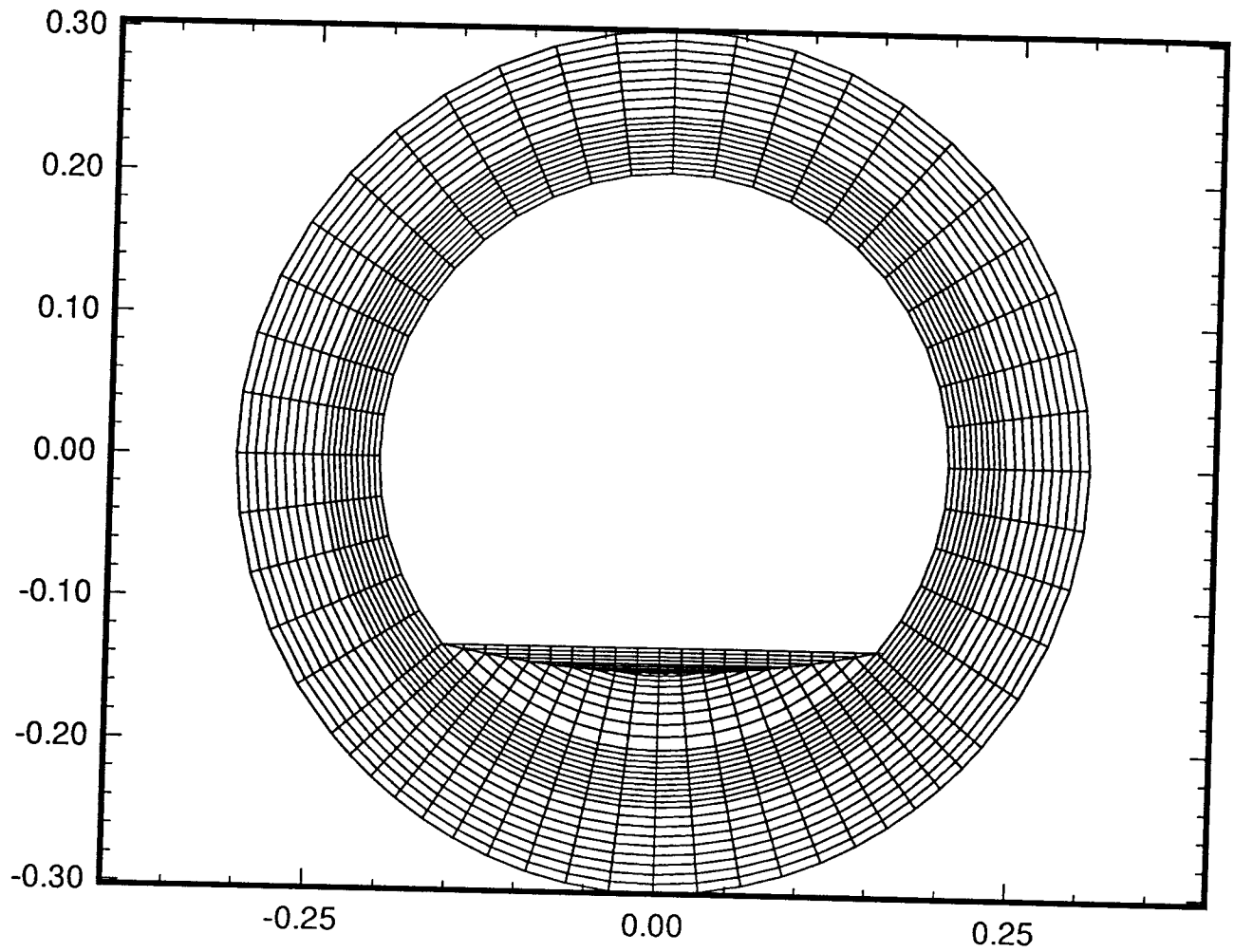


Figure 7.5. Mesh for cross-sectional Model

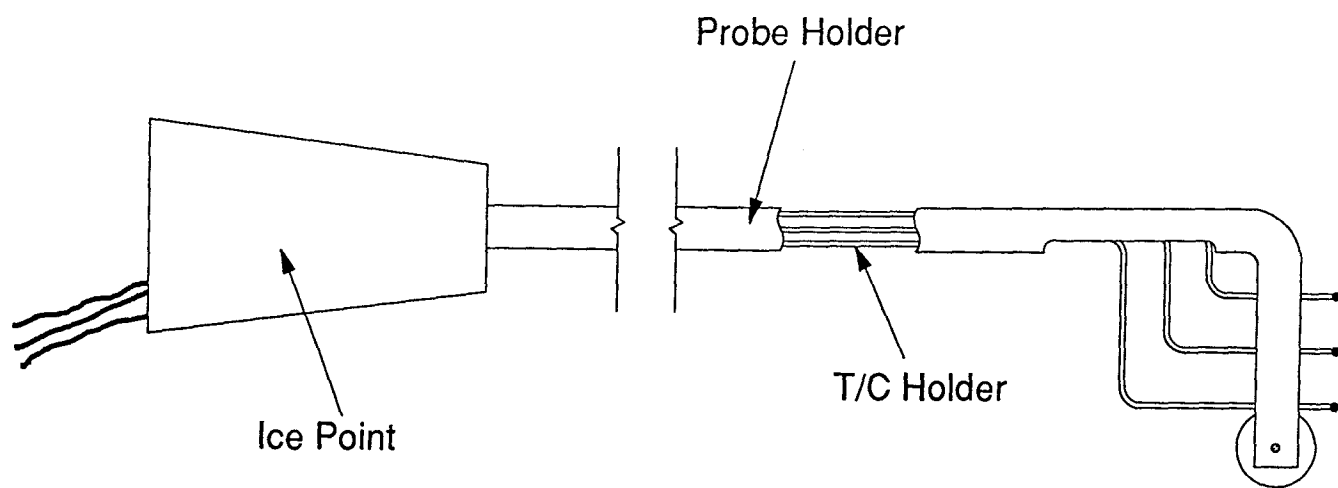


Figure 7.6. Stationary Thermocouple Probe

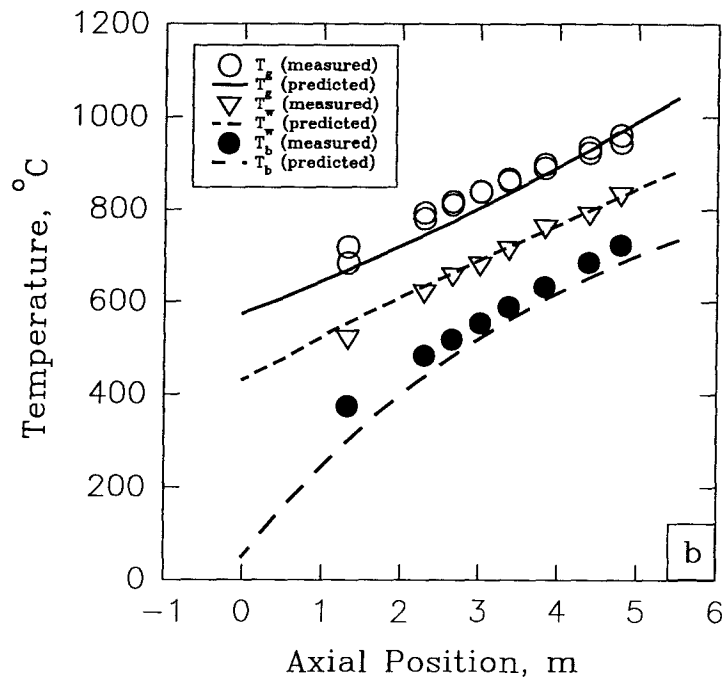
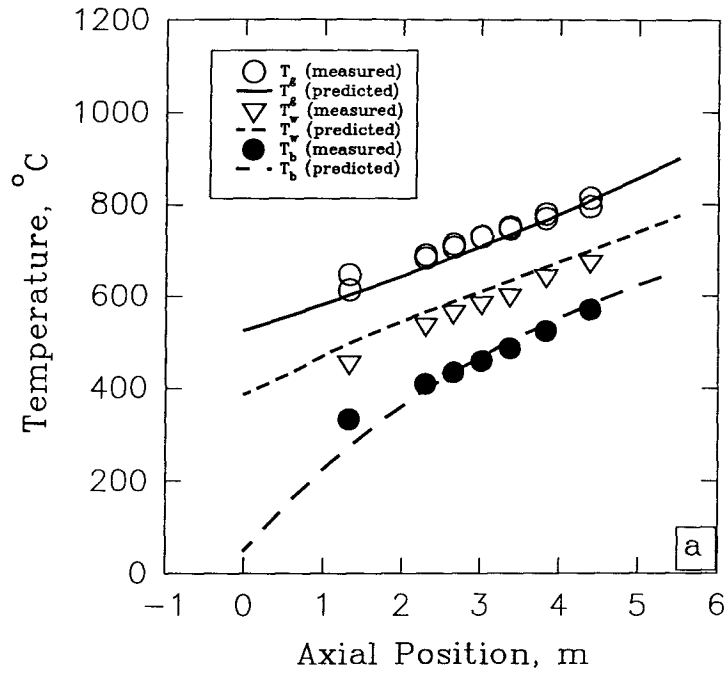


Figure 7.7. Predicted and Measured Axial Temperature Profiles for Freeboard Gas, Refractory Wall, and Bed Using One-dimensional Model; (a) Trial 1, (b) Trial 2.

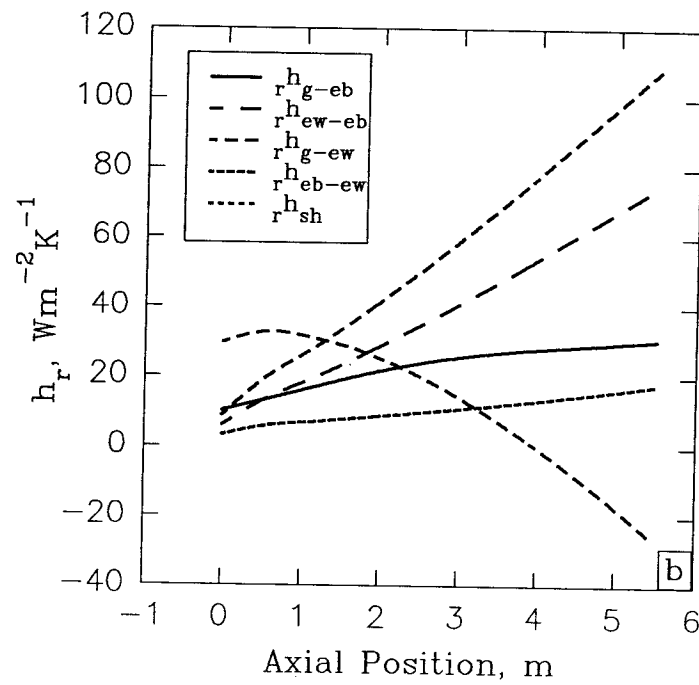
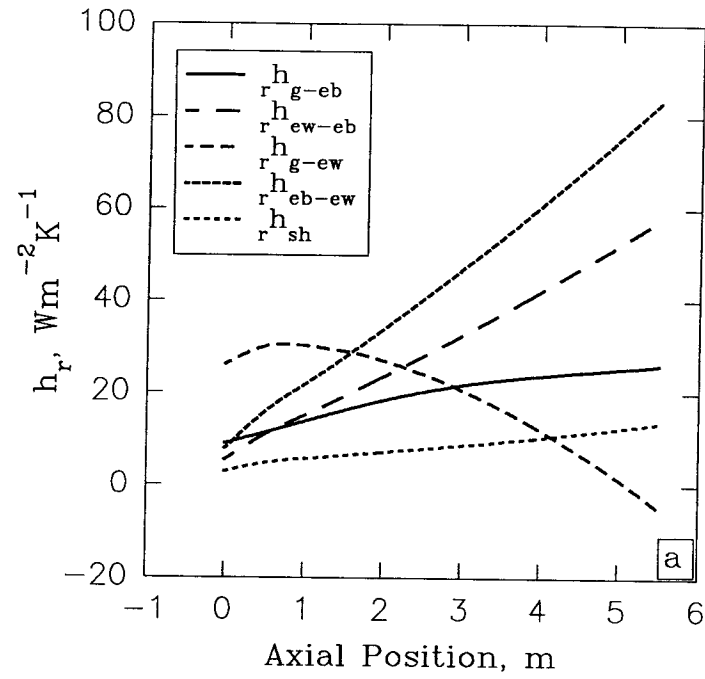


Figure 7.8. Predicted Radiative Heat Transfer Coefficients as Function of Axial Position; (a) *Trial 1*, (b) *Trial 2*.

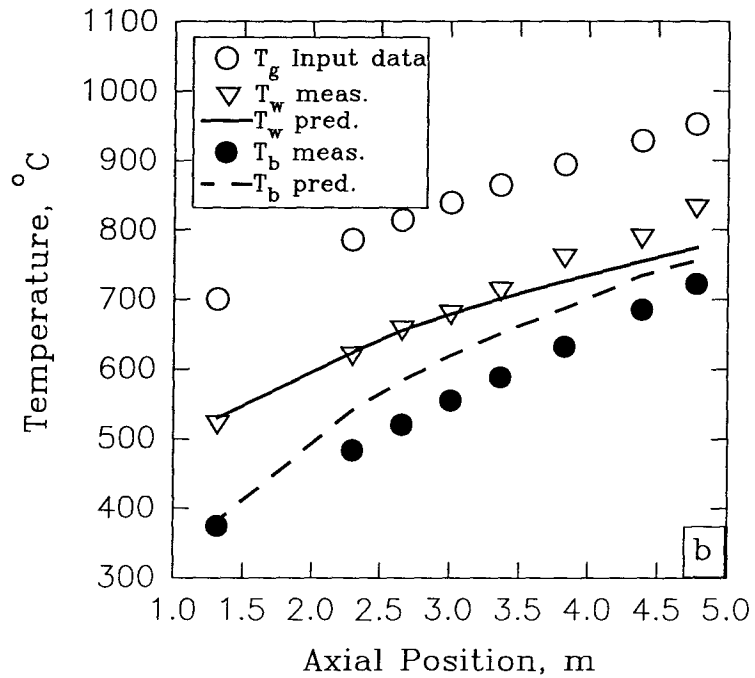
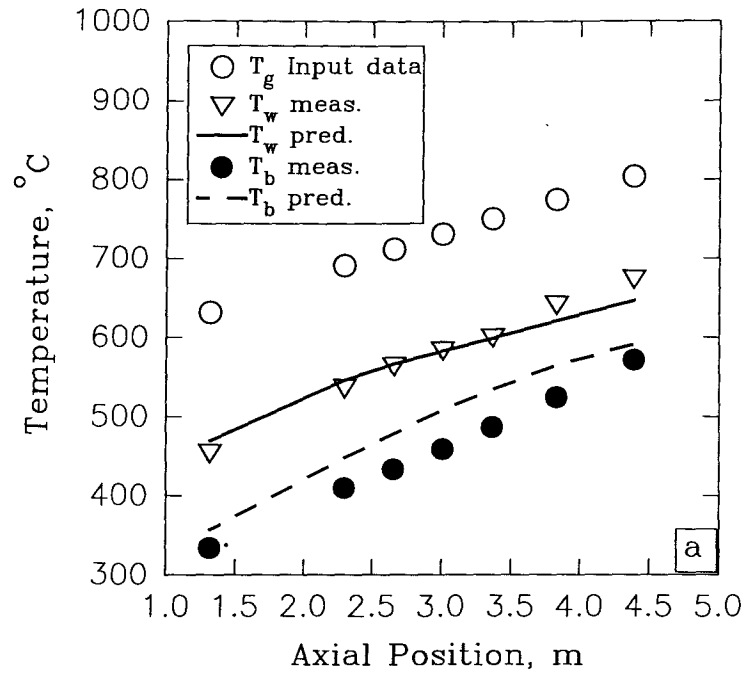


Figure 7.9. Predicted and Measured Axial Average Temperature for Refractory Wall, and Bed Using Two-dimensional Model; (a) Trial 1, (b) Trial 2.

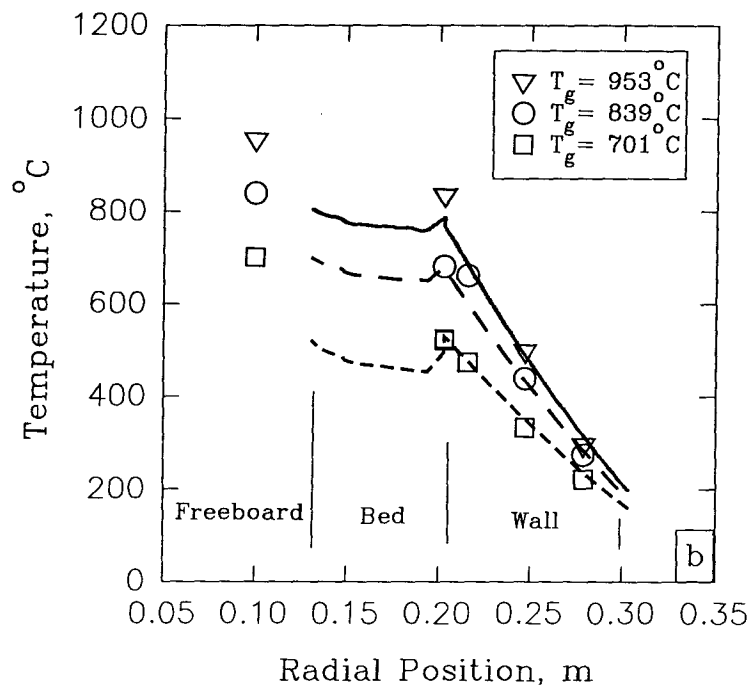
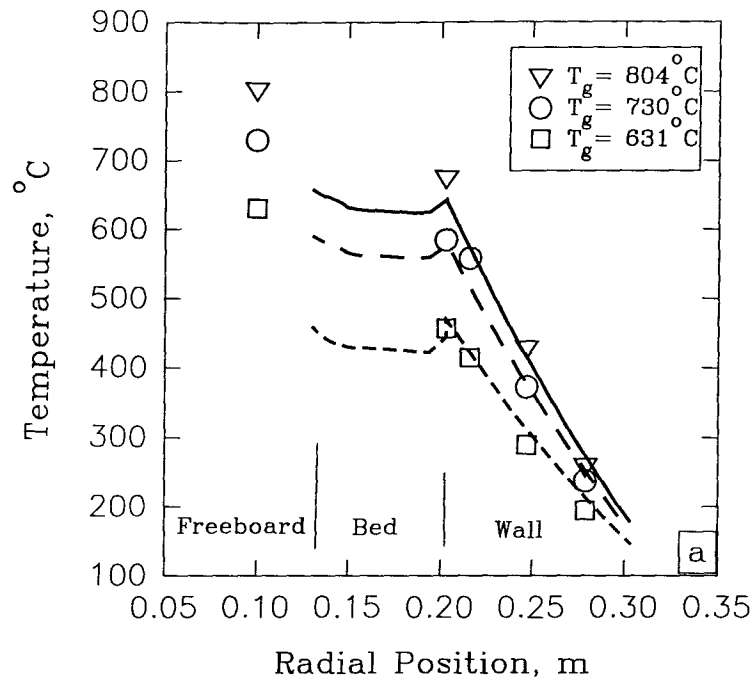


Figure 7.10. Predicted and Measured Temperature for Refractory Wall as Function of Radial Position for Several Freeboard Gas Temperatures; (a) Trial 1, (b) Trial 2.

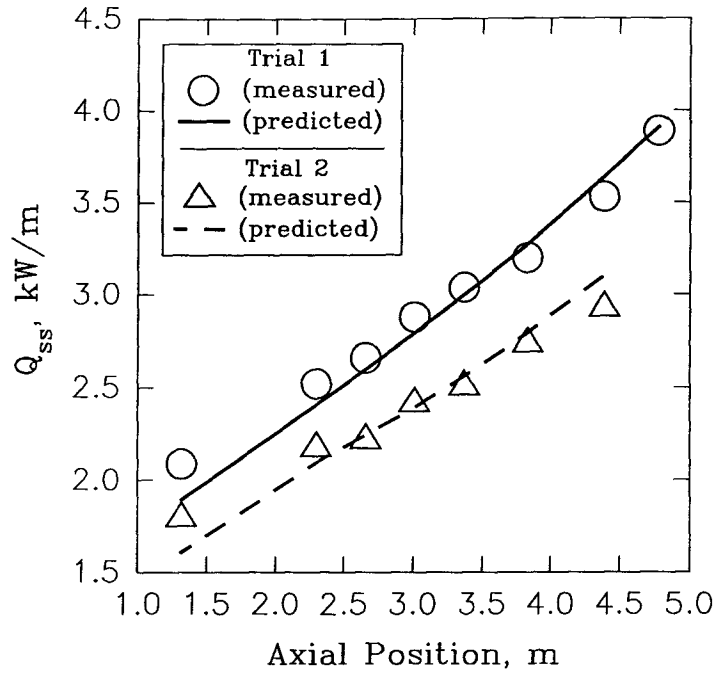


Figure 7.11. Predicted and Measured Steady-State Wall Heat Lost as Function of Axial Position.

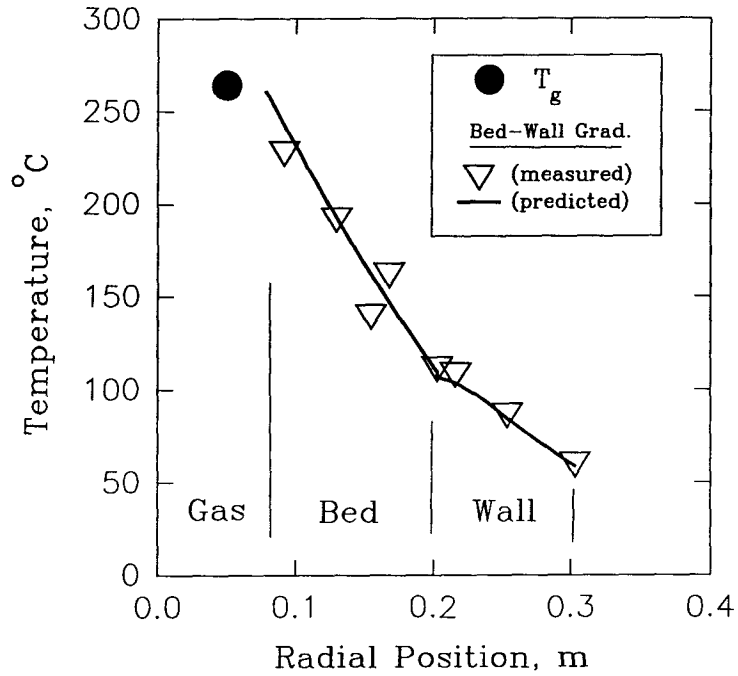


Figure 7.12. Predicted and Measured Temperatures in a Stationary Bed and Wall as Function of Radial Position at Mid-chord.

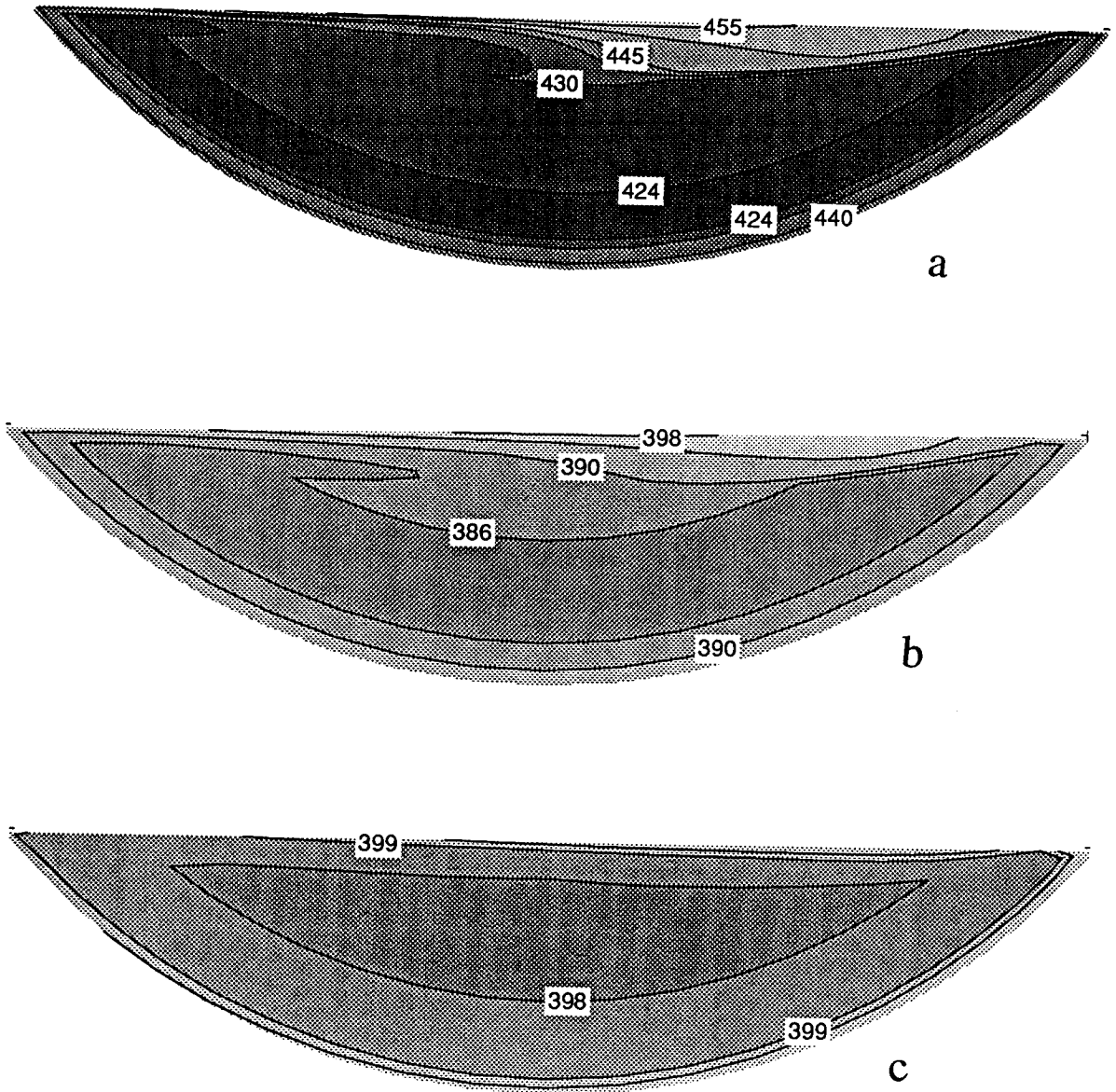


Figure 7.13. Contour Plots of Temperature Distribution Predicted by Two-dimensional 'Mixed Bed' Model Using Gas Temperature of 631°C for *Trial 1*: (a) 1.5 rpm; (b) 3 rpm; (c) 5 rpm: Bed Temperatures in °C.

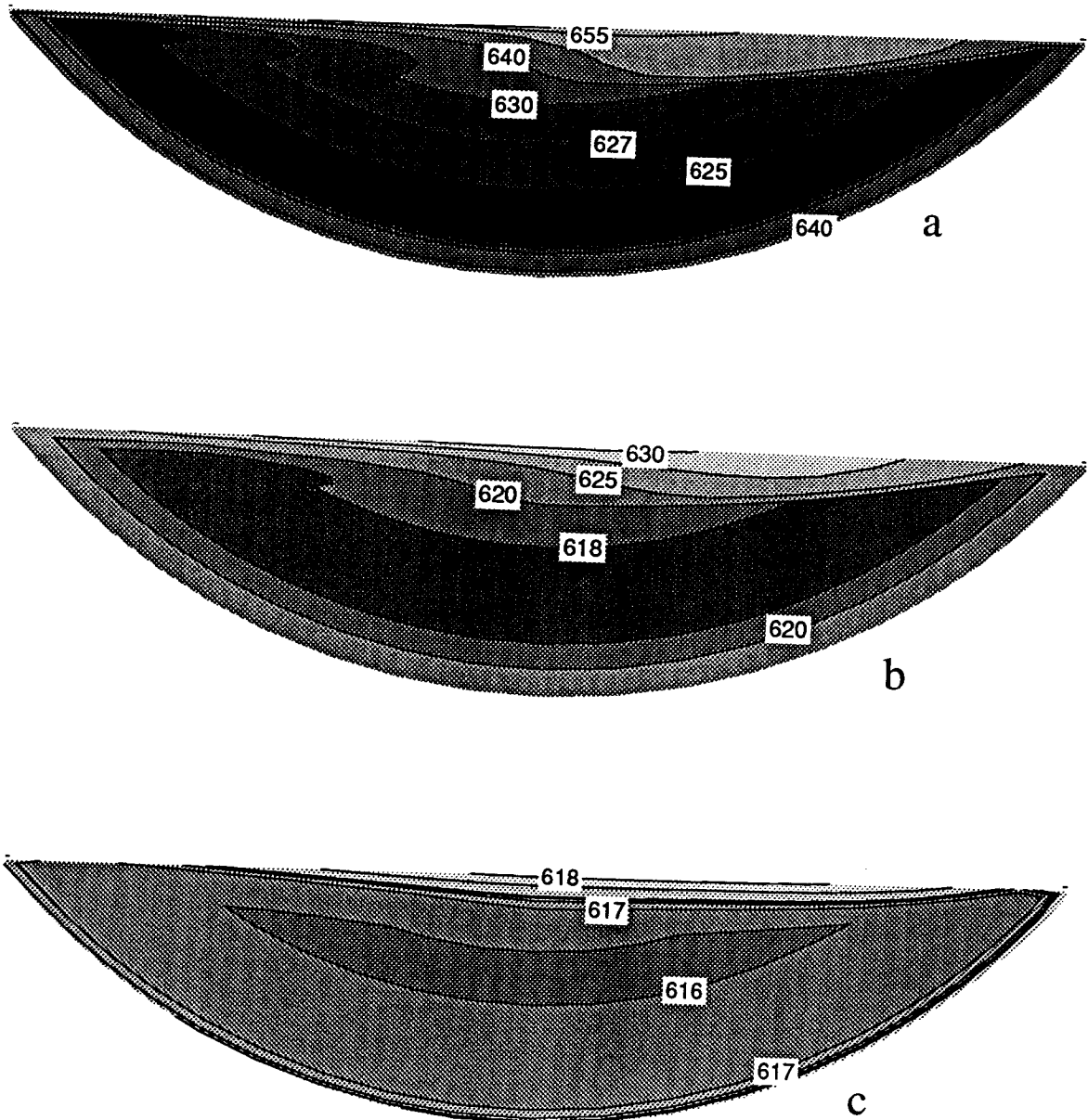


Figure 7.14. Contour Plots of Temperature Distribution Predicted by Two-dimensional 'Mixed Bed' Model Using Gas Temperature of 804°C for *Trial 1*: (a) 1.5 rpm; (b) 3 rpm; (c) 5 rpm: Bed Temperatures in $^{\circ}\text{C}$.

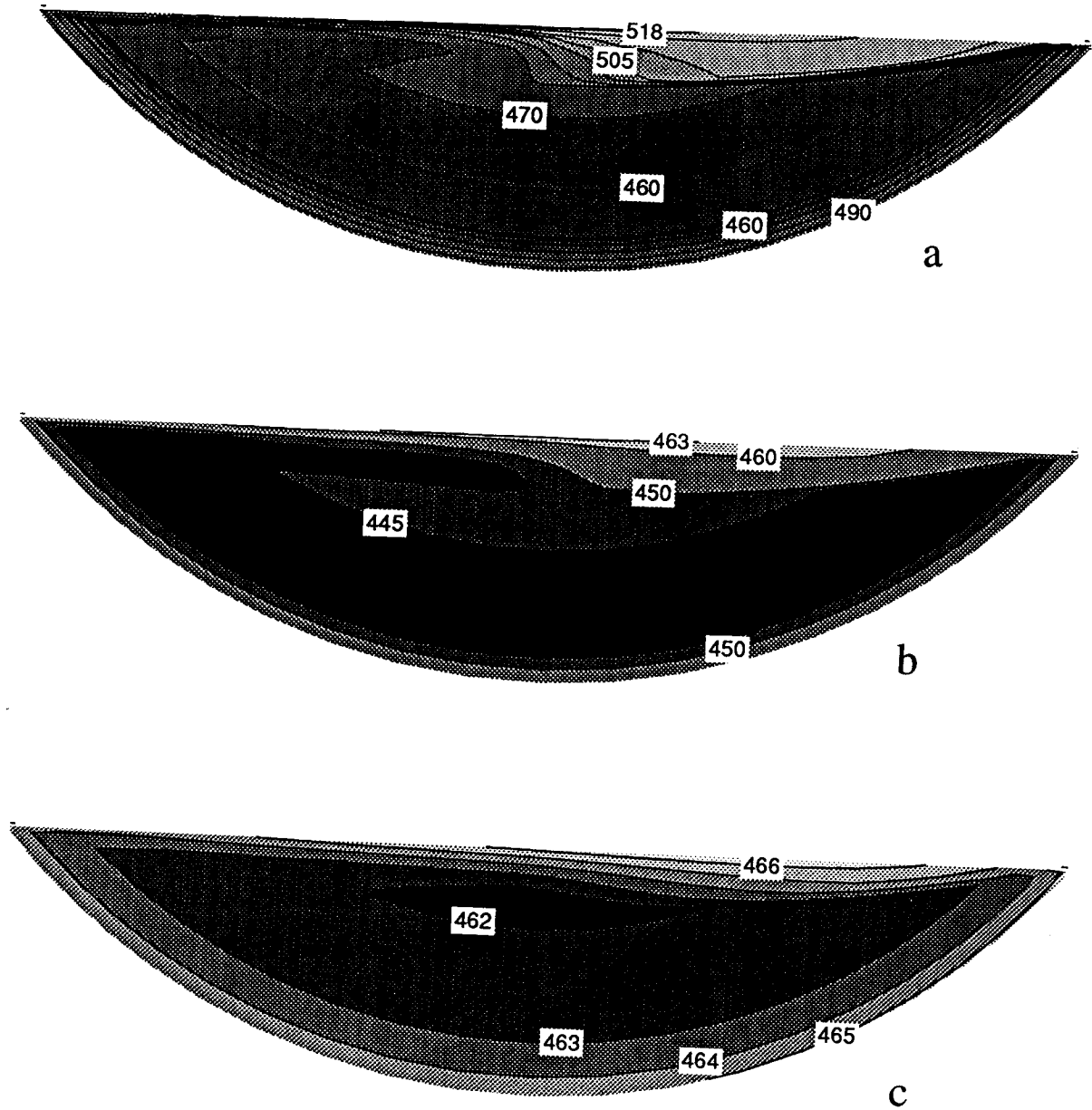


Figure 7.15. Contour Plots of Temperature Distribution Predicted by Two-dimensional 'Mixed Bed' Model for *Trial 2* at 701°C; (a) 1.5 rpm; (b) 3 rpm; (c) 5 rpm: Bed Temperatures in °C.

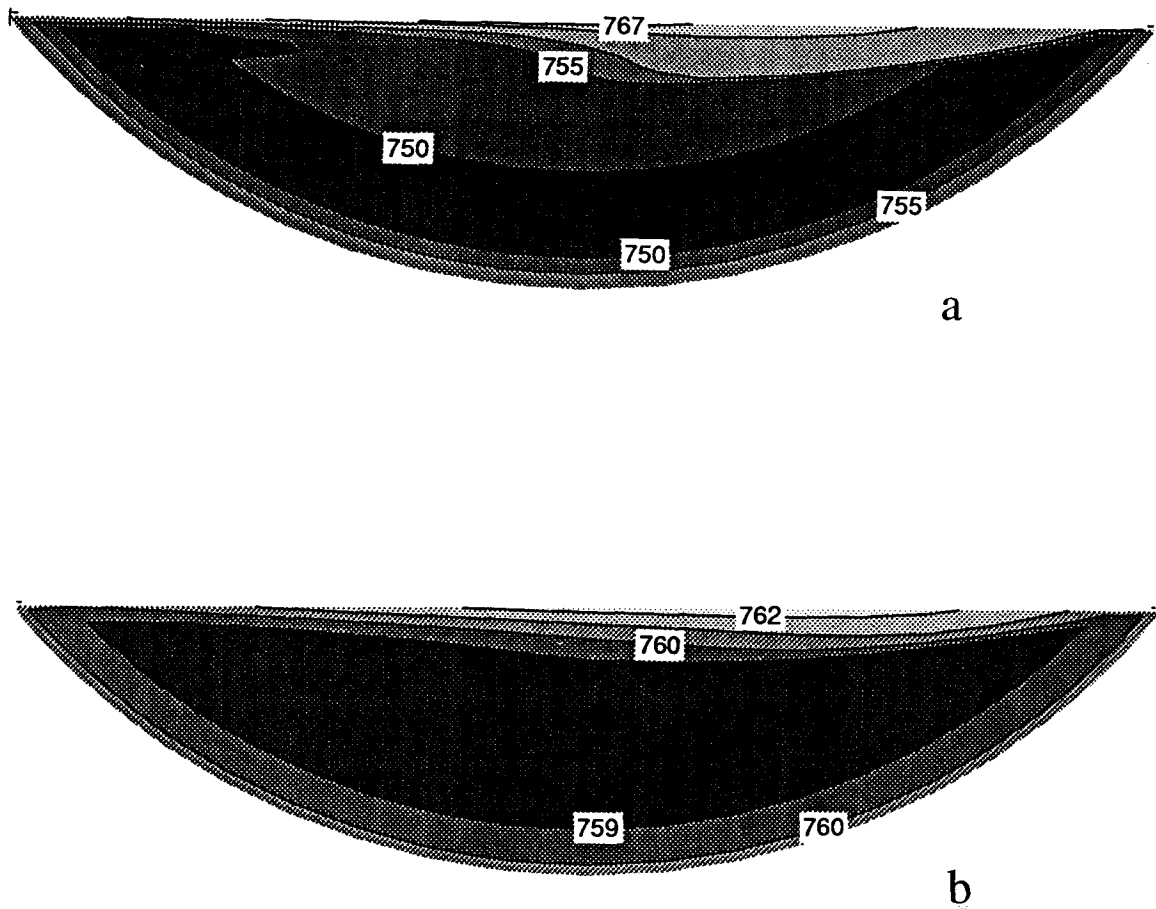


Figure 7.16. Contour Plots of Temperature Distribution Predicted by Two-dimensional 'Mixed Bed' Model Using Gas Temperature of 953°C for *Trial 2*: (a) at 1.5 rpm: (a); (b) 5 rpm: Bed Temperatures in °C.

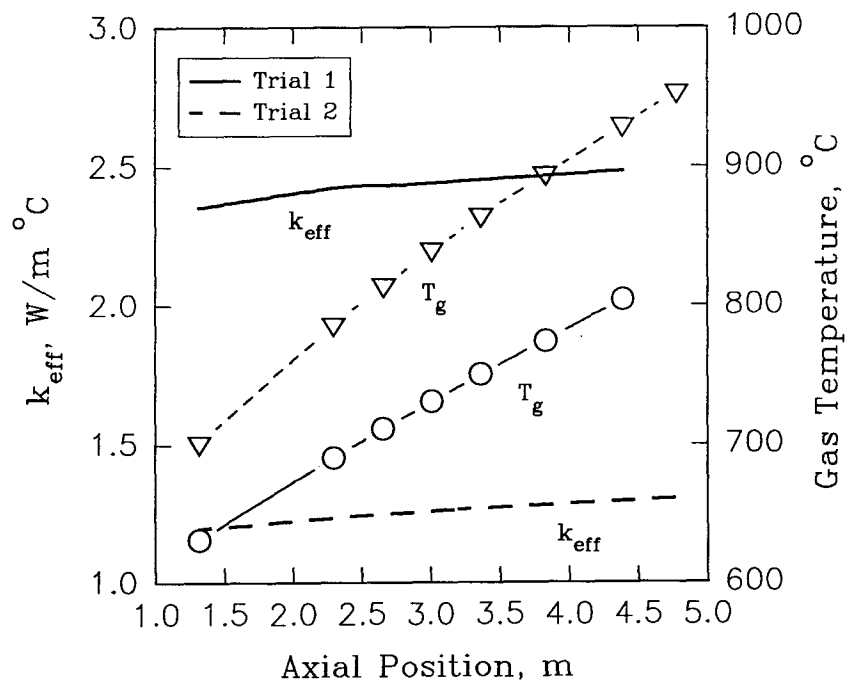


Figure 7.17. Predicted Thermal Conductivity (enhanced) as Function of Axial Position; Superimposed are Freeboard Gas Temperature Profiles.

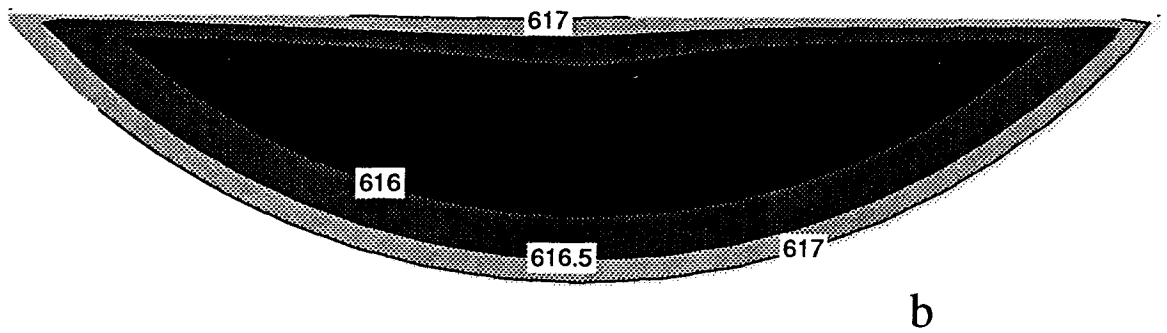
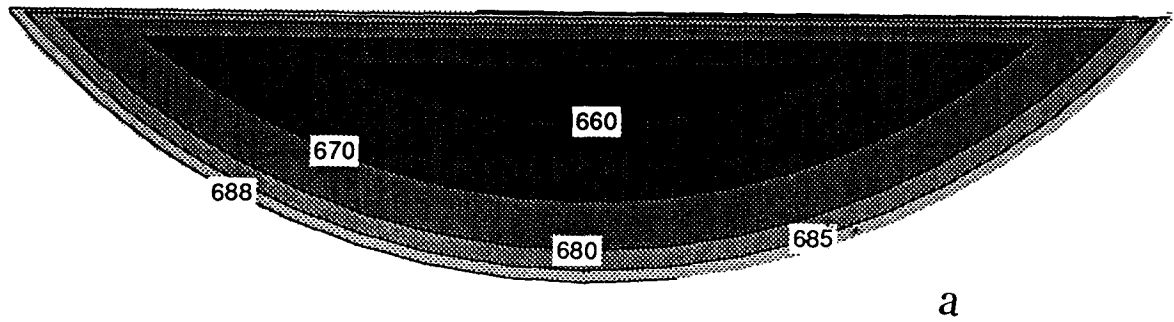


Figure 7.18. Contour Plots of Temperature Distribution Resulting from Running Two-dimensional Model without y-wise Velocity Vector but with Enhanced Bed Thermal Conductivity; *Trial 1* with $T_g = 804^\circ\text{C}$: (a) at 1.5 rpm; (b) 5 rpm: Bed Temperatures in $^\circ\text{C}$.

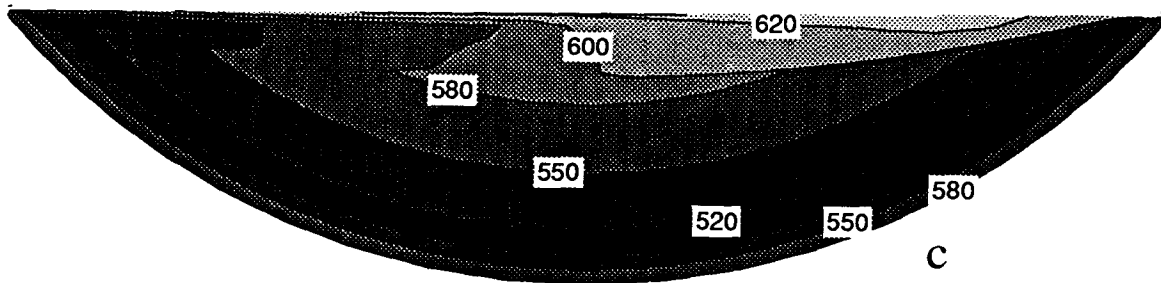
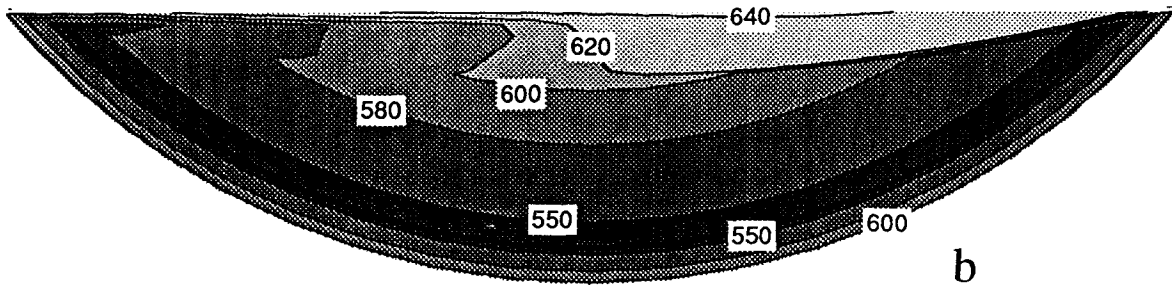
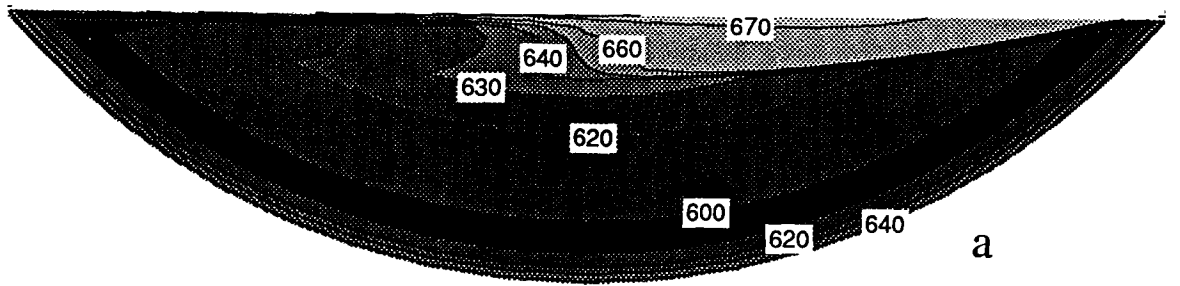


Figure 7.19. Contour Plots of Temperature Distribution Within the Bed Resulting from Running Two-dimensional Model with Percolation Velocity as y-wise Velocity and no Bed Enhanced Thermal Conductivity; *Trial 1* with $T_g = 804^\circ\text{C}$: (a) at 1.5 rpm; (b) 3 rpm; (c) 5 rpm: Bed Temperatures in $^\circ\text{C}$.

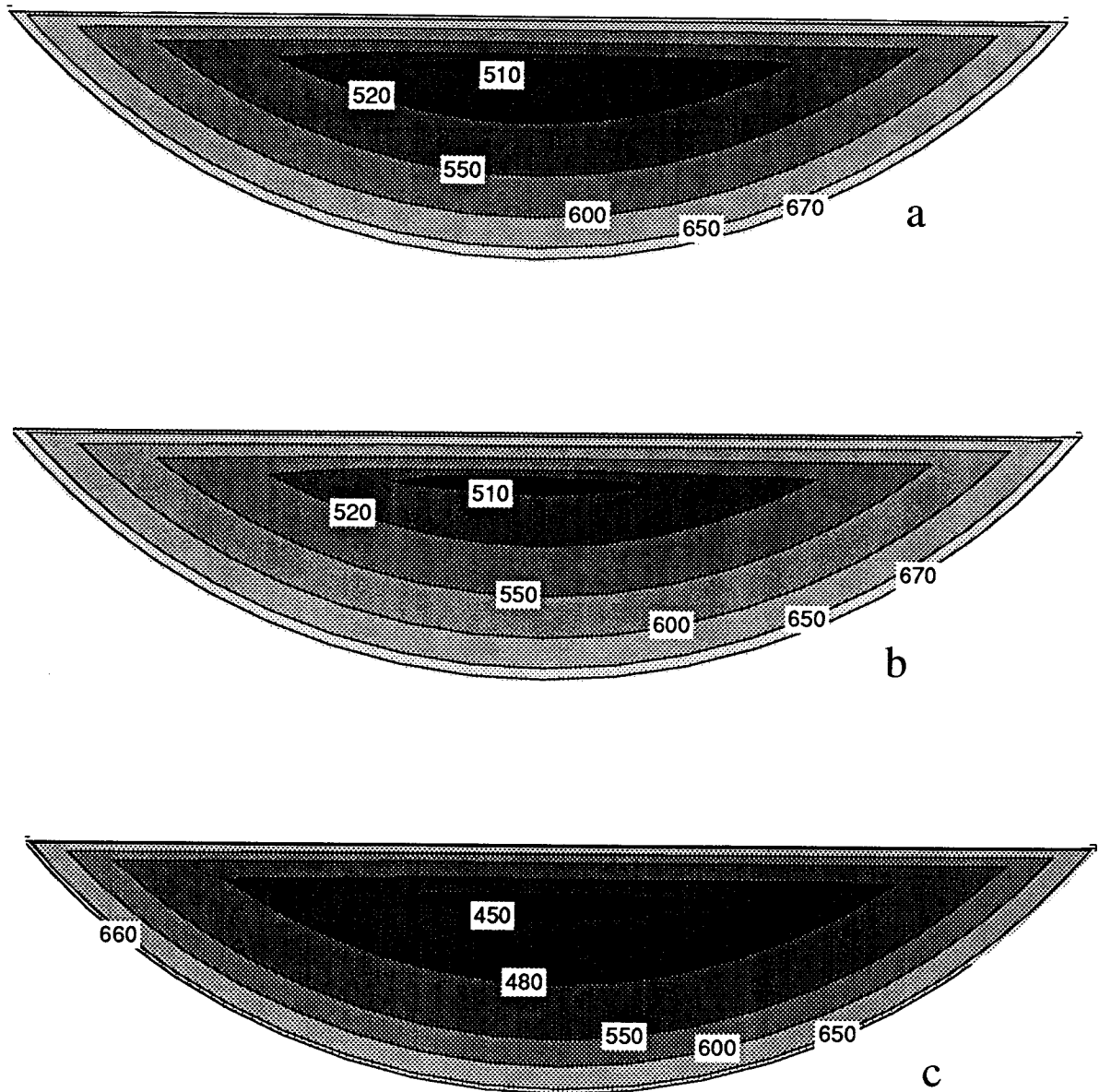


Figure 7.20. Contour Plots of Temperature Distribution Resulting from Running Two-dimensional Model without y-wise Velocity and no Bed Enhanced Thermal Conductivity; *Trial 1* with $T_g = 804^\circ\text{C}$: (a) at 1.5 rpm; (b) 3 rpm; (c) 5 rpm: Bed Temperatures in $^\circ\text{C}$.

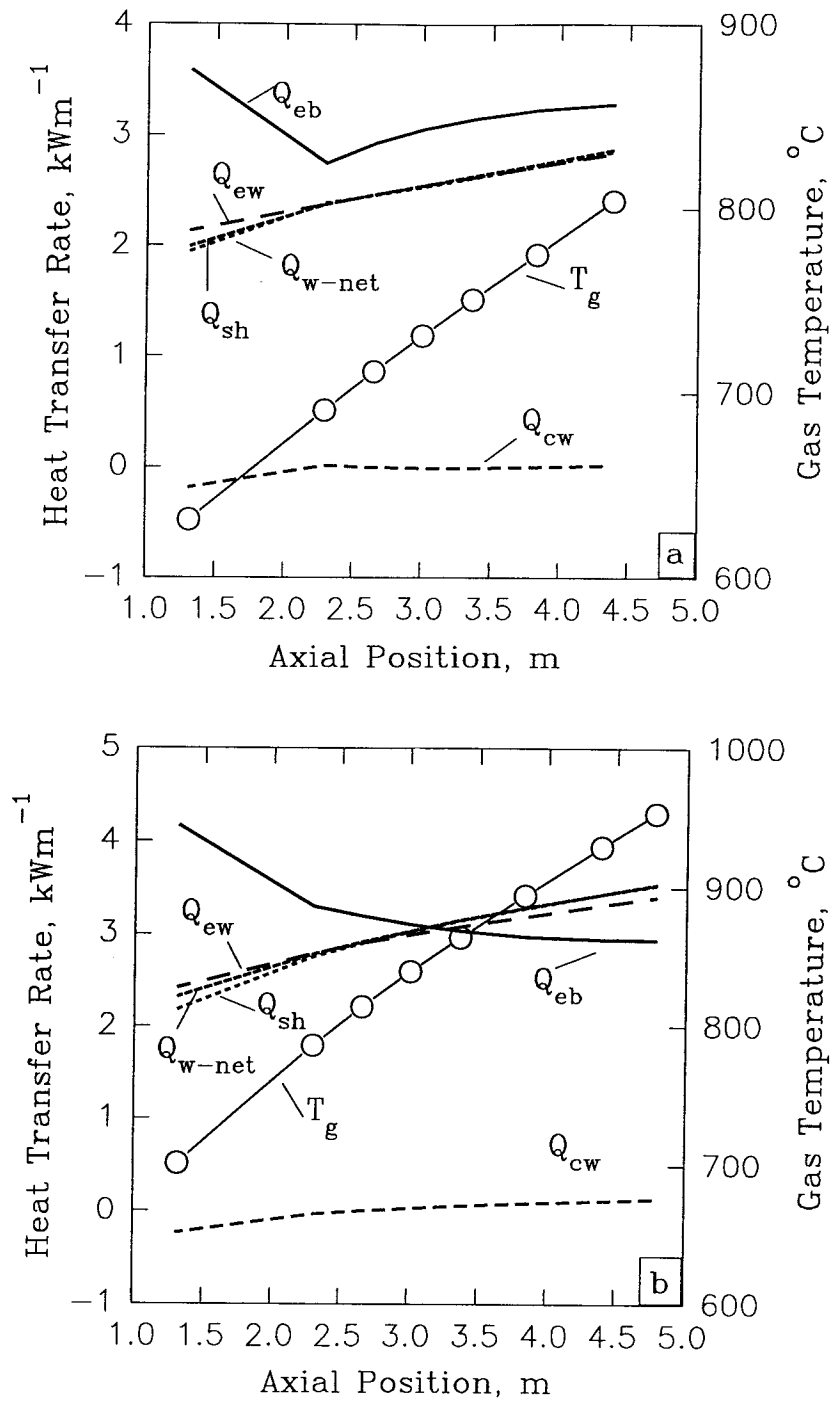


Figure 7.21. Predicted Heat Transfer Rates as Function of Axial Position with Superimposed Freeboard Gas Temperatures: (a) Trial 1, (b) Trial 2.

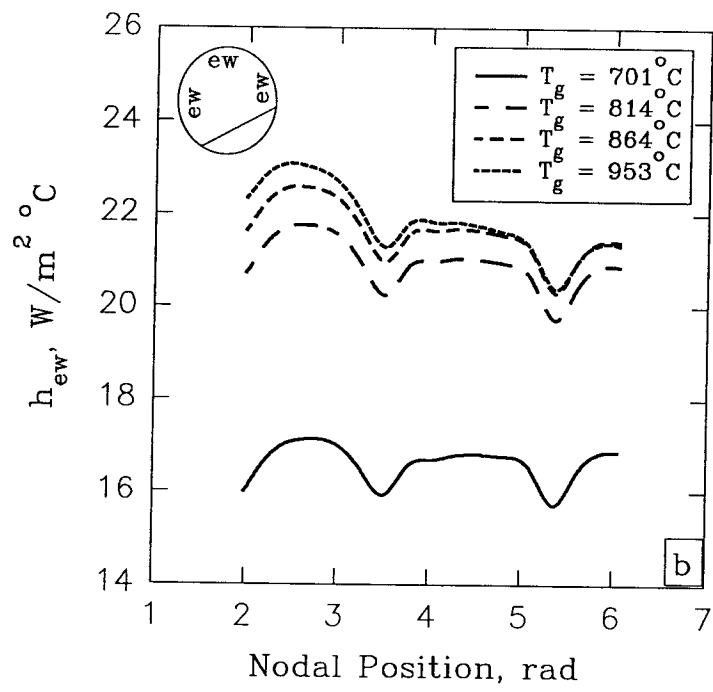
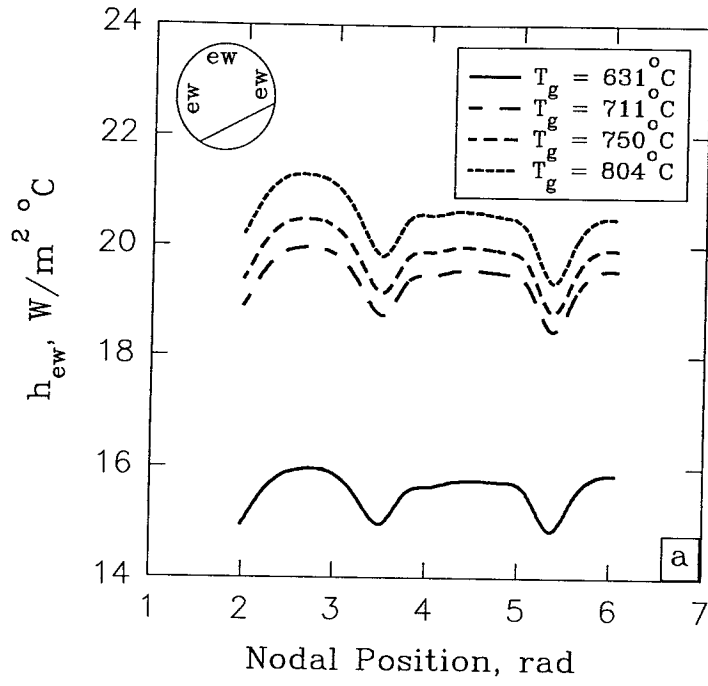


Figure 7.22. Predicted Exposed Wall Heat Transfer Coefficients as Function of Circumferential Position; (a) Trial 1, (b) Trial 2.

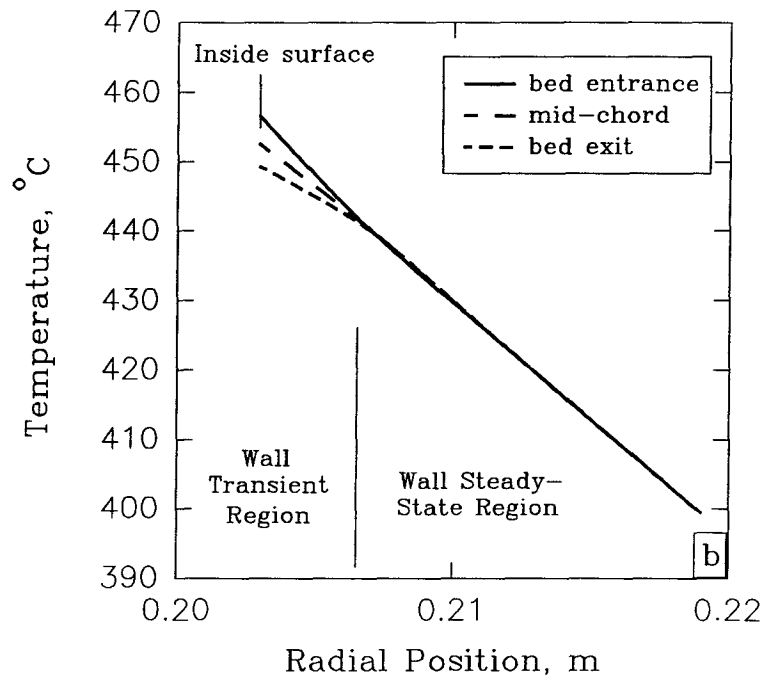
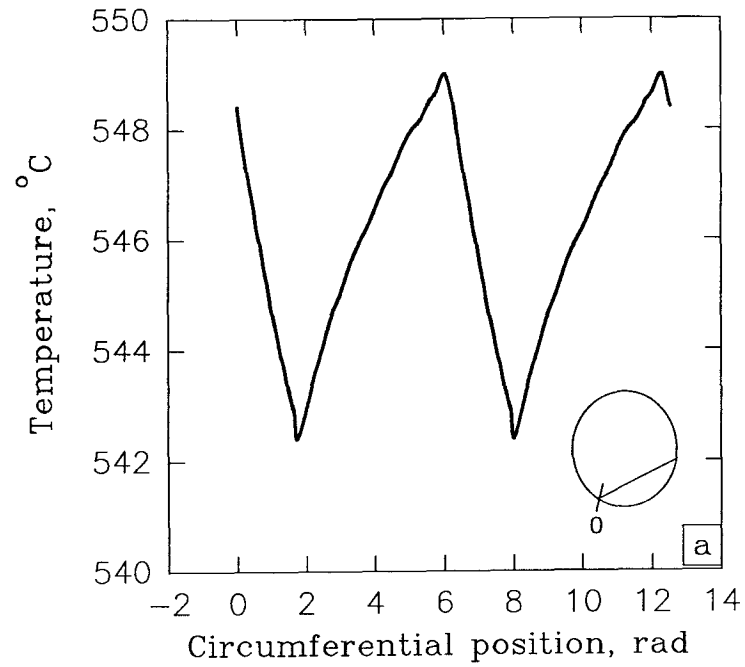


Figure 7.23. Regenerative Action of Refractory Wall: (a) Cycling Wall Surface Temperature as Function of Circumferential Position; (b) Covered Wall Temperature Gradients.

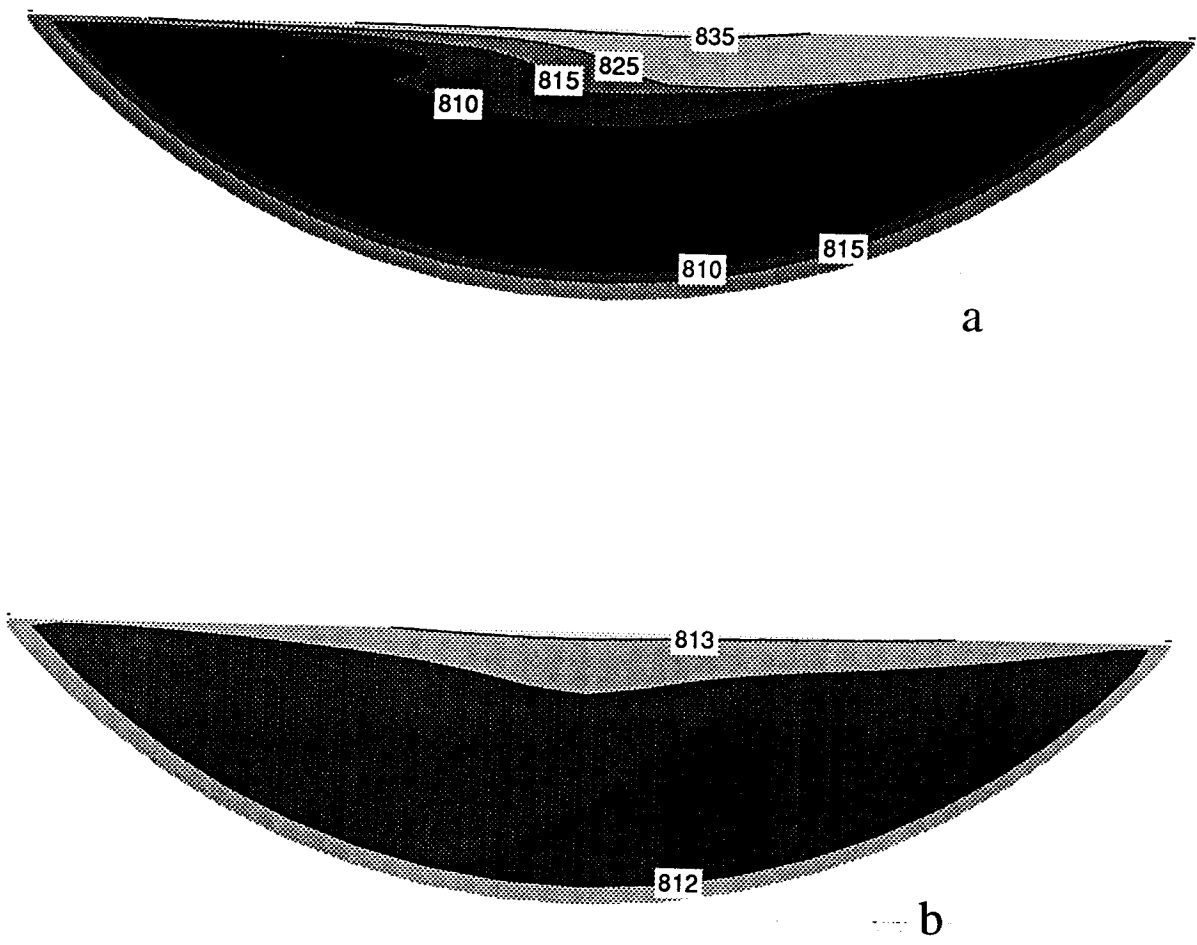


Figure 7.24. Contour Plots of Temperature Distribution in a 'Mixed Bed' at Local Gas Temperature of 1000°C: (a) 1.5 rpm; (b) 5 rpm: Bed Temperatures in °C.

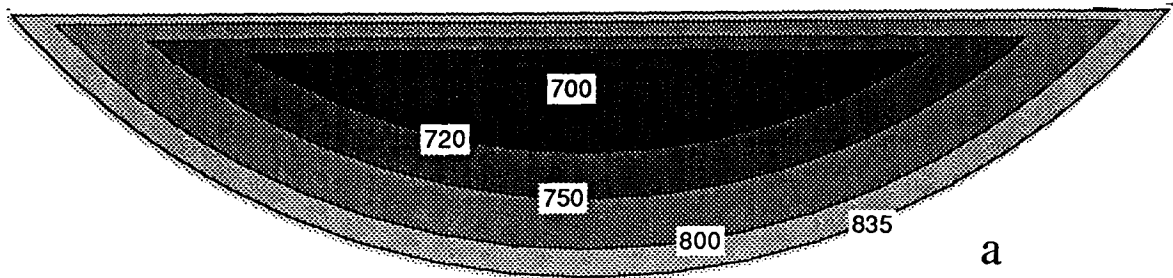


Figure 7.25. Contour Plots of Temperature Distribution in a 'Segregated Bed' at Local Gas Temperature of 1000°C: Bed Temperatures in °C.

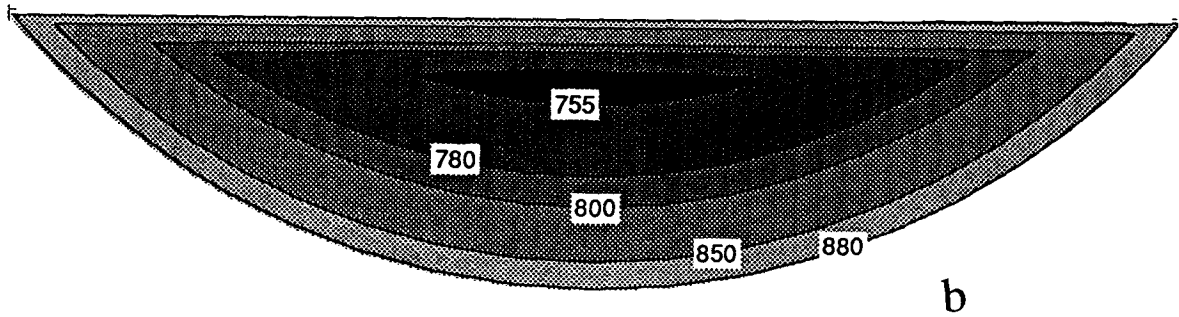


Figure 7.26. Contour Plots of Temperature Distribution in a 'Segregated Bed' at Local Gas Temperature of 1050°C: Bed Temperatures in °C.

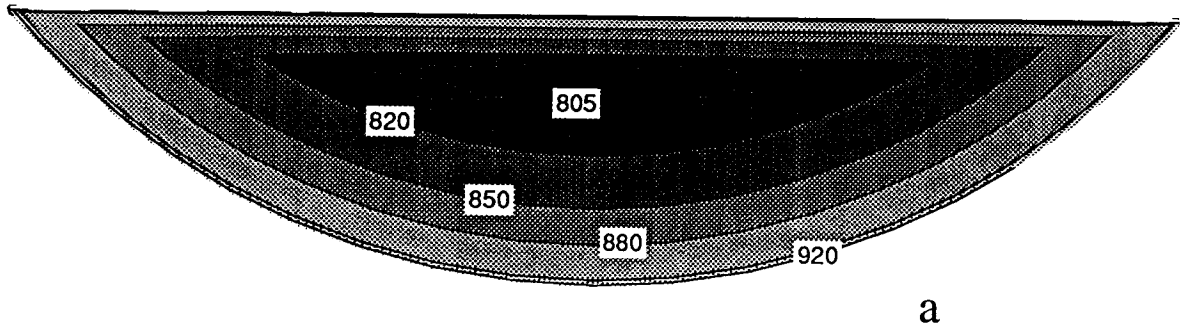


Figure 7.27. Contour Plots of Temperature Distribution in a 'Segregated Bed' at Local Gas Temperature of 1100°C: Bed Temperatures in °C.

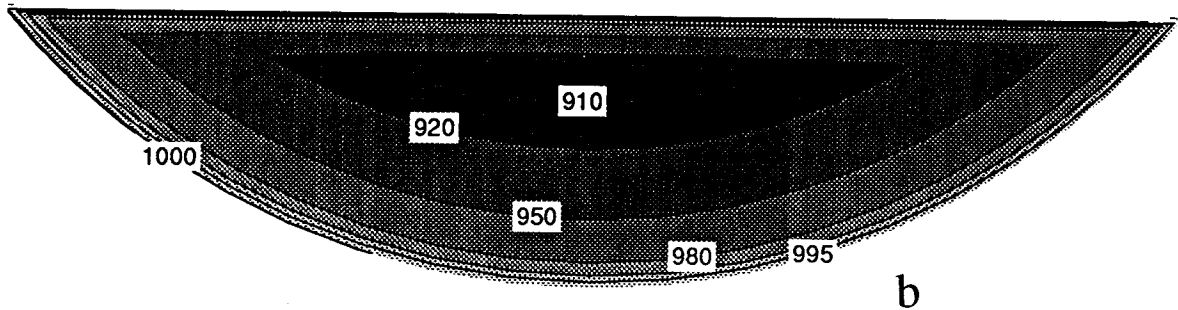


Figure 7.28. Contour Plots of Temperature Distribution in a 'Segregated Bed' at Local Gas Temperature of 1200°C: Bed Temperatures in °C.

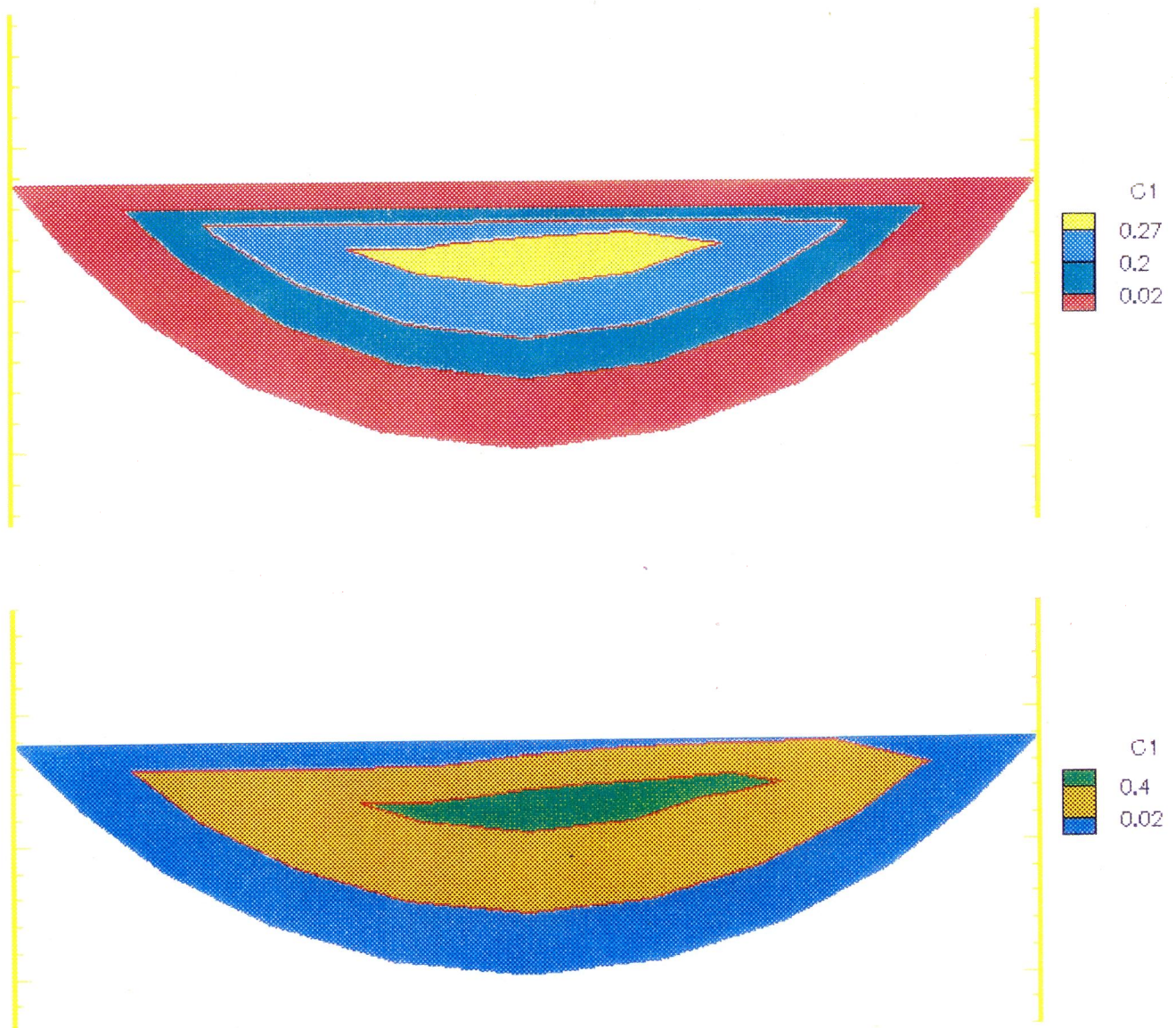


Plate 1. Contour Plots of Fines Concentration at Jetsam Loading of 10%:
Top - 0.41 m I.D Drum; *Bottom* - 2.5 m I.D Drum.

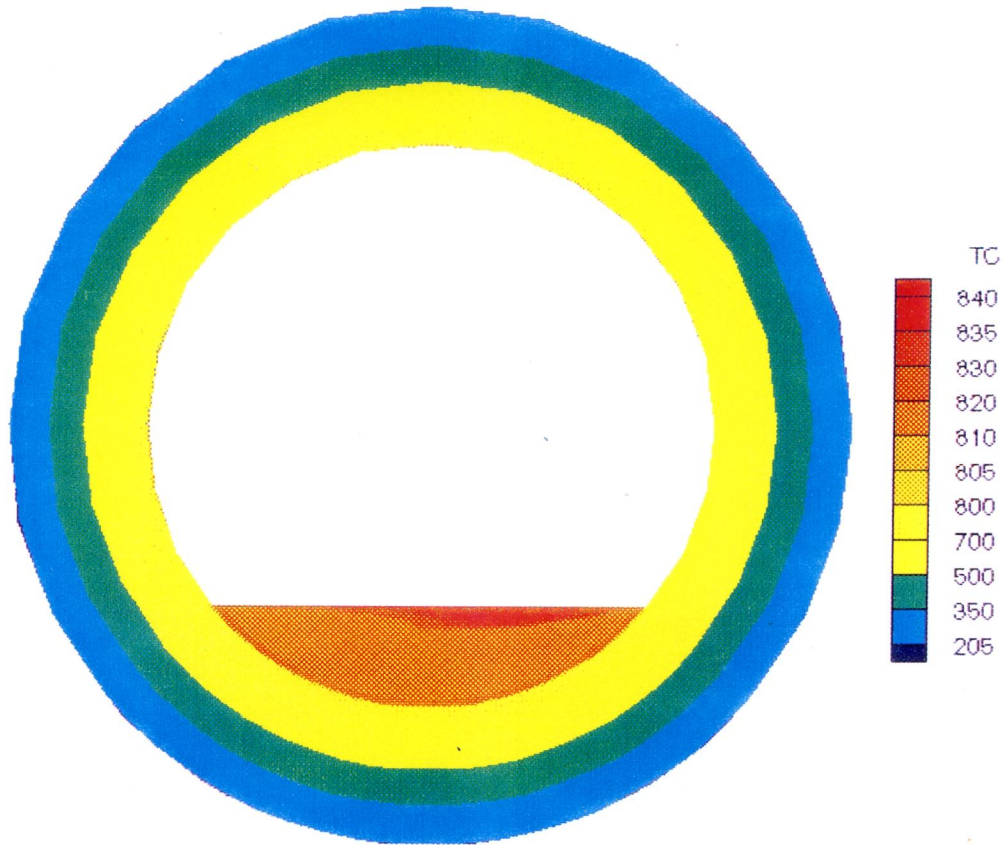


Plate 2. Contour Plots of Temperature Distribution in a Cross-section at Local Gas Temperature of 1000°C: Pilot Kiln 12% Fill @ 1.5 rpm (Bed Temperatures in °C).

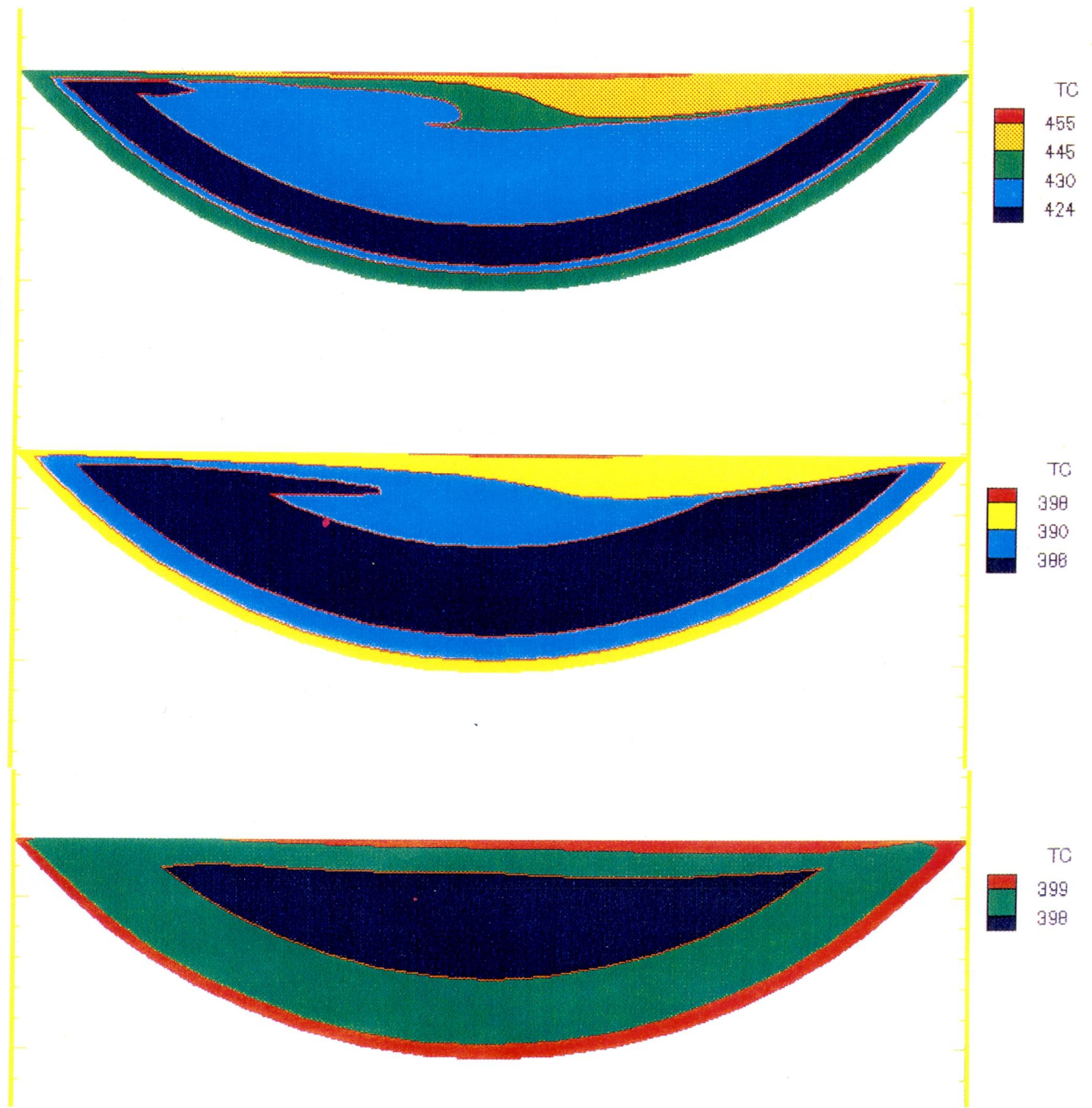


Plate 3. Contour Plots of Temperature Distribution in a 'Mixed Bed' at Local Gas Temperature of 631°C : Pilot Kiln 12% Fill @: *Top* - 1.5 rpm; *Center* - 3 rpm; *Bottom* - 5 rpm (Bed Temperatures in $^{\circ}\text{C}$).

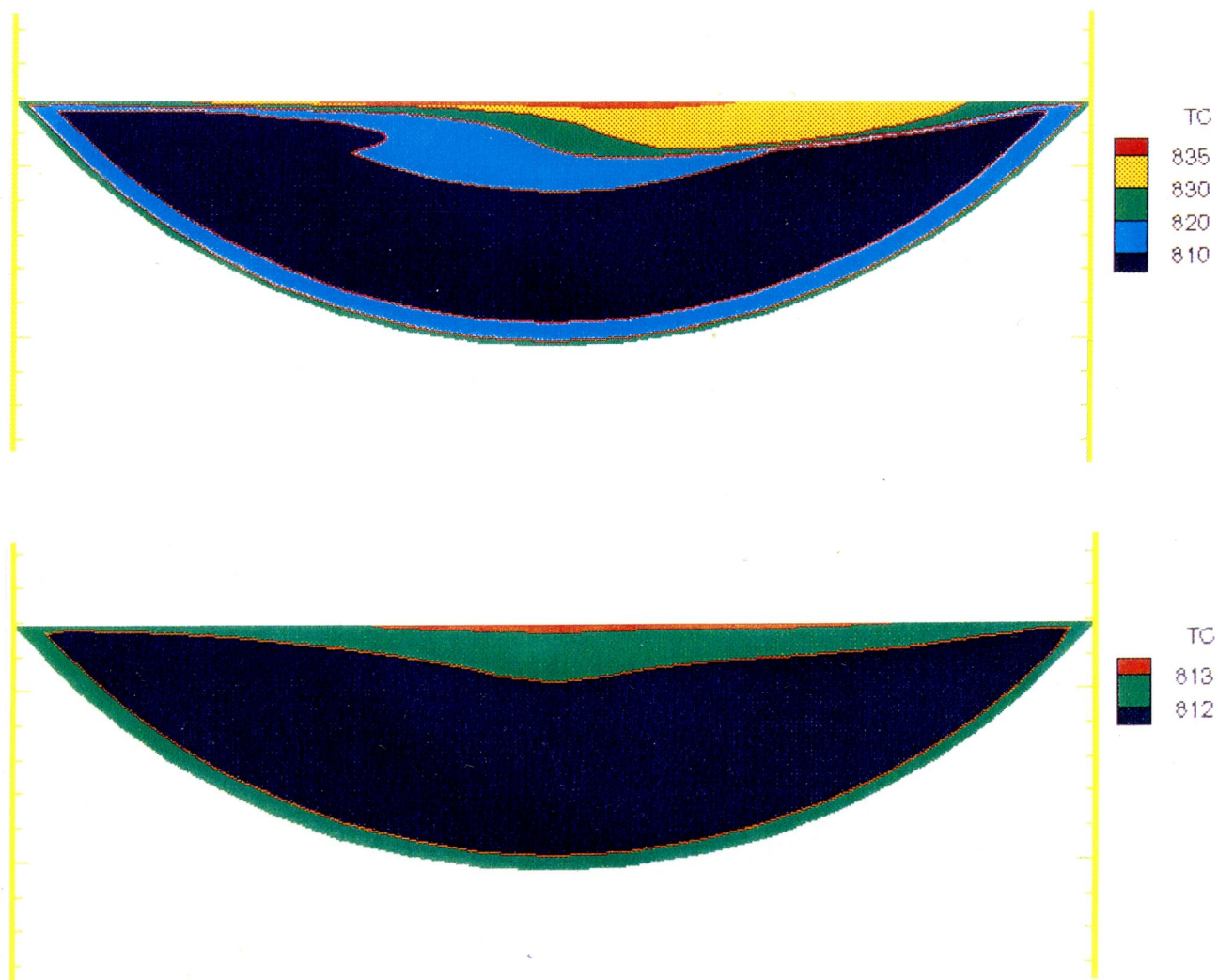


Plate 4. Contour Plots of Temperature Distribution in a 'Mixed Bed' at Local Gas Temperature of 1000°C: Pilot Kiln 12% Fill @: *Top* - 1.5 rpm; *Bottom* - 5 rpm (Bed Temperatures in °C).

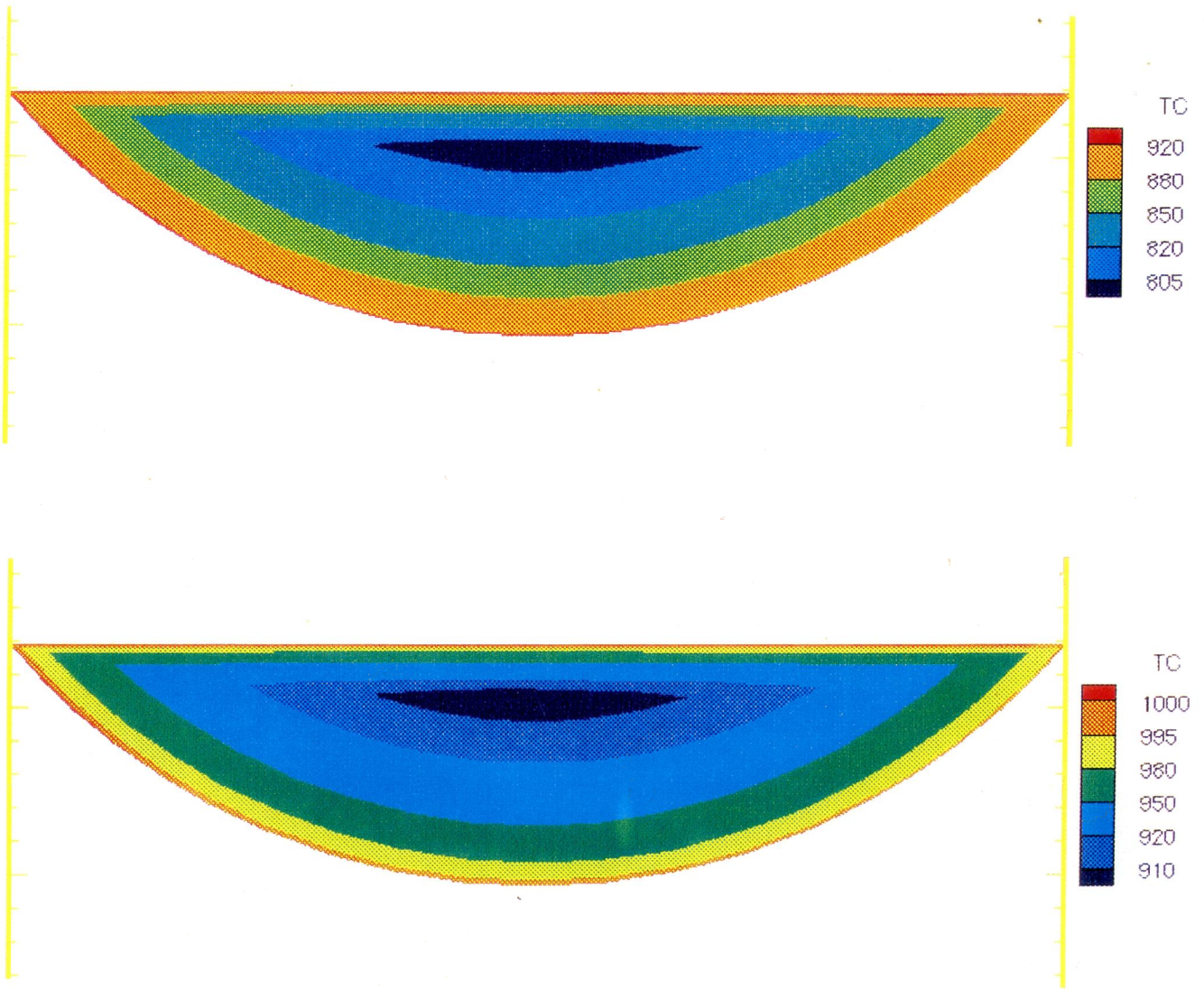


Plate 5. Contour Plots of Temperature Distribution in a 'Segregated Bed.'
Top - Local Gas Temperature of 1100°C; *Bottom* - Local Gas Temperature of 1200°C (Bed Temperatures in °C).

CHAPTER 8. CONCLUSIONS AND RECOMMENDATIONS

This Chapter summarizes the significant contributions made towards knowledge on rotary kiln transport phenomena. Based upon these accomplishments, further work required to improve our understanding and predictive capabilities of rotary kiln processes is recommended.

8.1 Conclusions

The complex flow of granular material in the cross-section of a rotary kiln, particle size segregation, and the concomitant effect of these phenomena on the distribution of energy within the granular bed have been investigated by means of mathematical models complemented by experimental studies. The components of the global model comprised (i) a granular flow model, (ii) a mixing and segregation model, and (iii) a heat transfer model. The latter combined the results of the former two models to develop a two-dimensional thermal model for the bed. The combination of this cross-sectional thermal model with existing axial models (one dimensional) produced a quasi-three-dimensional thermal model which has advanced our understanding of mechanisms of energy redistribution within the bed after this energy has been transferred from the freeboard gases and the rotating wall through the respective interfaces. Results from the granular flow model were in good agreement with particle velocity measurements made in a 0.964 m I.D rotary drum with the help of optical fibre probes. The predicted extent of a segregated core of fine particles in a kiln cross-section agreed with experimental results of Henein (1980). The thermal model results also compared favorably with temperatures measured in a 0.406 m I.D pilot kiln.

By choosing a local gas temperature, corresponding to any axial position of the kiln, detailed temperature distribution within the kiln cross-section, which results due to the effect of the particle flow field, particle mixing or segregation, and the heat transfer interactions, could be predicted. It is concluded that the bed material will be isothermal only when it comprises spherical particles of almost equal sizes. Under these conditions the bed behavior represents an idealized rolling bed and self diffusion in the active layer is enhanced. Because the mass diffusion coefficient, D , due to velocity fluctuations (estimated from the granular flow model) increases with kiln speed, the

bed effective thermal conductivity is increased by a factor $\rho D C_p$, and as a result, the bed tends to isothermal conditions with increased rotational rate. For segregated beds, which result from particle size differences (and also density differences, resilience, etc), the particles flow in streamlines, self diffusion is curtailed, and temperature gradients (about 100 °C for pilot kiln) result within the bed. The cooler region of the bed cross-section coincides with the segregated core where most of the finer particles are located.

This finding is equivalent to saying that, statistically, under the conditions of idealized rolling, all the particles have equal chances of exposure to the freeboard gas and temperature uniformity results. But for real situations in kiln operations, where particle sizes are neither uniform nor evenly spherical, temperature nonuniformities result in the bed. This is to say that the assumption of bed temperature uniformity at each axial position of the kiln, which has been imposed in existing models, although expedient to modelling, is deficient. The findings explain the reason for nonuniform product quality encountered in rotary kiln processes which are driven by particle size segregation, e.g., the process of limestone calcination.

Several other important conclusions, and new knowledge acquired, are as follows:

- (i) A novel experimental campaign has been successfully launched to study granular flow behavior in rotary kilns. Novel techniques include accurate measurements of flow characteristics in the transverse plane, using optical fibre probes, thereby avoiding errors which are associated with the use of visual techniques (e.g., particle filming) and also end-piece effects.
- (ii) Although the mathematical model for the granular flow adopts existing chute flow theories, the approximation of the active layer flow to thin flows and the application of integro-momentum equations to solve for the active layer depth and velocity, as well as mass diffusion, are novel approaches to predicting rotary kiln transport phenomena.
- (iii) It is found that the solids concentration (or voidage) is the most sensitive parameter governing the flow behavior. Particle velocity and the depth of the active layer increase with increased

dilation. The coefficient of restitution of the particles, which depends on the particle shape and elastic properties, determines the dynamic angle of repose. The higher the coefficient of restitution, the lower the angle of repose; this means that less energy would be required to move a bed of a material with a high coefficient of restitution.

(iv) The mathematical model for particle mixing and segregation, developed for this work, is unique because it is capable of making quantitative predictions of jetsam (fines) concentration gradients, and the extent of segregation in the cross-section of the kiln. Earlier models which have appeared in the literature, follow the probabilistic approach, which does not address problems of scale-up. It has been shown that eliminating segregation through density compensation (as suggested by earlier workers) is possible but not practicable in industrial kilns.

(v) Because of the prediction of particle velocity and segregation, it has been possible, for the first time, to construct a two-dimensional thermal model for each transverse slice of the kiln. This model allows for the possibility of extending existing heat transfer models (e.g., Gorog *et al.*, 1981 and Barr *et al.*, 1989) to the entire cross-section of the bed. The resultant quasi three-dimensional rotary kiln model, is capable of simulating conditions within the bed without the necessity of rigorously accounting for the very complex flow and combustion phenomena of the freeboard. It demonstrates that thermal gradients in the bed's transverse plane are predominantly segregation driven. Some of the features of the thermal model which are not found in existing rotary kiln models include (a) the estimation of the advective components of energy redistribution, and (b) the effect of segregation on temperature nonuniformities within the bed.

8.2 Recommendations

Based on the information and new knowledge obtained from this work, the following recommendations are made for future work:

- (i) An extension of the bed thermal model to include kinetics of heterogeneous reactions (e.g., shrinking core model). This will improve our knowledge on product quality. In addition, it will throw some light on dusting and accretion which result from chemical reactions within the bed.
- (ii) The flow model should be extended to incorporate radial profiles for granular temperature, and for solids concentration, in order to predict active layer mass diffusion in the two-dimensional field rather than one-dimensional (a function of chord length) as it presently stands.
- (iii) More flow experiments should be carried out in different size kilns in order to elucidate the effect of kiln size on flow characteristics.
- (v) On long term basis, the equations of motion employed for the granular flow must be solved in full and should incorporate Coriolis terms. This may possibly elucidate the origin of wave formation in kilns and the possible explanation of axial banding (not studied in the current work).

LITERATURE CITED

- Ahn, H., C.E. Brennen, and R.H. Sabersky (1991). "Measurements of Velocity, Velocity Fluctuation, Density, and Stresses in Chute Flows of Granular Materials," *Applied Mechanics*, **58**, 792-803.
- Ames, W.F. (1977). *Numerical Methods for Partial Differential Equations*, 2d ed., Academic Press, New York.
- Akerman, K., P. Hoffman, and W. Zablony (1966). "Mechanism and Rate of Passage of Materials in Rotary Kilns," *Brit. Chem. Eng.*, **11**(1), 26-29.
- Alonso, M., M. Satoh, and K. Miyanami (1991). "Optimum Combination of Size Ratio, Density Ratio and Concentration to Minimize Free Surface Segregation," *Powder Technol.*, **68**, 145-152.
- Anderson, D.A., J.C. Tannehill, and R.H. Pletcher (1984) *Computational Fluid Mechanics and Heat Transfer*, Hemisphere, New York.
- Arpaci, V.S. (1966). *Conduction Heat Transfer*, Addison-Wesley, London.
- Bagnold, R.A. (1954). "Experiments on a Gravity-free Dispersion of Large Solids Spheres in a Newtonian Fluid Under Shear," *Proc. R. Soc. London*, **A225**, 49-63.
- Barr, P.V. (1986). *Heat Transfer Processes in Rotary Kilns*, Ph.d Dissertation, The University of British Columbia, Vancouver.
- Barr, P.V., J.K. Brimacombe, and A.P. Watkinson (1989). "A Heat-Transfer Model for the Rotary Kiln: Part I. Pilot Kiln Trials," *Met. Trans. B*, **20B**, 391-402.
- ____ (1989). "A Heat-Transfer Model for the Rotary Kiln: Part II. Development of the Cross-Section Model," *Met. Trans. B*, **20B**, 403-419.
- Batchelor, G.K. (1967). *An Introduction to Fluid Dynamics*, Cambridge University Press, London.
- Masliyah, J. and J. Bridgwater (1974). "Particle Percolation: A Numerical Study," *Trans. Instn Chem Engrs*, **52**, 31-42.
- Boateng, A.A., W.P. Walawender, and L.T. Fan (1990). "Devolatilization Studies of Rice Hulls in a TGA and a Fluidized Bed," In: *Biomass for Energy & Industry*, %-th EC Conference, Vol. 2, *Conversion and Utilization*. Ed. G. Grassi, et al., Elsevier, London, 930-934.
- Bridgwater, J. (1976). "Fundamental Powder Mixing Mechanisms," *Powder Technol.*, **15**, 215-236.
- Bridgwater, J. and N.D. Ingram (1971). "Rate of Spontaneous Inter-Particle Percolation," *Trans. Instn Chem. Engrs*, **49**, 163-169.
- Bridgwater, J., M.H. Cooke, and A.M. Scott (1978). "Inter-Particle Percolation: Equipment Development and Mean Percolation Velocities," *Trans IChemE*, **56**, 157-167.
- Bridgwater, J., W.S. Foo and D.J. Stephens (1985). "Particle Mixing and Segregation in Failure Zones - Theory and Experiment," *Powder Technol.*, **41**, 147-158.

- Brimacombe, J.K. (1989). "The Extractive Metallurgist in an Engineering World of Materials," *Met Trans B*, **20B**, 291-313.
- Brimacombe, J.K. and A.P. Watkinson (1979). "Heat Transfer in a Direct Fired Rotary Kiln: Part I - Pilot Plant and Experimentation," *Met Trans B*, **9B**, 201-208.
- Campbell, C.S. and C.E. Brennen (1983). "Computer Simulation of Shear Flows of Granular Material," In *Mechanics of Granular Materials: New Models and Constitutive Relations* (ed. Jenkins, J.T. and M. Satake), Elsevier.
- Campbell, C.S., and A. Gong (1986). "The Stress Tensor in a Two-Dimensional Granular Shear Flow," *Fluid Mech.* **164**, 107-125.
- Chung, B.T.F, L.T. Fan, and C.L. Hwang (1972). "A Model of Heat Transfer in Fluidized Beds," *Heat Transfer*, February, 105-110.
- Cowin, S.C. (1974). "A Theory for the Flow of Granular Materials," *Powder Technol.*, **9**, 62-69.
- Davies, T.R.H. (1986). "Large Debris Flow: A Macro-Viscous Phenomenon," *Acta Mechanica*, **63**, 161-178.
- de Jong, G. de J. (1964). "Lower Bound Collapse Theorem and Lack of Normality of Strain Rate to Yield Surface for Soils," In *Rheology and Soil Mechanics Symposium*, Grenoble, 69-78.
- Diessler, R.G. and C.S. Eian (1952). National Advisory Comm., Aeronaut., Rm. ESZCJOS.
- Donald, M.B. and B. Roseman (1962). "Mixing and De-mixing of Solid Particles: I - Mechanisms in a Horizontal Drum Mixer," *Brit. Chem. Engr.*, **7**(10), 749-753.
- Fan, L.T. and J.R. Too (1981). "Stochastic Analysis and Modeling of Solids Mixing," *Proceedings of International Symposium on Powder Technology '81.*, 697-711.
- Fan, L.T. and R.H. Wang (1975). "On Mixing Indices," *Powder Technol.*, **11**, 27-32.
- Ferron, J.R. and D.K. Singh (1991) "Rotary Kiln Transport Processes," *AIChE J.*, **37**, 774-758.
- Ferron, J.R. *Personal Communications*.
- Friedman, S.J. and N.R. Marshall, Jr. (1949). "Studies in Rotary Drying I. Holdup and Dusting," *Chem. Eng. Progr.*, **45**(8), 482-493.
- Gauthier, C. (1991). *Etude du Mouvement Granulaire dans Cylindre en Rotation*, M.Sc Thesis, Universite du Quebec.
- Gorog, J.P., J.K. Brimacombe, and T.N. Adams (1981). "Radiative Heat Transfer in Rotary Kilns," *Met Trans B*, **12B**, 55-70.
- Gorog, J.P., T.N. Adams, and J.K. Brimacombe (1982). "Regenerate Heat Transfer in Rotary Kilns," *Met Trans B*, **13B**(2), 153-163.
- Gorog, J.P., T.N. Adams, and J.K. Brimacombe (1983). "Heat Transfer from Flames in a Rotary Kiln," *Met Trans B*, **14B**, 411-424.
- Guruz, H.K. and N. Bac (1981). "Mathematical Modeling of Rotary Cement Kilns by the Zone Method," *Can J. Chem Eng*, **59**, 540-548.

- Gibilaro, L.G. and P.N. Rowe (1974) "A Model for Segregating Gas Fluidised Bed," *Chem Eng. Sci.*, **29**, 1403-1412.
- Greenspan, H.P. (1968) *The Theory of Rotating Fluids*, Cambridge University Press, Cambridge.
- Haff, P.K. (1983). "Grain Flow as a Fluid-mechanical Phenomenon," *Fluid Mech.*, **134**, 401-430.
- Hanes, D.M. (1986). "Grain Flows and Bed-Load Sediment Transport: Review and Extension," *Acta Mechanica*, **63**, 131-142.
- Hanes, D.M. and A.J. Bowen (1985). "A Granular-Fluid Model for Steady Intense Bed-Load Transport," *J. Geophysical Research*, **90**(C5), 9149-9152.
- Henein, H., J.K. Brimacombe, and A.P. Watkinson (1983a). "Experimental Study of Transfer Bed Motion in Rotary Kilns," *Met Trans B*, **14B**(6), 191-205.
- _____ (1983b). "The Modeling of Transverse Solids Motion in Rotary Kilns," *Met Trans B*, **14B**(6), 207-220.
- Henein, H., J.K. Brimacombe, and A.P. Watkinson (1985). "An Experimental Study of Segregation in Rotary Kilns," *Met Trans B*, **16B**, p 763
- Hogg, R., K. Shoji, and L.G. Austin (1974). "Axial Transport of Dry Powders in Horizontal Rotating Cylinders," *Powder Technol.*, **9**, p 99.
- Holman, J.P. (1981). *Heat Transfer*, McGraw-Hill, New York.
- Hottel, H.C. and E.S Cohen (1958). "Radiant Heat Exchange in a Gas-filled Enclosure: Allowance for Nonuniformity of Gas Temperature," *J. AIChE*, **4**, 3-14.
- Hottel, H.C. and A. Sarofim (1967). *Radiative Transfer*, McGraw Hill, N.Y., N.Y.
- Hutter, K., F. Szidarovszky and S. Yakowitz (1986). "Plane Steady Shear Flow of a Cohesionless Granular Material Down an Inclined Plane. A Model for Avalanches. Part II: Numerical Results," *Acta Mechanica*, **63**, 87-112.
- Jenkins, B.G. and F.D. Moles (1981). "Modelling of Heat Transfer from Large Enclosed Flame in a Rotary Kiln," *Trans IChemE*, **59**, 17-25.
- Johnson, P.C. and R. Jackson (1987). "Frictional-Collisional Constitutive Relations for Granular Materials, with Application to Plane Shearing," *J. Fluid Mech.*, **176**, 67-93.
- Kanatani, K. (1979). "A Continuum Theory for the Flow of Granular Materials," *Theoretical and Applied Mechanics*, **27**, 571-578.
- Khodorov, E.I. (1961). "Entrainment of Materials from Rotary Kilns," *Khim Prom*, p 416.
- Kramers, H. and P. Crockewit (1952). "The Passage of Granular Solids through Inclined Rotary Kilns," *Chem. Eng. Sci.*, **1**(6), p. 259.
- Kunii, D. and J.M. Smith (1960). "Heat Transfer Characteristics of Porous Rocks," *AIChE J.* **6**(1), 71-78.
- Lehmberg, J., M. Hehl, and K. Schugerl (1977). "Transverse Mixing and Heat Transfer in Horizontal Rotary Drum Reactors," *Powder Technology*, **18**, 149-163

- Li, K.W. (1974a). "Entrainment in Rotary Cylinders," *AIChE J.*, **20**(5), 1031-1034.
- (1974b). "Application of Khodorov's and Li's Entrainment Equations to Rotary Coke Calciners," *AIChE J.*, **20**(5), 1017-1020.
- Lun, C.K.K., S.B. Savage, D.J. Jeffrey and N. Chepurnyi (1984). "Kinetic Theories for Granular Flow: Inelastic Particles in Couette Flow and Slightly Inelastic Particles in a General Flowfield," *J. Fluid Mech.* **140**, 223-256.
- Mandl, G. and R.F. Luque (1970). "Fully Developed Plastic Shear Flow of Granular Materials," *Geotechnique*, **20**(3), 277-307.
- Manitius, A., E. Kurcysz, and W. Kawecki (1974). "Mathematical Model of the Aluminum Oxide Rotary Kiln," *Ind. Eng. Chem. Process Des. Dev.*, **13**(2), 132-142.
- Mu, J. and D.D. Perlmutter (1980). "The Mixing of Granular Solids in a Rotary Cylinder," *AIChE J.*, **26**(6), 928-934.
- Nityanand, N., B. Manley, and H. Henein (1986). "An Analysis of Radial Segregation for Different Sized Spherical Solids in Rotary Cylinders," *Met Trans B*, **17B**, 247-257.
- Ogawa, S., A. Umemura, and N. Oshima (1980). "On The Equations of Fully Fluidized Granular Materials," *Z. Angew. Math Phys.* **31**, 187-202.
- Perron, J., V. Potocnik, and R.T. Bui (1988). "Modeling of the Coke Calcining Kiln," Presented 27th Annual Conf. of Metallurgists, CIM, Montreal.
- Patanker, S.V. (1980). *Numerical Heat Transfer and Fluid Flow*, Hemisphere, New York.
- Perron, J. and R.T. Bui (1990). "Rotary Cylinders: Solid Transport Prediction by Dimensional and Rheological Analysis," *Can J. Chem Eng.*, **68**, 61-68.
- Pershin (1988). "Energy Method for Describing Granular Motion in a Smooth Rotating Cylinder," *Teoreticheskie Osnovy Khimicheskoi Tekhnologii*, **22**(2), 255-260.
- Pickering, R.W., F. Feakes, and M.L. Fitzgerald (1951). "Time for Passage of Material through Rotary Kilns," *J. appl. Chem.*, **1**, 13-19.
- Pollard, B.L. and H. Henein (1989). "Kinetics of Radial Segregation of Different Sized Irregular Particles in Rotary Cylinders," *Can. Met. Quart.*, **28**(1), 29-40.
- Reif, F. (1965). *Fundamentals of Statistical and Thermal Physics*, McGraw Hill, N.Y.
- Roscoe, K.H. (1970). "The Influence of Strains in Soil Mechanics," *Geotechnique*, **20**, 129-170.
- Roseman, B. and M.B. Donald (1962a). "Effects of Varying the Operating Conditions of a Horizontal Drum Mixer," *Brit Chem Eng*, **7**(11), 823-827.
- (1962b). "Mixing and De-mixing of Solid Particles, II - Effects of Varying the Operating Conditions of a Horizontal Drum Mixer," *Brit. Chem. Eng.*, **7**(11), p 823.
- Rutgers, R. (1965). "Longitudinal Mixing of Granular Material Flowing through a Rotary Cylinder: Part I - Description and Theoretical," *Chem Eng Sci*, **20**, 1079-1087.

- Sass, A. (1967). "Simulation of the Heat Transfer Phenomenon in a Rotary Kiln," *I&EC Process Des. & Dev.*, **6**(4), 532-535.
- Savage, S.B. (1979). "Gravity Flow of Cohesionless Granular Materials in Chutes and Channels," *J. Fluid Mech.*, **92**, 53-96.
- Savage, S.B. and D.J. Jeffrey (1981). "The Stress Tensor in a Granular Flow at High Shear Rates," *J. Fluid Mech.*, **110**, 225-272.
- Savage, S.B. (1983). "Granular Flow Down Rough Inclines - Review and Extension," In *Mechanics of Granular Materials: New Models and Constitutive Relations* (ed. Jenkins, J.T. and M. Satake), 261-282, Elsevier.
- Savage, S.B. (1984). "The Mechanics of Rapid Granular Flows," *Advances in Applied Mechanics*, **24**, (ed. Wu, T.Y. and J. Hutchinson), 289-366, Academic.
- Savage, S.B. (1988). "Symbolic Computation of the Flow of Granular Avalanches," ASME Annual Meeting, Chicago.
- Savage, S.B. (1989). "Granular Flow Materials," In *Theoretical and Applied Mechanics* (ed. Germain, P., M. Piau and D. Caillerie), 241-266, Elsevier.
- Savage, S.B. and C.K.K. Lun (1988). "Particle Size Segregation in Inclined Chute Flow of Dry Cohesionless Granular Solids," *J. Fluid Mech.*, **189**, 311-335.
- Savage, S.B. and K. Hutter (1989). "The Motion of a Finite Mass of Granular Material Down a Rough Incline," *J. Fluid Mech.*, **199**, 177-215.
- Schlichting, H. (1979). *Boundary-Layer Theory*, McGraw-Hill, New York.
- Schlunder, E.V. (1982). "Particle Heat Transfer," *Proceedings of the Seventh International Heat Transfer Conference*, Munchen, FRG.
- Schotte, W. (1960). "Thermal Conductivity of Packed Beds," *JAIChE*, **6**(1), 63-67.
- Seaman, W.C. (1951). "Passage of Solids through Rotary Kilns: Factors Affecting Time of Passage," *Chem Eng Progress*, **47**(10), 508-514.
- Singh, D.K. (1978). *A Fundamental Study of the Mixing of Solid Particles*, Ph.D Dissertation, University of Rochester, New York.
- Sondergaard, R., K. Chaney, and C.E. Brennen (1990). "Measurements of Solid Spheres Bouncing Off Flat Plates," *J. Applied Mechanics*, **57**, 694-699.
- Sood, R.R., D.M. Stokes, and R. Clark (1972). *Static Design of Coke Calcination Kilns with Special Reference to the Proposed Brazilian Kiln*, Alcan Report No. AWT-72-B1-1.
- Spencer, A.J.M. (1964). "A Theory of the Kinematics of Ideal Soils under Plane Strain Conditions," *J. Mech. Phys. Solids*, **12**, 337-351.
- Sullivan, I.D., C.G. Maier, and D.C. Ralston (1927). *Passage of Solids Particles through Rotary Cylinder Kilns*, U.S. Bureau Mines Tech. Rep. No. 384.
- Sullivan, W.N. (1973). *Heat Transfer to Flowing Granular Media*, Ph.d Dissertation, California Inst. of Technology, Pasadena.

- Sullivan, W.N. and R.H. Sabersky (1975). "Heat Transfer to Flowing Granular Media," *Int J. Heat mass Transfer*, **18**, 97-107.
- Tackie, E.N., A.P. Watkinson and J.K. Brimacombe (1990). "Mathematical Modeling of the Elutriation of Fine Materials from Rotary Kilns," *Can. J. Chem. Eng.*, **68**, 51-60.
- Tscheng, S.H. (1978). *Convective Heat Transfer in a Rotary Kiln*, Ph.d Dissertation, UBC, Vancouver.
- Tscheng, S.H. and A.P. Watkinson (1979). "Convective Heat Transfer in Rotary Kilns," *Can J. Chem Eng*, **57**, 433-443.
- Watkinson, A.P. (1993). *Personal Communications*.
- Wes, G.W.J., A.A.H. Drinkenburg, and S. Stemerding (1976). "Heat Transfer in a Horizontal Rotary Drum Reactor," *Powder Technology*, **13**, 185-192.
- Whitaker, S. (1980). "Radiant Energy Transport in Porous Media," *Ind. Eng. Chem. Fundamentals*, **19**, 210-218.
- Williams, J.C. and M.I. Khan (1973). "The Mixing and Segregation of Particulate Solids of Different Particle Size," *The Chemical Engineer*, **269**, 19-25.
- Yagi, S. and D. Kunii (1965). "Studies on Effective Thermal Conductivities in Packed Beds," *AIChE J.*, **3**, p 373.
- Zablotny, W.W. (1965). "The Movement of the Charge in Rotary Kilns," *Intern. Chem. Eng.*, **5**(2), 360-366).
- Zhang, Y. and C.S. Campbell (1992). "The Interface Between Fluid-like and Solid-like Behaviour in Two-dimensional Granular Flows," *J. Fluid Mech.*, **237**, 541-568.

Appendix A1: On the Observed Instabilities in Material Flow

So far in the experimental campaign, the effects of the field variables, v , \tilde{T} , and u on the rheological behavior of the three materials have been quantitatively related and discussed. The stresses that carry the momentum transport can be attributed to the shear and normal stresses; while the latter is simply the overburden pressure, the former comprises the static, streaming, and collisional stresses. As was shown earlier, for any granular material at yield, the forces that act on the particles are the normal forces that determine the stiffness coefficient of the material, and the tangential forces that determine the coefficient of friction. It was also shown that the coefficient of restitution of the material determines the inelasticity of the collisions that contribute to the collisional stress component. Thus, it was shown that for rice and limestone which have a relatively low coefficient of restitution and higher angle of repose as compared to polyethylene, instabilities developed because of low energy dissipation. These instabilities appeared in the form of non-isotropic granular temperature, bifurcations in the dynamic friction angle, and hence structure and wave formation giving rise to multiple (periodic) velocity profiles on the lateral plane (see, Figure 4.20). Inhomogeneities, clustering, and structure formation are found in fluidized beds, sedimentation transport, etc. but it is only recently that more than a perfunctory attention has been given to instabilities in granular shear flows (Savage 1992). In his recent molecular dynamic simulation of couette granular flow Savage introduced slight perturbations into the constitutive equations of Lun *et al.* (1984) and the permissible solutions were sinusoidal plane waves with wave number relating to the mean shear flow. The computer simulation revealed that at low coefficient of restitution ($e_p \leq 0.1$) strong anisotropy in granular temperature emerged; the resulting instabilities were attributed to low energy dissipation associated with low coefficient of restitution of the material.

The origin of the perturbations in the flow in rotary kilns that brought about the granular temperature results presented in the text for rice and limestone cannot be attributed to only the forces mentioned earlier (i.e., normal, tangential, and collisional) but must also be due to additional forces created by the rotating boundary conditions. The fluid-like behavior of granular flows will obviously

enhance the importance of the centrifugal as well as the Coriolis forces as is found in real fluids rotating as a whole (Greenspan, 1968). Although the former plays a role in establishing behavior boundaries and has been included in the net forces for which the material would cascade over the bed surface, i.e., after leaving the plug flow region (Henein, *et al.*, 1981; Pershin, 1988), in the 'fluidized' or grain inertia regime, which the active layer can be represented, it plays a trivial role. As in real fluids, it is rather the restoring effect of Coriolis forces that restricts the displacement of the fluid-like 'elements'. The extent of this restoring effect depends on the relative magnitudes of the Coriolis forces and the inertia forces acting on the particles. For example, for real fluids in rotating frames if u is the translational velocity relative to the rotating axes and L is the distance over which the velocity varies, e.g. the chord length of exposed bed surface in the rotary drum, the ratio of the magnitudes of the inertia term, $u \cdot \nabla u$, and the Coriolis term, $2\omega \times u$, is of order $R_o (= u/L\omega)$, the *Rossby number* (Batchelor, 1967). When $R_o \gg 1$, Coriolis forces are likely to cause only a slight effect on the flow pattern; but when $R_o \ll 1$, there is the tendency for Coriolis forces to oppose any expansion in the lateral plane, and Coriolis forces are likely to be dominant (i.e., the Coriolis forces tend to overcome lateral expansion and result in cascading free surface). For a Rossby number of order unity a mixture of the effects is likely to develop. In the lateral plane of the rotary kiln, therefore, in the limit as $R_o \rightarrow 0$, the form of the streamlines formed in the active layer must be consistent with a zero rate of expansion or dilation in the lateral plane. In view of this, therefore, for low coefficient of restitution materials in which there are few elastic collisions (analogous to inviscid fluid) there is little or no dissipation of energy and it follows that the displacement which is given to the particles by the rotating wall near the right apex may set up an oscillation. Like in real fluids (Batchelor, 1967) this raises the possibility that a train of waves can propagate through a rotating fluid, with different phases of the waves being associated with positive and negative values of expansion in the lateral plane. It is therefore not surprising to see multiple parabolic profiles in the surface velocity measurements.

In the experiments carried out here in the present work, the Coriolis effect discussed above was not restricted to the lateral plane alone; there was also a dynamic imbalance set by Coriolis acceleration in the axial direction as well and waves were created along the axial plane. Particularly for limestone, which had a wider particle size range, forced oscillations were visually observed. These oscillations resulted into banding (axial segregation) whereby structure formation of smaller and larger particles formed along the length of the drum. These bands had width of as wide as 15 cm and moved back and forth alternating positions in a bounded oscillatory wave motion. In order to ascertain that such imbalance was not a result of the batch process or malfunction due to the drum design, investigations were pursued in the pilot kiln as well. It was found that these waves were present also in the pilot kiln except that, because of the continuous operation and unbounded ends, this axial wave motion was dumped as free oscillations. It is possible to speculate that there is a direct relationship between axial segregation and instabilities that are created as a result of the rheological behavior of low coefficient of restitution materials in the rotary kiln. Suffice to say that the axial segregation problem has plagued rotary kiln performance for years (Donald and Roseman, 1962, Roseman and Donald, 1962) and the solution to the problem is still formidable in industrial kilns. The Rossby number, $v_{ax}/R\omega$, formed from the axial velocity and the kiln rotation is a measure of the relative importance of the effect of the axial translation and rotation of the body of particles. Because the particles make over three turns in the kiln during one complete revolution, this ratio is expected to be small and, in the limit, the rate of expansion in the lateral plane, on the whole, will be zero everywhere in the cross-section. This requires that the axial component of the velocity be independent of the chord length, which is possible only when an axial advance of particles is accomplished and a column of material is pushed ahead. As is explained in Batchelor (1967) experiments on fluids in a rotating cylinder show the validity of this phenomenon. In view of the above, the oscillatory motion may occur even when the drum is horizontal and such was the observation in the current experiments. On this note, it may be pointed out that whenever there is

a range of particle size distribution there will be the tendency for the small particles to be separated from the larger ones in the axial direction since larger particles move farther than smaller ones in a flow field.

In conclusion, it can be said that for low coefficient of restitution materials low energy dissipation results in instabilities in the bulk movement of the active layer. This phenomenon is analogous to instabilities encountered in fluid flow in rotating frames and can be attributed to the effects of Coriolis forces tending to overcome inertia forces. Periodic function of multiple parabolic velocity profiles therefore develop at the exposed bed surface for limestone at high speeds of rotation. In the axial plane, the Coriolis effect results in forced oscillation which is bounded by the two end-pieces. Although more work is imperative in this direction, this wave formation is believed to be the source of axial segregation, also known as banding, in industrial kilns.

Appendix A2: Transformation of the Equations of Motion into Primitive Variables

The governing equations for granular flow are given as;

$$\frac{\partial \rho}{\partial t} + \nabla \cdot (\rho \mathbf{u}) = 0$$

$$\rho \frac{D\mathbf{u}}{Dt} = \rho \mathbf{g} - \nabla \cdot \mathbf{P}$$

$$\frac{3}{2} \rho \frac{D\tilde{T}}{Dt} = -\nabla \cdot \mathbf{q}_{PT} - \mathbf{P} : \nabla \mathbf{u} - \gamma$$

with the kinetic contribution of the stress tensor given as

$$\begin{aligned} \mathbf{P} = & [\rho \tilde{T} (1 + 4\eta v g_o) - \eta \mu_b \nabla \cdot \mathbf{u}] \mathbf{I} \\ & - \left\{ \frac{2\mu}{\eta(2-\eta)g_o} \left(1 + \frac{8}{5} \eta v g_o \right) \left[1 + \frac{8}{5} \eta (3\eta - 2) v g_o \right] + \frac{6}{5} \mu_b \eta \right\} \mathbf{S} \end{aligned}$$

\mathbf{S} is the deviatoric stress and is given by the equation,

$$\mathbf{S} = \frac{1}{2} (\mathbf{u}_{i,j} + \mathbf{u}_{j,i}) - \frac{1}{3} \mathbf{u}_{k,k} \delta_{ij}$$

where δ_{ij} is the kronecker delta.

The flux of pseudo-thermal energy is given as;

$$\begin{aligned} \mathbf{q}_{PT} = & -\frac{\lambda_i}{g_o} \left\{ \left(1 + \frac{12}{5} \eta v g_o \right) \left[1 + \frac{12}{5} \eta^2 (4\eta - 3) v g_o \right] \right. \\ & \left. + \frac{64}{25\pi} (41 - 33\eta) (\eta v g_o)^2 \right\} \nabla \tilde{T} \\ & - \frac{\lambda_i}{g_o} \left(1 + \frac{12}{5} \eta v g_o \right) \frac{12}{5} \eta (2\eta - 1) (\eta - 1) \frac{d}{dv} (v^2 g_o) \frac{\tilde{T}}{v} \nabla v \end{aligned}$$

where the dissipation of energy due to inelastic collisions is also given as;

$$\gamma = \frac{48}{\sqrt{\pi}} \eta(1-\eta) \rho_p \frac{v^2}{d_p} \tilde{T}^{3/2}$$

Let us make the following representations:

$$A = \rho \tilde{T} (1 + 4\eta v g_o) \quad (A2.1)$$

$$B = \eta \mu_b \quad (A2.2)$$

$$C = \frac{2\mu}{\eta(2-\eta)g_o} \left(1 + \frac{8}{5} \eta v g_o \right) \left[1 + \frac{8}{5} \eta(3\eta - 2) v g_o \right] + \frac{6}{5} \mu_b \eta \quad (A2.3)$$

The stress tensor, therefore, becomes

$$\mathbf{P} = [A - B(\nabla \cdot \mathbf{u})] \mathbf{I} - C \mathbf{S} \quad (A2.4)$$

Let also $D = A - B(\nabla \cdot \mathbf{u})$, then for a two-dimensional domain,

$$D = A - B \left(\frac{\partial u_x}{\partial x} + \frac{\partial u_y}{\partial y} \right)$$

$$\nabla \cdot \mathbf{P} = \begin{pmatrix} \frac{\partial P_{xx}}{\partial x} + \frac{\partial P_{xy}}{\partial y} \\ \frac{\partial P_{yx}}{\partial x} + \frac{\partial P_{yy}}{\partial y} \end{pmatrix} \quad (A2.5)$$

The deviatoric stress tensor is given for the two-dimensional coordinate system as;

$$\mathbf{S} = \frac{1}{2} \left(\frac{\partial u_i}{\partial x_j} + \frac{\partial u_j}{\partial x_i} \right) - \frac{1}{2} \frac{\partial u_k}{\partial x_k} \delta_{ij}$$

$$\delta_{ij} = \mathbf{I} = \begin{pmatrix} 1 & 0 \\ 0 & 1 \end{pmatrix}$$

$$\mathbf{S} = \begin{pmatrix} S_{xx} & S_{xy} \\ S_{yx} & S_{yy} \end{pmatrix}$$

Therefore

$$\mathbf{S} = \begin{pmatrix} \frac{\partial u_x}{\partial x} - \frac{1}{2} \left(\frac{\partial u_x}{\partial x} + \frac{\partial u_y}{\partial y} \right) & \frac{1}{2} \left(\frac{\partial u_x}{\partial y} + \frac{\partial u_y}{\partial x} \right) \\ \frac{1}{2} \left(\frac{\partial u_x}{\partial y} + \frac{\partial u_y}{\partial x} \right) & \frac{\partial u_y}{\partial y} - \frac{1}{2} \left(\frac{\partial u_x}{\partial x} + \frac{\partial u_y}{\partial y} \right) \end{pmatrix} \quad (\text{A2.6})$$

The stress tensor is expanded as

$$\mathbf{P} = \begin{pmatrix} A - B \left(\frac{\partial u_x}{\partial x} + \frac{\partial u_y}{\partial y} \right) - CS_{xx} & -CS_{xy} \\ -CS_{yx} & A - B \left(\frac{\partial u_x}{\partial x} + \frac{\partial u_y}{\partial y} \right) - CS_{yy} \end{pmatrix} \quad (\text{A2.7})$$

also,

$$\nabla \cdot \mathbf{u} = \begin{pmatrix} \frac{\partial u_x}{\partial x} & + & \frac{\partial u_x}{\partial y} \\ \frac{\partial u_y}{\partial x} & + & \frac{\partial u_y}{\partial y} \end{pmatrix}$$

$$\nabla \cdot \mathbf{q} = \begin{pmatrix} \frac{\partial q_x}{\partial x} & + & \frac{\partial q_x}{\partial y} \\ \frac{\partial q_y}{\partial x} & + & \frac{\partial q_y}{\partial y} \end{pmatrix}$$

therefore

$$\mathbf{P} \cdot \nabla \mathbf{u} = P_{xx} \frac{\partial u_x}{\partial x} + P_{xy} \frac{\partial u_y}{\partial x} + P_{yx} \frac{\partial u_x}{\partial y} + P_{yy} \frac{\partial u_y}{\partial y} \quad (\text{A2.9})$$

Substituting Eq. A2.1 through Eq. A2.9 into the equations of motion gives;

$$\frac{\partial u}{\partial x} + \frac{\partial v}{\partial y} = 0 \quad (\text{A2.10})$$

$$\rho \left[u \frac{\partial u}{\partial x} + v \frac{\partial u}{\partial y} \right] = \rho g \sin \xi - \frac{\partial P_{xx}}{\partial x} - \frac{\partial P_{xy}}{\partial y} \quad (\text{A2.12})$$

$$\rho \left[u \frac{\partial v}{\partial x} + v \frac{\partial v}{\partial y} \right] = -\rho g \cos \xi - \frac{\partial P_{xy}}{\partial x} - \frac{\partial P_{yy}}{\partial y} \quad (\text{A2.13})$$

$$\rho \left[u \frac{\partial \tilde{T}}{\partial x} + v \frac{\partial \tilde{T}}{\partial y} \right] = - \left[\frac{\partial q}{\partial x} + \frac{\partial q}{\partial y} \right] - \left[P_{xx} \frac{\partial u}{\partial x} + P_{xy} \frac{\partial v}{\partial x} + P_{yx} \frac{\partial u}{\partial y} + P_{yy} \frac{\partial v}{\partial y} \right] - \gamma \quad (\text{A2.14})$$

These are the granular flow equations given as Eq. 5.7 through Eq. 5.10 in the text.

Appendix A3: Normalization of the Equations of Motion

In order to apply boundary layer solution to the active layer flow, it is important to perform an order of magnitude analysis and to establish which of the terms in the equation will predominate. This analysis is carried out by normalizing the equations with the active layer depth and the chord length. The scaling parameters were given in the text as;

$$(x, y) = ([L]x^*, [\Delta]y^*)$$

$$(u, v) = \left([(gL)^{1/2}]u^*, \left[\frac{\Delta}{L} (gL)^{1/2} \right]v^* \right) \quad (5.11)$$

$$(P_{xx}, P_{yy}, P_{xy}) = [\rho g \cos \xi \Delta] (P_{xx}^*, P_{yy}^*, \tan \xi P_{xy}^*) \quad (A3.1)$$

Substituting these parameters into the equations of motion would yield;

continuity equation:

$$\frac{\partial [(gL)^{1/2}]u^*}{\partial [L]x^*} + \frac{\partial \left[\frac{\Delta}{L} (gL)^{1/2} \right]v^*}{\partial [\Delta]y^*} = 0$$

Rearranging the equation would give;

$$\frac{(gL)^{1/2}}{L} \frac{\partial u^*}{\partial x^*} + \frac{(gL)^{1/2} \Delta}{\Delta L} \frac{\partial v^*}{\partial y^*} = 0$$

but

$$\frac{(gL)^{1/2}}{L} \cdot \frac{\Delta L}{(gL)^{1/2} \Delta} = 1$$

Therefore the continuity equation becomes;

$$\frac{\partial u^*}{\partial x^*} + \frac{\partial v^*}{\partial y^*} = 0 \quad (A3.2)$$

x-wise momentum equation:

$$\begin{aligned} & \rho \left[(gL)^{1/2} u^* \frac{\partial [(gL)^{1/2} u^*]}{\partial [L]x^*} + \left[\frac{\Delta}{L} (gL)^{1/2} \right] v^* \frac{\partial [(gL)^{1/2} u^*]}{\partial [\Delta]y^*} \right] \\ & = \rho g \sin \xi - \frac{\partial [\rho g \cos \xi] P_{xx}^*}{\partial [L]x^*} - \frac{\partial [\rho g \cos \xi \Delta] P_{xy} \tan \xi}{\partial [\Delta]y^*} \end{aligned}$$

rearranging the equation would yield,

$$\begin{aligned} & \rho \frac{(gL)^{1/2} \cdot (gL)^{1/2}}{L} u^* \frac{\partial u^*}{\partial x^*} + \rho \frac{\frac{\Delta}{L} (gL)^{1/2} (gL)^{1/2}}{\Delta} v^* \frac{\partial u^*}{\partial y^*} \\ & = \rho g \sin \xi - \rho g \cos \xi \frac{\Delta}{L} \frac{\partial P_{xx}^*}{\partial x^*} - \rho g \cos \xi \tan \xi \frac{\partial P_{xy}^*}{\partial y^*} \end{aligned}$$

by making the substitution $\varepsilon = \Delta/L$, and dividing by ρg , the x-wise momentum equation reduces to;

$$u^* \frac{\partial u^*}{\partial x^*} + v^* \frac{\partial u^*}{\partial y^*} = \sin \xi - \varepsilon \cos \xi \frac{\partial P_{xx}^*}{\partial x^*} - \sin \xi \frac{\partial P_{xy}^*}{\partial y^*} \quad (A3.3)$$

y-wise momentum equation:

$$\begin{aligned} & \rho \left[(gL)^{1/2} u^* \frac{\partial \left[\frac{\Delta}{L} (gL)^{1/2} \right] v^*}{\partial [L]x^*} + \frac{\Delta}{L} (gL)^{1/2} v^* \frac{\partial \left[\frac{\Delta}{L} (gL)^{1/2} \right] v^*}{\partial [\Delta]y^*} \right] \\ & = -\rho g \cos \xi - \frac{\rho g \cos \xi \tan \xi \Delta}{L} \frac{\partial P_{xy}^*}{\partial x^*} - \frac{\rho g \cos \xi \Delta}{\Delta} \frac{\partial P_{yy}^*}{\partial y^*} \end{aligned}$$

rearranging gives;

$$\begin{aligned} & \left[\rho (gL)^{1/2} \frac{\Delta (gL)^{1/2}}{L} \right] u^* \frac{\partial v^*}{\partial x^*} + \left[\rho (gL)^{1/2} (gL)^{1/2} \frac{\Delta}{L} \cdot \frac{\Delta}{L \Delta} \right] v^* \frac{\partial v^*}{\partial y^*} \\ & = -\rho g \cos \xi - \frac{\Delta}{L} \rho g \cos \xi \tan \xi \frac{\partial P_{xy}^*}{\partial x^*} - \rho g \cos \xi \frac{\partial P_{yy}^*}{\partial y^*} \end{aligned}$$

the y-wise momentum equation also reduces to;

$$\varepsilon \left[u^* \frac{\partial v^*}{\partial x^*} + v^* \frac{\partial u^*}{\partial y^*} \right] = -\cos \xi - \varepsilon \cos \xi \tan \xi \frac{\partial P_{xy}^*}{\partial x^*} - \cos \xi \frac{\partial P_{yy}^*}{\partial y^*} \quad (\text{A3.4})$$

Recognizing that the active layer depth, even at mid-chord, is only a few particles away, the terms involving ε may be very small compared with the remaining terms. Therefore, as $\varepsilon \rightarrow 0$, Eq A3.2, A3.3, and A3.4 respectively reduce to;

$$\begin{aligned} \frac{\partial u^*}{\partial x^*} + \frac{\partial v^*}{\partial y^*} &= 0 \\ u^* \frac{\partial u^*}{\partial x^*} + v^* \frac{\partial u^*}{\partial y^*} &= \sin \xi - \sin \xi \frac{\partial P_{xy}^*}{\partial y^*} \\ \frac{\partial P_{yy}^*}{\partial y^*} &= 1 \end{aligned} \quad (\text{A3.5})$$

Eq. A3.5 are the boundary layer equations given in the text.

Appendix A4: About the Apparent Viscosity

The term C' from the constitutive relations of Lun *et al.* (1984) represents the 'apparent viscosity' if an analogy is drawn from fluid flow. In this Appendix, the expression for C' is derived in terms of the coefficient of restitution of the particles, the solid volume fraction, particle size, and the granular temperature. Having derived this relationship, a numerical example is given with known data so as to gain an insight on the numerical values of this apparent viscosity by comparing it with fluid flow data. Recalling that the shear stress term was given in the test as;

$$P_{xy} = \frac{\partial}{\partial y} \left(C' \frac{\partial u}{\partial y} \right)$$

where $C' = C/2$

$$C = \frac{2\mu}{\eta(2-\eta)g_o} \left(1 + \frac{8}{5}\eta v g_o \right) \left[1 + \frac{8}{5}\eta(3\eta-2)v g_o \right] + \frac{6}{5}\mu_b \eta \quad cf(A2.3)$$

and

$$\mu_b = 256\mu v^2 g_o / 5\pi$$

$$\mu = 5m(\tilde{T}/\pi)^{1/2} / 16d_p^2$$

$$m = \rho_p V = \rho_p \frac{\pi}{6} d_p^3$$

substitution of these equations into C' would yield;

$$C' = \frac{5\sqrt{\pi}}{96} \rho_p d_p \tilde{T}^{1/2} \left[\frac{1}{\eta(2-\eta)g_o} \left(1 + \frac{8}{5}\eta v g_o \right) \left\{ 1 + \frac{8}{5}\eta(3\eta-2)v g_o \right\} + \frac{768}{25\pi} v^2 g_o \right] \quad (A4.1)$$

the term in the square bracket may be expanded to give;

$$C' = -g_2(v, \epsilon_p) \rho_p d_p \tilde{T}^{1/2} \quad (A4.2)$$

with $g_2(v, \varepsilon_p)$ given as;

$$g_2(v, \varepsilon_p) = \frac{5\sqrt{\pi}}{96} \left[\frac{1}{\eta(2-\eta)g_o} + \frac{8(3\eta-1)v}{5(2-\eta)} + \frac{64}{25} \left\{ \frac{\eta(3\eta-2)}{2-\eta} + \frac{12}{\pi} \right\} v^2 g_o \right] \quad (A4.3)$$

Data

$$\rho_p = 2.7 \text{ g/cm}^3 \quad v = 0.35$$

$$\varepsilon_p = 0.9 \quad d_p = 200 \mu\text{m} = 0.2 \text{ cm}$$

From chute flow experiments (Ahn *et al.*, 1991) a reasonable value for the granular temperature is taken as $\tilde{T} = 13.475 \text{ cm}^2/\text{s}^2$. Substituting these values into the terms in C' the viscosity terms become,

$$\mu = \frac{5 \times 1.131 \times 10^{-5} \left(\frac{13.475}{3.141} \right)^{1/2}}{16 \times 0.02^2} = 0.0366$$

$$\mu_b = \frac{256 \times 0.0366}{5 \times 3.141} \times 0.35^2 \times 1.339 = 0.0978$$

and the other parameters would be;

$$\eta = 0.95$$

$$\frac{2\mu}{\eta(2-\eta)g_o} = 0.0548$$

$$\frac{1}{2} \left(1 + \frac{8}{5} \eta v g_o \right) = 0.856$$

$$1 + \frac{8}{5} \eta (3\eta - 2) v g_o = 1.6055$$

$$\frac{6}{5} \mu_b \eta = 0.1115$$

substitution into C gives,

$$\begin{aligned}
C &= 0.055 \times 0.856 \times 1.6055 + 0.1115 = 0.18686 \text{ g/cm} \cdot \text{s} \\
C' &= C/2 = 0.09343 \text{ g/cm} \cdot \text{s} \\
&= 0.93 \times 10^{-2} \text{ kg/m} \cdot \text{s}
\end{aligned}$$

Noting that the viscosity of liquid lead is reported as $1.03 \times 10^{-2} \text{ kg/m} \cdot \text{s}$, the value of C' calculated for sand particles at solid volume fraction of 0.35 is quite reasonable. The example shows that the material coefficients that are mathematically derived from the collision theory can be quite comparable with conventional fluid flow coefficients. Obviously the value of C' depends on the velocity fluctuations (granular temperature) and the coefficient of restitution of the particles as well as the dilation.

Similar expressions like Eq. A4.2 may be given for normal stress, the flux of velocity fluctuations, and the energy dissipation as (Johnson and Jackson, 1987):

The normal stress

$$P_{xx} = P_{yy} = \rho_p g_1(v, \epsilon_p) \tilde{T} \quad (\text{A4.4})$$

The flux of fluctuating energy in the normal direction is given as;

$$q_y = -\rho_p d_p \left(g_3(v, \epsilon_p) \tilde{T}^{1/2} \frac{d\tilde{T}}{dy} + g_4(v, \epsilon_p) \tilde{T}^{1/2} \frac{dv}{dy} \right) \quad (\text{A4.5})$$

and finally, the dissipation rate per unit volume due to inelastic collisions is also given as;

$$\gamma = \frac{\rho}{d_p} g_5(v, \epsilon_p) \tilde{T}^{3/2} \quad (\text{A4.6})$$

The coefficients g_1 , g_2 , g_3 , g_4 , and g_5 are functions of the solids volume fraction and the coefficient of restitution of the particles. They are also related to the solids linear concentration function, $g_o(v)$; they are given by Johnson and Jackson (1987), and shown in Table 5.A1

Table 5.A1

$$g_o(v) = \left(1 - \frac{v}{v_*}\right)^{-1/3}$$

$$g_1(v, \epsilon_p) = v + 4\eta v^2 g_o(v)$$

$$g_2(v, \epsilon_p) = \frac{5\sqrt{\pi}}{96} [1/\eta(2-\eta) \cdot 1/g_o(v) + 8/5(3\eta-1)/(2-\eta) \cdot v \\ + \frac{64}{25}\eta((3\eta-2)/(2-\eta) + 12/\pi)\eta^2 g_o(v)]$$

$$g_3(v, \epsilon_p) = 25\sqrt{\pi}/16\eta(41-33\eta) [1/g_o(v) + 12/5\eta\{1 + \eta(4\eta-3)\}\eta \\ + 16/25\eta^2\{9\eta(4\eta-3) + 4/\pi(41-33\eta)\}v^2 g_o(v)]$$

$$g_4(v, \epsilon_p) = \frac{15\sqrt{\pi}}{4} (2\eta-1)(\eta-1)/(41-33\eta) (1/v g_o(v) + 12/5 \cdot \eta) \frac{d}{dv} \{v^2 g_o(v)\}$$

Appendix A5: Derivation of Integro-Momentum Equations

(i) Mass flow through plane 1

$$\int_0^H \rho u dy$$

(ii) Momentum flow through plane 1

$$\int_0^H \rho u u dy = \int_0^H \rho u^2 dy$$

(iii) Momentum flow through plane 2

$$\int_0^H \rho u^2 dy + \frac{d}{dx} \left(\int_0^H \rho u^2 dy \right) dx$$

(iv) Mass flow through plane 2

$$\int_0^H \rho u dy + \frac{d}{dx} \left(\int_0^H \rho u dy \right) dx$$

Considering mass conservation and the fact that no mass enters the control volume through the free surface, the additional mass in the mass flow equation must come from the active layer/plug flow interface. This mass carries with it, in the x-direction, a momentum which is equal to

$$u_{\delta} \frac{d}{dx} \left(\int_0^H \rho u dy \right) dx$$

where

$$u_{\delta} = -u_r \cos \theta$$

From Figure 5.3, θ is the angular measure of any x-position on the surface plane. Hence θ_{\max} will be the maximum angle subtended by the entire bed depth and depicts another measure of the degree of fill of the kiln. The net momentum flow out of the control volume is therefore,

$$\frac{d}{dx} \left(\int_0^H \rho u^2 dy \right) dx - u_\delta \frac{d}{dx} \left(\int_0^H \rho u dy \right) dx \quad (A5.1)$$

By employing the mathematical manipulation (see, e.g., Holman, 1981),

$$\begin{aligned} d(\zeta\phi) &= \zeta d\phi + \phi d\zeta \\ \zeta d\phi &= d(\zeta\phi) - \phi d\zeta \end{aligned}$$

and allowing the following transformation,

$$\phi = \int_0^H \rho u dy \quad ; \quad \zeta = u_\delta$$

the following equations are obtained

$$\begin{aligned} u_\delta \frac{d}{dx} \left(\int_0^H \rho u dy \right) dx &= \frac{d}{dx} \left(u_\delta \int_0^H \rho u dy \right) dx - \frac{du_\delta}{dx} \left(\int_0^H \rho u dy \right) dx \\ &= \frac{d}{dx} \left(\int_0^H \rho u_\delta u dy \right) dx - \frac{du_\delta}{dx} \left(\int_0^H \rho u dy \right) dx \end{aligned} \quad (A5.2)$$

where u_δ has been placed inside the integral in the last relationship as if it were independent of y .

Substituting Eq. 5.16 into 5.15 the net momentum equation becomes;

$$\rho \frac{d}{dx} \left(\int_0^H (u^2 - u_\delta u) dy \right) dx + \frac{du_\delta}{dx} \left(\int_0^H \rho u dy \right) dx \quad (A5.3)$$

Appendix A6: Velocity Profile for Flow in the Active Layer

The velocity profile with the appropriate boundary conditions are;

$$u = a_o + a_1y + a_2y^2 \quad (A6.1)$$

$$@ \quad y = \alpha \quad u = 0 \quad (A6.1a)$$

$$@ \quad y = \delta \quad u = u_\delta \quad (A6.1b)$$

$$@ \quad y = 0 \quad u = u_s \quad (A6.1c)$$

Substituting the boundary condition gives three equations

$$u_s = a_o \quad (A6.2a)$$

$$0 = a_o + a_1\alpha + a_2\alpha^2 \quad (A6.2b)$$

$$-u_\delta = a_o + a_1\delta + a_2\delta^2 \quad (A6.2c)$$

which can be reduced to the following two equations

$$a_1\alpha\delta + a_2\alpha^2\delta = -u_s\delta \quad (A6.3a)$$

$$a_1\alpha\delta + a_2\alpha\delta^2 = -(u_s + u_\delta)\alpha \quad (A6.3b)$$

from which

$$a_2 = \frac{u_s\delta - (u_s + u_\delta)\alpha}{(\alpha\delta^2 - \alpha^2\delta)} \quad (A6.4)$$

But from Eq. A4.2b

$a_1 = -u_s - a_2\alpha^2/\alpha$ which, therefore, upon substitution of a_2 into a_1 , gives

$$a_1 = \frac{-u_s\delta^2 + (u_s + u_\delta)\alpha^2}{\alpha\delta^2 - \alpha^2\delta} \quad (A6.5)$$

Substituting a_0 , a_1 and a_2 into Eq. A4.1 yields;

$$u = u_s + \frac{u_s(\alpha^2 - \delta^2) + u_\delta \alpha^2}{\alpha\delta^2 - \alpha^2\delta} y + \frac{u_s(\delta - \alpha) - u_\delta \alpha}{\alpha\delta^2 - \alpha^2\delta} y^2 \quad (A6.6)$$

Recognizing that $u_s = C_o \omega R$ and $u_\delta = \omega r_x$,

$$u_s = \frac{C_o R}{r_x} u_\delta = \kappa u_\delta \quad (A6.7)$$

and therefore by rearranging Eq. A6.6 the velocity profile may be given as:

$$\frac{u}{u_\delta} = \kappa + \frac{\kappa\alpha^2 - \kappa\delta^2 + \alpha^2}{\alpha\delta^2 - \alpha^2\delta} y + \frac{\kappa\delta - \kappa\alpha - \alpha}{\alpha\delta^2 - \alpha^2\delta} y^2 \quad (A6.8)$$

For example when $\alpha = 0.75\delta$ is substituted into Eq. A4.8 and rearranged, the resulting velocity profile will be,

$$\frac{u}{u_\delta} = \kappa + (3 - 2.33\kappa) \left(\frac{y}{\delta}\right) - (4 - 1.33\kappa) \left(\frac{y}{\delta}\right)^2 \quad (A6.9)$$

or

$$\frac{u}{u_\delta} = \kappa + a_1 \left(\frac{y}{\delta}\right) - a_2 \left(\frac{y}{\delta}\right)^2 \quad (A6.10)$$

Equations A4.9 and A4.10 are given in the text, respectively, as Eq. 5.33 and Eq. 5.34.

Appendix A7: Relationship Between Jetsam Loading and Number Concentration

The relationship between jetsam loading and number concentration is established as follows:

Let the respective weight fractions of jetsam and flotsam loading be Wt_J and Wt_F so that;

$$\begin{aligned} Wt_J &= \frac{1}{6}n_J\pi d_{pJ}^3\rho_J \\ Wt_F &= \frac{1}{6}n_F\pi d_{pF}^3\rho_F \end{aligned} \quad (A7.1)$$

The jetsam concentration at kiln loading will be

$$\begin{aligned} C_{JO} &= \frac{Wt_J}{Wt_J + Wt_F} \\ &= \frac{1/6n_J\pi d_{pJ}^3\rho_J}{1/6n_J\pi d_{pJ}^3\rho_J + 1/6n_F\pi d_{pF}^3\rho_F} \end{aligned} \quad (A7.2)$$

For equal density particles, $\rho_J = \rho_F$,

$$C_{JO} = \frac{n_J d_{pJ}^3}{n_J d_{pJ}^3 + n_F d_{pF}^3} \quad (A7.3)$$

Letting $\bar{\eta} = n_J/n_F$ and $\bar{\sigma} = d_{pJ}/d_{pF}$, Eq. A7.3 becomes,

$$C_{JO} = \frac{\bar{\eta}\bar{\sigma}^3}{\bar{\eta}\bar{\sigma}^3 + 1} \quad (A7.4)$$

where the solid fraction has been assumed unity. From the above relationship the number ratio required for the calculation of the percolation velocity can be computed for any jetsam loading by specifying the size ratio.

Appendix A8: Application of Hopf Transformation

The differential equation given for CASE III can be solved by Hopf transformation (see, e.g., Ames, 1965). The equation may be re-written as;

$$D \frac{\partial^2 C}{\partial y^2} + v(1-2C) \frac{\partial C}{\partial y} - u \frac{\partial C}{\partial x} = 0 \quad (\text{A8.1})$$

Let

$$R(x, y) = 2C(x, y) - 1 \quad (\text{A8.2})$$

so that

$$\begin{aligned} \frac{\partial R(x, y)}{\partial y} &= 2 \frac{\partial C(x, y)}{\partial y} \\ \frac{\partial^2 R(x, y)}{\partial y^2} &= 2 \frac{\partial^2 C(x, y)}{\partial y^2} \\ \frac{\partial R(x, y)}{\partial x} &= 2 \frac{\partial C(x, y)}{\partial x} \end{aligned} \quad (\text{A8.3})$$

Substituting Eq. A8.3 into Eq. A8.1 gives;

$$D \frac{\partial^2 R(x, y)}{\partial y^2} = vR(x, y) \frac{\partial R(x, y)}{\partial y} + u \frac{\partial R(x, y)}{\partial x} \quad (\text{A8.4})$$

Set $R = \partial S / \partial y$ so that

$$\begin{aligned} \frac{\partial R}{\partial y} &= \frac{\partial^2 S}{\partial y^2} \\ \frac{\partial^2 R}{\partial y^2} &= \frac{\partial^3 S}{\partial y^3} \\ \frac{\partial R}{\partial x} &= \frac{\partial^2 S}{\partial y \partial x} \end{aligned} \quad (\text{A8.5})$$

Substituting Eq. A8.5 into Eq. A8.4 gives the transformation

$$D \frac{\partial^3 S}{\partial y^3} = v \frac{\partial S}{\partial y} \cdot \frac{\partial^2 S}{\partial y^2} + u \frac{\partial^2 S}{\partial y \cdot \partial x} \quad (\text{A8.6})$$

for which the first two terms can be rearranged as

$$\frac{\partial}{\partial y} \left[D \frac{\partial^2 S}{\partial y^2} - \frac{v}{2} \left(\frac{\partial S}{\partial y} \right)^2 \right] = 0$$

Integrating w.r.t y, having set the arbitrary function of x to zero, gives the solution of the differential equation as;

$$D \frac{\partial^2 S}{\partial y^2} - \frac{v}{2} \left(\frac{\partial S}{\partial y} \right)^2 = 0 \quad (\text{A8.7})$$

When the function w.r.t x is introduced the original differential equation Eq. A8.1 becomes

$$D \frac{\partial^2 S}{\partial y^2} = \frac{v}{2} \left(\frac{\partial S}{\partial y} \right)^2 + u \frac{\partial S}{\partial x} \quad (\text{A8.8})$$

It is desired to make Eq. A8.8 a linear equation of the form;

$$D \frac{\partial^2 \tilde{Q}}{\partial y^2} = u \frac{\partial \tilde{Q}}{\partial x} \quad (\text{A8.9})$$

where

$$T(x, y) = F(S(x, y))$$

$$\frac{\partial T}{\partial y} = F'(S(x, y)) \cdot \frac{\partial S}{\partial y}$$

$$\frac{\partial T}{\partial x} = F'(S(x, y)) \cdot \frac{\partial S}{\partial x}$$

$$\frac{\partial^2 T}{\partial y^2} = F''(S(x, y)) \frac{\partial S}{\partial y} \cdot \frac{\partial S}{\partial y} + F'(S(x, y)) \frac{\partial^2 S}{\partial y^2} \quad (\text{A8.10})$$

Substituting Eq. A8.10 into Eq. A8.9 gives

$$D \left[F''(S) \left(\frac{\partial S}{\partial y} \right)^2 + F'(S) \frac{\partial^2 S}{\partial y^2} \right] = u F'(S) \frac{\partial S}{\partial x} \quad (\text{A8.11})$$

divide by $F'(S)$ for $F'(S) \neq 0$ so that

$$D \left[\frac{F''(S)}{F'(S)} \left(\frac{\partial S}{\partial y} \right)^2 + \frac{\partial^2 S}{\partial y^2} \right] = u \frac{\partial S}{\partial x} \quad (\text{A8.12})$$

By identifying Eq. A8.12 with Eq. A8.8 the following can be written

$$D \frac{F''(S)}{F'(S)} = -\frac{v}{2}$$

or

$$F''(S) = -\frac{v}{2D} F'(S)$$

which is integrated to give

$$F(S) = A \exp(-vS/2D) + B \quad (\text{A8.13})$$

Setting $A=1$ and $B=0$, and inverting gives

$$\begin{aligned} S &= -\frac{2D}{v} \ln F(S) \\ &= -\frac{2D}{v} \ln \tilde{Q} \end{aligned}$$

but $R = \partial S / \partial y$; therefore

$$R(x, y) = -(2D/v) \frac{\partial}{\partial y} (\ln \tilde{Q}) \quad (\text{A8.14})$$

Substituting Eq. A8.14 into Eq. A8.2 yields the solution for jetsam concentration for mixing and segregation in the active layer as;

$$\begin{aligned} C(x, y) &= \frac{1}{2}[R(x, y) + 1] \\ &= \frac{1}{2} \left[1 - \frac{2D}{v} \frac{\partial}{\partial y} (\ln \tilde{Q}) \right] \end{aligned} \quad (\text{A8.15})$$

where T is the solution for the special case of diffusional mixing given for CASE II in text.

Appendix A9: Density Compensation of Size Segregation

In order to prevent flotsam particles to float in a segregating medium the mass flux of upward and downward movement must balance. Thus, knowing the percolation velocities for each component, the mass flux must be set to zero, i.e.,

$$\rho_J v_{pJ} = \rho_F v_{pF}$$

where v_p is net percolation velocity. The density ratio required to accomplish the flux balance can be established by substituting the percolation velocities for jetsam and flotsam, i.e.,

$$\frac{\rho_F}{\rho_J} = \left[\bar{E} - E_m + 1 + \frac{(1 + \bar{\eta})\bar{\sigma}}{1 + \bar{\eta}\bar{\sigma}} \right] \exp \left[\frac{(1 + \bar{\eta})\bar{\sigma}/(1 + \bar{\eta}\bar{\sigma}) - E_m}{\bar{E} - E_m} \right] / \left[\bar{E} - E_m + 1 + \frac{(1 + \bar{\eta})}{1 + \bar{\eta}\bar{\sigma}} \right] \exp \left[-\frac{(1 + \bar{\eta})/(1 + \bar{\eta}\bar{\sigma}) - E_m}{\bar{E} - E_m} \right]$$

for a dilute case where, in the limit, $\bar{\eta} \rightarrow 0$,

$$\frac{\rho_F}{\rho_J} = \frac{[\bar{E} - E_m + 1 + \bar{\sigma}] \exp[(\bar{\sigma} - E_m)/(\bar{E} - E_m)]}{[\bar{E} - E_m + 2] \exp[-(1 - E_m)/(\bar{E} - E_m)]}$$

The above equation is simply the ratio of the probabilities of the formation of a voids diameter ratio, \bar{E} ; i.e., (D_v/\bar{D}) . By allowing the size of the void to be that of the jetsam particles, $D_v = d_{pJ}$, $E = 2/(1 + d_{pF}/d_{pJ})$. But $\bar{\sigma} = d_{pJ}/d_{pF}$ so therefore, a functional relation can be set between the density ratio and the size ratio; i.e.,

$$\frac{\rho_F}{\rho_J} = f \left(\frac{d_{pF}}{d_{pJ}} \right)$$

For closest packing $E_m = 0.1547$, and for a simple cubic array, $E_m = 0.414$.